Exploration of microbial activities that cause oxygen microenvironments within oxygenic photogranules for wastewater treatment

Hicham Ouazaite

THÈSE POUR OBTENIR LE GRADE DE DOCTEUR DE MONTPELLIER SUPAGRO

En Génie des Procédés

École doctorale GAIA – Biodiversité, Agriculture, Alimentation, Environnement, Terre, Eau
Portée par

Unité de recherche : Laboratoire de Biotechnologie et de l'Environnement, INRAE Narbonne

Exploration des activités microbiennes à l'origine du microenvironnement oxique dans les photogranules destinés au traitement des eaux usées

Exploration of microbial activities that cause oxygen microenvironments within oxygenic photogranules for wastewater treatment

Présentée par Hicham OUAZAITE
Le 09 mars 2021

Sous la direction de Jérôme HAMELIN
et Elie LE QUEMENER & Kim MILFERSTEDT, encadrants

Devant le jury composé de

Thierry RUIZ, Professeur, Université de Montpellier	*Président de jury*
Olivier BERNARD, DR, INRIA-Sophia Antipolis	*Rapporteur*
Filipa LOPES, Maître de conférences, CentraleSupélec, Paris Saclay	*Rapportrice*
Caitlyn BUTLER, Associate Professor, University of Massachusetts Amherst, USA	*Examinatrice*
Yolaine BESSIÈRE, Maître de conférences, INSA Toulouse	*Examinatrice*
Jérôme HAMELIN, DR, INRAE Occitanie-Montpellier	*Directeur de thèse*
Elie LE QUÉMÉNER, CR, INRAE Occitanie-Montpellier	*Invité*
Kim MILFERSTEDT, CR, INRAE Occitanie-Montpellier	*Invité*

UNIVERSITÉ DE MONTPELLIER

Montpellier SupAgro

Acknowledgments

This thesis work could never have been possible and completed without the moral support, friendship, dedication, and wise counsel of several people, to whom I would like to express my acknowledgments, gratefulness, and thanks.

First and foremost, I wish to express my gratitude and appreciation and to thank my supervisors, **Jérôme Hamelin**, **Kim Milferstedt** and **Elie Le Quéméner**. Thank you for trusting me and for accepting me as a PhD student. I learned a lot during this scientific journey and particularly from your advices that I will always keep preciously. Thank you for the freedom you gave me during my thesis. I thank you again for your sympathy and good mood, your disposition and especially for having allowed me to participate in the Franco-South Korea, Franco-Nederland adventures on photogranules research. Without forgetting also, the scientific cooperation ECOS with Mexico, which allowed me to supervise and share knowledge with other scientists. You were strongly involved in this thesis and the scientific discussions were motivating and of course you provided productive criticism. You have transferred technical and project management skills to me through rich and numerous discussions. Thank you for your patience and your encouragement especially these last months. Please know all my gratitude.

Special thanks to **Olivier Bernard** and **Felipa lopes** for agreeing to report my thesis work. I would like to thank also **Caitlyn Butler, Yolaine Bessière, Thierry Ruiz** agree to evaluate and examine this thesis manuscript.

My sincere thanks go to **Cristian Picioreanu**, you taught me a lot of things, I thank you for the knowledge you have given me, your scientific rigor, and your availability. Visiting your group in Delft University has been a huge milestone in my PhD life. There we started working on some initial ideas together on the modeling of the formation of photogranules in static conditions.

A big thanks also to **Thierry Ruiz** and **Nicolas Bernet** for their participation in my thesis committee and for your support and guidance along this thesis.

This project was made possible thanks to the LBE team. I would like to express my thanks to you all. **Philippe Sousbie** in particular contributed a lot to this project. Thank you for your involvement.

A special thanks to **Sylvie**, **Nadine**, **Annie**, **Alexandra**, **Véronique** and **Marjolaine** who are always there to help us, with your good mood.

And of course, a big thank you to the unbeatable SookJai Thai volleyball team: Captain **Anaïs**, **Chen**, **Yolanda**, **Yann**, **Florian**, **Chen**, **Ball, David, Gérald**, **Stephane** and of course the two pillars the great Alexander and Kevin.

This work is built on the shoulders of many, friends, and colleagues. **Lucia**, **Pablo**, **Kevin,** and **Alex** have been a great source of inspiration both for my scientific and day-to-day life. I will always remember your sharp ideas, help, discussions and of courses jokes (Kevin 😉). I know I still owe you a Tajine. I promise to invite you the day I handle this thesis.

I would like to thank my friend and my partner in crime (of course photogranules 😊) **Esmee Joosten.** Thank you for always being there with your smile and your friendship, and of course for sharing with me the challenges and the obstacles.

I would like to thank also my symbiose army: **Imane, Omar, Rachid, Samir, Yassine and, khay l3zawi Abdelhamid** for their support and encouragement and especially for being there during the Corona lockdown. A big and special thank you to our best friends **Adnan**, **Reda**, **Abdelaziz** and **Noureddine**.

I also thank **Noémie, Julien, Tonton Roland, Marie, Kevin D, Morand, Flo, Felipe, Yolanda**, **Farouk, Fernanda, Gaetano, Julie** and many other for making the atmosphere in the team always pleasant. And especially to you dear **Doha, Amine, Mohammed** for your friendship, your advice and your listening. **Yasser, Yassine, Sara, Jamal, Ikram** I thank you all for your friendship and your advices, the thesis is over, we can bag-pack now, no excuse!!

Most importantly, I thank my family, for their endless love and continuous encouragements. They supported me with their hard work so I can reach these days; I cannot imagine how difficult it must have been for them. It is impossible to record how grateful I am to them.

“Not until we are lost, do we begin to find ourselves.” Henry David Thoreau

Table of Contents

List of Figures

List of abbreviations

ADM: Anaerobic digestion model

AHLs: Acyl-Homoserine Lactones

ASM: Activated Sludge Models

CAD: Computer-Aided Design

CAS: Conventional Activated Sludge

COD: Chemical Oxygen Demand

CSTR: Continuously Stirring Tank Reactor

dCOD: Dissolved Organic Carbon

D_{eff}: Diffusion Coefficient

DO: Dissolved Oxygen

EPS: Extracellular Polymeric Substances

FEM: Finite Element Method

IbMs: Individual-based models

MAE: Mean Absolute Error

ODE: Ordinary Differential Equation

OPG: Oxygenic Photogranule

PAR: Photosynthetic Active Radiation

PDE: Partial Differential Equations

Pn: Net Photosynthesis

SBR: Sequencing Batch Reactor

SND: Simultaneous Nitrification and Denitrification

SSE: Sum of Squared Errors

TN: Total Nitrogen

UASB: Upflow Anaerobic Sludge Blanket Digestion

Abstract

Oxygenic photogranules (OPGs) are compact aggregates with a size up to 5 mm in diameter, composed of a light driven complex consortium of phototrophic and non-phototrophic microorganisms embedded into a matrix of extracellular polymeric substances. They have been recently the subject of growing interest for wastewater treatment and may constitute a potential alternative for the conventional activated sludge process.

This thesis was carried out in the frame of the PSST (Photogranules Shake Sewage Treatment up) ANR project, which aims to understand mechanisms of OPGs formation and to evaluate their potential for wastewater treatment. OPGs biological activity is driven by several parameters, like microbial composition, granule morphology and abiotic factors (i.e., light, available organic carbon in the surrounding environment). Experiments (microscopy, microsensors & planar optodes) as well as mathematical modelling (1D & 2D reaction-diffusion models) were combined during this work. The objective of this PhD thesis was to model the role of OPGs morphology and abiotic factors in shaping oxygen concentrations at the microscale.

A first series of experiments was carried out with filamentous OPGs in order to understand how this architecture influenced oxygen concentrations distribution in space and time. Planar optode measurements were coupled with a 2D reaction-diffusion model to deconvolute biological activities and oxygen mass-transfer. Then, a second series of experiments was conducted on roughly spherical OPGs to evaluate effects of short-term changes of irradiance on oxygen production levels using oxygen microsensor measurements and 1D reaction-diffusion model, depending on the active photosynthetic zone and OPGs structure. Then, a final series of experiments was conducted to evaluate the combined effects of abiotic factors (dissolved oxygen, dissolved organic carbon and, light intensity) on oxygen concentrations inside OPGs at the microscale.

This PhD thesis work opens new insights in the ecological relationships causing oxygen microenvironments within OPGs. It provides some guidelines to select a combination of optimal size/shape of OPGs and suitable abiotic conditions with the objective of a larger scale application OPGs-based process for wastewater treatment.

KEYWORDS: Oxygenic photogranules, Microenvironment, Modelling, Wastewater treatment, Phototrophic biofilms

Résumé

Les photogranules (OPGs) sont des agrégats compacts d'un diamètre pouvant atteindre 5 mm, composés d'un consortium complexe de micro-organismes phototrophes et non phototrophes intégrés dans une matrice de substances polymériques extracellulaires. Ils apparaissent particulièrement intéressants pour le traitement des eaux usées et constituent une alternative prometteuse au procédé classique par boues activées.

Cette thèse a été réalisée dans le cadre du projet ANR PSST (Photogranules Shake Sewage Treatment up), qui vise à comprendre les mécanismes de formation des photogranules (OPGs) et à évaluer leur potentiel pour le traitement des eaux usées. L'activité biologique des OPGs est déterminée par plusieurs paramètres, comme la composition microbienne, la morphologie des granules et des facteurs abiotiques (lumière et le carbone organique disponible dans le milieu environnant). Des expériences utilisant des approches de microscopie, microélectrodes et optodes planaires, ainsi que des modélisations mathématiques (modèles de réaction-diffusion 1D et 2D) ont été combinées dans cette thèse avec pour objectif d'élucider le rôle de la morphologie des OPGs et des facteurs abiotiques dans l'établissement des gradients d'oxygène à l'échelle microscopique.

Une première série d'expériences a été réalisée avec des OPGs filamenteux afin de comprendre comment cette architecture particulière influence la distribution des concentrations d'oxygène dans l'espace et le temps. Des mesures d'optodes planaires ont été couplées à un modèle de réaction-diffusion 2D pour déconvoluer les activités biologiques et la diffusion de l'oxygène. Ensuite, une deuxième série d'expériences a été menée sur des OPGs à peu près sphériques pour évaluer les effets des changements à court terme de l'illumination sur les niveaux de production d'oxygène en utilisant des mesures de microélectrodes et un modèle de réaction-diffusion 1D permettant d'évaluer les activités des microorganismes phototrophes et hétérotrophes. Enfin, une dernière série expériences de plus grande ampleur a été menée pour évaluer les effets combinés des facteurs abiotiques (oxygène dissous, carbone organique dissous et intensité lumineuse) sur les concentrations d'oxygène à l'intérieur des OPGs.

Ce travail de thèse ouvre de nouvelles perspectives sur les relations écologiques à l'origine des microenvironnements oxiques dans les OPGs. Il a, par ailleurs, permis d'identifier des combinaisons de tailles/formes optimales de photogranules et de conditions abiotiques pour l'application des procédés à OPG au traitement des eaux usées.

MOTS CLÉS : Photogranules, Microenvironnement, Modélisation, Traitement des eaux usées, Biofilms phototrophes.

Résumé étendu

1. Contexte général

La croissance démographique et l'industrialisation de la planète doivent être réalisées en tenant compte des exigences du développement durable. Parmi les objectifs de développement durable définis par l'ONU, la préservation des ressources naturelles est une grande priorité, et en particulier de garantir l'accès de tous à des services d'alimentation en eau et d'assainissement gérés de façon durable. Cet objectif passe par une amélioration des usages de l'eau, le déploiement des solutions existantes de traitement des eaux usées, et la mise en place de nouvelles méthodes innovantes de traitement des eaux usées. Le défi du traitement des eaux usées est d'éliminer efficacement les polluants avec un minimum d'impact environnemental.

Depuis plus d'un siècle, un grand pas a été franchi pour le traitement des eaux usées grâce à l'invention du procédé de traitement biologique par « boues activées ». Ce procédé est très énergivore car il consiste à insuffler de l'air à des eaux usées collectées dans un bassin d'aération afin de favoriser la croissance de bactéries hétérotrophes qui se nourrissent des éléments polluants solubles contenus dans les eaux usées. Les bactéries s'agrègent en flocs qui sont récoltés après une phase de décantation sous la forme de boues de station d'épuration. Le procédé biologique de traitement des eaux usées est performant mais consomme beaucoup d'énergie pour l'aération mécanique (Capodaglio and Olsson, 2019; Stillwell et al., 2010) et nécessite de trouver une voie de valorisation durable aux boues activées résiduaires (Cieślik et al., 2015). Un des enjeux pour les années à venir est de développer de nouveaux procédés biologiques à énergie positive et à plus faible impact environnemental, générant des sous-produits qui peuvent trouver un usage et être recyclés dans la bioéconomie.

Une alternative aux boues activées pour le traitement des eaux usées est l'utilisation de microorganismes photosynthétiques (microalgues et cyanobactéries). Diverses solutions technologiques ont été proposées au cours des dernières décennies (Oswald et al., 1953; Renuka et al., 2013; Sood et al., 2015). Le point commun de ces approches est que l'oxygène nécessaire à la dégradation du carbone organique et de l'azote est apporté par photosynthèse, évitant ainsi l'aération forcée très énergivore, qui est responsable d'environ la moitié des coûts de fonctionnement du procédé standard à boues activées pour le traitement des eaux usées.

Les technologies à photobioréacteurs atteignent actuellement des capacités épuratoires tout à fait comparables aux boues activées et peuvent se révéler très avantageuses d'un point de vue économique (Longo et al., 2016; Shoener et al., 2014). Cependant, l'inconvénient majeur limitant le développement de la filière des photobioréacteurs réside dans la mauvaise décantation des microorganismes de l'eau traitée. Récemment, plusieurs procédés favorisant la formation d'agrégats ou de granules, qui facilitent ensuite la décantation, ont été développés parallèlement (Abouhend et al., 2018; Quijano et al., 2017; Tiron et al., 2015; Van Den Hende et al., 2014). Ces nouveaux procédés à granules phototrophes sont en cours de développement et méritent encore d'être mieux caractérisés du point de vue des processus écologiques à l'œuvre et des performances épuratoires à attendre. Parmi ces nouveaux agrégats photosynthétiques, les photogranules oxygéniques (OPGs) associent des bactéries hétérotrophes et des cyanobactéries filamenteuses mobiles comme partenaire syntrophique phototrophe.

Les photogranules oxygéniques ont récemment été décrits comme des écosystèmes hautement structurés qui abritent de nombreuses espèces bactériennes imbriquées dans une matrice organique pouvant contenir aussi des précipités minéraux. Cet écosystème artificiel a été conçu dans un objectif de génie des procédés, mais possède des caractéristiques uniques qui en font un objet d'étude très intéressant en écologie microbienne. En effet, le phénomène de photogranulation à partir des boues activées se produit sans agitation. Le fait de former un granule dans un environnement sans force hydrodynamique externe est très original, et est en contradiction avec les hypothèses classiquement admises pour la formation des autres types de granules : granules aérobies (ex., procédé Nereda®), granules anaérobies en méthanisation (ex., UASB), granules d'oxydation anaérobie de l'ammonium (anammox), granules pour la production d'hydrogène par fermentation sombre. Ce travail de thèse s'est focalisé sur l'étude de la structure spatiale et du microenvironnement oxygéné des photogranules afin de mieux comprendre et d'optimiser le processus de conversion de la pollution dans les photogranules.

L'étude bibliographique réalisée dans le **chapitre I** indique que les photogranules sont constitués de divers microorganismes, à la fois hétérotrophes et phototrophes. Des structures microbiennes naturelles similaires ont été observées à la surface des glaciers (cryoconite), au fond de certains lacs ou en mer Baltique. Ces agrégats naturels sont surtout étudiés pour leur rôle écologique dans les cycles biogéochimiques des nutriments et du carbone. Les microorganismes phototrophes sont

essentiellement localisés dans les couches supérieures, formant une enveloppe cohésive enfermant un noyau interne avec une matrice plus lâche. Le diamètre observé peut varier de 0.2 à 5 mm. Les photogranules présentent des morphologies diverses (c'est-à-dire des granules filamenteux ou lisses) dont la cohésion est assurée par des substances polymériques extracellulaires (EPS) et l'agencement des cyanobactéries filamenteuses formant un tissu. L'organisation spatiale de la communauté bactérienne au sein des photogranules permet des interactions nutritionnelles à l'échelle microscopique. En outre, cette structuration induit des gradients physiques et chimiques importants (ex., lumière, concentration en matière organique et en O_2). La présence simultanée au sein d'un photogranules de zones oxiques à l'extérieur et de zones anoxiques à l'intérieur permet la coexistence de processus biologiques essentiels pour le traitement des eaux usées, comme la nitrification et la dénitrification, qui sont généralement obtenus séquentiellement par aération forcée.

En raison des informations limitées sur les systèmes de traitement des eaux usées à photogranules, il est nécessaire d'effectuer des études fondamentales sur les processus biologiques et physiques au sein des photogranules. Ce travail de thèse a couplé des expérimentations (mise en œuvre de photobioréacteurs, observation microscopique, mesure d'activité par microélectrodes) et de la modélisation (1D, 2D) afin de :

a. Caractériser les microenvironnements du photogranule en termes de gradients de lumière et d'oxygène, en fonction de la matière organique à disposition ;
b. Caractériser la relation entre la structure spatiale et l'activité biologique du photogranule ;
c. Évaluer le potentiel des photogranules à éliminer la matière organique contenue dans les eaux usées.

2. Relation entre la morphologie des photogranules filamenteux et la distribution spatiale des activités biologiques

Les photogranules présents dans un même photobioréacteur peuvent avoir des morphologies différentes, filamenteux ou lisses. Il n'existe pas de méthode standard pour estimer l'activité photosynthétique à l'échelle d'un photogranule filamenteux (filaments labiles, interface liquide/solide floue) car l'utilisation des microélectrodes n'est possible que pour des objets biologiques aux interfaces bien délimitées. Dans le **chapitre II**, des optodes planaires ont été utilisées pour capturer les variations temporelles et spatiales de la concentration d'O_2 autour d'un photogranule filamenteux. L'optode planaire permet de visualiser en 2D les gradients d'oxygène à

l'échelle sub-micrométrique de façon non destructive (**Figure 1**). Cependant, l'optode planaire a ses limites car elle capte uniquement les phénomènes sensibles à la surface en contact du film de détection, excluant les régions les plus denses du photogranule. De plus, le temps de collecte de la distribution de l'oxygène de plusieurs secondes et la détérioration du capteur à la lumière ont également limité son application. Néanmoins, la méthode et l'approche décrivant les dynamiques de l'oxygène sont extrapolables à l'étude d'autres structures biologiques aux interfaces mal délimités.

L'approche de modélisation a complété les résultats expérimentaux à l'échelle du micron grâce à un modèle de réaction-diffusion prenant en compte l'activité de microorganismes hétérotrophes et phototrophes. Ce modèle a révélé que la pénétration de la lumière dans le photogranule était le facteur prépondérant qui contrôlait les activités au sein du photogranule, plus que la distribution spatiale des bactéries hétérotrophes et des phototrophes. La réponse photosynthétique des filaments à la lumière était détectable en quelques secondes. En replaçant ce résultat dans un contexte de bioréacteur, les photogranules qui subissent des périodes alternées d'éclairage et d'obscurité voient leur activité fluctuer de façon dynamique. Il parait donc important d'analyser la dynamique de l'exposition à la lumière des photogranules individuels lors de leur croissance dans les photobioréacteurs.

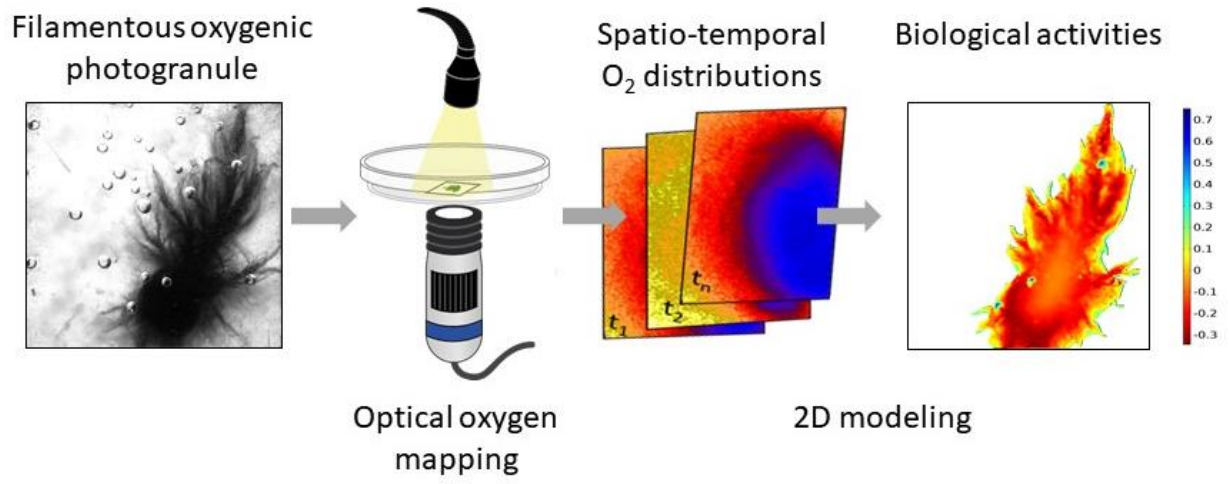

Figure 1 *Résumé graphique de l'approche utilisée pour étudier l'activité biologique des photogranules filamenteux.*

3. La lumière pilote l'activité microbienne à l'échelle microscopique

Afin de compléter l'étude précédente réalisée avec les optodes planaire qui a montré l'importance de la pénétration de la lumière comme moteur de l'activité microbienne, on s'est intéressé dans le (**chapitre III**) à caractériser les gradients d'oxygène et de lumière à l'intérieur des photogranules lisses avec une interface liquide solide bien délimitée. Pour ce faire, une série d'expériences a été menée sur des OPGs à peu près sphériques pour décrire l'oxygène dissous et les profils lumineux dans le microenvironnement des photogranules et d'évaluer l'impact de l'intensité lumineuse et de la disponibilité du carbone organique sur ces derniers. Les gradients d'oxygène et de lumière ont été mesurés à l'aide de microélectrodes et fibre optique. Un modèle 1D a été aussi développé pour évaluer les activités des microorganismes phototrophes et hétérotrophes. Le modèle prend en compte la distribution spatiale des activités microbiennes et la réaction-diffusion de l'oxygène dissous et du carbone organique.

- Il a été montré que la lumière pénètre jusqu'à 700 µm à l'intérieur du photogranule. C'est un facteur clé pour la stratification des photogranules, en particulier pour l'épaisseur de la couche phototrophe. Cependant, l'utilisation du spectre lumineux disponible par les pigments photosynthétiques est complexe. Il est donc essentiel de comprendre ce qui limite l'efficacité de l'utilisation de la lumière et les conditions dans lesquelles le rendement de conversion est optimisé.
- Le taux net de photosynthèse des photogranules augmente linéairement avec l'intensité lumineuse, au moins jusqu'à 150 $\mu moles_{PAR} \cdot m^{-2} \cdot s^{-1}$. Des intensités lumineuses supérieures peuvent entraîner une inhibition de la photosynthèse. L'excès de lumière peut également endommager les systèmes photosynthétiques, entraînant une réduction durable des performances.
- L'approche de modélisation a permis d'étudier la distribution spatiale des populations dans les photogranules et leurs activités biologiques. Elle a permis de prédire la colocalisation des bactéries phototrophes et des hétérotrophes et de mettre en évidence des différences marquées d'activités biologiques (photosynthèse et respiration) pour des photogranules issus de photobioréacteurs aux fonctionnements contrastés. Ces différences peuvent être dues aux conditions de croissance des photogranules. Cependant, ce travail préliminaire ne permet pas de proposer de stratégie d'ingénierie pour produire des photogranules avec des structurations spatiales aux populations microbiennes définies.

- Les photogranules présentent de forts gradients de concentration en oxygène et en carbone organique de la surface au centre. Il a été souvent observé des zones anoxiques au centre des photogranules (**Figure 2)**. La proportion d'anoxie dépend de la lumière apportée, du carbone organique disponible, de l'oxygène présent dans l'espace environnant et du diamètre des photogranules. Le pilotage des conditions opératoires à l'échelle d'un bioréacteur devrait permettre à terme de maitriser la proportion de zones oxiques/anoxiques au sein des photogranules, et de permettre la présence simultanée d'activités nitrifiantes/dénitrifiantes. Un meilleur contrôle sur l'élimination de l'azote permettrait une réduction de l'impact environnemental du traitement des eaux usées par photogranules (Brockmann et al., 2021). Une manière de contrôler le biovolume anoxique serait de sélectionner une gamme étroite de tailles de photogranules (ex., réacteurs cyclones ou réacteur avec étage de tamisage).

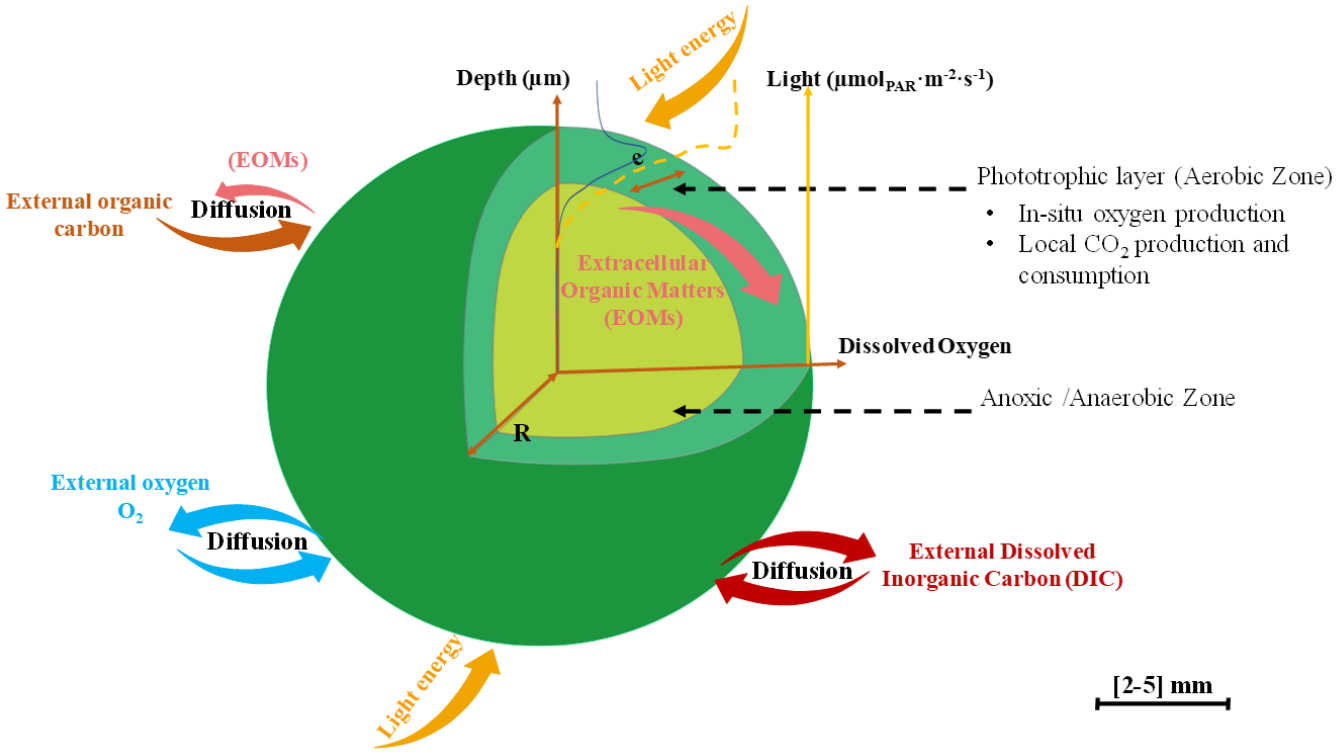

Figure 2 *Illustration des principales interactions à l'échelle micrométrique en lien avec l'environnement des photogranules.*

4. Régulation de la photosynthèse brute et des microzones anoxiques des photogranules

Le traitement des eaux usées par boues activées nécessite une succession de périodes oxiques et anoxiques, et en particulier pour l'élimination de l'azote, cette alternance favorise successivement les processus de nitrification et de dénitrification. Avec des procédés granulaires, la nitrification et la dénitrification peuvent fonctionner simultanément ce qui leur confère un avantage clé par rapport aux systèmes conventionnels à boues activées. La nitrification-dénitrification simultanée requiert (1) la formation simultanée de conditions d'oxydoréduction oxiques (favorisant la nitrification) et de conditions anoxiques (favorisant la dénitrification), et (2) la disponibilité de donneurs d'électrons dans des conditions d'oxydoréduction anoxiques (pour la dénitrification). Par conséquent dans le **chapitre IV**, on s'est intéressé à évaluer l'effet de la concentration d'oxygène dissous dans l'environnement proche du photogranule, de la disponibilité en matière organique dissoute et de la lumière incidente sur la régulation de la photosynthèse brute et des microzones anoxiques des photogranules dans l'optique d'un fonctionnement de photobioréacteur alimenté en batchs séquenciels (*SBR – sequencing batch reactor*). Pour ce faire, la même approche expérimentale et de modélisation appliquée dans le **chapitre III** a été menée, mais de plus grande ampleur, pour évaluer les effets combinés des facteurs abiotiques (oxygène dissous, carbone organique dissous et intensité lumineuse) sur les concentrations d'oxygène à l'intérieur des OPGs. Ce travail a pour but d'optimiser l'utilisation de la lumière dans un SBR à base d'OPGs.

L'éclairage d'un photobioréacteur permet aux photogranules de produire de l'oxygène. Cet oxygène est disponible pour la nitrification et la respiration aérobie de la matière organique à disposition. En absence d'oxygène (au cœur du photogranule ou à l'obscurité), la matière organique résiduelle peut encore être réduite par dénitrification. Dans ce travail, le volume de la zone anoxique à l'intérieur du photogranule a été modulé par la concentration d'oxygène dissous dans l'environnement proche du photogranule, par la matière organique dissoute et par l'intensité de la lumière appliquée.

Dans un photobioréacteur alimenté en batchs séquenciels, le début du cycle est marqué par l'abondance de matière organique, où respiration aérobie et dénitrification coexistent. En fin de cycle au contraire, la matière organique devient rare et l'oxygène s'accumule dans le milieu environnant. D'un strict point de vue énergétique, l'éclairage du photobioréacteur pourrait être diminué (ou le cycle SBR raccourci) car l'oxygène produit n'est plus utilisé localement. Cependant,

lorsque l'effluent à traiter contient une forte concentration d'ammonium, cette stratégie peut conduire à une oxydation incomplète de l'ammonium. Enfin, les phénomènes de diffusion, en particulier pour des photogranules de gros diamètres, peuvent ralentir les activités microbiennes. Layer et al. (2020) ont prédit que les taux de dénitrification dans les boues granulaires aérobies lors du traitement des eaux usées municipales et complexes sont cinq à six fois plus faibles que lors du traitement des eaux usées simples des AGVs. Par conséquent, sur la base de nos résultats, l'adoption d'une diminution continue de l'intensité lumineuse appliquée induira une diminution de la concentration d'oxygène à l'intérieur du photogranule, et permettra de maintenir un niveau souhaitable de biovolume anoxique durant toute la période du cycle SBR. Cette stratégie de conduite de réacteur n'a pas été évaluée expérimentalement et peut conduire à une instabilité de la structure physique des photogranules ou même à l'échec de la photogranulation. Il est donc nécessaire d'envisager des études en photobioréacteurs de laboratoire pour évaluer le comportement des photogranules sur le long terme.

5. Conclusion du travail de thèse

L'utilisation des photogranules pour le traitement des eaux usées constitue une innovation dans le domaine de l'assainissement, et une véritable rupture technologique capable de transformer cette activité en un processus plus durable. Le gain potentiel est déjà évident en termes de consommation d'énergie, même pour un procédé en cours de développement. Afin d'inscrire les photogranules dans l'économie circulaire, il reste encore à évaluer le potentiel de valorisation des photogranules produits (ex., extraction de molécules valorisables dans la bioéconomie, EPS, pigments).

Cette thèse s'est intéressée à la compréhension des interactions syntrophiques entre les microorganismes hétérotrophes et phototrophes au cœur du fonctionnement biologique des photogranules. L'approche scientifique, combinant l'acquisition de données expérimentales et la modélisation mathématique, s'est focalisée sur le devenir du carbone. Le travail a permis de démontrer la colocalisation des activités hétérotrophes et photosynthétiques au sein des photogranules de différentes morphologies, ainsi que la stratification des populations microbiennes qui jouent un rôle important dans la détermination de l'activité globale du photogranule. Ce travail a permis aussi de mettre en évidence l'importance relative de plusieurs facteurs physico-chimiques (lumière, oxygène dissous, matière organique disponible, diamètre du granule) sur les activités microbiennes.

6. Perspectives du travail de thèse

Un certain nombre de progressions naturelles à ce travail pourront compléter les connaissances fondamentales acquises sur la biologie des photogranules, et plus concrètement, sur le comportement des photogranules en photobioréacteurs.

Étude des trajectoires de photogranules en bioréacteur :

Les photogranules sont cultivés dans des bioréacteurs agités en présence de lumière naturelle ou artificielle. La lumière est bien sûr le facteur clé dans le processus de photosynthèse des photogranules, responsable de l'apport d'oxygène nécessaire à l'élimination biologique de la pollution contenue dans les eaux usées. Un photobioréacteur est constitué d'une enceinte dans laquelle est mis en suspension des particules, avec un éclairage latéral et/ou en surface. À tout instant, chaque particule reçoit une quantité de lumière différente en fonction de sa proximité à la source lumineuse et de l'ombrage des autres particules dans le photobioréacteur. Chaque particule à un instant donné à l'intérieur du réacteur va avoir sa propre trajectoire dans le photobioréacteur et sa propre activité de photosynthèse. Cependant, l'augmentation du mélange pourrait entraîner l'échec de la formation des photogranules ou leur désintégration. Par conséquent, la performance opératoire globale va dépendre d'une combinaison de facteurs : de la qualité du mélange des particules, de la lumière apportée au système et de la concentration totale de biomasse active. Une étude couplant modélisation du mouvement des particules en bioréacteur et validation avec des expérimentations en photobioréacteurs de laboratoire serait parfaitement indiquée.

Réponse dynamique des photogranules à des éclairages intermittents :

Toutes les données expérimentales de ce travail de thèse ont été obtenues à l'équilibre mais le temps nécessaire pour atteindre les équilibres fonctionnels pouvait atteindre près de 30 minutes. Or, les modifications de l'environnement local des photogranules au sein d'un bioréacteur sont extrêmement rapides, de l'ordre de la seconde. Il suffit d'imaginer la lumière perçue par un photogranule évoluant librement dans un réacteur agité éclairé de façon continue. Pour mimer la lumière réellement perçue par ce photogranule, il est possible d'étudier expérimentalement la dynamique de l'activité microbienne d'un photogranule en condition d'éclairage intermittent. Le

même dispositif technique (banc de microélectrode) utilisé pour ce travail de thèse pourrait être utilisé pour ces études en dynamiques.

Effet de divers paramètres sur les activités microbiennes (pH, formes d'azote) :

Les cyanobactéries peuvent survivre dans une large gamme de pH (Stal, 1995). Une condition légèrement alcaline favorise la croissance des cyanobactéries. Le pH mesuré à l'intérieur des photogranules est localement très élevé (>11). Le pH est lié à la spéciation du carbone inorganique dissous (CO_2 (aq), HCO_3, CO_3^{2-}). Or, le carbone inorganique dissous est l'élément clé de la croissance phototrophique. Ainsi, la détermination de la dynamique du pH à l'intérieur des photogranules permettra de mieux définir les équilibres physico-chimiques présents localement, pouvant induire des précipitations et une minéralisation des photogranules.

Les biofilms phototrophes sont caractérisés par un gradient d'oxydoréduction élevé en raison des forts gradients des accepteurs et des donneurs d'électrons (Roeselers et al., 2008). Par conséquent, les photogranules peuvent également être sensibles aux gradients d'oxydoréduction. Il est alors recommandé d'étudier le microenvironnement d'oxydoréduction et de le relier aux informations de l'environnement immédiat.

La compréhension de la biochimie des conversions de l'azote dans les photogranules nécessite des mesures à micro-échelle des composés azotés. Les interactions de ces conversions ont été étudiées avec succès grâce à l'utilisation de microélectrodes pour le NO_3^-, le NO_2^- et le N_2O dans des communautés microbiennes stratifiées, telles que les biofilms, les agrégats et les sédiments. Une telle étude n'a pas encore été menée sur les photogranules, et devrait permettre d'acquérir des connaissances précieuses sur la structure et les activités liées au cycle de l'azote.

Etude du cycle de vie d'un photogranule (formation, croissance, désagrégation) :

Contrairement aux bioréacteurs à cellules libres en suspension avec un mélange homogène de la biomasse et du milieu de culture, les biofilms et granules sont par nature hétérogènes. Au sein d'un même photobioréacteur, des particules de tailles et de morphologies différentes coexistent. Un petit photogranule peut provenir du détachement d'un photogranule âgé, ou bien être issu de l'agrégation de quelques cellules isolées. Mieux connaitre le cycle de vie d'un photogranules pourrait être utile pour sélectionner les particules les plus actives au sein d'un photobioréacteur. En raison de l'agrégation des cellules, le transfert de masse à l'intérieur des biofilms denses repose

principalement sur la diffusion. En conséquence, des gradients de concentration, notamment de carbone inorganique dissous ou de lumière, se forment à l'intérieur des biofilms phototrophes. Il est intéressant de souligner que la technologie des biogranules et celles des biofilms en général, est basée principalement sur les gradients redox et chimiques verticaux abrupts (~microns au millimètres) qui s'établissent au sein ces matrices biologiques (matière organique, oxygène et nutriments). Ces composants essentiels sont d'abord adsorbés sur la surface du biofilm, puis transportés par des processus de diffusion, d'abord à travers le film liquide, puis à travers l'interface liquide/biofilm, et enfin à travers le biofilm, où ils sont métabolisés par la communauté microbienne. Les produits de biodégradation finaux ont un flux inverse, étant dirigés vers l'extérieur du biofilm.

Dans une perspective à long terme, il serait intéressant de développer un modèle individu-centré pour déchiffrer le mécanisme de la photogranulation. Ce modèle devrait combiner le rôle des éléments suivants dans la formation des photogranules : (i) le phototactisme des cyanobactéries qui permet de se positionner dans des conditions optimales de luminosité pour assurer leur survie, (ii) l'environnement biogéochimique et physique afin d'élucider si la colocalisation des interactions syntrophiques peut être justifiée par l'échange de nutriments, ou si un mécanisme physiologique, tel que la détection du quorum ou la libération de toxines, sont nécessaire à l'agrégation, (iii) les interactions mécaniques afin d'étudier comment les différentes morphologies des cellules (ratio longueur/largeur des filaments, etc.), ainsi que les propriétés mécaniques telles que (élasticité, flexibilité, mobilité, etc.) sont impliquées dans les formes spécifiques des photogranules.

Ce travail de thèse s'est focalisé sur la modélisation des activités microbiennes et des relations syntrophiques entre bactéries hétérotrophes et phototrophes. Il constitue un premier pas vers une meilleure compréhension des processus biologiques qui structurent le fonctionnement des photogranules. Comme tout travail de modélisation, les résultats obtenus reflètent une certaine réalité mais ne permettent pas de capturer l'ensemble de la complexité biologique du système. Il sera bien sûr nécessaire de complémenter ce travail avec une étude d'écologie microbienne pour identifier plus précisément la diversité microbienne et la nature des interactions microbiennes qui régissent le fonctionnement biologique des photogranules.

Chapter I

Literature review and thesis objectives

1. Oxygenic Photogranules (OPGs)

Oxygenic Photogranules (OPGs) are a light driven consortium of phototrophic and non-phototrophic microorganisms. Microorganisms in OPGs are embedded in a matrix of extracellular polymeric substances (EPS) (**Figure I.1**). OPGs are typically roughly spherical structures (Milferstedt et al., 2017a, 2017b) with an approximate diameter between 0.2 and 4.5 mm (Abouhend et al., 2020). The phototrophic microorganisms in photogranules are a mix of algae and/or mostly filamentous cyanobacteria. OPGs are described also as layered microbial ecosystems with a concentric, cohesive phototrophic layer that may vary in thickness from a few hundreds of micrometers to 1 millimeter (**Figure I.1** C and D) (Abouhend et al., 2020).

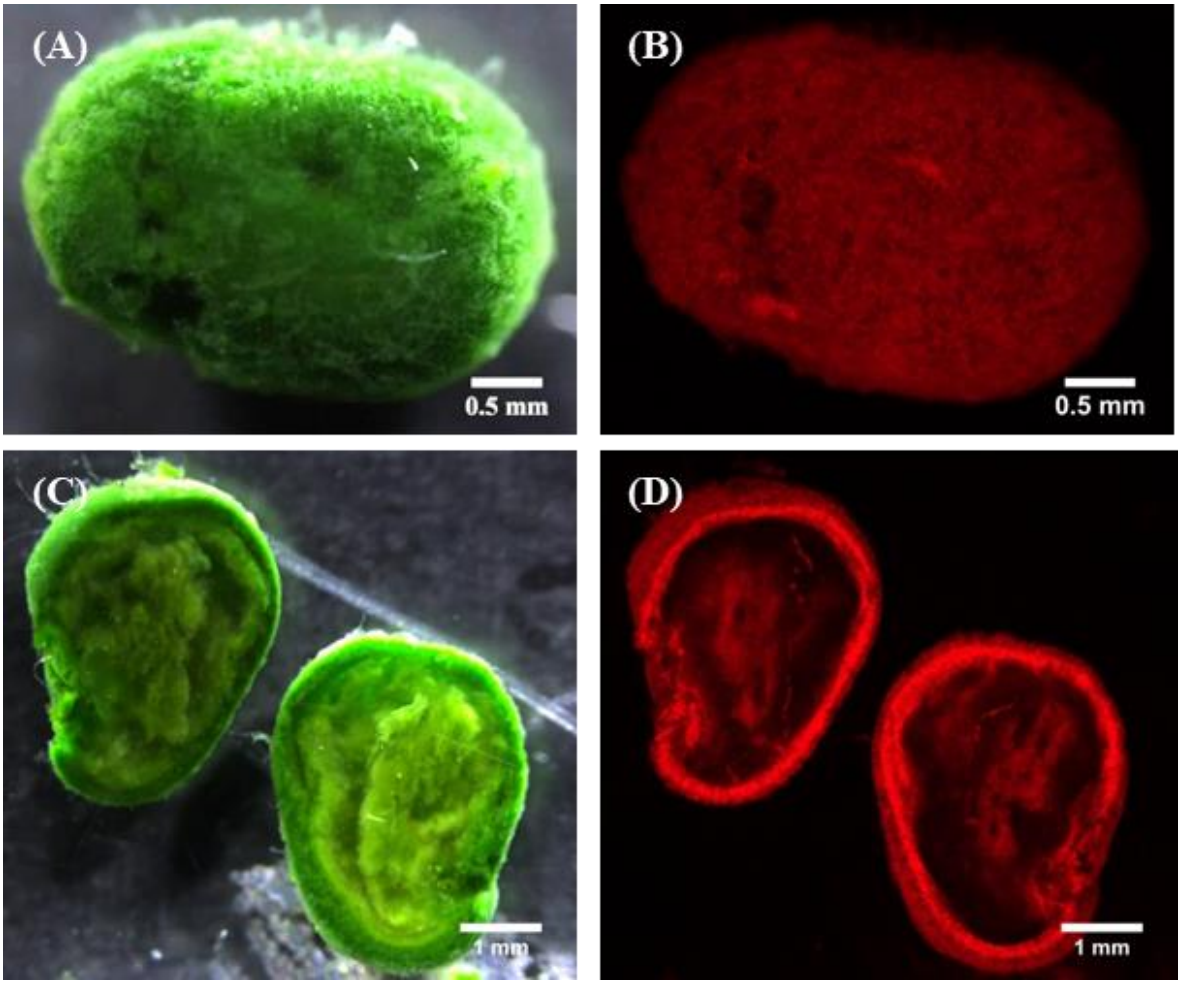

Figure I.1 *Microscopic images showing the structure of an oxygenic photogranule (A-C) Surface and cross-section of photogranule viewed by brightfield light microscopy. (B−D) The same surface and the cross-section viewed by red filter for the detection of phycocyanin autofluorescence. High autofluorescence in panel D represents the phototrophic layer.*

The first observations of photogranules were done by Park and Dolan in 2015. Activated sludge from an urban wastewater treatment plant was incubated at room temperature in 20 mL scintillation vials without mechanical agitation and was exposed to natural light. Over a few weeks this biomass transformed into an oxygenic photogranule (**Figure I.2**). Then, they seeded reactors intended for wastewater remediation and biomass generation with these photogranules. More information about issue were detailed further in **section 1.1.2.**

Figure I.2 *Photogranulation of activated sludge under static conditions (vial diameter is 2.5 cm).*

Structures like photogranules have been found in nature. Among these structures are cryoconite granules. These biologically active aggregates are black-green in color and spherical in shape. They generally consist of mineral particles, organic matter, and bacteria, especially cyanobacteria. This type of granule is generally found in glaciers around the world (biogenic surface dust on glaciers) (Cook et al., 2016). They are distributed on surfaces and varied in size up to 4 mm in diameter (Takeuchi et al., 2010). The layered structure observed in photogranules also appears in cryoconite granules (**Figure I.3**) (Segawa et al., 2020; Takeuchi et al., 2001). The formation of these granules is driven and guided by the activity of cyanobacteria (Uetake et al., 2019). The role of cryoconite granules is not completely understood and still uncertain, yet they are suspected to contribute to carbon recycling and increasing ice melting (Cook et al., 2016; Hodson et al., 2008; Stibal et al., 2012).

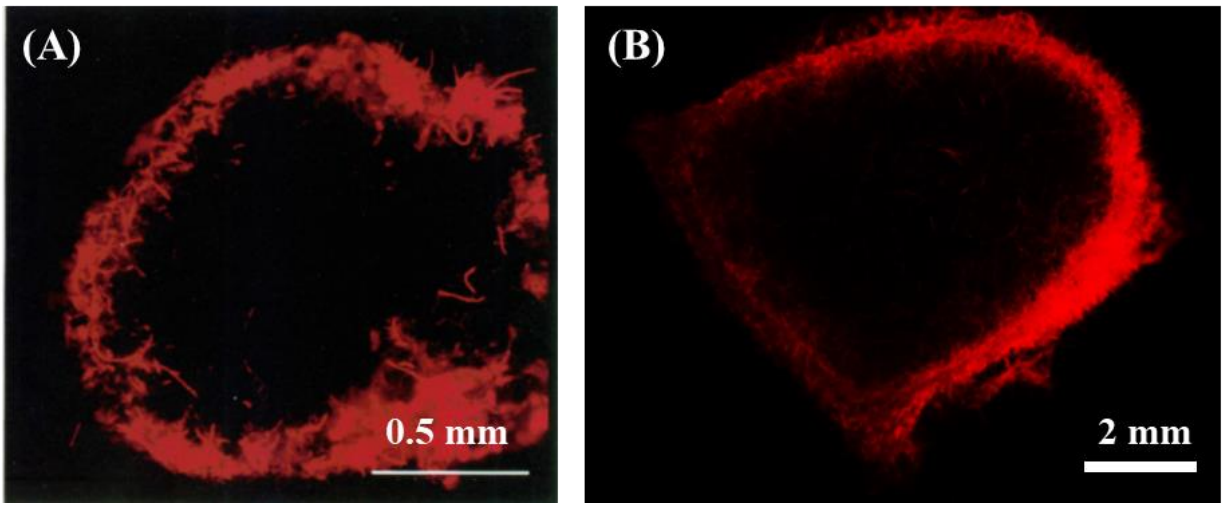

Figure I.3 *(A) The cross section of a cryoconite granule observed by fluorescent microscopy (Takeuchi et al., 2010) (B) The cross section of an oxygenic photogranule produced under static conditions observed by fluorescent microscopy (Milferstedt et al., 2017b).*

Another variant of photogranules are the cyanobacterial aggregates observed during cyanobacterial blooms during warm periods when temperatures and light intensities are high. This occurs in aerated surface waters such as in freshwater lakes (Boedeker and Immers, 2009; Fang et al., 2014) (**Figure I.4** A) and in the Baltic sea (Klawonn et al., 2015) (**Figure I.4** B). The latter aggregates contain microalgae, cyanobacteria, and non-phototrophic bacteria. They form rounded and dense colonies with sizes up to 2 mm. The contained cyanobacteria are responsible for supplying nitrogen to the water thanks to their genes for N_2 fixation. In addition to this, the heterotrophic activity in these aggregates allows the occurrence of anoxic zones that favor biological processes such as denitrification and sulfate reduction. Consequently, it can promote N-recycling processes in the water (Klawonn et al., 2015; Tuomainen et al., 2003).

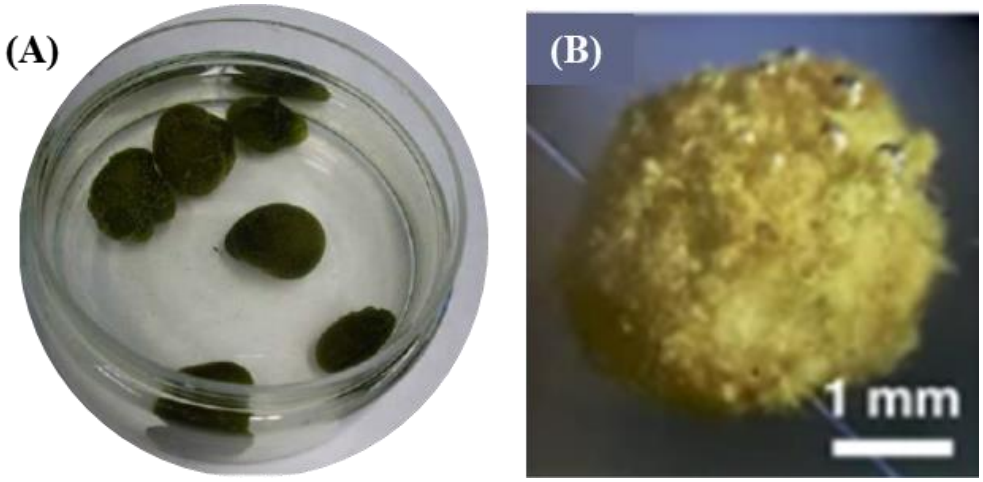

Figure I.4 *Cyanobacterial aggregates resembling oxygenic photogranule. (A) Nostoc pruniforme aggregates from Naardermeer lake in the Nederland (petri dish diameter =10 cm) (modified from Boedeker and Immers (2009)). (B) N. spumigena aggregate collected from the Baltic sea (modified from Klawonn et al. (2015)).*

1.1. Diversity of OPGs morphology

OPGs present a diversity of morphologies: smooth and filamentous granules (**Figure I.5**). Smooth photogranules can be categorized based on the different aggregate sizes: flocs / proto-photogranule <0.2 mm, small granules (0.2−1.0 mm) and large granules >1.0 mm. When OPG grows larger, filamentous cyanobacteria become enriched, particularly in the outer layer as interwoven web. It was demonstrated that photogranules greater than 3 mm in diameter start developing a distinct concentric layer of filamentous cyanobacteria and extracellular polymeric substances (EPS) that encloses an unconsolidated interior (Abouhend et al., 2020). Furthermore, the authors reported that the size of photogranules impacts the specific oxygen production capability of photogranules (Abouhend et al., 2020). The authors speculated also that the optimal size for a maximum oxygen production would be between 0.5 and 1 mm. This finding was argued and defended by the fact that this size class showed a maximum of the mass fraction of photosynthesis pigments (i.e., phycobilin and chlorophyll a) in the OPG biomass. Chlorophyll a is an essential pigment for photosynthesis while phycobilin is a light-harvesting pigment that complement the light-capturing ability of chlorophyll (Frank and Cogdell, 2012). Further, Abouhend et al. (2020) reported the decreases in the fractions of chlorophyll b and chlorophyll c in the larger size classes. In addition, they suspected the limitation of the light with depth, thus phototrophs in deeper layers experience less light. However, the light microenvironment, i.e., light penetration, and its impacts on the system

performance has not been discussed and remained unknown. Yet, since the photogranules have a large and dense structure, steep vertical redox and chemical gradients (~microns to millimeters) would be expected as reported also for the phototrophic biofilms and mats (Roeselers et al., 2008). Moreover, it is known that size plays a role in mass transfer (i.e., the diffusional lengths increase with the increase of size). Therefore, size may affect the physicochemical gradients in biological aggregates and the microbial community. Ali et al. (2019) and Li et al. (2019) showed that bacteria belonging to functional groups responsible for nitrogen and phosphorus removal were progressively enriched with an increase of the size of aerobic granular sludge. Other results showed that larger microbial aggregates harbor slow growing organisms such as anammox bacteria in a granular nitritation-anammox reactor (Volcke et al., 2012) and phosphate accumulating organisms PAO in aerobic granular reactors (de Kreuk and Van Loosdrecht, 2004). This suggests that next to the class size 0.5-1 mm mentioned before, the larger photogranules may be also important and be involved in some specific biological activity (e.g., simultaneous nitrification and denitrification (SND)).

Next to photogranules with a smooth surface, filamentous OPG have been observed in photobioreactors (Arcila and Buitrón, 2016; Milferstedt et al., 2017a; Ouazaite et al., 2020). These filamentous photogranules usually consist of bundled filaments attached to an inner core (**Figure I.5** B) or are just interwoven (**Figure I.5** C). Such morphologies were also observed in (Brehm et al., 2003; Capone, 1997; Castenholz, 1967) for cyanobacterial aggregates.

The surface shape of the granule is important for the overall performance of a granule reactor. In fact, once filamentous granules dominate the reactor, settleability may become poor and consequently biomass will be washed out. Moreover, the shape of surface affects the external mass transfer resistance (i.e., boundary layer). In biofilm theory, it was demonstrated that under the condition of pure diffusive mass transfer, rough biofilms appeared to show higher mass transfer flux due to the large liquid-biofilm interface providing more contact to substrates (C. Li et al., 2016; Picioreanu et al., 2000a). However, the complex surface shape in biofilms as in the filamentous granule causes technical problems when one is interested in the chemical microscale measurements. Indeed, the spatial heterogeneity makes it a challenging task to determine the interface between bulk and biological matrix, and secondly limitation of one-dimensional description of the system due to the presence of biomass heterogeneities in the different directions.

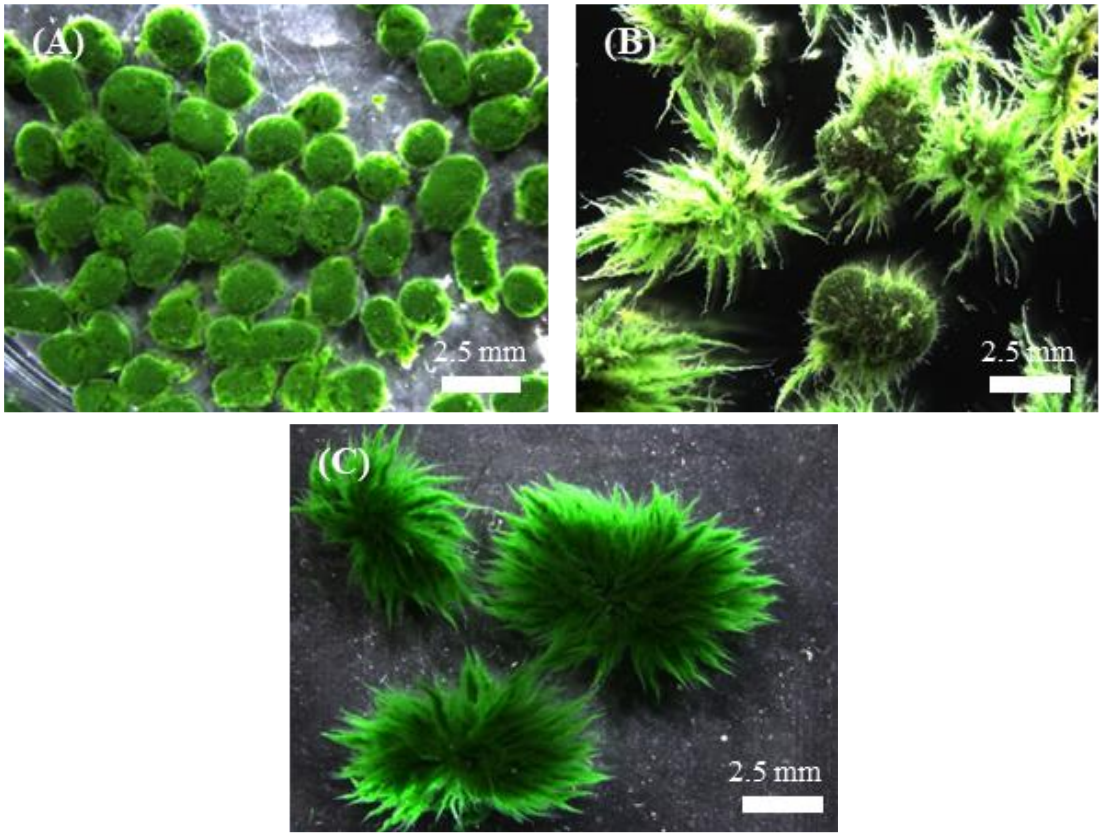

Figure I.5 *Different morphologies of oxygenic photogranules produced developed under turbulent mixed conditions. (A) Bald photogranule. (B) Filamentous photogranule with inner core. (C) Filamentous photogranule without inner core (star like structure).*

1.2.Formation of OPGs in turbulent mixed reactors

The generation of OPGs in turbulent mixed reactors may be realized via seeding the reactors with hydrostatically formed photogranules (Abouhend et al., 2020, 2018; Ansari et al., 2019; Milferstedt et al., 2017b). However, the OPGs may be also produced via different strategies including mixture of aerobic granules and unicellular microalgae consortia (Liu et al., 2017), activated sludge and phototrophic biofilms (Arcila and Buitrón, 2017, 2016; Tiron et al., 2017) and aerobic granules and previously formed photogranules (Ahmad et al., 2017). The OPGs used for this thesis works, were sampled from reactors that were seeded by hydrostatically formed photogranules. Milferstedt et al. 2017b followed the progression of photogranulation in turbulently mixed, sequencing batch environments. They reported that the granules disintegrate due to shear stress as a first step. Then particles resembled to bacterial flocs are formed. They are referred as protogranules and have diameters of less than 200 μm. As the SBR operates with the periodic addition of organic carbon,

the protogranules continued to increase in size and number over time until maintaining a balanced biomass concentration. However, the formation mechanisms of OPGs in turbulent mixed reactors are still unknown and are currently investigated (Abouhend et al., 2020; Trebuch et al., 2020). In literature, several hypotheses have been proposed to explain biogranulation and four steps have been suggested to be common (Liu, 2006a; Zhang et al., 2016) and which may probably also be shared by the photogranulation in turbulent mixed reactors.

- First step: the physical movement is important to initiate and to ensure contact between the microorganisms. The physical movement is guaranteed either by hydrodynamics force or by the microorganisms' mobility.
- Second step: the attractive forces are identified to be responsible to keep stable the contact between microorganisms, namely van der Waals forces, hydrophobicity, and thermodynamic forces (e.g., surface energy; surface tension (Thaveesri et al., 1995)).
- Third step: the microbial growth enhances the aggregation and the production of extracellular polymers necessary for adhesion and cohesion of the granule leading to the formation of the three-dimensional structure. The success of the photogranulation depends mainly on the triggering of its mechanisms, which in turns depends on the (a)biotic factors (e.g., temperature, light intensity and quality, ionic charge, microorganism's activity, etc.)
- Final step: Attachment and detachment via hydrodynamic shear force, shape the three-dimensional appearance of the granule into a certain structured community.

The first two processes are not required when photogranulation is attempted from already formed aggregates such as activated sludge flocs. In **Figure I.6**, a simple and general model of the formation of oxygenic photogranules under turbulent mixed reactors is suggested. Furthermore, during these steps, many factors are known to affect the granulation process. Each of these factors will be discussed later on:

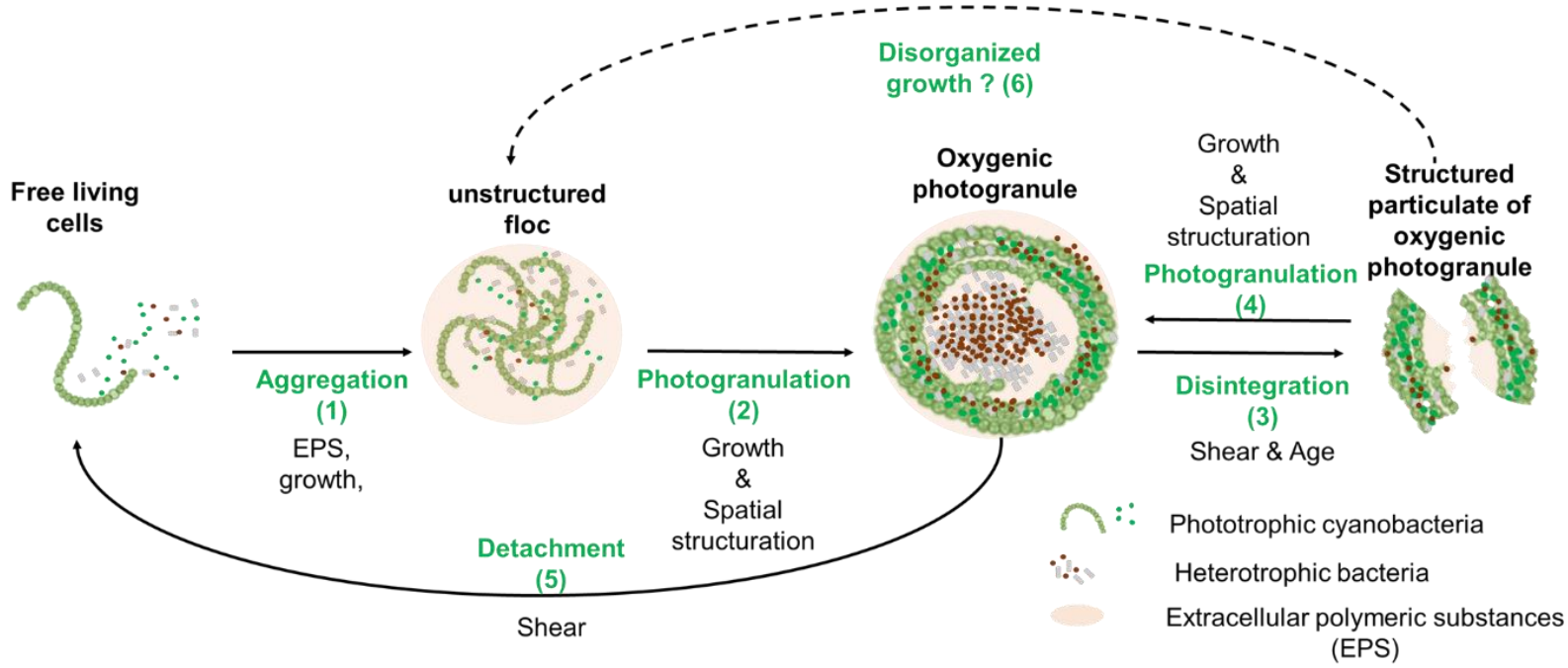

Figure I.6 *A simple model proposed for the formation of oxygenic photogranules under turbulent mixed reactor. The figure illustrates a proposed sequence of events for the formation of the photogranules: (1) Aggregation: Transition from free-living cells and the formation of an unstructured bacterial floc (Aqeel et al., 2019; Sengar et al., 2018); (2) Photogranulation: Spatial structuration of the photogranule (Joosten et al., 2020; Milferstedt et al., 2017b); (3) Disintegration of the photogranule due to age and shear stress (Yuan et al., 2017); (4) Formation of new photogranules from broken parts of mature photogranules (Abouhend et al., 2020; Ansari et al., 2019; Trego et al., 2019); (5) Disintegration: dispersal of cells from the already mature formed granules (D'Acunto et al., 2019a; Solano et al., 2014); (6) Disorganized growth: Potential formation of unstructured floc from broken bits of oxygenic photogranules.*

- Cyanobacterial characteristics

It was reported that motile filamentous cyanobacteria are a keystone microorganisms in the formation of oxygenic photogranules (Milferstedt et al., 2017b; Trebuch et al., 2020). The filamentous characteristics of the cyanobacteria favors their attachment on photogranule precursors and then the formation of a three-dimensional network where other microorganisms could be entrapped easily. This phenomenon has been called the Spaghetti theory (Hulshoff Pol et al., 1983; Lettinga et al., 1987). The aggregate develops further through the growth of the microorganisms and forms a denser structure. Cyanobacteria are known to grow over a large range of light intensities, including extremely low intensity levels (1 $\mu moles_{PAR} \cdot m^{-2} \cdot s^{-1}$) and bright light conditions (700 $\mu moles_{PAR} \cdot m^{-2} \cdot s^{-1}$) (Stal, 1995; Tandeau de Marsac and Houmard, 1993; Vézina and Vincent, 1997). Depending on the incident light, cyanobacteria use their motility to move into a suitable light environment (Checcucci et al., 2003; Nultsch and Häder, 1979). The movement depending on the light intensity of cyanobacteria was reported to be involved in the formation of cyanobacterial mats and cyanobacteria ball-like aggregation (Garcia-Pichel and Castenholz, 2001; Walter et al., 1976). However, the role of this phototactism in photogranulation in turbulent mixed reactors is questionable, given the high flow velocity in the reactors, albeit, it may be involved in the stratification of microorganisms within the oxygenic photogranules as shown in the **Figure I.1**.

- Role of Extracellular Polymeric Substances (EPS)

EPS are essential to the development of granules (Liu et al., 2004; Milferstedt et al., 2017a). Many microorganisms are able to produce EPS (Wimpenny et al., 2000), including cyanobacteria (Parikh and Madamwar, 2006) and microalgae (Lewin, 1956). The EPS matrix brings cohesion to the granule, and protection against desiccation. The EPS matrix allows the three-dimensional structuring of the biofilm (Flemming et al., 2007; Flemming and Wingender, 2010). It was also reported that EPS may serve also as an alternative carbon source for heterotrophic bacteria in cyanobacterial biofilm and mats when no other carbon source is available (Stuart et al., 2016a, 2016b).

- Shear forces

Shear forces has been found to be an essential parameter for the formation of dense biofilm aggregates in aerobic biofilm reactors (Kwok et al., 1998; Liu and Tay, 2002) and aerobic granules (Di Iaconi et al., 2005). The density of biofilm on support materials increases also with increasing

shear stress (Van Benthum et al., 1996). The same finding was reported also for aerobic granules. As discussed earlier, the shear forces provide the convection of the fluid which in turn guarantee and initiate the contact between the microorganisms involved in the photogranules formation. However, the contribution of shear forces is still under debate. Several lines of discussion minimize this contribution. First, the photogranules can be formed under conditions where shear is completely absent, with larger sizes than in turbulent reactors (Milferstedt et al., 2017b; Stauch-White et al., 2017). Second, a recent study speculates that even by reducing mixing from 100 to 50 rpm, the photogranule still develops with size up to 5 mm (Abouhend et al., 2020). However, the shear forces may also be involved in shaping the granules morphologies and increasing the density. So far, no information was reported on the impact of the shear forces on the formation, structure, and metabolism of oxygenic photogranules. Nevertheless, it is worth emphasizing the importance of agitation to ensure mixing in bioprocess photobioreactors and, to provide the necessary flux to ensure the light indispensable for the growth of phototrophs, given that the lighting is applied to the walls of the reactor.

- Light

In natural and artificial light environments, continuous or intermittent illumination can be imagined. Artificial light provides more flexibility in the light wavelength spectrum, intensity, or frequency of illumination.

Arcila & Buitron (2017) studied the influence of light intensity on the formation of microalgae-bacterial aggregates. They investigated three different solar average irradiance levels on the water surface of an 80 L outdoor high-rate algae pond (HRAP), treating municipal wastewater. They found that high light intensities (>500 $\mu moles_{PAR} \cdot m^{-2} \cdot s^{-1}$) inhibited the generation of microalgal granules (Arcila and Buitrón, 2017). On the other hand, it was found that low light intensities in the range of 150 $\mu moles_{PAR} \cdot m^{-2} \cdot s^{-1}$ were assumed to trigger the production of the signal molecule N-acyl-homoserine lactones (AHLs) which in turn regulate the production of EPS (Arcila and Buitrón, 2017; Quijano et al., 2017; Zhang et al., 2019).

The light attenuation through the biofilm/granule is the major factor leading to the stratified microstructure of these ecosystems (Stolz, 2000), with the available light spectrum and intensity that determine the spatial location of phototrophic microorganisms (Al-Najjar et al., 2012; Stolz, 1990). For example, in microbial mats illuminated with strong natural light, phototrophs that do

not withstand high intensities are not located directly on the biofilm surface (Stal et al., 1985). Kühl et al. (1996) postulated that in epilithic cyanobacterial biofilms, "*the surface structure changed due to lateral migration of cyanobacterial filaments into dense tufts at the highest investigated irradiances (150-200 $\mu moles_{PAR} \cdot m^{-2} \cdot s^{-1}$)*" (Kuhl et al., 1996). Furthermore, the photosynthetic activity of the phototrophs creates steep chemical and redox gradients across the microbial mats which lead to different microenvironments, and consequently a stratified microbial composition (Stal, 2002).

- Others

Other factors were proposed to be involved in the mechanisms of photogranulation. Trebuch et al. (2020) investigated the impact of hydraulic retention time on photogranulation and showed that photogranulation was enhanced at low retention times. They also suggested that settling time and feeding regime of sequencing batch reactor operation mode should play a role (Trebuch et al., 2020). Zhang et al. (2019) suspected that biotic interactions between phototrophs and non-phototrophs can also be involved in the mechanisms of granulation especially the production of quorum sensing signals (Zhang et al., 2019). Other factors such as the presence of cations can also be involved by analogy to the mechanisms of formation of aerobic granules (Liu, 2006b).

1.3. Microbial community structure and syntrophies in OPGs

In general, photogranules are described as spherical biofilm ecosystems of phototrophic and heterotrophic microorganism with a gel-like consistence. The most frequent phototrophic populations are composed of filamentous cyanobacteria and of unicellular algae (Milferstedt et al., 2017b; Trebuch et al., 2020). Regarding the bacteria (excluding cyanobacteria), the authors reported the presence of different functional groups namely nitrifiers, methanotrophs, phosphorous accumulators and the fast growing and biofilm producing denitrifiers such as *Zoogloea* and *Thauera*. Cyanobacteria are always associated with heterotrophic bacteria both in nature or engineered ecosystems (Abed, 2010; Cole et al., 2014; Salomon et al., 2003). Even in culture collections, cyanobacteria are merely axenic cultures, but most often as monoclonal cultures surrounded by several undefined heterotrophic bacterial species. It has been speculated that cyanobacteria require the presence of aerobic heterotrophic bacteria for their growth (Rippka, 1988; Roeselers et al., 2007), probably through symbiotic interactions (Besemer, 2015; Paerl, 1977; Tuomainen et al., 2006). Similar associations were reported for the microalgae.

Within OPGs, the basic interaction reported so far is the coupling of photosynthesis with aerobic respiration (Milferstedt et al., 2017b). The oxygen produced by phototrophs through photosynthesis is used by aerobic heterotrophs to oxidize organic matter. Heterotrophic bacteria produce CO_2 through respiration and oxidation of organic matter, which is in turn used as a carbon source by the phototrophs. The organic matter could be provided externally (e.g., wastewater) and/or from exopolymers produced by microorganisms. During illumination conditions, the dense phototrophic biomass in the uppermost layer of OPGs excrete extracellular polymeric substances (EPS) that are mainly composed of polysaccharides (Decho and Gutierrez, 2017; Di Pippo et al., 2013; Rossi and De Philippis, 2015). These EPS can be distinguished to two types. Firstly, a capsular polysaccharide which constitute the sheaths of cyanobacteria. Secondly, polysaccharides that are freely present in the medium. These EPS provide a source of organic carbon for aerobic heterotrophic bacteria in carbon-starve conditions. While, in darkness and lack of external carbon, cyanobacteria can incorporate organic matter derived from EPS (Stuart et al., 2016a, 2016b). It was also reported that besides the synergistic relationships between phototrophs and heterotrophs (i.e. direct exchange and internal re-cycling of nutrients essential for phototrophic biofilm growth and survival), bacteria potentially minimize oxygen accumulation in the microenvironments around the cells by using the oxygen to degrade dissolved organic matter (Jones and Cannon, 1986; Perera et al., 2019; Subashchandrabose et al., 2011). The oxygen would otherwise inhibit photosynthetic activity (i.e. photorespiration) (Orf et al., 2016; Stal, 2002).

In this thesis work, the focus will be solely on the exchange of oxygen between the two main functional groups (i.e., phototrophic, and heterotrophic microorganisms) (**Figure I.7**). To this end, it is crucial to investigate the microenvironments that are responsible for the OPGs biological processes and the formation of ecological niches for microorganisms with specific needs.

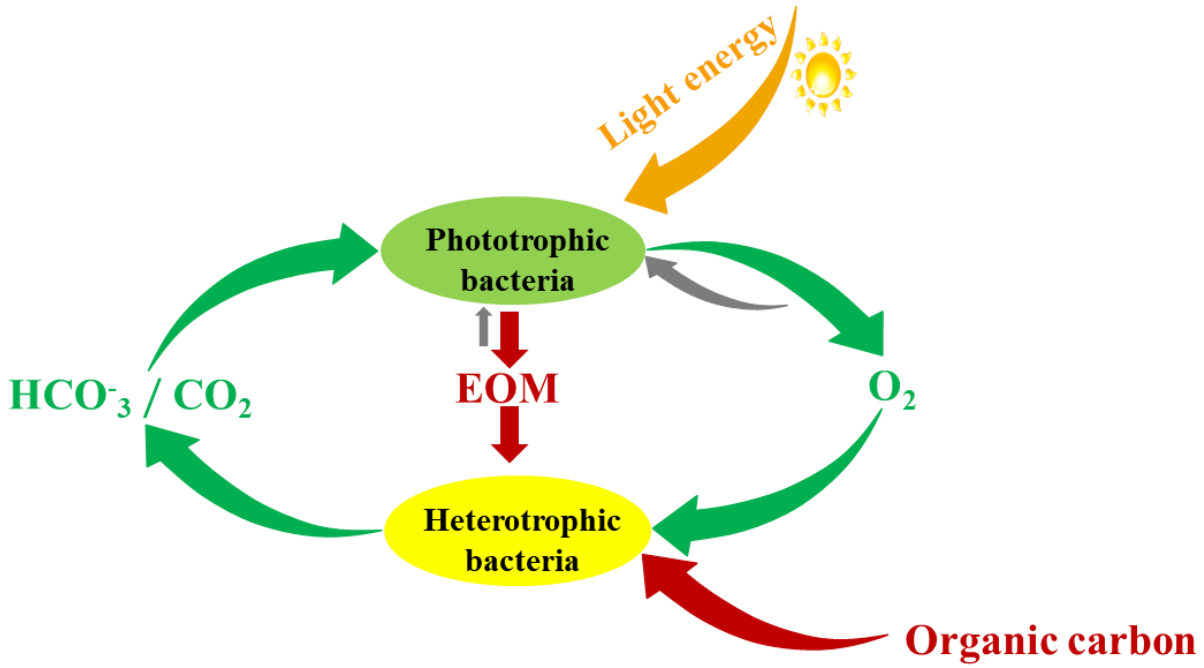

Figure I.7 *Conversion processes and trophic interactions between phototrophic bacteria and heterotrophic bacteria in the photogranule. Green arrows indicate the oxygen and carbon dioxide exchanges in the presence of light (yellow arrow). Red arrows indicate the production of the Extracellular Organic Matters (EOM) by the phototrophs and the consumption of organic matters by the heterotrophs. Grey arrows indicate the metabolism of the phototrophs in the absence of light (Consumption of EOM and oxygen)*

Understanding the microbial interactions within OPGs is essential to gain insights into the ecology and biogeochemistry of these systems. Furthermore, understanding these interactions will also allow linking bioreactor function to the microbial communities and to the environmental and operational conditions. In addition, knowing and underlying the positive or/and negative microbial interactions of the microbial community structure in oxygenic photogranules and the operational conditions is crucial for deciphering the mechanisms of photogranulation.

2. Investigating the microenvironment of biofilms and photogranules

2.1.Microenvironment and mass transfer

The spatial organization of OPGs, as in general for multispecies biofilms, arises from a complex interplay of biotic and abiotic interactions at different scales resulting in emergent activities and functions (Gupta et al., 2020). The variation in abiotic parameters affects behaviors from

centimeters to meters (e.g. reactor scale), while inter-microbial interactions affect community behaviors from micrometers to centimeters (e.g. OPG scale) (Cordero and Datta, 2016; Datta et al., 2016). It has been shown that the spatial structure of microbial communities influences the ecological stability, functional activities, and responses to environmental perturbation (Hol et al., 2015; Røder et al., 2020). The understanding of the mechanisms governing the spatial assembly and functioning of consortia in OPGs remains limited. However, it is expected that microbial patterns emerge from local trophic interactions between individuals of varied genotypes in spatially heterogeneous environment. Many similar biological ecosystems to the OPGs, were the subject of microenvironmental studies, namely microbial mats (Babauta et al., 2014), phototrophic biofilm (Kuhl et al., 1996), aerobic granules (Chiu et al., 2007) and electroactive biofilms (Lee and de Beer, 1995). These microscopic scale studies provide a first level understanding of the factors, processes and mechanisms that lead to a certain spatial structure or spatialization of the activity. The mentionned studies involve investigation of chemical/physical gradients of light gradient, oxygen, pH, redox and spatial distribution of microorganisms. It is then, necessary to move beyond macroscale analysis and investigate microscale environments in OPGs.

Traditionally, it was recognized that in an ideal ecosystem with a minimum of microbial interactions and with well homogenous mixed nutrients, physical processes (e.g. diffusion, advection) govern the biological activities of individual microorganisms and the availability of the resources (Dusenbery, 2011; Rusconi and Stocker, 2015). However, these ecosystems are rarely found in nature. In fact, most microorganisms form complex sessile communities (e.g. biofilms, granules, microbial mats). The close association and density of organisms within photogranules makes carbon and energy transfers very efficient. Such close vicinity modify the rate at which microorganisms encounter solutes of consumable resources (Großkopf and Soyer, 2016; Kiørboe et al., 2002). In addition, the physiological states of the microorganisms that form the biofilm are diverse and are determined by the position of the cells in the multiple layers of the biofilm (de Beer and Stoodley, 2006). Microorganisms located in the upper layers of the biofilm are more active due to greater accessibility to nutrients. Moreover, these microorganisms get rid of their metabolic products more easily compared to cells located at the bottom of the biofilm (Anwar et al., 1992; Salgar-Chaparro et al., 2020). It is therefore important to explore microscale mass transfer in the photogranule environment. Mass transfer is a physical phenomenon that occurs when mass is transported from one location to another under the effect of a driving force, such as a concentration

gradient or fluid flow. Resistance to mass transfer is a common property of biological systems such as microbial mats, biofilms and biogranules (de Beer and Kühl, 2000; Gonzalez-Gil et al., 2001; Liu et al., 2005). This resistance is due both to the boundary layer between the biological matrix and the surrounding environment and to low diffusion within the biological matrix. Advection of nutrients can often be neglected due to the limited water flow in the biological matrix, especially in the absence of liquid transport into the surrounding environment, leading to the development of steep gradients within the biological matrix. This has a subsequent impact on biological processes. Whereas, in the presence of liquid displacement or during the movement of the biological matrix (i.e., granules) in a liquid phase, the mass transfer was reported to be influenced by the hydrodynamics. de Beer and Stoodley (1995, 2006) sought to characterize the shape of the boundary layer above the biofilm (de Beer et al., 1994; de Beer and Stoodley, 1995). They used oxygen microelectrodes on the surface of a biofilm. They observed at low liquid velocity (7.8 $mm \cdot s^{-1}$) that the oxygen concentration gradients were perpendicular to the biofilm and the diffusional boundary layer was parallel to the biofilm. Conversely, at higher liquid velocities (115 $mm \cdot s^{-1}$), the oxygen concentration gradients were more or less perpendicular to the irregularities of the biofilm surface. Then the diffusional boundary layer closely followed the shape of the biofilm. This experimental study was complemented by a modelling approach by Picioreanu et al. (2000b). The transfer coefficient at the biofilm-liquid interface is then strongly related to the irregularities of the biofilm. The conditions under which convection plays a role have not yet been clarified and the link between tangential flow and flow in biofilm has been little formalized so far.

Mass transfer in OPGs is supposed to consist of three domains, as illustrated in the **Figure I.8** below. First, the mass that represents the macroscopic environment. Second, the boundary layer at the bulk/biomatrix interface through which a solute must pass before being assimilated (grey area in **Figure I.8A**). The thickness of the boundary layer depends on several factors such as flow velocity, interface roughness, temperature, etc. The thickness of the boundary layer depends on several factors such as flow velocity, interface roughness, temperature, etc... The thickness of the boundary layer can vary from <0.1 mm to several millimetres. Thirdly, internal mass transfer is generally considered to be diffusional and therefore frequently described using a single effective diffusion coefficient (D_{eff}). When biological process and mass transfer are combined within a biogranule, different profiles of solutes may occur (dots area in **Figure I.8B**)

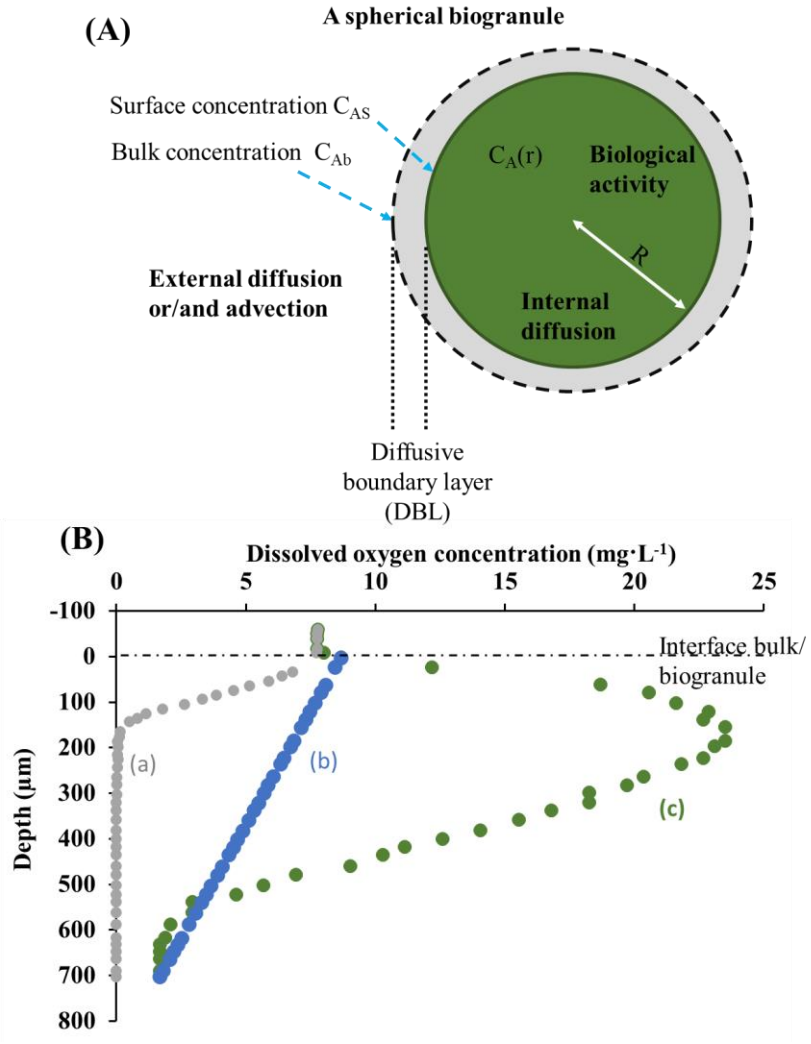

Figure I.8 *Mass transfer steps for a spherical biogranule resulting from reaction and diffusion. (A) Different compartments that distinguish the mass transfer in interfacial spatial structured ecosystems. (B) Steady state dissolved oxygen (DO) gradient in: (a) aerobic granules where the main process are related the diffusion and consumption of DO (Li et al., 2014), (b) DO gradient when diffusion is the only mass transfer ($C_A = a \times depth + C_{AS}$) with a non-flux in middle and (c) in phototrophic biofilm where diffusion, consumption and production are in equilibrium (Li et al., 2016a).*

Interpretation and prediction of the OPGs behavior are difficult without knowlegde about their microenvironment. Direct observations on physico-chemical gradients in OPGs are then needed. In the next paragraphs, short descriptions of some methods used to study mass transfer phenomena and microbial processes in biofilms are presented.

2.2. Phototrophic biofilm modeling

2.2.1. Generalities on biofilm modeling

The development of the experimental methods and technologies allowing to explore the microenvironment of biofilms, has led to change dramatically the vision and the understanding of biofilms structure (Caldwell et al., 1993; Costerton et al., 1994; Lawrence et al., 1991; Wessel et al., 2013). The biofilms at first were considered more or less as homogenous layers of micro-organisms in gel-like matrix, afterwards, different types of biofilm heterogeneities were recognized (Bishop and Rittmann, 1995; Stewart and Franklin, 2008; Wimpenny et al., 2000). Besides biological and chemical heterogeneities, biofilms present geometrical heterogeneity (e.g., thickness, surface roughness) and, physical heterogeneity (e.g., density, solute diffusivity). This reorganization has led to the development of a plethora of mathematical models that can range from very simple empirical correlations (Williamson and McCarty, 1976) to sophisticated and computationally intensive algorithm (Klapper and Dockery, 2010; Mattei et al., 2017; Picioreanu et al., 2000b, 1998; Wang and Zhang, 2010; Wanner, 2015). The varying levels of biofilm description are apparent in mathematical modeling methods which contain different levels of complexity. The most significant distinctions are made between one-dimensional (1D) and two- and three-dimensional models (2D/3D), dynamic and steady state models, single or multi species/substrates models and continuum or discrete models.

Mathematical modeling of biofilm is more complicated than modeling of suspended growth (Boltz et al., 2010b). Indeed, the geometrical domain of interest is usually divided in three compartments in 1D models: the bulk liquid, the boundary layer, and the biofilm itself (**Figure I.8**). Whereas in suspend growth models, the domain is considered zero dimension. The most known of these suspended models are the International Water Association (IWA) activated sludge models (ASM1, 2 & 3) (Henze et al., 2015, 1987) and the anaerobic digestion model (ADM1) (Batstone et al., 2002). Those models are generally based on the simulation of biochemical transformation processes using ordinary differential equations (ODEs). Those models are often used as a chassis and/or submodules in biofilms models for biological processes (Mannina et al., 2011; Randall and Sen, 1996). The growth rate of a microorganism in those models is commonly modeled by multiplying its maximum growth rate (μ_{max}) with several limiting terms, which are specific for each microbial group:

$$R_{x,growth} = \mu_{max} \cdot X \cdot \prod_1^n f_j \qquad (\textbf{\textit{Equation I.1}})$$

The limitation terms fj in the equations above, may be of saturation (e.g., Monod-type kinetics (Monod, 1949)), inhibition or optimum type. In addition, the consumption and the production of solutes is the sum of yielded growth rates involved in its production or disappearance.

Biofilm models are generally based on solving convection/diffusion/reaction models as simple partial differential equations (PDEs).

$$\frac{dX}{dt} - D_x \cdot \Delta X + \nabla(u_x \cdot X) = R_x \qquad (\textbf{\textit{Equation I.2}})$$

$$\frac{dS}{dt} - D_S \cdot \Delta S + \nabla(u_S \cdot S) = R_S \qquad (\textbf{\textit{Equation I.3}})$$

Where:

- X, S: microorganisms and substrate concentration in biofilm
- t: time
- D_s, D_x: microorganisms and substrate diffusion coefficient in the biofilm
- R_x, R_s: rate of microorganisms' growth and substrate conversion per biofilm volume respectively
- u_x, u_s: displacement velocity of microorganisms and substrate respectively.

However, some spatialized biological ecosystems present a high degree of complexity and coupled phenomena. Thus, it needs to be asked to which level one should incorporate the complexity of the studied system. Vannecke et al. (2015) as many others, recommended that the developed model should be as simple as possible and integrate the level of complexity depending on the intended use (Vannecke et al., 2015). In fact, biofilms involve also different length (e.g., micrometer to centimeters) and time scales (e.g., from milliseconds to days) (Morgenroth and Milferstedt, 2009; Wood and Whitaker, 1999), Theoretically, modeling the multi-scale biofilm situation can be solved by direct numerical simulation. However, this approach requires to solve the model at the lowest order of magnitude of the characteristics of biofilm system (Morgenroth and Milferstedt, 2009; Picioreanu et al., 2000a). Indeed, a model integrating the whole mechanisms involved in the function of a biofilm system, allows a better and fundamental understanding of the system behavior, and provides even more information when used for prediction. It can also help in identifying pertinent physical, biological, and chemical parameters as well as discerning irrelevant

ones. However, this approach may be a double-edged sword and, instead of gaining understanding with a global model, one cannot identify and evaluate the essential elements and processes due the tight connection between all elements involved. The model could be limited to engineering practice and requires an extremely high computer cost that is not feasible for field-scale applications. Thus, one usually tries to avoid to increase the model complexity when same results and finding could be provided with a simplest one.

To date, the one-dimensional Wanner-Gujer model (Wanner and Gujer, 1986; Wanner and Reichert, 1996) is still the base of many studies on engineered biofilm applications (Gupta et al., 2020b) like aerobic granular sludge (Layer et al., 2020), granule-floc anammox reactor (Chen et al., 2020) and, biofilms for continuous lactic acid production (Cuny et al., 2019). This model encodes the biomass as a continuum and rests on the assumption that all changes in biomass and dissolved solutes occur in the perpendicular direction of the substratum. The model includes also, adhesion detachment and attachment, biofilm generation by growth and EPS production, substrate, and product transport to and from the biofilm (**Figure I.9**). It provides a quantitative understanding of the processes within the biofilm. It is very suitable for describing the macroscopic coverings of a biofilm system and for giving a reasoned description of the layers that structure the biofilm. Nevertheless, several points have been criticized in this model (Eberl and Wade, 2020). A first point of criticism was the biofilm hollowing phenomenon (Hunt et al., 2004; Purevdorj-Gage et al., 2005; Rahman et al., 2015). In fact, the construction of the Wanner-Gujer model suppose that the sum of the volume fractions at any position in the biofilm is equal to one, thus it will not be able to predict the presence of cavities. A second point of criticism was to 1D models in general. Those are limited when considering a biofilm that grows with lateral growth gradients or has a network of pores contributing to substrate conversion within the biofilm (Alpkvist and Klapper, 2007). Many other points are reported basically related to the mechanical properties (e.g. detachment, deformation) (Picioreanu et al., 2018; Sudarsan et al., 2016) and to the moving free boundary layer (D'Acunto et al., 2019b, 2018).Therefore, further research has been conducted and more detailed models have been developed (Kagawa et al., 2015; Liehr et al., 1988; Picioreanu et al., 2000c). The dynamics of spatial distribution of particulates is computed using cellular automata (Picioreanu et al., 1998), individual based (Kreft et al., 2001; Picioreanu et al., 2005) or continuum methods (Eberl et al., 2000). These models were the subject of number of review studies dealing with modeling of biofilm systems namely the advances, challenges and perspectives in the biofilms

modeling (Dzianach et al., 2019; Eberl and Wade, 2020; Horn and Lackner, 2014; Klapper and Dockery, 2010; Picioreanu et al., 2004).

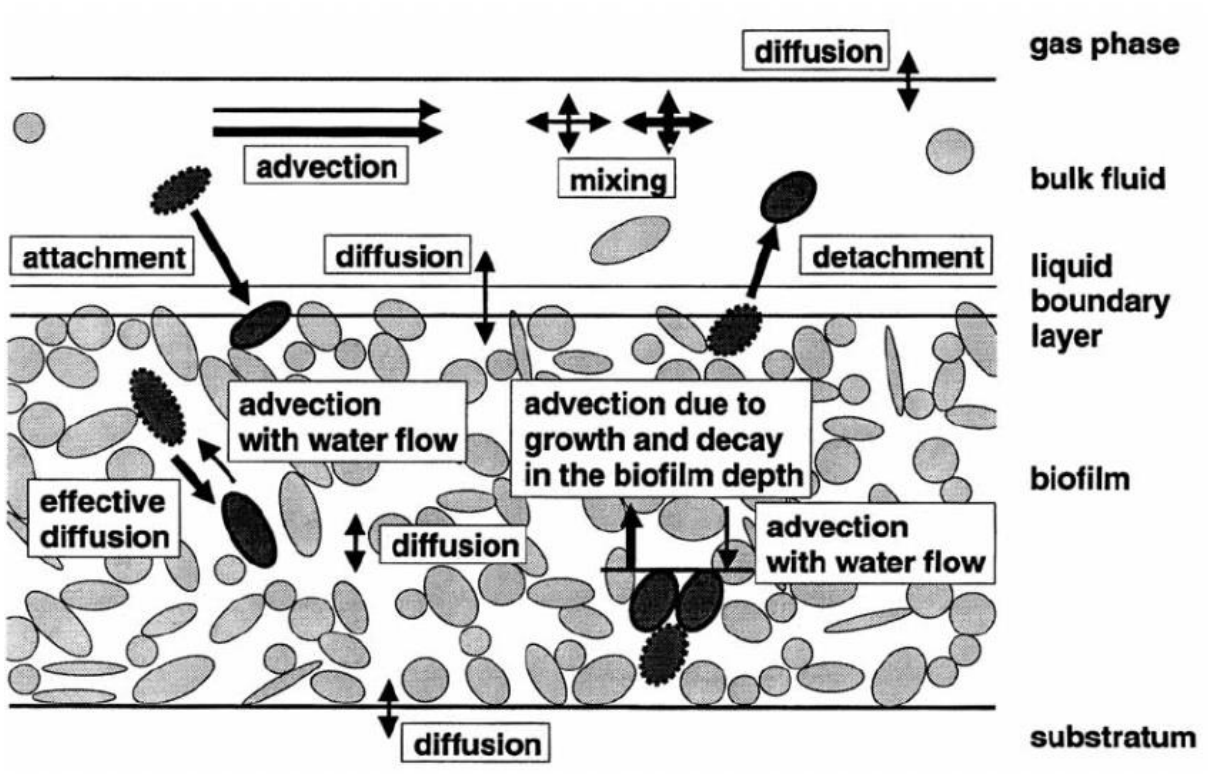

Figure I.9 *Description of the different transport processes of microorganisms (thick arrows) and dissolved solutes (thin arrows) (from Wanner and Reichert, (1996)).*

In the present thesis work, the mathematical models are used as practical tools providing a structural basis for theoretical experimentation. More particularly, to aid in determining physical and biological quantities that are not accessible directly with experimental measurements. This work focuses on already formed mature photogranules. Therefore, all the modeling work is based on solving the **Equation I.3** and **Equation I.4** which model substrates gradients in the OPGs.

2.2.2. Phototrophic biofilm modeling

In recent decades, the study of phototrophic biofilms has become an important field of research. They are a credible alternative to wastewater treatment (Guzzon et al., 2019; Milferstedt et al., 2017b; Roeselers et al., 2008), oil degradation (Abed, 2010; Roeselers et al., 2008), biohydrogen production (Strieth et al., 2018). The interest in these biofilms has led to the development of several mathematical models to understand their formation and potential applications (Clarelli et al., 2013;

Muñoz Sierra et al., 2014; Polizzi et al., 2017; Wolf et al., 2007). These models differ from the non-phototrophic biofilm models by the light component, more specifically, the photosynthetic active radiation (PAR) (i.e., the wavelengths between 400 and 700 nm) which is the major factor driving growth of phototrophs when there is no limitation by nutrients or carbon dioxide. Due to their dense and compact characteristics, light is attenuated during its passage through the phototrophic biofilm; the top cells shade the cells beneath and so on for the deeper cells in the biofilm. Thus, less light is available deeper in the biofilm. The light attenuation across the biofilm is usually modeled by the Lambert-Beer law:

$$I_{(z)} = I_{in} \cdot e^{-K_e \cdot (L_f - z)} \qquad \textbf{(Equation I.4)}$$

where I_{in} is the incident light intensity on top of the biofilm, z the biofilm space coordinate perpendicular to the biofilm surface, L_f the biofilm thickness, and K_e is the light attenuation coefficient. This coefficient depends on the composition of the biofilm and their optical properties (transmission, absorption, and reflection). The Lambert-Beer law seems to approximate the attenuation of light in many ecosystems, however it is criticized for underestimating or overestimating the penetration of light in systems where many factors interact with light in its path (Fernández et al., 1997). Thus, several alternatives were proposed, namely solving radiative transfer equation (RTE) (Houf and Incropera, 1980) using Monte Carlo simulations (Zhu and Liu, 2013). Although these methods are good at estimating the distribution of light, they are computationally intensive. The choice of a method, should be justified and validated by in-situ experimental measurement. In the present thesis work, light attenuation was measured experimentally and mainly modeled using the Lambert-Beer law or an approximation to this law.

Furthermore, as mentioned in paragraph 1.1.2 for cyanobacteria, phototrophs in general have specific light requirement. In fact, the growth and photosynthetic activity of the phototrophs within the biofilm is related to light intensity and consequently to the biofilm growth (Liehr et al., 1990). Different light regimes could be then distinguished: light limitation, saturation, and inhibition regimes (**Figure I.10**). Several studies have looked at this dependency and many models have been proposed, ranging from linear to complex ones (Béchet et al., 2013). Regarding light regime for cyanobacteria, those regimes dependent mainly to the stain. Several studies ranged the light limitation and the starting of the light saturation at the range of 50 to 100 $\mu moles_{PAR} \cdot m^{-2} \cdot s^{-1}$ (Albertano, 2012; Riegman et al., 1985; Tilzer, 1987) and the starting of the light inhibition at the

range of 170 $\mu moles_{PAR} \cdot m^{-2} \cdot s^{-1}$ (Tilzer, 1987). In this work, only light limited condition and the starting of the light saturation were investigated.

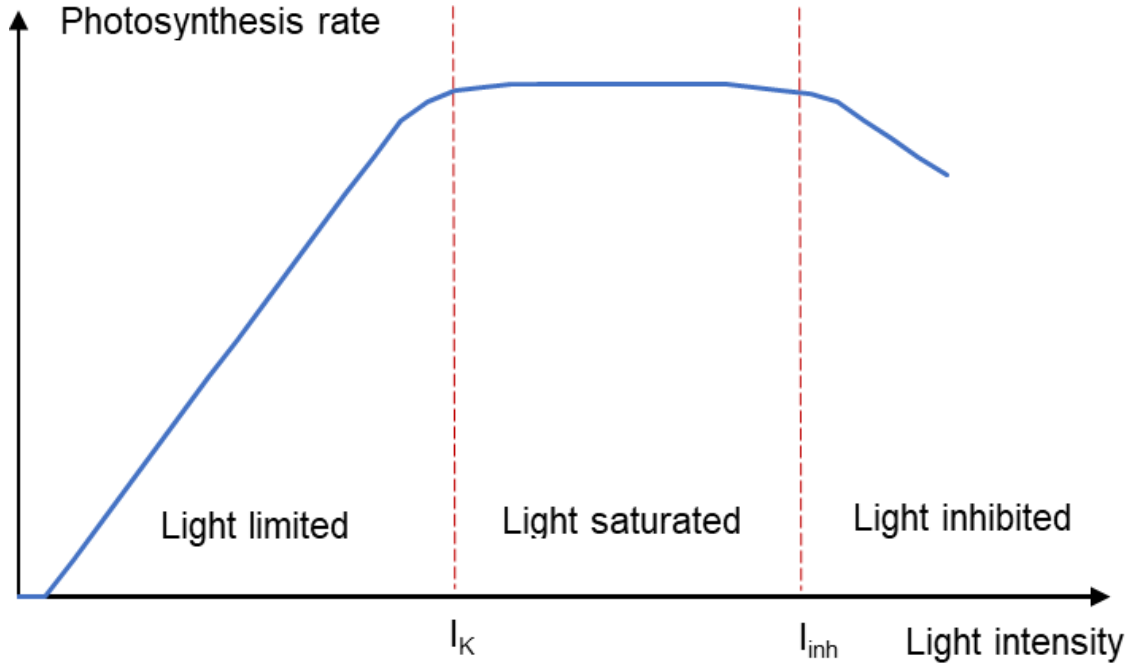

Figure I.10 *Typical relationship between light intensity and photosynthesis rate.*

Research on photosynthetic biofilms via mathematical modeling focuses on understanding and deciphering the mechanisms of their formation, as well as their potential applications. Flora et al (1995) was interested in modeling algal biofilms, specifically the effect of multiple environment background on the flux of inorganic carbon into the biofilms and pH gradients (Flora et al., 1995). Another modeling study was interested in microbial mats ecosystem which shares many common features with the phototrophic biofilm (de Wit et al., 1995). They interested in the ecological interactions between different species depending on the environmental parameters. Later, Wolf et al (2007) were interested in developing a global kinetic model considering interactions between different functional groups in mixed community phototrophic biofilms (PHOBIA Model). They detailed the biological mechanisms involved in the formation and the mass transfer between all the considered components (Wolf et al., 2007). Then, the model was used by (Staal et al., 2007) to evaluate the depth integrate consumption rate of inorganic carbon ($CO_{2(aq)}$ and HCO_3^-) during the development of the biofilm. However, the spatial distribution of different functional groups and their interactions were not described and discussed. Clarelli et al (2013, 2016) also took attention to cyanobacterial biofilm and they developed 1D, 2D and 3D model in order to study the

development of the biofilm structure, and the influence of light and temperature on their growth (Clarelli et al., 2016, 2013). Different models were also developed in order to investigate the potential application of the phototrophic biofilm whether for wastewater treatment or for biomass and biofuel production (Blanken et al., 2017a, 2017b; Li et al., 2016b; Polizzi et al., 2017).

Table I.1 *Summary of the most known mathematical models developed for phototrophic biofilms*

Model	Ecosystem studied	Type	Dimension	Objective
Flora et al. (1995)	Microalgal biofilm	Monospecies model	1D	Kinetics and biochemistry of the biofilm
de Wit et al. (1995)	Microbial mats	Multispecies model	1D	Microenvironment investigation
Staal et al. (2007) & Wolf et al. (2007)	Phototrophic biofilm	Multispecies model	1D	Microenvironement investigation
Polizzi et al. (2017)	Microalgal biofilm	Monospecies model	1D / 2D	Biofuel production
Clarelli et al. (2013,2016)	Cyanobacteria biofilm	Monospecies model	2D / 3D	Formation and structure
Celler et al. (2014)	Phototrophic *Diatoma* biofilms in streams	Monospecies model	3D	Structure and behavior to environment hydrodynamic
Muñoz Sierra et al. (2014)	Phototrophic biofilm	Multispecies model	2D	Wastewater treatment
Li et al. (2016b)	Immobilized microalgal biofilm	Monospecies model	1D	Biomass production
Blanken et al. (2017b)	Microalgal biofilm	Monospecies model	1D	Biomass production

Based on the above studies on phototrophic biofilm, modelling appears to be important and contributes enormously to the understanding of the formation mechanisms and the microenvironment of phototrophic biofilm. Consequently, the acquisition of essential information are necessary for the development and optimization of the application of phototrophic biofilms. It is therefore necessary to acquire in-situ data that allow the calibration and validation of the model. To this end, several technological tools were developed such as computational software for modeling or microsensors for experimental measurement.

2.2.3. Computational environment

Biofilms modeling is mostly based on PDEs. The latter are difficult to be solved using analytical approach when the interest is multi species/substrates biofilm. Therefore, numerical approaches are preferred. The mathematical description of the biofilm is converted to a system of algebraic equations and solved by the integration routines and numerical algorithms implemented in solver engine. Numerical solvers for biofilm models are increasingly available (Boltz et al., 2010a). A successful and well known software for one-dimensional biofilm is AQUASIM (Wanner and Morgenroth, 2004). Many recent and flexible software were developed for more complex simulations, such as COMSOL Multiphysics® (www.comsol.com). This software allows coupling several physics in one single and practical interface. Comsol solvers are based on the finite element method (FEM) to discretize the PDEs in the space variables (x, y, z). for stationary (steady state), time-dependent studies. Many studies have been used this software for biofilms modeling (Li et al., 2016; Muñoz Sierra et al., 2014; Picioreanu et al., 2010; Wolf et al., 2007).

One of the advantageous functionalities of Comsol is the possibility to connect it with other softwares such as Computer-Aided Design (CAD) softwares, MATLAB and JAVA in order to integrate more complexity desired (e.g. Karimifard et al., 2019; Picioreanu et al., 2010; Wu et al., 2020). In this thesis, Comsol was used to implement the models developed and to solve numerically mainly **Equation I.4**. More information on the model implementation in Comsol are described in the section of materials and methods in **Chapters II, III** and **IV.**

2.3.Sensors

Characterizing and understanding mass transfer in biological microenvironments needs direct measurement of microscale gradients using appropriate tools. Among the most used tools in microscale environment research are microsensors. Those are electronic devices that transform a physical or chemical quantity into an electrical measurement. Microsensors used in environmental studies can be separated by operating principle into two groups: electrochemical microsensors and optical microsensors. Electrochemical microsensors are called microelectrodes, referring to their electrode origin, and optical microsensors are called fiber-optic microsensors, referring to their construction using fiber-optic cabling.

2.3.1. Electrochemical microsensors: Microelectrodes

Among the electrochemical microsensors, there are potentiometric microsensors whose measurement is obtained by ion exchange through a membrane. The charge difference (characterized by a potential difference) is expressed by Nernst's law. Three micro-sensors are commonly used: the semi-cellular Ag/Ag^+ electrode, the ion exchange electrode (LIX: liquid ion-exchange) (de Beer and Schramm, 1999; Kühl and Jørgensen, 1992; Revsbech, 1989; Schramm et al., 1997) and the pH electrode. The pH microelectrode is a miniature version of the electrode commonly used in industry with an H^+ ion selective membrane. Some micro-sensors need the association with a reference electrode which can be either external (separate electrode) or internal.

Amperometric probes are also available. These types of microsensors are used to measure O_2, H_2S, H_2, N_2O and HClO (Ebert and Brune, 1997; Jeroschewski et al., 1996; Revsbech, 1989). Their principle is based on an electrochemical reaction that generates a current measured by pico-amperometry. This current is proportional to the concentration of the solute measured. The best known microsensor is the dissolved oxygen electrode with a cathode immersed in an electrolyte held by a silicone membrane.

Microbiosensors, finally, use cellular activity at the tip of the sensor (Damgaard and Revsbech, 1997; Santegoeds et al., 1998). In the literature, the most common are the glucose biosensor (based on glucose oxidation), the nitrate and methane biosensor. However, unlike the other sensors, these have a limited life span.

Figure I.11 illustrates the experimental setup that is used usually for microscale measurement. The microsensor is mounted in a motorized micromanipulator (e.g., Unisense, Denmark) and controlled by PC or manually, this allowed advances finer vertical steps up < 10 µm through the sample to be studied. The detected electrical signal (current/voltage) is acquired by a potentiometer or picoammeter. The signal is converted then to digital data by a device (ADC) connected to the acquisition system. The data are then recorded by a computer software. In case of optical microsensors, the acquisition is a spectrophotometer. A typical set-up for the measurement of dissolved oxygen is used in this thesis. This step is presented below in the **Figure I.11**. More information on the experimental set-up are detailed in the section of materials and methods of the **Chapter III** and **Chapter IV.**

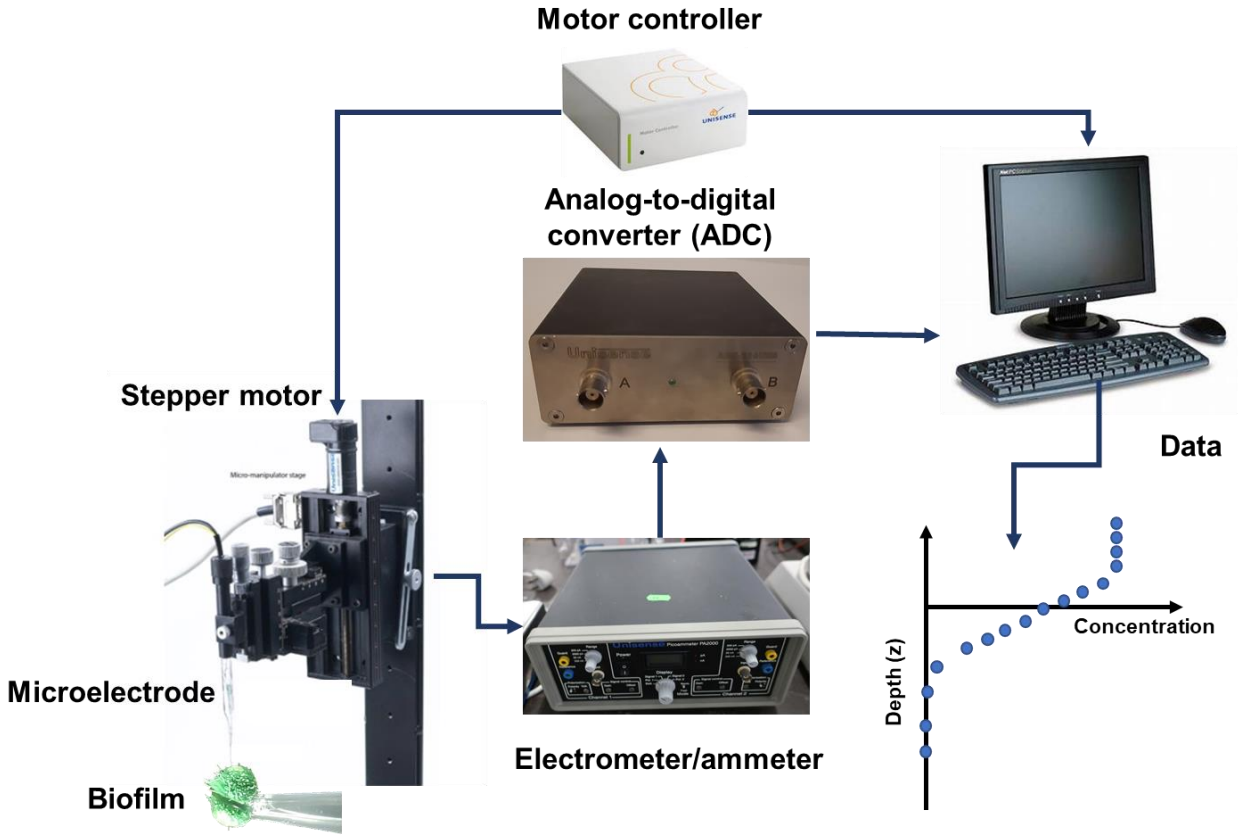

Figure I.11 *Conventional measurement setup and components used to operate microelectrodes in biofilm research.*

2.3.2. Optical microsensors

Among the optical microsensors, there are sensors dedicated for solutes measurement such as dissolved oxygen and sensors for quantifying scalar and spectral irradiance penetration. These are known as fiber-optic probes.

The light sensors are based on the collection of the light field integral (e.g., light intensity, spectral composition, or fluorescence) from all possible directions depending on the aperture of the fiber (Lassen et al., 1992). It is also possible to integrate a beam splitter and filters to further customize the measurement. The quantification of light penetration in microbial mats, phototrophic biofilm, corals are examples of application of this configuration.

The optical microsensors dedicated for solutes measurement are based on changes in the optical indicator (fluorophore) immobilized on the tip of the microsensor (**Figure I.12**). The tip detects

the fluorescent signal emitted by the solution to be measured (Wolfbeis, 2006). The signal is collected and directed into an optical fiber then into the opto-electronic measuring system (Holst et al., 1999). For instance, the measurement of dissolved oxygen using such a microsensor is based on ruthenium salts immobilized on the tip of the fiber. (Klimant et al., 1995). Those sensors are commercialized and wide range of tip diameter is available [5-500 µm] (www.unisense.com).

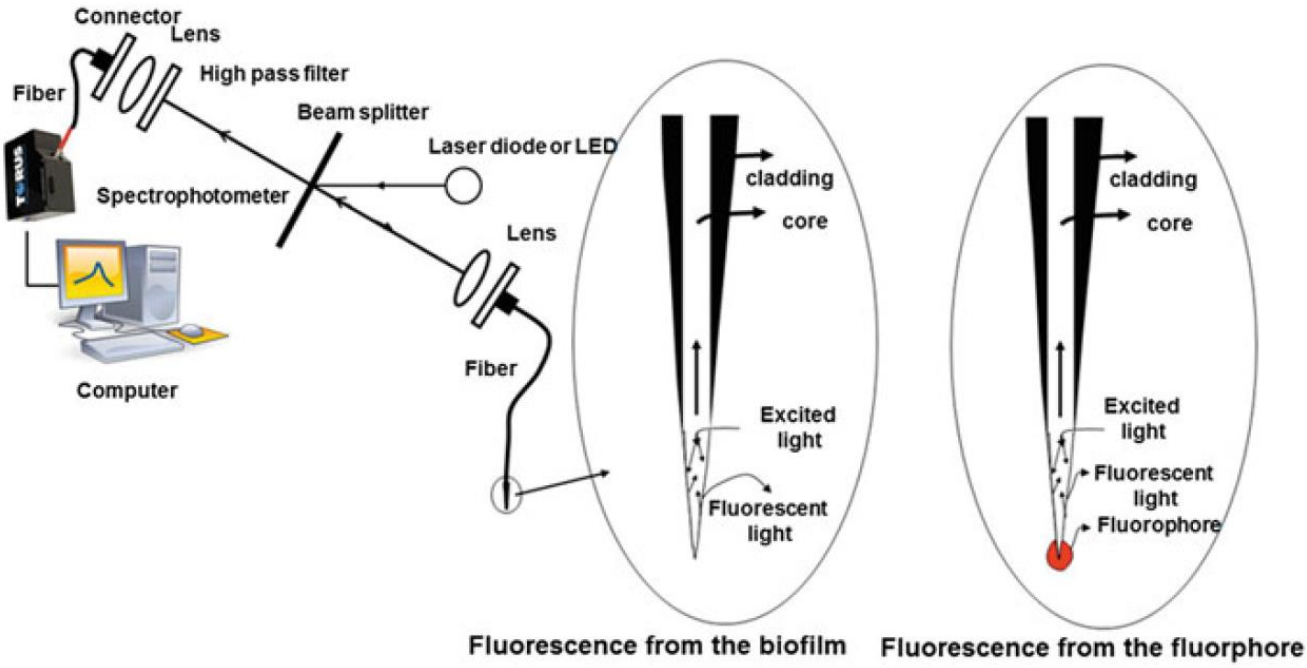

Figure I.12 *A Schematic illustration of an optic microsensor system which is based on detecting fluorescence from the biofilm (adapted Beyenal and Babauta, (2013)).*

Planar optodes are a new technology to investigate the spatio-temporal distributions of O_2, pH, CO_2 in studied system (Glud, 2008; Rubol et al., 2018; Wenzhöfer and Glud, 2004), in sediments and soils (Koop-Jakobsen et al., 2018; Pischedda et al., 2008). This technology is based on the luminescence of the indicators immobilized in a hydrophobic polymeric matrix. The measurement is based on the indicator dye quenched by the molecule of interest, and the emitted light is then recorded by a ratiometric camera (Larsen et al., 2011; Quaranta et al., 2012). This imaging technology allows micro-investigation of samples with complex structures systems with high spatial heterogeneity that could not be detected with microsensors, especially in non-steady states.

This technology is considered non-invasive and allows imaging in living samples. More than 100,000 measurement points can be recorded within one image and analyzed with the included

image processing and evaluation software (**Figure I.13**). Those planar optodes are commercialized and developed for the measurements of oxygen, pH, or carbon dioxide distributions in heterogeneous samples (www.presens.de). This technology was used in this work for 2D visualization and measurement of oxygen distributions in filamentous OPGs. More information on the experimental set-up are detailed in the section of materials and methods of the **Chapter II.**

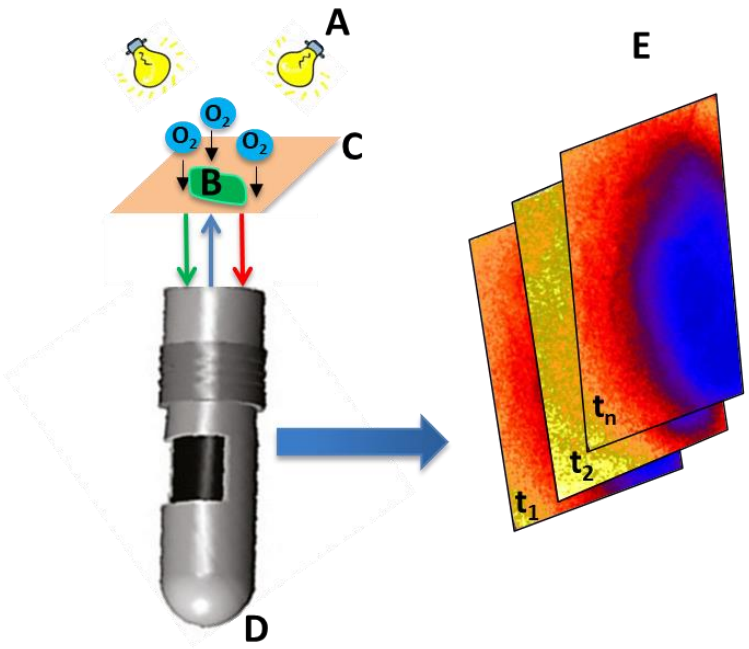

Figure I.13 *Schematic of a planar optode used for mapping spatio-temporal evolution of oxygen concentration of a biological sampled. The system is composed of a detector unit (Camera) and a sensor foil. The sensor foil is attached to the inside of a sample vessel; the side of the sensor foil without the color tag must be in direct contact with the sample. The sensor foil is read out through the transparent vessel wall. The time series recorded image are calibrated and converted to times series of oxygen concentration. (A) light source, (B) biological sample, (C) sensor foil, (D) recording camera, (E) time series of oxygen images.*

3. OPGs for wastewater treatment

For over 100 years, conventional activated sludge (CAS) has been the most widely used biological process for wastewater treatment. The CAS process is based on the biological oxidation of organic matter, which is then converted into biomass and carbon dioxide. Although CAS processes have shown satisfactory efficiency in terms of pollutant removal in wastewater, they require complex,

multi-stage operations and the need for large bioreactor spaces to meet the legal limitations for environmental discharge. Therefore, in order to ensure proper operation and development, it is important to evaluate it operational efficiency. Several studies have shown that the activated sludge process faces pressing challenges, notably high energy consumption and waste activated sludge (Elalami et al., 2019; Hosomi, 2016; Wichelns et al., 2015; Zhang and Ma, 2019). It is estimated that 40-60% of a wastewater treatment plant's energy consumption is caused by the biological treatment steps. This energy is generally used for aeration of wastewater to stimulate the conversion of organic matter (**Figure I.14**).

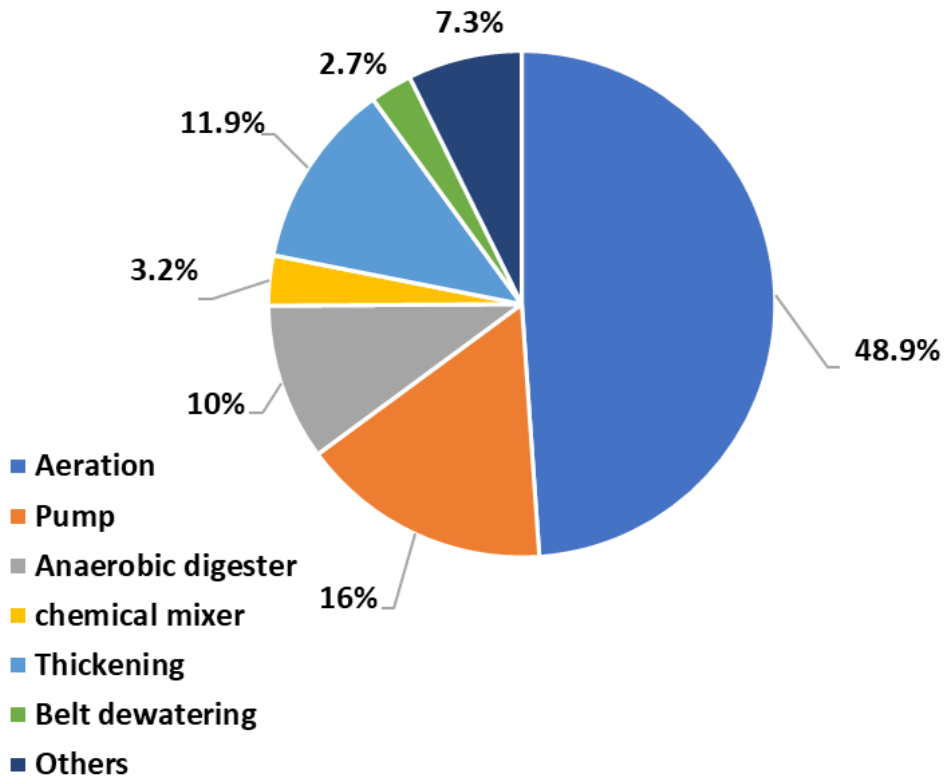

Figure I.14 *An example of energy consumption of a conventional activated sludge process with a treatment capacity of 38 thousand cubic meters wastewater per day (adapted from Zhang and Ma, (2020)).*

Furthermore, the generated sludge is a major challenge for CAS processes. Before being released into the environment, the treated wastewater must be separated from the biomass by settling. The cost of sludge disposal may account for up to 60% of the operating cost in a wastewater treatment plant (Canales et al., 1994). The becoming of sludge disposal is also an issue to be dealt with.

Current regulations tend to prohibit the use of untreated sludge and encourage the assessment and updating of the risks associated with the application of sludge to agricultural land or to any other utilization (Hudcová et al., 2019; Inglezakis et al., 2014) (Directive 86/278/EEC).

Therefore, in order to meet these challenges (i.e., energy needs for aeration, bi-products harvest, and valorization), new technologies and processes must be developed and applied ensuring efficient wastewater treatment with a minimum footprint, reducing energy consumption, and allowing a valorization of its by-products. To this end, OPG-based bioprocesses as ambitious energy neutral systems for wastewater treatment were recently proposed. OPGs allow in-situ oxygen production, thus eliminating the mechanical aeration. In addition to that, OPGs are easily separated from the effluent due to their higher density and settling velocity.

The use of phototrophic microorganisms (microalgae and cyanobacteria) for wastewater treatment has been developing for more than 60 years (Oswald et al., 1953). This approach is very attractive because the oxygen necessary for the conversion of organic carbon and nitrogen is provided via photosynthesis. In addition, it is considered as an alternative wastewater treatment pathways capable of simultaneous CO_2 capture and utilization (Arajo et al., 2014; Lu et al., 2018). Furthermore, the harvested phototrophic biomass presents an interesting source of high value by-products such as photopigments, biofuels, lipids or energy (Quijano et al., 2017). Photobioreactor technologies currently achieve purification capacities that are very comparable to activated sludge and can be very advantageous from an economic point of view (Longo et al., 2016; Shoener et al., 2014; Yang et al., 2011). Indeed, the OPGs showed 15-20% higher biological potential methane comparing with the activated sludge (Park et al., 2015). Furthermore, based on laboratory scale photogranule bioprocess data, a recent environmental life cycle analysis study, was conducted and revealed that a wastewater treatment system using OPGs could achieve a neutral energy system (Brockmann et al., 2021). In addition, phototrophic biomass in general, has been the subject of numerous studies focusing on the extraction of high-value molecules of interest that could be economically beneficial (Cuevas-Castillo et al., 2020; Levasseur et al., 2020; Vassilev and Vassileva, 2016; Zabed et al., 2020). However, many bottlenecks and challenges limit the feasibility of phototrophic-based biorefineries (Gifuni et al., 2019; Schiano di Visconte et al., 2019). The challenges are mainly related to the poor light penetration into the culture system especially when the biomass concentration is increased. High costs related to the development to the industrial scale photobioreactors and to the extraction of the high value-added molecules are

other important issues that slow down the integration of the microalgal biorefinery into the circular bioeconomy (Imbimbo et al., 2020; Kothari et al., 2017; Yin et al., 2020). Therefore, the development of a biorefinery based on wastewater using OPGs requires a thorough examination, from deciphering the mechanisms of photogranulation to the valorization of the biomass produced, through transposition to industrial scale.

Several processes promoting the formation of granules, which enable nutrient removal and free external aeration, have been developed in several research laboratories (Abouhend et al., 2018; Kumar et al., 2015; Milferstedt et al., 2017a, 2017b; Quijano et al., 2017; Tiron et al., 2017, 2015). Thanks to their rapid gravity settling, they facilitate solid-liquid separation. Those photogranules range in size from 0.2 to 5 mm in diameter with associated settling rates in the range of 12-360 $m \cdot h^{-1}$. Activated sludge flocs used in conventional wastewater treatment typically settle at less than 15 $m \cdot h^{-1}$ (Milferstedt et al., 2017a).

OPGs have been applied in discontinuous Sequencing Batch Reactors (SBR) and continuous wastewater treatment processes, at different loads of organic matter, using real or synthetic wastewater. The concentrations of applied organic matter were reported in the range of 90-900 $mg_{COD} \cdot L^{-1}$. OPGs are reported to be applied also under artificial or natural light. Different illumination strategies have been tested, i.e., continuous, or cyclic illumination (dark/ light). The light intensity was in the range of 0-330 $\mu moles \cdot m^{-2} \cdot s^{-1}$ photosynthetically active radiation (PAR) (Arcila and Buitrón, 2017). Higher light intensities were used when exposed to sunlight, but breakdown of the photogranulation and the disintegration of the granules were observed. **Table I.2** summarizes the main studies on photogranules for wastewater treatment application. In order to gain more understanding on the potentials and the performance of OPG-based bioprocess, this thesis work focuses on the activity of OPGs at the scale of individual. This study may help to provide insights in current or prospective bioprocess development and optimisation.

Table I.2 *Example of applied photogranule in wastewater treatment and application conditions (adapted from Zhang et al. (2020)).*

Wastewater Type	Wastewater characteristics ($mg \cdot L^{-1}$)			Reactor volume (L)	Light intensity ($\mu moles_{PAR} \cdot m^{-2} \cdot s^{-1}$)	Light-dark cycles (h) (L:D)	Aeration	Granule size (mm)	Filamentous outgrowth?	Main micro-organisms	Reference
	COD	N_NH^{4+}	P_PO4^{3-}								
Diluted dairy wastewater	100-400	8.7-42	0.8-12	1.5	235	15:09	No	0.6-1.9	No	Micro-algae	Tiron et al. (2017)
Local domestic wastewater	90-300	23-39	3.4±0-39	1.5	150	2.5:3.5	No	0.8-2.9	Yes	Cyanobacteria	Abouhend et al. (2018) ; Milferstedt et al. (2017b)
Municipal	816	64	15	50	240	-	No	1.3	Yes	Micro-algae	Arcila and Buitrón (2016)
Synthetic wastewater	600	100	10	1.4	Sunlight	20:04	Yes	0.78	No	Micro-algae	Huang et al. (2015)
Synthetic wastewater	300	35	10-11	2	81	12:12	Yes	0.6-1.5	No	Micro-algae	Liu et al. (2017,2018)
Synthetic wastewater	600	50	10	2	135	12:12	Yes	3.1	No	Micro-algae	Meng et al. (2019)
Synthetic wastewater	200	100	10	1.7	500	12:12	No	0.35-2.6	No	Cyanobacteria	Trebuch et al. (2020)
Primary effluent wastewater	90-300	23-39	3.4±0.7	1.5	150	3.5:2.5	No	0.1-4.5	No	Cyanobacteria	Abouhend et al. (2019)
Synthetic wastewater	960	36	37	1.7	120	12:12	Yes	0.5-4	No	Cyanobacteria	Kumar et al. (2015)

4. Scope and objectives

The long-term goal of OPG research is to provide a novel functional biomass for conversion processes in biotechnology, e.g., wastewater treatment or biosynthesis of molecules of interest. Stably operating these processes requires a detailed understanding of the OPG formation and of the conversion processes in this ecosystem. There are numerous internal interactions among process variables, such as light intensity to be provided, oxygen mass transfer, distribution of morphology and size. All of them have significant effects on the overall reactor performance. Obviously, then a sound understanding of microenvironment investigation is essential. Yet, little information is known about the light and oxygen microscale behavior in OPG so far. In this thesis, I aimed to model the role of OPG morphology and abiotic factors in shaping oxygen concentrations at the microscale.

Within the photobioreactor, we have observed a set of different OPG morphologies, with the coexistence of filament-covered and bald morphologies (**Figure I.5**). It is likely that the various morphologies influence their respective physiological activities. It is of interest to understand **how this filamentous architecture is linked with oxygen concentration distribution in space and time.** In fact, the filamentous surface of those OPGs presents a real challenge for oxygen microscale measurement using conventional microsensors. To this end, I used oxygen planar optodes to map the spatio-temporal distribution of oxygen concentrations that cannot be accurately observed by another point measurement device. Then the experimental measurements were combined with 2-dimensional reaction-diffusion modeling that incorporates the spatial heterogeneity of filamentous structure and can provide insights into the spatial distribution of state variables, then evaluation of the relative contributions of respiration, photosynthesis, and diffusion. The results of this study are described in **Chapter II.**

Biological processes in OPGs are mainly driven by concentration gradients of oxygen and the amount of available light. The oxygen concentration is the result of diffusion, light availability, conversion rates, OPG size, and the spatial biomass distribution. In fact, OPGs during their residence in the photobioreactor are exposed to continuous changes in the incident light intensity due to the mixing. Therefore, they undergo dynamic adjustments based on the incident light available in their microenvironment. Thus, I investigated **how the incident light affect the local light availability for progressively deeper OPG regions and consequently their stratification.**

For this purpose, I used a light microsensor to measure the attenuation of scalar and field irradiances in the OPGs. This study is addressed in **Chapter III.**

Besides the changes in incident light intensity, the OPGs are also subjected to different bulk environmental conditions. During the feeding phase of the photobioreactor, the high organic matters concentrations will result in a rapid turnover of oxygen, leading to overall low oxygen concentrations in the system. When the organic matter concentration decreases over the cycle, oxygen consumption will slow down, leading to increasing oxygen concentrations within the OPG. The variations of oxygen concentrations within the OPG influence and is influenced mutually with the bulk oxygen concentration. Furthermore, irradiation will influence oxygen production and thus influence oxygen availability across the depth gradient of an OPG. All these factors (incident light intensity, bulk oxygen, and organic carbon concentrations) strongly influence the oxygen gradients. I was then interested in on **how light intensity affects oxygen gradients within an OPG.** Oxygen microgradients were measured using oxygen microsensors under different light intensities during famine and feast readily biodegradable organic carbon regimes. Then, the dependencies of oxygen gradients in the OPG on available light and organic matter were included in a 1-dimensional model. The latter allows to differentiate between the biological activities (photosynthesis/aerobic respiration) and physical mass transfer (diffusion). This analysis is described in **Chapter III.**

OPGs also undergo a variation in the bulk concentration of oxygen. Moreover, as pointed out in previous sections, size is key feature of OPGs. Therefore, it is important to understand **the effect of different combined conditions of incident light, COD, and oxygen concentrations in bulk that an OPG encounter during an SBR cycle.** To answer this question, measurements of oxygen concentration profiles in OPGs of the different sizes were carried out. The experimental data were used to improve the model developed in the previous chapter, then used to evaluate a much larger number of scenarios than could have ever be done experimentally. The result of this work is presented in the **Chapter IV.**

The final **Chapter V** summarizes the main findings and proposes future research lines based on the work presented in this thesis.

Chapter II

Mapping the biological activities of filamentous oxygenic photogranules[1]

[1] Ouazaite, H, Milferstedt, K, Hamelin, J, Desmond-Le Quéméner, E. Mapping the biological activities of filamentous oxygenic photogranules. *Biotechnology and Bioengineering*. 2020; 1–11 https://doi.org/10.1002/bit.27585

Abstract

Oxygenic photogranules have been suggested as alternatives to activated sludge in wastewater treatment. Challenging for modelling photogranule-based processes is the heterogeneity of photogranule morphologies, resulting in different activities by photogranule type. The measurement of microscale-activities of filamentous photogranules is particularly difficult because of their labile interfaces. We present here an experimental and modeling approach to quantify phototrophic O_2 production, heterotrophic O_2 consumption and O_2 diffusion in filamentous photogranules. We used planar optodes for the acquisition of spatio-temporal oxygen distributions combined with 2D mathematical modelling. Light penetration into the photogranule was the factor controlling photogranule activities. The spatial distribution of heterotrophs and phototrophs had less impact. The photosynthetic response of filaments to light was detectable within seconds, emphasizing the need to analyze dynamics of light exposure of individual photogranules in photobioreactors. Studying other recurring photogranule morphologies will eventually enable the description of photogranule-based processes as the interplay of interacting photogranule populations.

Keywords

wastewater treatment, syntrophy, modelling, phototrophic biofilms, oxygen gradients

1. Introduction

Recently, oxygenic photogranules (OPGs) have been described as a novel kind of photogranular biofilm (Milferstedt et al., 2017b, 2017a). OPGs are dense bacterial aggregates, typically a few millimeters in diameter, characterized by an outer layer mainly composed of filamentous cyanobacteria. The production of oxygen by these cyanobacteria via photosynthesis is typically coupled to the oxygen consumption of heterotrophic bacteria that convert organic matter, e.g., from wastewater, into CO_2, which is immediately used by cyanobacteria for biomass synthesis. This syntrophic relationship between bacteria makes photogranules a promising candidate biomass for wastewater treatment (Abouhend et al., 2020, 2018). External aeration in conventional activated sludge is currently the major energy expenditure of wastewater treatment plants (Longo et al., 2016; Shoener et al., 2014). In an OPG process, external aeration is not necessary (Abouhend et al., 2018). However, this energy may be off-set in a bioprocess using OPGs by the energetic requirements of mixing and the potential supply of electric light for pollution removal. In contrast to conventional activated sludge, a putative OPG based bioprocess has the advantage of recovering otherwise released CO_2 in freshly grown and easily harvestable phototrophic biomass. This biomass may serve as resource in the environmental biorefinery and makes OPG-based wastewater treatment a candidate for the future Water Resource Recovery Facility. So far, no details on the biological activity at the micro-scale of an OPG have been reported as current OPG research mostly focusses on deciphering the mechanisms of photogranulation (Abouhend et al., 2020; Ansari et al., 2019; Milferstedt et al., 2017b; Stauch-White et al., 2017) and on the potential application of these granules for wastewater treatment (Abouhend et al., 2018; Trebuch et al., 2020).

Within a single laboratory-scale photobioreactor, we have observed the coexistence of a range of different OPG morphologies, from filament-covered OPGs to OPGs resembling nearly perfect spheres. It is likely that the various morphologies influence their respective physiological activities.

Oxygen fluxes within spherical OPGs (**Figure II.1**) can be resolved using conventional microelectrodes of the Clark type (Revsbech and Jørgensen, 1986) or polarographic electrodes (Mancuso et al., 2000). These tools are suitable for biofilms, or more specifically granules, with well resolved, stable interfaces for gradient measurements from the surface to the inside of the sample. From a limited number of measurements, the behavior of a larger surface or volume can often be extrapolated. OPGs with labile, flexible, and potentially moving filaments at the surface (**Figure II.1)** do not have a stable granule-bulk interface. Their biological activity is greatly

influenced by external flow and the boundary conditions. The use of micro-electrodes and the interpretation of their results is challenging as sufficient data reflecting this heterogeneity cannot be easily recorded. This type of filamentous morphologies requires the development of dedicated approaches.

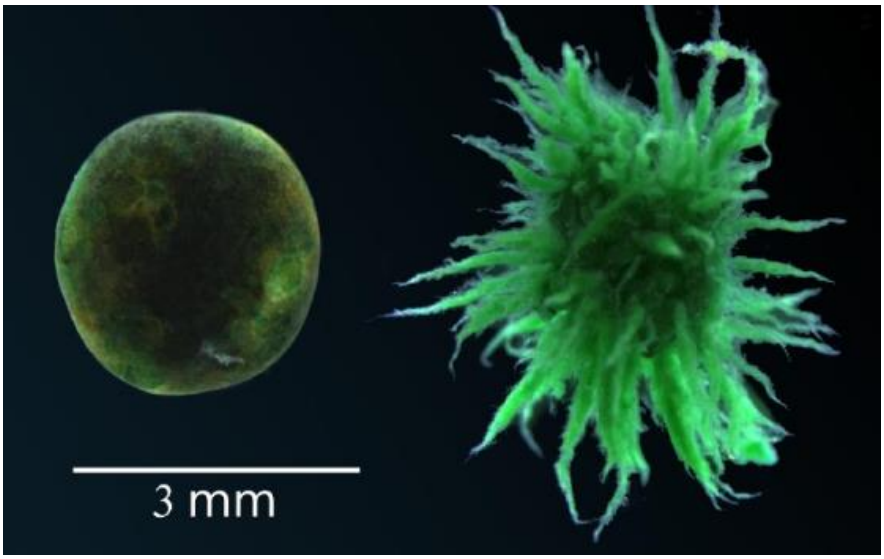

Figure II.1 *Different photogranule morphologies as observed in one photobioreactor: left a sphere-like morphology; right a filamentous morphology.*

Planar optodes have been used to investigate the spatio-temporal distributions of O_2 in microbial assemblages (Glud et al., 2001; Rubol et al., 2018; Wenzhöfer and Glud, 2004) sediments and soils (Koop-Jakobsen et al., 2018; Pischedda et al., 2008) and possibly filamentous photogranules. The optode technology uses the luminescence of oxygen sensitive indicators immobilized in a hydrophobic polymeric matrix. The measurement is based on the indicator dye quenched by the molecule of interest. Emitted light from the molecules is then recorded by a ratiometric camera (Larsen et al., 2011; Quaranta et al., 2012), making it possible to resolve 2D oxygen distributions in and around objects of poorly defined geometries. We apply this promising technology here to examine its suitability for measuring time-series of oxygen dynamics as proxy for activity of filamentous photogranules at the microscopic scale. Mapping their metabolic activity will help optimizing the overall performance at the process scale.

The net activity of a photogranule results from various processes happening at the same time, i.e., respiration, photosynthesis, and diffusion. However, their individual contributions are not accessible from the oxygen distributions derived from the optode measurements but can be mathematically disentangled. We hypothesize that a simple 2D reaction-diffusion model using only two parameters, maximum oxygen production rate (q_{p0}) and maximum respiration rate (q_{r0}),

is sufficient to decipher the relative contributions of respiration, photosynthesis, and diffusion. The model allowed us to test different hypothesis of spatial distributions between phototrophs and heterotrophs within the granule.

The deconvoluted data obtained from our experimental approach coupled to mathematical modelling provide the characterization of filaments of a photogranule as part of the description of a diverse range of observed photogranule morphologies found in an OPG-based bioprocess.

2. Materials and Methods

2.1 Bioreactor operation and photogranule sampling

A four-litter sequencing batch photobioreactor was operated with 6-hours cycles under constant illumination of 100 $\mu moles_{PAR} \cdot m^{-2} \cdot s^{-1}$ of photosynthetic active radiation (PAR) at the reactor surface. The characteristics of the photobioreactor such as geometry, mixing and sequential operation configurations are described in more detail in Milferstedt (2017b). The feed was a synthetic wastewater with a chemical oxygen demand of 120 $mg \cdot L^{-1}$ and the following composition according to Nopens et al. (2001): peptone 8.7 $mg \cdot L^{-1}$, yeast extract 26.1 $mg \cdot L^{-1}$, starch 61 $mg \cdot L^{-1}$, sodium acetate 42.2 $mg \cdot L^{-1}$, KH_2PO_4 11.7 $mg \cdot L^{-1}$, $MgHPO_4 \cdot 3\ H_2O$ 14.5 $mg \cdot L^{-1}$, urea 45.9 $mg \cdot L^{-1}$, NH_4Cl 34.2 $mg \cdot L^{-1}$, $FeSO_4 \cdot 7\ H_2O$ 2.9 $mg \cdot L^{-1}$.

The OPGs in the photobioreactor showed different morphologies, with the coexistence of spherical and filamentous OPGs (**Figure II.1**). One filamentous OPG of the maximum dimensions of 8.5 mm and 4.5 mm with an inner core of approximately 2.3 mm diameter (**Figure II.3 a**) was sampled at the end of a SBR cycle, i.e., after 5 hours of the reaction cycle and was immediately used for extensive imaging of oxygen distributions. Note that a filamentous OPG is an aggregate with long filaments compared to the more solid inner core. The extended filaments lead to the maximum dimensions of this photogranule. For our objective, the evaluation of the optode technology and demonstrating its applicability of capturing oxygen dynamics, the in-depth evaluation of one filamentous photogranule is sufficient. However, a generalizable description of filamentous photogranules requires the use of more individuals and is not attempted in this work.

2.2 Dynamics of oxygen distribution

Oxygen imaging was performed with a PreSens VisiSensTM planar optode (Tschiersch et al., 2012) (**Figure II.2**). A piece of about 60 mm^2 oxygen sensitive sensor foil (SF-RPSU4, PreSens) was glued inside a Petri dish using silicone gel (Silicone rubber compound RS 692-542, RS Components Ltd., Corby, UK). The filamentous OPG was then placed on the sensing foil and a microscopy cover slip was carefully placed on it to prevent the photogranule to float, making sure not to flatten or otherwise disturb the photogranule geometry.

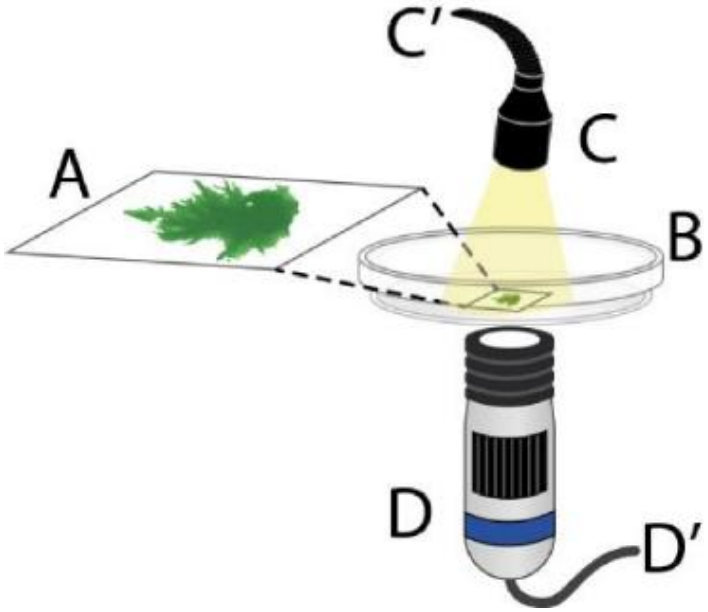

Figure II.2 *Schematic display of the experimental set-up to map the oxygen dynamics in a photogranule. (A) filamentous OPG on oxygen sensitive sensor foil in a (B) Petri dish filled with water; (C) goose neck providing light at an intensity of 100 µmoles$_{PAR}$·m^{-2}·s^{-1}, connected to (C') an external LED light source. Dynamics of oxygen were collected using (D) a camera and recorded on (D') a personal computer.*

The experimental set-up allows the measurement of oxygen distributions at the photogranule surface in contact with the sensor foil. Some minor parts of the photogranule periphery could not be placed onto the reactive surface of the sensor foil because of steric reasons. This did not impact the experimental set-up and analysis.

Then, the Petri dish was filled with air-saturated tap water and closed. The Petri dish was immediately placed on top of the VisiSens camera (Detector Unit DU01, PreSens). The experiment was conducted over 112 minutes during which 130 images of oxygen distributions were recorded over two dark phases (0 – 35 min, 70 – 88 min) and two light phases (35 – 70 min, 88 – 112 min). Each image acquisition consisted of a cycle with a length of 52 s, partitioned in a reaction part (32 s) and an image acquisition part (20 s). The acquisition time is comparably long but cannot be reduced due to the chemical requirements of the sensor foil. Depending on the illumination phase, the reaction part was either in darkness (dark phases) or illuminated with externally provided cold white light at 100 µmoles$_{PAR}$·m^{-2}·s^{-1} of photosynthetically active radiation (PAR) (SCHOTT KL2500LED). For technical reasons, illumination can only be provided from the top of the petri dish, i.e., opposite of the camera, because the recording camera must be placed directly under the sensor foil. The acquisition phase was always in the absence of external light. Corrected for the time of image acquisition, the photogranule received on average

61 PAR during the light phases of the experiment. During image acquisition, the VisiSens system emits 9 $\mu moles_{PAR} \cdot m^{-2} \cdot s^{-1}$ as PAR at the lens of the camera. This light is required for the excitation of the photosensitive film, even during the dark phases and did not have a measurable effect on photosynthesis of the system.

The VisiSens images were calibrated after their acquisition according to the manufacturer's procedure by recording a single image of the sensor foil and applying a two-point calibration with a drop of deoxygenated water (tap water stripped with N_2) for 0% O_2 and a drop of water in equilibrium with air for 21% O_2 saturation.

At the end of the experiment, the exact position and geometry of the filamentous OPG on the sensor foil was determined on an image taken with a stereomicroscope (M205FA, Leica Microsystems GmbH, Wetzlar, Germany). The original color image was converted to an 8-bit grey level image.

2.3 Data acquisition and analysis

The time series of oxygen distributions were recorded as PNG images (AnalytiCal 1 Software VA.12, VisiSens). The calibration was performed using the evaluation module of the software following the manufacturer's instructions. The calibrated images were saved in the VisiSens proprietary RAW format and then converted into the ImageJ format "IMJ" (Schneider et al., 2012) using the VisiSens Raw data Interface. Each image has the size of 1280 × 1024 pixels, displaying the oxygen sensitive sensor foil on an area of 925 × 880 pixels. This area corresponds to about 8.3 × 7.5 mm^2. The spatial resolution on the images is 8.9 µm $pixel^{-1}$. The images were then imported as arrays to MATLAB (version R2018b, MathWorks, USA) and dynamics of oxygen concentrations were associated with the morphology of the photogranule.

2.4 Model description, linking oxygen fluxes and microbial activities

A 2D model describing the dynamics of oxygen diffusion with consumption, and production through heterotrophic and phototrophic activities was created to differentiate the impact of each process on the dynamics of measured oxygen concentrations. We used COMSOL Multiphysics (version 5.3a, Comsol Inc., Burlington, USA) for this model. We opted for a 2D model as the three-dimensional (3D) shape of the photogranule was complex and could not be approximated with a simple geometry.

The computational domain (**Figure II.3 b**) was extracted from the stereomicroscopic image (**Figure II.3 a**) using the MATLAB contour function and then imported to COMSOL Multiphysics using the live link COMSOL-MATLAB interface. The domain was scaled to the

size of the oxygen images (8.3 × 7.5 mm^2). The Petri dish wall was used as boundary condition without mass flow and an O_2 flux set to zero. A triangular mesh was applied on the whole image, with a finest meshing at the vicinity of the photogranule contour. The maximum resolution of 8.9 $\mu m \cdot pixel^{-1}$ for the recorded oxygen images was used for the finest meshing (**Figure II.3c**). At this resolution, numerical problems caused by derived unbalanced forces could be avoided. This resolution was not applied on the whole image to avoid prohibitive computing times.

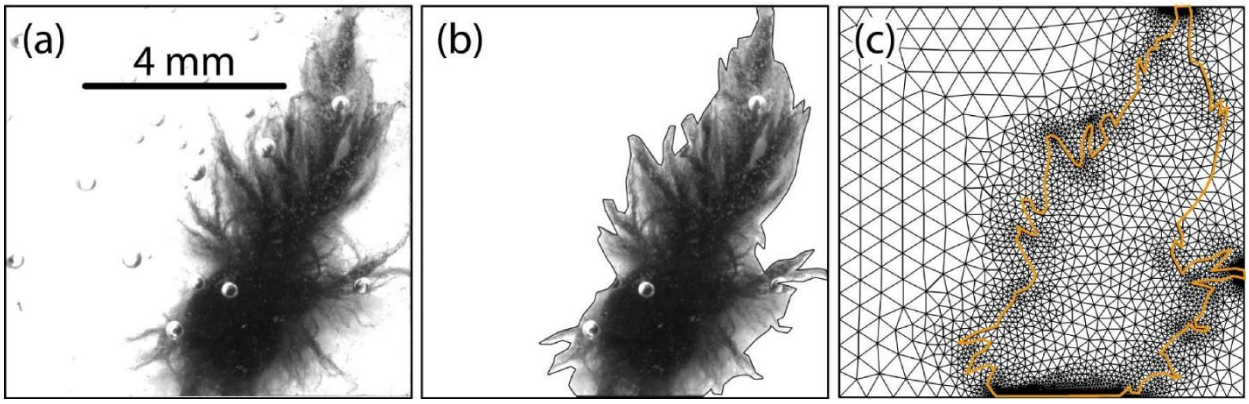

Figure II.3 *OPG image and its processing for computation of the geometry: (a) stereomicroscopic image for determination of biomass density based on grey levels; (b) OPG contour calculated based on (a); (c) domain mesh for modelling, with smaller mesh size where oxygen dynamics were higher, e.g., the bulk-photogranule interface, or where for numerical convergence a higher density of points was required, e.g., at the boundaries.*

2.5 Assumptions for the mathematical model

Growth of bacteria was neglected since the experimental duration of 112 min was short compared to the assumed growth rates of microorganisms in photogranules. During the experiment the availability of organic matter for heterotrophic respiration and HCO_3^- for photosynthesis was assumed to remain constant. Organic matter is present as extracellular polymeric substances (EPS) secreted by microorganisms especially by cyanobacteria. Unpublished preliminary experiments showed that EPS were sufficiently present to maintain respiratory OPG activities for several hours. HCO_3^- was present in excess for photosynthesis due to the hardness of the local tap water of 4.0 ± 0.2 mM as HCO_3^- (https://orobnat.sante.gouv.fr/orobnat/rechercherResultatQualite.do). This concentration was considered not rate-limiting for photosynthesis as the K_S for HCO_3^- of 0.1 mM HCO_3^- (Wolf et al., 2007) is well above the natural availability of HCO_3^-. Thus, dissolved O_2 was the only chemical species considered in this analysis.

The dynamic diffusion-reaction **(Equation II. 1)** for dissolved O_2 is:

$$\frac{\partial c}{\partial t} - \nabla \cdot (D \cdot \nabla c) = r \qquad \textit{(Equation II. 1)}$$

where *c* is the dissolved oxygen concentration, *D* the diffusion coefficient for oxygen and *r* the net oxygen reaction rate. The diffusion coefficient for oxygen (*D*) is taken as constant throughout the photogranule and equals the diffusion coefficient in water at 20 °C (Wolf et al., 2007). Therefore, *D* equals 2.01 10^{-9} $m^2 \cdot s^{-1}$ as for dilute solutions. This assumption was upheld by the fact that the photogranule porosity is rather large as it is mainly composed of filaments. For OPGs found in a photobioreactor with mixing, advective/dispersive transport could potentially play a role within OPGs. This could be taken into account by an effective diffusion coefficient larger than the one in bulk water (Davit et al., 2013).

The net O_2 reaction rate (r) is zero outside the granule, while being computed from photosynthesis (r_p) and heterotrophic respiration rates within the photogranule (r_r) **(Equation II. 2):**

$$r = r_p - r_r \qquad \textit{(Equation II. 2)}$$

The rate of oxygen production by phototrophs was considered linearly proportional to light intensity and could be approximated to first order kinetics **(Equation II. 4),** since the experiments were performed under light-limiting conditions for filamentous cyanobacteria (Faizi and Steuer, 2019; Staal et al., 2002). The rate of oxygen consumption was modeled using a Monod kinetics **(Equation II. 3):**

$$r_r = q_r(f) \cdot \frac{C}{C+K} \qquad \textit{(Equation II. 3)}$$

$$r_p = q_p(f) \cdot I(f) \qquad \textit{(Equation II. 4)}$$

where $q_r(f)$ is the maximal respiration rate, C the dissolved O_2 concentration, K the half saturation constant with a value of 0.5 mg L^{-1} (Horn and Hempel, 1997), $q_p(f)$ the maximal photosynthesis rate and I(f) the light intensity. The variable f was introduced to account for an assumed local biomass density. For this, grey levels in **Figure II.4 g** were converted to a variable f comprised between 0 (white) and 1 (black) (**Figure II.4 f**) which was used as a proxy for surface-based biomass density. The use of the function f is introduced in the Results section below (**Table II.1**), leading to the final equations for r_r and r_p in **(*Equation II. 6*)** and **(*Equation II. 7*).**

2.6 Parameter estimation and sensitivity analysis

A major factor in dynamic modelling of biological systems is the estimation of model parameters. To estimate the parameters for the current models, a nonlinear least-squares optimization problem was formulated **(Equation II. 5),** with the objective of minimizing the least absolute errors (LAE):

$$LAE = \sum_{i=1}^{i=10} \sum_{j=1}^{j=130} \left| c(t_j, x_i, y_i) - c_{exp}(t_j, x_i, y_i) \right| \quad \textbf{(Equation II. 5)}$$

where $c_{exp}(t_j, x_i, y_i)$ is the experimental concentration of oxygen and $c(t_j, x_i, y_i)$ the predicted oxygen concentration from the model for ten chosen points on the sensor foil geometry. Four of the points are located near the center of the photogranule, four points are within its filaments and two points are in the bulk (**Figure S 1**). (x_i, y_i) are the x- and y-coordinates of point *i* and t_j is the acquisition time of image *j*.

The parameter estimation was carried out using the MATLAB function 'fmincon' which allows finding the minimum of a constrained nonlinear multivariable function. The two parameters q_{r0} and q_{p0} were estimated during this minimization problem (**Table II.1).**

3. Results

3.1 Spatio-temporal oxygen distribution

The photogranule used in this study and the area analyzed with the VisiSens system are shown in **Figure II.4 g**. Area-based biomass density is approximated as grey levels on the image where darker grey level mean higher biomass density. The photogranule contour (**Figure II.3 b**) resulted from manual thresholding, best differentiating the spatial domain of the photogranule (grey levels) from the bulk liquid (white). Maps of oxygen concentrations were extracted from images acquired after exciting the oxygen-sensitive film placed underneath the photogranule. Local oxygen concentrations were extracted and plotted over time for points P1-P5 (**Figure II.4 f** and **g**). Note that the optode measures oxygen at the interface between the oxygen sensitive sensor foil and the photogranule. Therefore, positions of the points are strictly speaking found at this interface as indicated in **Figure II.4 f**. Points P1 and P2 are located under the core area of the photogranule. Here, the initial oxygen concentration starts around 20% oxygen saturation and rapidly decreases to less than 5% during the first dark phase. It then remains stable at this level until the end of the experiment. Points P3 and P4 are located within the filaments. The oxygen concentrations here are initially at 50-60% of the saturation concentration and decrease in the first dark phase to around 5% for P3 and 10% for P4. Especially at P4, an oscillation of the concentration is then observed with an increase of about 5% during the light phases and a decrease of about 5% during the dark phase. At point P5, located outside the photogranule, the oxygen concentration oscillates in a similar manner as at P3 and P4. The mean value and the amplitude of the oscillations are, however, greater for P5 than for P3 and P4, with values around 60% and 10%, respectively. These differences between measurements obtained for the bulk (P5) and for the area underneath the

filaments (P3-P4) confirm that the filaments are close enough to the sensor foil to avoid the formation of boundary layers.

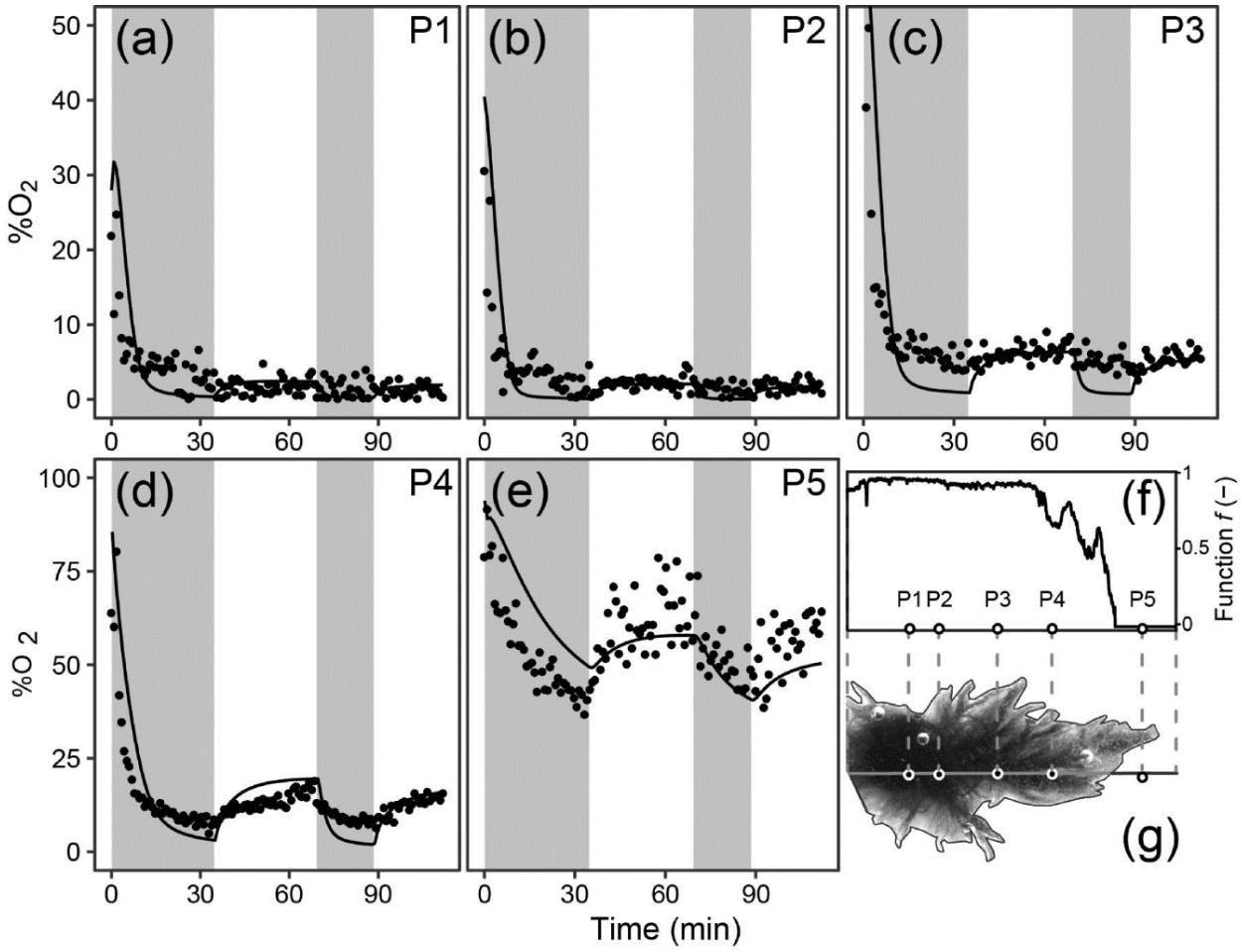

Figure II.4 *Oxygen dynamics at five points of interest and their location in the photogranule. (a) – (e) Oxygen concentrations (with respect to the saturation concentration when exposed to air) at points P1 to P5 over time. The points are measured data, solid lines are the model output using scenario 4 (**Table II.1**). The shaded areas indicate the dark and light phases of the experiment. (f) The transformed grey level profile of the transect connecting points P1-P5 in the photogranule, as used for function f in **Equation II. 3**, **Equation II. 4** and **Equation II. 7** and **Table II.1**. (g) Bird's eye view of the location of points P1 – P5 in the photogranule. Note: This image is a rotated version Fig. 3b.*

3.2 2D reaction-diffusion model

With the 2D model, we tested a set of scenarios relating respiration and phototrophic activities to the local biomass densities *f* (**Table II.1**). Among the scenarios, we identified the one that best captured the influence of the 3D structure of the photogranule on the dynamics of oxygen

concentrations at the surface of the VisiSens sensitive film, evidenced by the best fit between model and experimental data.

The scenarios in **Table II.1** include configurations in which (i) both, respiration, and phototrophic activities ($q_r(f)$ and $q_p(f)$, respectively), are proportional to local biomass densities (scenarios 1 or 5); (ii) only one of them is proportional local biomass densities (scenarios 2, 3, 6, 7); or (iii) both are independent of local biomass densities (scenarios 4 and 8). Also, light intensity $I(f)$ was tested as a function of local biomass densities: (i) $I(f)$ could be inversely proportional to biomass density, (scenarios 1-4). This corresponds to photosynthetic activity predominantly towards the outside of the photogranule, where local biomass densities are low and being attenuated towards the center of the photogranule. (ii) Alternatively, $I(f)$ was tested to equal I_0 = 61 PAR throughout the photogranule if we assume that the measured photosynthetic activity results from the whole photogranule (scenarios 5-8).

For each scenario of the model, parameters q_{r0} and q_{p0} were optimized to obtain the best fit for ten selected points (P1-P5 and five additional points, see **Figure S 1**). Estimated rates and mean absolute error (MAE) are shown in **Table II.1**. Scenarios 1-4 deviate less from the experimental measurements than scenarios 5-8, as indicated by their lower MAE. This is confirmed by a more detailed analysis of the fits in which we analyzed the local behavior at each of the ten selected points (supplementary material **Figure S 2– Figure S 11**). Including a light dependency related to biomass density in the model apparently improves the quality of the model output. Among these scenarios, scenarios 1, 3 and 4 have the lowest MAE and behave similarly at the ten examined points (**Figure S 1**). We thus decided to retain the simplest of the three, scenario 4, for all consequent analyses. Using scenario 4 **(Equation II. 3)** and **(Equation II. 4)** become:

$$r_r = q_{r0} \cdot \frac{C}{C+K} \qquad \textit{(Equation II. 6)}$$

$$r_p = q_{p0} \cdot I_0 \cdot (1 - f) \qquad \textit{(Equation II. 7)}$$

The model then allowed us to deconvolute the three processes of respiration, photosynthesis, and diffusion from spatially-structured oxygen measurements. We integrated their rates over the total 2D surface delimited by the contour of the photogranule (**Figure II.3 b**). The dynamics of surface integrated rates are shown in **Figure II.5**. At the beginning of the two dark phases, the initial respiration was relatively high, as indicated by relatively low negative rates of -10.5 and -7.6 $nmol \cdot m^{-1} \cdot s^{-1}$. The respiration activity then decreased during the phases and the associated rates reached -4.3 and -3.7 $nmol \cdot m^{-1} \cdot s^{-1}$ during the first and second dark phase, respectively. At the end of the phases, the system was close to steady state and diffusion nearly compensated oxygen

consumption by respiration with rates of 4.7 and 3.6 nmol·m^{-1}·s^{-1}. Conversely, respiration rates increased during light phases and reached -7.6 and -7.3 nmol·m^{-1}·s^{-1}. This was associated with a constant photosynthesis rate of 5.3 nmol·m^{-1}·s^{-1}. The oxygen flux towards the photogranule by diffusion was lower during light phases than during dark phases (2.7 and 2.0 nmol·m^{-1}·s^{-1}), but the photogranule remained a net consumer of externally provided oxygen. At the end of each dark or light phase, the system was near steady state. Steady state was reached only during the first light phase that lasted 35 minutes. Globally, for all the phases, a time on the order of 30 minutes is required for the system to reach a steady state.

Table II.1 *Evaluation of various scenarios relating respiration ($q_r(f)$), photosynthetic activities ($q_p(f)$) and light availability ($l(f)$) to surface-based biomass densities (f). For each scenario, maximum respiration, and photosynthesis rates (q_{r0} and q_{p0}) as used in the reaction-diffusion model (**Equation II. 3** and **Equation II. 4**) were estimated, using the least absolute errors as criterion from which the mean absolute error (MAE) was computed. Scenario 4 (in bold) was retained for all further analyses.*

Model scenarios				**Estimated rates and error**		
#	$q_r(f)$	$q_p(f)$	$I(f)$	q_{r0} (mmol·m^{-3}·s^{-1})	q_{p0} (m^{-1})	**MAE (% air saturation)**
1	$q_{r0} \cdot f$	$q_{p0} \cdot f$	$I_0 \cdot (1 - f)$	0.75	25.4	3.7
2	q_{r0}	$q_{p0} \cdot f$	$I_0 \cdot (1 - f)$	0.45	16.6	4.4
3	$q_{r0} \cdot f$	q_{p0}	$I_0 \cdot (1 - f)$	1.04	26.6	3.8
4	$\boldsymbol{q_{r0}}$	$\boldsymbol{q_{p0}}$	$\boldsymbol{I_0 \cdot (1 - f)}$	**0.55**	**17.5**	**3.8**
5	$q_{r0} \cdot f$	$q_{p0} \cdot f$	I_0	0.22	5.6	8.4
6	q_{r0}	$q_{p0} \cdot f$	I_0	0.52	5.6	5.4
7	$q_{r0} \cdot f$	q_{p0}	I_0	4.71	2.6	8.9
8	q_{r0}	q_{p0}	I_0	2.93	33.6	8.7

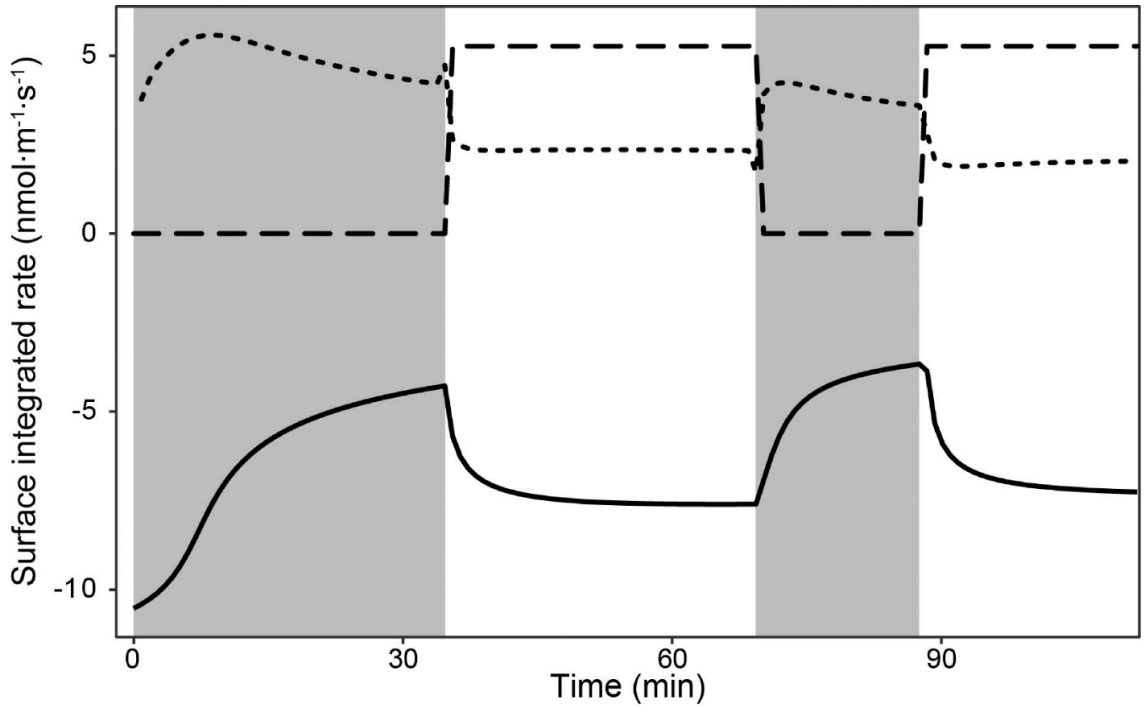

Figure II.5 *Surface integrated rates of modeled respiration (solid line), photosynthesis (dashed line) and diffusion (dotted line) over the course of the experiment for the entire photogranule. The surface used for the integration corresponds to the area inside the contour in Fig. 3b. The shaded areas here indicate the dark and light phases of the experiment.* O_2 *consumption by respiration is expressed as a negative rate while* O_2 *production by photosynthesis is positive. Diffusion can be either positive when* O_2 *is imported into the photogranule or could be negative when it is exported.*

3.3 Sensitivity analysis

We assessed the uncertainty of parameters q_{r0} and q_{p0} by varying their values around their optima of 0.55 mmol·m^{-3}·s^{-1} and 17.5 m^{-1} (**Table II.1**) and computing the resulting MAE (**Figure II.6**). At a MAE of up to 4 %O_2 (i.e., an increase in MAE of about 5% compared to the optimal MAE of scenario 4), the retained couples of (q_{r0}, q_{p0}) fall within the central ellipse in **Figure II.6**. The minimal and maximal values associated with this ellipse are between 0.52 and 0.65 for q_{r0} and between 15.6 and 22.6 for q_{p0}. However, there is a strong positive correlation between q_{r0} and q_{p0}, i.e., when q_{r0} increases, also q_{p0} increases. The uncertainty on the values for q_{r0} and q_{p0} is quite high with a possible relative error of 18% and 29%, respectively, when we compare the optimal couple (0.55 mmol·m^{-3}·s^{-1}, 17.5 m^{-1}) with the extreme acceptable values of (0.65 mmol·m^{-3}·s^{-1}, 22.6 m^{-1}).

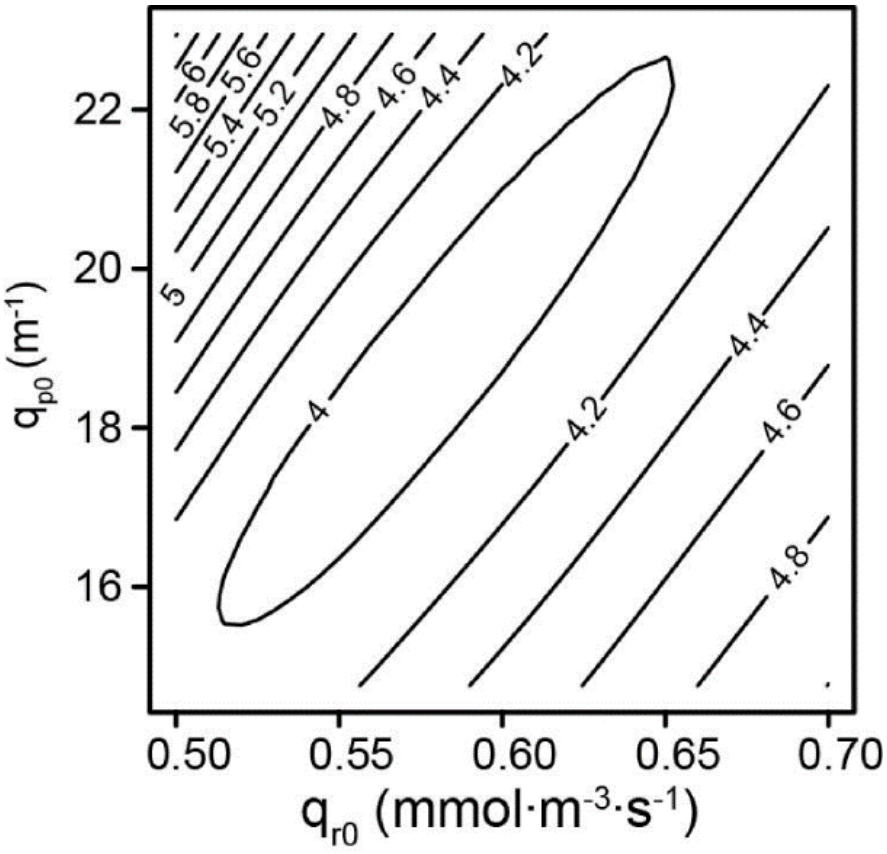

Figure II.6 *Contour plot of mean absolute error (MAE in $\%O_2$) of the model as function of q_{r0} and q_{p0}. The minimum is found for q_{r0} = 0.55 mmol·m^{-3}·s^{-1} and q_{p0} = 17.5 m^{-1} as shown in Table 1. The area within the ellipse where MAE = 4 $\%O_2$ corresponds to combinations of q_{r0} and q_{p0} for which MAE ≤ 4$\%O_2$.*

4. Discussion

The coexistence of multiple granule morphologies is common in granular sludge bioreactors. This was reported for phototrophic algal-bacterial biomass under batch or continuous cultivation with synthetic medium (Brehm et al., 2003) or real wastewater (Arcila and Buitrón, 2017) for anammox sequencing batch reactors treating municipal wastewater (Pijuan et al., 2020) or sequencing batch reactors with aerobic granular sludge treating synthetic or real wastewater (Layer et al., 2019; M. Pronk et al., 2015; Schambeck et al., 2020). In our photobioreactor, we observed the coexistence of a range of morphologies, from filament-covered photogranules to nearly spherical photogranules (**Figure II.1**). System performance results from the interactions of microorganisms within each granule but also between the populations inhabiting granules of diverse morphologies and sizes (Kuroda et al., 2016; Liu et al., 2020). The different morphologies of biomass are believed to be essential for the proper functioning of the bioreactors (Vannecke et al., 2015). Therefore, breaking down the contributions by morphologic granule population may become

necessary for predicting overall reactor performance, especially when the abundance distributions of size and morphology classes may be changing. This could be done by physically separating major populations and quantifying the performance of a more uniform composite sample (Abouhend et al., 2020), or by measuring the activities of individual granules. With data from both approaches, whole reactor performance can be extrapolated using mathematical models. These models do not exist yet but would be preferable over an "average biomass" model as these models would be able to take into consideration temporally non-steady distributions of granule size and morphology.

The microenvironment of individual granules with a clearly defined boundary and a somewhat solid structure is readily accessible using microelectrodes as done for example by Okabe et al (2011) in anammox granules. Using the classic microelectrode approaches, examining the microenvironment of photogranules of filamentous morphology is more challenging because of the ill-defined boundary of the photogranule and its flexible filaments.

We demonstrate here first advances for measuring the activity of filaments in a filamentous photogranule morphology using optodes. In this technology, an oxygen sensitive sensor foil is used to generate an optical signal proportional to the measured oxygen concentration. The resulting images represent a map of oxygen concentrations at the interface with the oxygen sensitive sensor foil. For thin filaments and other labile objects as for example streamers, e.g., points P4 and P5 (**Figure II.4 d** and **e**) the measurement can be assumed to represent the behavior of the biomass. However, for denser regions of photogranules, e.g., at points P1 and P2 (**Figure II.4 a** and **b**), the biomass in contact with the oxygen sensitive sensor foil may not be photosynthetically active. Indeed, as light may not penetrate all the way through the denser regions, no photosynthetically active radiation reaches the oxygen sensitive sensor foil. Consequently, the potential local photosynthetic activity cannot be directly measured.

To an extent, mathematical modeling circumvents this limitation. Using a reaction-diffusion model, we were able to deconvolute the images of oxygen concentrations acquired with the optode into photosynthetic oxygen production, heterotrophic respiration, and diffusive transport from the bulk liquid into the photogranules (**Figure II.5**). This knowledge cannot be easily deduced from the interpretation of the raw experimental data.

A remarkably simple model structure containing two parameters was able to capture the essential dynamics of photogranule activities (**Figure II.4**). We tested various scenarios of spatial distributions of phototrophic and heterotrophic biomass and two illumination types (non-obstructed and attenuated light) (**Table II.1**). The best fits of experimental data with the model

was achieved in scenarios where light was attenuated following the function f (**Figure II.4 f**). None of the non-obstructed light scenarios (**Table II.1**, scenarios 5-8), including all tested biomass distributions, reached similarly well-fitting results. Three biomass distributions (scenarios 1, 3 and 4) were similar in their fits but we retained scenario 4 as the most parsimonious model. It assumes a homogenous distribution of heterotrophic and phototrophic biomass at all points within the photogranule domain. In scenario 4, light is available for photosynthesis inversely proportional to the surface-based biomass density (function f). It appears that the attenuation of light as a function of the surface-based biomass density was more important for the fit of the model than the biomass distributions. Our results indicate that a focus of future research should be the penetration of light into phototrophic biomass as this phenomenon seems a more sensitive factor for activity than the distribution of biomass. Our result confirms what Abouhend et al (2020) found when relating specific oxygen production rates to photogranule size. The optimal size range of photogranules were found to have diameters between 0.5 and 1 mm, corresponding to photogranules with a homogeneous distribution of phototrophs and diameter allowing light penetration throughout the photogranule (Abouhend et al., 2020).

The presence of larger photogranules (size up to 5 mm) was reported (Abouhend et al., 2020). These larger OPGs are of great importance since they allow the coexistence of different zones (oxic, anoxic, anaerobic) and favor, for example, simultaneous nitrification and denitrification. This range of sizes (up to 4 mm) found for photogranules is comparable with sizes reported for aerobic or anaerobic granules and are compatible with standard mixing used for WWT (Batstone and Keller, 2001; de Graaff et al., 2020; Pronk et al., 2015; Zheng et al., 2006).

Under the current experimental conditions, even under illumination, the oxygen supply by diffusion is not negligible, especially considering that respiration was limited to residual organic matter contained in the photogranule. With a greater pool of readily available organic matter, as for example contained in wastewater, respiration would be expected to be higher, requiring a higher oxygen supply. Considering our measurements, this higher contribution could not be provided through photosynthesis with an average irradiation of 61 PAR. Our model allows us to test the influence of changing light conditions on the photogranule activity. Using the parametrized model on the identical photogranule geometry as used in this study, we calculated that an illumination of at least 120 PAR would satisfy oxygen requirements beyond endogenous respiration, enabling the degradation of externally supplied organic matter.

Abouhend et al (2020) observed the degradation of externally supplied organic matter at 150 PAR. Even though our calculations and a comparison with literature values may be used to indicate

possible light requirements for wastewater treatment using photogranules, this consideration should be taken with care, as the values were obtained using very different experimental procedures and systems. The minimum light requirements may be lower as we assume as our experimental procedure using the optodes may underestimate or hinder oxygen production.

From the model, a maximum volumetric rate of oxygen production ranging from 1.66 to 2.66 $mmol \cdot m^{-3} \cdot s^{-1}$ for 100 PAR light intensity and a maximum volumetric rate of respiration ranging from 0.45 to 1.04 $mmol \cdot m^{-3} \cdot s^{-1}$ were estimated for the four best scenarios. The range estimated for the volumetric rate of respiration is consistent with the values ranging from 0.1 to 1.5 $mmol \cdot m^{-3} \cdot s^{-1}$ found in the literature for different types of phototrophic biofilms (Kühl et al., 1996; Ploug, 2008; Rubol et al., 2018). However, the range for volumetric oxygen production rate is one order of magnitude lower than values ranging from 8 to 40 $mmol \cdot m^{-3} \cdot s^{-1}$ reported in the literature (Kühl et al., 1996; Kühl and Polerecky, 2008; T. Li et al., 2016a). These values highly depend on the biofilm structure, density, and nutrient availability, yet this confirms the underestimation of the oxygen production or the low activity of the photogranule used in this study.

One identified reason for underestimating actual oxygen production is linked to the required exposure time of 20 s for image acquisition of the optode system. During acquisition, external photosynthetically active radiation needed to be stopped, while the light-independent oxygen consumption continued. The resulting images thus represent an integral over 20 s of oxygen consumption. Due to the possible non-linearity of the responses, we refrained from estimating a consumption term to compensate this loss. A further drawback of the long acquisition time, though less relevant in our situation, is the detection of processes with shorter characteristic times than needed for acquisition, e.g., oxygen production in moving filaments.

Our 2D model, by definition, only considers a projection of a three-dimensional photogranule onto a two-dimensional surface. This projection, however, is not a true average signal over the depth of biomass, but in a sense a weighted average, giving most weight to the interface with the oxygen sensitive sensor foil. The global photosynthetic activity may thus be underestimated. Indeed, photosynthetic activity at the light-exposed surface of the photogranule, e.g., above points P1 and P2, may not be detectable at the film interface as all oxygen will have been consumed in upper parts of the photogranule. The effect of the projection may explain the discrepancy between model and experimental data at P3 (**Figure II.4 c**). Here, the model underestimates the experimentally measured oxygen concentrations possibly because diffusion from the bulk phase overlaying the photogranule may supply oxygen that is unaccounted for in the 2D model. It may also happen that available surface for photosynthesis, e.g., filaments protruding into the bulk

phase in the dynamic flow field during reactor operation, may collapse during the hydrodynamically static experiment and thus reduce the available area for photosynthetic activity.

Knowing that the photogranules from our reactor are in principle able to provide sufficient quantities of oxygen for the degradation of a synthetic wastewater (unpublished data), we assume that a reduction in photosynthetic activity must have happened during our experiments. Otherwise, we would have noticed a gradual aeration of the bulk phase, eventually leading to supersaturation with respect to atmospheric oxygen as regularly observed in the lab scale reactors. Instead, at distant points from the photogranule, a decrease in oxygen concentrations was detected (e.g., P6 in **Figure S 1**). This indicates that oxygen consumption due to respiration in the photogranule was always higher than oxygen production due to photosynthesis at the applied light intensity. The decrease of oxygen concentration in the bulk influences the diffusion of oxygen towards the photogranule and lowers the flux. This is consistent with the decreased respiration rates of the heterotrophs in the second dark phase (-3.7 nmol m^{-1} s^{-1}) when compared with the first one (-4.3 nmol m^{-1} s^{-1}). From the microscale experiments using optodes, we can qualitatively describe the functioning of filamentous photogranules but further work is required to optimize the microscale experiments to deliver comparable results as obtained in laboratory-scale photobioreactors.

Despite the experimental limitations of the optode system for the activity measurement of filamentous photogranules, this kind of technology coupled to mathematical modeling is able to provide essential data on the activity of filaments, i.e., their activity per surface as done here (**Figure II.4** and **Figure II.5**). This information is useful for optimizing a bioprocess using photogranules. We were able to demonstrate that in the filaments the characteristic response time of changes in the oxygen dynamics after phases of darkness is on the order of seconds. This implies that the exposure to varying light on the trajectory of a photogranule in a photobioreactor may influence the activity of photogranules, even reversing oxygen gradients. The response of oxygen concentrations in filaments is also linked to the heterotrophic respiration. Filaments therefore do not only offer a surface for oxygen production, but at the same time can be a preferential location for nitrogen and carbon conversion. On the photogranules' trajectory in the flow field of a photobioreactor, changing exposure to light may induce a rapid shift of oxic and anoxic conditions in the depth of the photogranules, possibly resulting in shifts in nitrification and denitrification activities. The specific metabolic activities may be tested using targeted media composition, e.g., containing ammonium or nitrate. This is of particular interest for the application of photogranules in the context of wastewater treatment.

5. Conclusion

Our ultimate goal is mathematical description of a photogranular system containing all morphologic populations of photogranules. The simple reaction-diffusion model provided in this work reproduces major metabolic activities in filamentous photogranules and is a first step towards the description of heterogeneous photogranule morphologies. Obtaining a unified vision of the activity of this morphotype of photogranules, including all regions within the photogranules, remains to be developed. The use of optodes alone as done in this study is able to map metabolic activities in the filaments of photogranule but needs to be complemented, e.g., by classic microelectrode work, to characterize the denser regions even in filamentous photogranule.

6. Acknowledgements

We are grateful to Philippe Sousbie for assisting in reactor operation during this research, and to Cristian Picioreanu (TU Delft, The Netherlands) for his advice in modeling. We are also grateful having received the VisiSens system free of charge by PreSens, Regensburg, Germany.

7. Funding information

This work was financed through the French “Agence Nationale de la Recherche” grant ANR-16-CE04-0001-01 (“PSST: Photogranules shake sewage treatment up”), the INRAE division MICA and the University of Montpellier for a travel grant through the Gaïa doctorate school.

8. Declaration of interest

We wish to draw the attention of the Editor to a fact which may be considered as potential conflict of interest: PreSens – Precision Sensing GmbH in D-93053 Regensburg, Germany, graciously provided the VisiSens system free of charge for testing purposes. PreSens was neither involved in the design and conduct of the experiments and nor the analysis of the results. PreSens did not in any way influence the evaluation of the VisiSens system, nor was PreSens involved in the writing of the manuscript. We are therefore confident that our evaluation of the system is free of a conflict of interest.

Chapter III

Light as a microenvironmental control for carbon conversion using oxygenic photogranules[2]

In the previous chapter, I showed that the use of planar optode as experimental approach is limited to the characterization at the surface of the photogranule and does not cover the oxygen variation in deeper regions. Furthermore, I showed that the adequate modeling of light penetration was the most important factor for the model to reproduce the experimental measurements. Thus, in this chapter, I move forward in the examination of light and oxygen concentration gradients in the deeper regions of the photogranules. This study combines microelectrode measurements and 1D modeling.

[2] Article in preparation. This work has benefited from a collaboration with Jacob Lamb (PHC Auroa) and Cristian Picioreanu (PHC van Gogh).

Abstract

Oxygenic photogranules (OPGs) are spherical-like phototrophic granular biofilms, suggested as a promising bioprocess for aeration-free and energy neutral wastewater treatment. The performance of an OPG based bioprocess depends mainly on lighting at the photobioreactor scale and at the scale of individual photogranules. However, the direct measurement and characterization of the microenvironment state of the photogranules are required for better understanding and in prospective for industrial designs. To this end, effects of light intensities (0-170 $\mu mol_{PAR} \cdot m^{-2} \cdot s^{-1}$) and organic carbon (dissolved chemical oxygen demand - acetate) on oxygen production and consumption, were investigated inside OPGs. Experiments (light and oxygen microsensors) were used in combination with mathematical modeling. Our results showed that light intensity decreases exponentially when penetrating photogranules and was completely attenuated at a depth of 700 µm. Oxygen concentration profiles showed a high dependency to the availability of organic carbon, light and photogranule diameter. The uptake of oxygen in the upper layers of OPGs led to transport limitations of oxygen toward the inner core resulting in the formation of anoxic microenvironments. The consequence is the coexistence of oxic and anoxic zones in OPG, which is favorable for simultaneous nitrification and denitrification. Our experiments and simulations demonstrated that those microzones are favored under low oxygen concentration in the bulk and high dissolved organic matter. On the opposite, strong light intensities and small diameter promoted aerobic conditions in the whole OPG. Our results represent a first insight for understanding the complex dynamics of environmental variables and metabolic processes in OPG and underline that optimized lighting and feeding strategies are required in the development of an OPG-based bioprocess for wastewater treatment.

Key words: Phototrophic biofilm, microprofiling, wastewater treatment, photogranule, microenvironment investigation, 1D modeling, dissolved oxygen

1. Introduction

Recently oxygenic photogranules (OPGs) have shown a promising potential for aeration-free and energy neutral wastewater treatment system (Abouhend et al., 2018; Brockmann et al., 2021). Typical OPGs are thought of as dense and roughly spherical phototrophic biofilms, even though various morphologies can coexist in a single photobioreactor (Milferstedt et al., 2017a; Ouazaite et al., 2020). OPGs are characterized by a phototrophic outer layer, dominated by filamentous cyanobacteria (Milferstedt et al., 2017b). When exposed to light, the phototrophs produce oxygen, that is consumed by the heterotrophic organisms. The CO_2 released by the heterotrophs is simultaneously taken up by the phototrophs in a syntrophic relationship. The good settleability of OPGs overcomes the bottleneck of biomass harvesting reported for suspended cultures. Easy biomass recovery facilitates a biotechnological exploitation (Milferstedt et al., 2017a; Tiron et al., 2017). However, we currently know very little about the mechanistic functioning within OPGs. This knowledge will help in designing an optimized OPG-based bioprocess, for example for advanced wastewater treatment.

The combined effects of mass transfer, biological activities within the biofilm and the spatial arrangement of the OPGs cause the development of dissolved oxygen (DO) gradients as often found as well in other phototrophic and non-phototrophic biofilms (Li et al., 2016a; Ouazaite et al., 2020; Wolf et al., 2007). These gradients make it possible for microorganisms with different oxygen-sensitivities to co-exist in close spatial proximity, e.g., microorganisms performing nitrification and denitrification. However, the oxygen gradients within the photogranules are driven by microbial activities, and might vary depending on light, oxygen, and carbon availability in the surrounding environment.

Experimentally, microelectrodes can be used to quantify oxygen and light gradients in biofilms or microbial mats, and sediments (de Beer, 2011; Gieseke and de Beer, 2004; Segawa et al., 2020). Li et al. (2014) used microelectrodes to relate the structure of aerobic granular sludge to their oxygen gradients. Fang et al. (2014) investigated oxygen, pH, and redox gradients of cyanobacterial aggregates to manage cyanobacteria bloom. Microelectrode were also used by Li et al. (2016) to describe the oxygen dynamics in a biofilm photobioreactor. The micro-scale distribution of light in phototrophic biofilm ecosystems has been widely studied over the past few decades (Al-Najjar et al., 2012; Kühl et al., 1994; Lassen et al., 1992; Mobberley et al., 2017).

Light availability is central to oxygen generation and the syntrophic activities in phototrophic biofilms. However, these processes have not yet been quantified in OPGs.

It is impossible to deduce the contributions of the individual processes directly from microelectrode data, as for example for oxygen gradients, only a net response of the ecosystem is measured, confounding effects from simultaneously active processes. A good computational model is useful for assigning a contribution to each of identified processes as for example done by Wolf et al. (2007) in phototrophic biofilms. A mathematical model provides insight in the most important factors that affect the distribution of different functional groups in the OPGs and can predict behaviors for environmental conditions that were not tested experimentally.

In this manuscript, we fed experimental microelectrode data for oxygen and light measurements into a mathematical model for OPGs to (i) characterize light penetration, and (ii) oxygen production under different environmental conditions. We then (iii) identified parameters (i.e., light intensity, diameter, bulk concentration of oxygen and dissolved organic matter) controlling the development of oxic/anoxic zones within the OPGs. We used scalar irradiance fiber optic microprobes to investigate the penetration of light. Then, we used oxygen microelectrode to investigate the short-term effects of changes in light intensity on oxygenic photosynthesis and oxygen consumption under different organic carbon environments. We built a simple 1D reaction-diffusion model to quantify photosynthetic and heterotrophic activities and the contribution of the diffusion. Finally, we showed how the model could be used to predict light intensities and OPG characteristics that could favor anoxic zones inside OPGs depending on DO and dissolved organic carbon thus paving the way for online control in photobioreactors.

2. Materials and Methods

Our objective was to study dissolved oxygen and light profiles in the microenvironment of photogranules and to evaluate how they are impacted by light intensity and by the availability of organic carbon. Oxygen and light gradients were measured using microelectrodes and a one-dimensional model considering spatial distribution of microbial activities and reaction-diffusion of dissolved oxygen and organic carbon was developed.

2.1. Experiments

2.1.1. Reactors operation and photogranules sampling

The OPGs used in this work were sampled from two independently operated photobioreactors. One was stably operated as Continually Stirred Tank Photobioreactor (CSTR) fed with dissolved methane in tap water as sole source of organic carbon. Details can be found in Safitri et al. (submitted). The second reactor was stably operated as Sequencing Batch Reactor (SBR) fed with synthetic wastewater prepared with deionized water with the following composition: sodium acetate 138 $mg \cdot L^{-1}$, KH_2PO_4 11.7 $mg \cdot L^{-1}$, $MgHPO_4 \cdot 3\ H_2O$ 14.5 $mg \cdot L^{-1}$, NH_4Cl 34.2 $mg \cdot L^{-1}$, $FeSO_4 \cdot 7\ H_2O$ 2.9 $mg \cdot L^{-1}$. This composition gave a chemical oxygen demand (COD) in the influent to the reactor of 100 $mg \cdot L^{-1}$. A total of five granules were randomly taken one at a time at the end of five different SBR cycles. The photogranules had different diameters of 3.2, 3.4 ,3.7, 4.5, and 5 mm, respectively. Also, five granules were sampled one at a time from the CSTR with diameters of 2, 3, 3.5,4 and 4.5 mm.

Table III.1 *Reactor operation conditions used for sampling OPGs.*

	Sampling 1	Sampling 2
Operation mode	SBR	CSTR
Illumination ($\mu moles_{PAR} \cdot m^{-2} \cdot s^{-1}$)	100	45
HRT (h)	12	12
Length of cycle (h)	6	NA
COD ($mg \cdot L^{-1}$)	100	70
Main organic carbon sources	Acetate	Methane
Mixing (rpm)	100	125
Reactor volume (L)	4	1.8
References	Present study	Safitri et al. (submitted)

2.1.2. O_2 microsensor measurements

Steady-state dissolved oxygen gradients were measured using a Clark-type oxygen microelectrode (Unisense, Denmark) with a tip diameter of 50 μm, a 90% response time of <0.5 sec and a stirring sensitivity of 1%. Linear calibration was done in air-saturated medium and a nitrogen-sparged anoxic solution. The output current from the microelectrode was recorded by a Microsensor

Amperemeter (Unisense) coupled to a computer. Microelectrodes were inserted into the photogranule using a motor-driven micromanipulator (Unisense), at vertical intervals of 50 or 100 µm. The OPGs were fixed in a lasso made of nylon thread, connected to a pipette tip, and placed in the middle of a transparent 500 mL box as approached by Hille et al. (2005) (**Figure III.1**). The OPGs were illuminated from the sides using a white cold LED light source with a collimating lens (Schott KL2500LED; Schott AG, Germany). Oxygen gradients inside OPGs were measured in air saturated tap water with varying concentrations of dissolved organic matter (sodium acetate) expressed as dissolved chemical oxygen demand of 0, 30, 500 $mg_{COD} \cdot L^{-1}$, depending on the OPG. These values were chosen to mimic typical acetate concentrations found in the context of wastewater treatment (30 $mg_{COD} \cdot L^{-1}$ for CSTR operation, 500 and 0 $mg_{COD} \cdot L^{-1}$ representing the concentrations found at the beginning and at the end of an SBR cycle respectively). All measurements were performed at steady-state after incubation for 30 min.

Oxygen gradient were measured between the top and the bottom of OPGs. This gradient was split into two at the minimum concentration in the center of the OPG. The resulting two data series were considered as intra-granules replicates to consider biological variability in the morphology of OPGs.

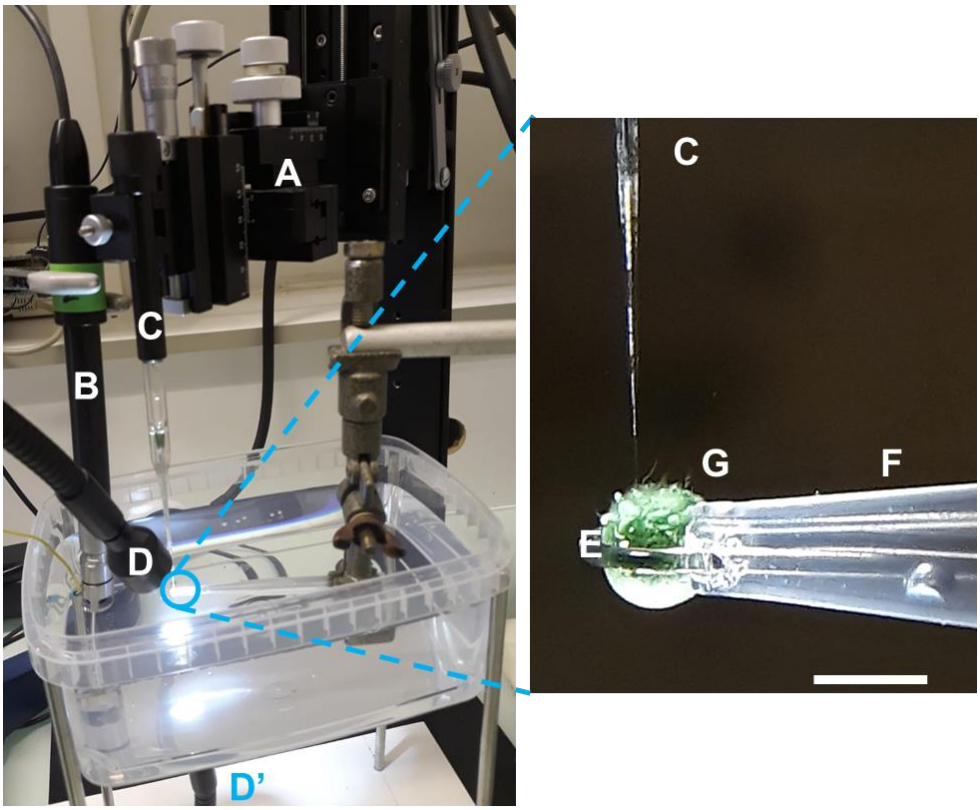

Figure III.1 *Image display of the experimental set-up to measure the oxygen gradients in OPGs. (A) micromanipulator motor (B) oxygen bulk sensor; (C) oxygen microelectrode with a tip diameter of 50 µm, (D & D') goose neck providing light at a controlled intensity, (E) nylon thread used to fix OPGs (F) Pipit tip to support the (G) OPG. Scale bar 3 mm.*

2.1.3. Scalar irradiance microsensor measurements

The scalar spectral irradiance was measured using a fiber optic light microprobe (37° aperture and 200 µm outer diameter) installed on the motor-driven micromanipulator device). The microprobe was inserted into the OPG at vertical intervals of 100 µm from the upper to the lower side of a photogranule placed in a water bath exposed to light (**Figure S01).** The probe was connected to a micro-spectrometer (USB2000 + Vis-NIR; Ocean Optics, FL, USA) using the acquisition software Spectra Suite (Ocean Optics, FL, USA). The measurements were carried out on OPGs from CSTR operating with sizes 2, 3, 3.5, and 4 mm and incident light intensities of 48, 104, and 155 $\mu moles_{PAR} \cdot m^{-2} \cdot s^{-1}$. Incident light was provided by a white cold LED lamp with a collimating lens (Schott KL2500LED; Schott AG, Germany). The sensor was calibrated with a PAR meter (LICOR Light Meter LI-250A, USA).

2.2. Modeling

2.2.1. Model geometry, dimensions

The model assumes 1D computational domain representing the depth (*z* direction) of the OPG. Each hemisphere of the OPG was considered as separate computational domain. The oxygen concentration at the top boundary condition ($C_{b,O2}$) was set to the measured bulk oxygen concentration. The bottom boundary condition was set to a symmetry condition (Flux null).

2.2.2. Components and state variables

The model integrates the postulated syntrophic relation proposed by Stuart et al. (2016a) for cyanobacterial biofilms and for OPGs (Milferstedt et al., 2017b). Therefore, the model considers two types of essential functional guilds: phototrophs and heterotrophs. The model considers acetate as soluble organic carbon (C_s), extracellular organic matter (C_{EPS}) and oxygen (C_{O2}). The consideration of the local biomass concentration was considered via the introduction of two biomass functions $f_p(z)$, $f_h(z)$ for phototrophs and heterotrophs respectively. These two functions were bounded from 0 to 1 and their shape were inspired from gray level on phycocyanin autofluorescence on cross section photogranule. Then, they were optimized to obtain best predictions of oxygen gradients. The optimized parameters for the two functions were the size of the two transition zones at the surface and towards the inner core, and the plateau level at the granule center.

2.2.3. Biological process and governing equations

The model only includes biological processes for the production and consumption of oxygen (**Table III.2**).

Oxygen production via photosynthesis: When light is present, the phototrophs produce oxygen and Extracellular Polymeric Substances (C_{EPS}) via photosynthesis and consume inorganic carbon. The photosynthesis rate is modeled as proportional to a hyperbolic tangent function to the light intensity I ($\mu moles_{PAR} \cdot m^{-2} \cdot s^{-1}$) as proposed in Jassby and Platt (1976). CO_2 was assumed to be not rate-limiting. The photosynthesis rate was assumed to be proportional to the local biomass activity $q_p \cdot f_p(z)$ where q_p is the maximum rate for photosynthesis and $f_p(z)$ the biomass function introduced above.

Respiration of phototrophs in absence of light: It is known that cyanobacteria in phototrophic biofilms produce an extensive organic extracellular matrix (Bharti et al., 2017), providing the community with a rich source of nutrients. It was also reported that they can reuse EPS instead of the CO_2 as carbon source in the absence of light (Stuart et al., 2016b). Therefore, the modeled phototrophic biomass consumes the available oxygen (C_{O2}) and organic matter (C_{EPS}) only in absence of light. This dark respiration was modeled using a specific maximum oxygen rate (q_{end}) and Monod-type kinetics. The phototrophs spatial distribution was considered using the $f_p(z)$ distribution and an inhibition term was introduced using a threshold intensity (K_i). We consider no organic carbon limitation from EPS since we have worked here with large OPGs and prior experiments (data not shown) have shown that EPS can sustain activity over several hours, much longer than the duration of the experiments presented in this study.

Oxygen consumption by heterotrophs: in the model the heterotrophs were supposed to oxidize acetate (Cs) when available and EPS (C_{EPS}) otherwise. EPS consumption rate was expressed using a specific maximum rate (q_{EPS}) and Monod kinetics for oxygen (C_{O2}). The heterotrophs spatial distribution was considered using the function $f_h(z)$. We did not consider any limitation of EPS. Acetate consumption was modeled similarly to EPS consumption (q_{EPS}), using a specific maximum oxygen rate (q_{Ac}) and Monod kinetics for acetate (Cs).

Table III.2 *Nomenclature and process rates used for modelling of biological activity of phototrophs and heterotrophs.*

Trophic group of microorganisms	Process	Process rates in the model
Phototrophs (X_{ph})	Photosynthesis	$r_p = q_p \cdot \tanh\left(\frac{I}{I_k}\right) \cdot f_p(z)$
	Dark respiration using EPS	$r_{end} = q_{end} \cdot \frac{C_{O_2}}{C_{O_2} + K_p} \cdot \frac{K_i}{K_i + I} \cdot f_p(z)$
Heterotrophs (X_{het})	Respiration using EPS	$r_{EPS} = q_{EPS} \cdot \frac{C_{O_2}}{C_{O_2} + K_h} \cdot f_h(z)$
	Respiration using Acetate	$r_{Ac} = q_{Ac} \cdot \frac{C_{O_2}}{C_{O_2} + K_h} \cdot \frac{C_s}{C_s + K_{S,h}} \cdot f_h(z)$

Oxygen diffuses in/out of the OPG and it is consumed/produced by bacteria. Mathematically, this results in a system of partial differential equations. Thus, the steady-state diffusion-reaction equations (***Equation III.1)*** and **(Equation III.2)** for the dissolved oxygen and the organic carbon are:

$$-\mathrm{D_{O_2}}\cdot\nabla^2\mathrm{C_{O_2}} = \mathrm{r_{O_2}} \qquad \textit{(Equation III.1)}$$

$$-D_S\cdot\nabla^2 C_s = r_S \qquad \textit{(Equation III.2)}$$

Where:

$$\mathrm{r_{O_2}} = \mathrm{r_p} - \mathrm{r_{end}} - \mathrm{r_{EPS}} - \mathrm{r_{Ac}} \qquad \textit{(Equation III.3)}$$

$$\mathrm{r_S} = -\mathrm{Y_{\frac{O_2}{S}}}\cdot\mathrm{r_{Ac}} \qquad \textit{(Equation III.4)}$$

The diffusion coefficients D_{O2} and D_S of oxygen and acetate were assumed constant in the photogranules and taking the value $2.1e^{-9}$ $m^2\cdot s^{-1}$ and 1.2 e^{-9} $m^2\cdot s^{-1}$ at 20 °C in water. This assumption was upheld by the fact that the oxygen and acetate are small molecules and the porosity of biofilm are mainly reported to be large (Bryers and Drummond, 1998; Horn and Morgenroth, 2006).

Light extinction: Light intensity decreases exponentially in photogranules. This was modeled using Beer-Lambert law. The light source was placed on top and the bottom of the granule, so that light gets extinct along the direction z according to:

$$\mathrm{I} = \mathrm{I_s}\cdot\mathrm{e}^{-\mathrm{Ke}\cdot(\mathrm{R}-\mathrm{z})} \qquad \textit{(Equation III.5)}$$

With K_e the light extinction coefficient (m^{-1}). The latter was considered independent of biomass density in line with the presented experimental results. As boundary condition, on the interface between the boundary layer and the photogranule surface, the light intensity was fixed to the value I_S that was applied experimentally ranging from 0 to 170 $\mu moles_{PAR}\cdot m^{-2}\cdot s^{-1}$, depending on experiments. The attenuation coefficient was estimated based on the light gradient measured in OPGs of various sizes, thus already dependent on the biomass distribution function (***Figure III.2*** **B**).

2.2.4. Model solution and parameter estimation

The model was implemented in COMSOL Multiphysics 5.4 (COMSOL Inc., Burlington, MA, USA). The computational domains were discretized with a uniform mesh of 100 nodes, based on the precision of experimental data collected (≈50 measurement over 3 mm). The parameters optimization was done using the genetic algorithm of MATLAB R2018b (version R2018b, MathWorks, USA) using the following objective function for Sum of Squared Errors (SSE) between measured and simulated values (**Equation III.6)**):

$$SSE = \sum_{i=1}^{N_p} \sum_{j=1}^{N_d} (C_{O2}(i, z_j) - C_{O2,exp}(i, z_j))^2 \qquad \textbf{\textit{(Equation III.6)}}$$

Here, $C_{O2,exp}$ is the experimental concentration of oxygen and $C_{O2,mod}$ the predicted oxygen concentration from the model. *"i"* corresponds to the measured oxygen profile. *"z_j"* corresponds to the coordinate of the depth where the oxygen concentration was measured. Parameter estimation for the kinetics parameters (q_p, q_{end}, q_{EPS}, q_{Ac}, I_k) and the two biomass distribution functions (f_p and f_h) was done by evaluating the fit of the simulation results with the experimental data by changing their values and the biomass distributions for both hemispheres of each OPGs separately. When we attempted to use identical kinetic parameters and biomass distributions for OPGs from both type of reactors (CSTR and SBR), the model failed to reproduce oxygen gradients within the OPGs. Thus, the experimental data were separated by reactor type (i.e., CSTR, SBR) and individual sets of parameters and biomass distributions were determined. Afterward, the models were simulated using a unique biomass functions specific to photogranule from CSTR and a second one specific to the photogranules from SBR. **Table S01** lists the parameter values for default and estimated model simulation.

3. Results

3.1. Light penetration in OPGs

Light penetration was measured with a fiber optic probe directly inserted in OPGs for light intensities ranging from 0 to 170 $\mu moles_{PAR} \cdot m^{-2} \cdot s^{-1}$. ***Figure III.2*** **A** illustrates steep gradients observed for three light intensities, i.e., 50, 105, 155 $\mu moles_{PAR} \cdot m^{-2} \cdot s^{-1}$. Intensity and spectrum of light entering the tip of the fiber optic probe was recorded along the depth of the OPGs (***Figure III.2*** **A** and **Figure S01**). An exponential attenuation fitted the gradients ($R^2 > 0.97$) with an observed attenuation coefficient Ke_{obs} ranging from 6.18 to 6.58 mm^{-1} and an average ± standard deviation of 6.39±0.16 mm^{-1}. Ke_{obs} was independent of the diameter of the OPGs in the tested diameter range of 2 to 4 mm (ANOVA test, p-value 0.99). This indicates that the surface layer of OPGs have similar light permeability regardless of size. Using the model, we determined that at a depth z_0 of 700 µm, the light intensity is almost completely attenuated ($I < 1\% I_S$). For all the OPGs used in this study, with diameters ranging from 2 to 4 mm, it is safe to assume that their cores do not receive light. Using the model parameters to fit the measured oxygen gradients (***Figure III.3***), the model predicts the presence of phototrophs mostly in the top 500 µm (***Figure III.2*** **B**). This is consistent with our visual observations. The model also predicted a co-localization of phototrophic and heterotrophic activities. Photosynthesis and respiration rates predicted for the OPG from the CSTR intended to polish effluents from dissolved methane were three times lower than rates predicted for the OPGs from the SBR intended for synthetic wastewater treatment.

3.1.Light as a driver for oxygen gradients inside OPGs

Dissolved oxygen profiles were measured for the photogranule from CSTR at two different acetate concentrations (0 and 500 $mg_{COD}L^{-1}$) and with different light intensities ranging from 0 to 170 $\mu moles_{PAR} \cdot m^{-2} \cdot s^{-1}$ (dots in ***Figure III.3***). ***Figure III.3*** **A** shows oxygen profiles when no acetate was added. In the absence of light, there was no oxygen production and oxygen concentrations decrease from air saturation oxygen concentrations values (8.9 $mg \cdot L^{-1}$) to around 2 $mg \cdot L^{-1}$ over the first 500 µm in the photogranule. It then decreases slowly with increasing depth reaching 0 $mg \cdot L^{-1}$ at the center of the OPG. When the OPG was illuminated with intensities ranging from 20 to 170 $\mu moles_{PAR} \cdot m^{-2} \cdot s^{-1}$, photosynthetic activity was shown by increasing oxygen concentrations along the profile.

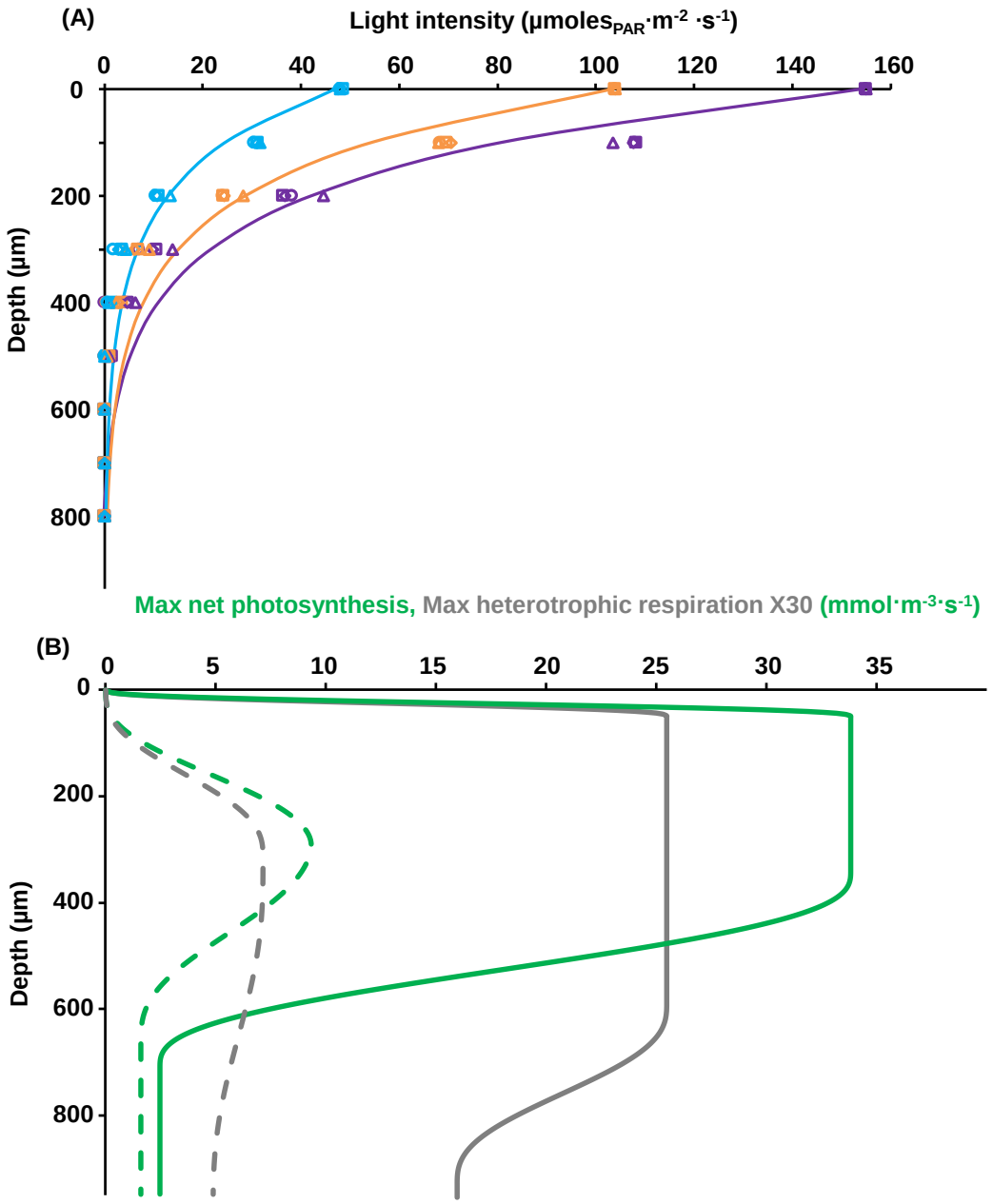

Figure III.2 *Light attenuation and distribution of biomass in OPGs. (A) Measured light attenuation: Three incident light intensities are presented in blue (48 µmoles$_{PAR}$·m^{-2}·s^{-1}), orange (104 µmoles$_{PAR}$·m^{-2}·s^{-1}) and purple (155 µmoles$_{PAR}$·m^{-2}·s^{-1} respectively, for different photogranule diameters with circles (2 mm), rectangles (3 mm), diamonds (3.5 mm) and triangles (4 mm). Solid lines indicate the Beer-Lambert fit using the average observed attenuation coefficient Ke$_{obs}$. (B) Modelled spatial distribution of metabolic activity in OPGs. Green: maximum net photosynthesis. Grey: 30-fold magnification of maximum heterotrophic respiration. Data for OPG from the SBR are represented as solid line and for the OPG from the CSTR as dashed line.*

With light intensities above 50 $\mu moles_{PAR} \cdot m^{-2} \cdot s^{-1}$, the OPG became supersaturated and the photogranules became net oxygen producers. Oxygen concentrations peaked locally at 20 $mg \cdot L^{-1}$ ($\approx$ 2.2 times air-saturation) at 750 µm deep inside the photogranule with the maximal light intensity tested of 170 PAR. When the surrounding medium was amended with 500 $mg \cdot L^{-1}$ acetate (dots in **Figure III.3 B**) and in the absence of light, we observed that oxygen decreased from air saturation oxygen concentration (8.9 $mg \cdot L^{-1}$) to 0 $mg \cdot L^{-1}$ over the first 500 µm in the photogranule. When the photogranule was illuminated, oxygen concentrations increased. With intensities above 110 $\mu moles_{PAR} \cdot m^{-2} \cdot s^{-1}$, the OPG became supersaturated with oxygen concentration reaching 19.75 $mg \cdot L^{-1}$ for a light intensity of 170 $\mu moles_{PAR} \cdot m^{-2} \cdot s^{-1}$. In comparison with profiles measured without acetate addition (**Figure III.3 A**) oxygen concentrations measured for the various light intensities are lower and in the absence of light, the OPG harbors a large anoxic zone.

Oxygen profiles were also measured for OPGs with different diameters (3.2, 3.4, 3.7, 4.5 and 5 mm) from SBR, with a fixed concentration of acetate of 30 $mg \cdot L^{-1}$ and under different light intensities ranging from 0 to 80 $\mu moles_{PAR} \cdot m^{-2} \cdot s^{-1}$. Representative results are shown for diameters 3.2, 3.7, 4.5 and 5 (dots in **Figure III.4 A**, for granule 3.4 mm in **the supplementary material**). Overall oxygen profiles were similar to those obtained for the CSTR OPG (**Figure III.3).** For small OPGs with diameters of 3.2 and 3.4 mm, oxygen concentrations never reached to zero even at the center of the photogranule due to oxygen diffusion from the bulk (**Figure III.4 A** & **B**). Conversely, for large OPGs with diameters over 4.5 mm, the oxygen decreases from air saturation concentration (8.9 $mg \cdot L^{-1}$) to 0 $mg \cdot L^{-1}$ over the first 500 µm in depth when the OPGs were not illuminated or under a low light intensity of 10 $\mu moles_{PAR} \cdot m^{-2} \cdot s^{-1}$ (**Figure III.4 C** & **D**). In all cases, with intensities above 60 $\mu moles_{PAR} \cdot m^{-2} \cdot s^{-1}$ the OPGs became supersaturated with oxygen reaching up to 17.5 $mg \cdot L^{-1}$ ($\approx$ 2 times air-saturation) for a light intensity of 80 $\mu moles_{PAR} \cdot m^{-2} \cdot s^{-1}$.

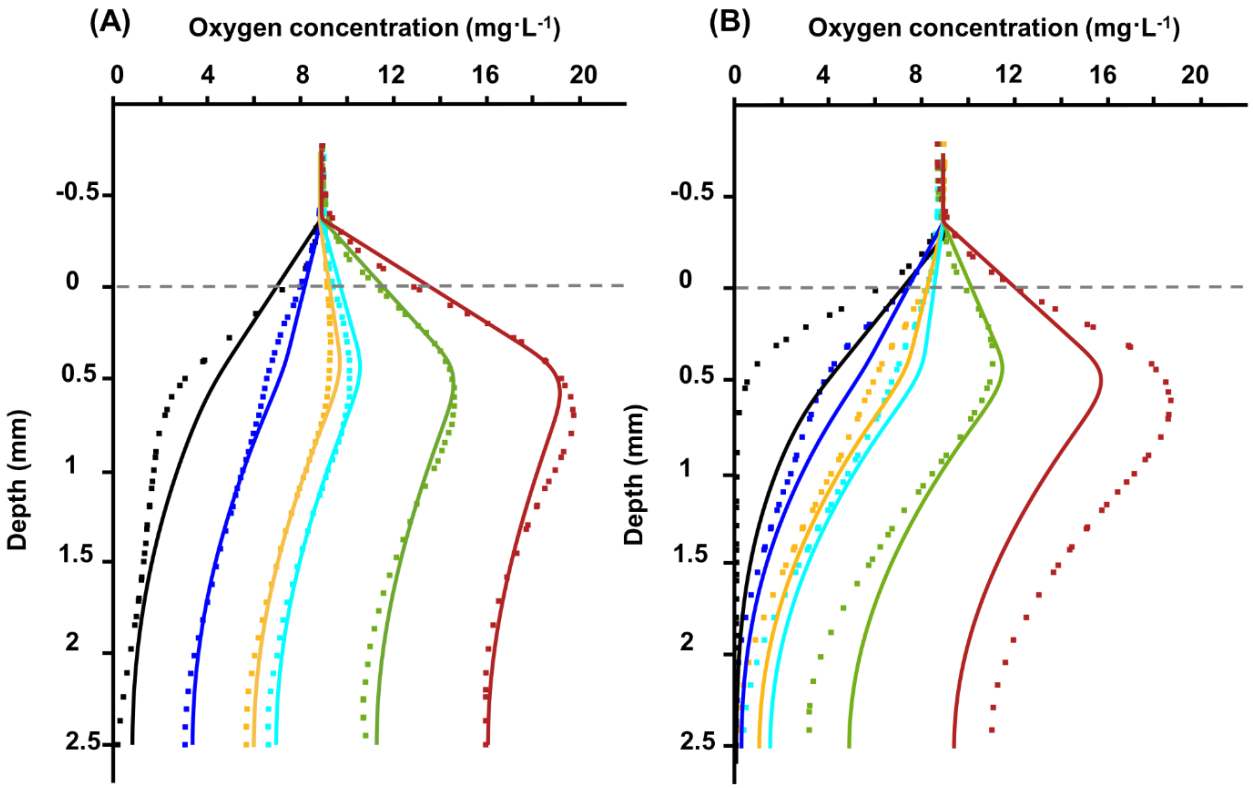

Figure III.3 *Concentration of dissolved oxygen profiles in an OPG of 4.5 mm diameter, exposed to different light intensities (black: 0, blue: 20, gold: 50, cyan: 60, green: 110, marron: 170 $\mu moles_{PAR} \cdot m^{-2} \cdot s^{-1}$), and within two carbon environment condition. (A) OPG exposed to a starve carbon environment (only tap water). (B) OPG exposed to a rich carbon environment (500 $mg \cdot L^{-1}$ of Acetate). Dots indicates the experimental measurement and solid lines indicates the model results. Grey dashed line represents the OPG surface.*

The oxygen oversaturation from the OPG from CSTR in depleted acetate environment under 60 $\mu moles_{PAR} \cdot m^{-2} \cdot s^{-1}$ (cyan dots in **Figure III.3 B**) was much lower than for the OPGs from SBR of the same diameter under same illumination 60 $\mu moles_{PAR} \cdot m^{-2} \cdot s^{-1}$ and 30 $mg_{COD} \cdot L^{-1}$ of acetate (cyan dots in **Figure III.4 C**). The latter presents high oxygen concentration and a peak value of oxygen at 16 $mg \cdot L^{-1}$, whereas the former one had a peak value of oxygen at 10 $mg \cdot L^{-1}$.

For all OPGs, a change of incident light intensity induced a measurable change of oxygen level in the OPG to reach pseudo steady state equilibrium in about 14 to 25 min depending on the OPG size and light intensity (data not shown). Furthermore, the direct, spatially resolved measurements of steady-state oxygen profiles revealed slight differences between the top and bottom hemisphere

of the OPGs (**Figures supplementary material),** indicating non-homogeneous distributions of biomass or microbial activities.

A 1D model was developed to account for photosynthesis, heterotrophic respiration, and diffusion, in order to describe oxygen profiles inside an OPG. The biomass distributions (**Figure III.2 B**) were adjusted in order to fit experimental oxygen distribution data (**Figures III.3** and **III.4**). Oxygen profiles predicted by the model are shown in plain lines on **Figures III.3** and **III.4**. The model was able to capture well the overall variations in oxygen gradients associated with a wide range of light intensities, acetate and OPG diameters. For the CSTR OPG in presence of dissolved organic matters (dCOD), the model diverged from experimental points for extreme light intensities of 0 and 170 $\mu moles_{PAR} \cdot m^{-2} \cdot s^{-1}$. For SBR OPGs, oxygen peaks within the first 500 µm of the OPGs at high light (I > 60 $\mu moles_{PAR} \cdot m^{-2} \cdot s^{-1}$) were not well captured, but oxygen values observed for deeper regions were well predicted. One exception is the oxygen profile associated with Is= 60 $\mu moles_{PAR} \cdot m^{-2} \cdot s^{-1}$ for the largest OPG with 5 mm diameter which was overestimated by the model. **Table S02** lists the sum of squared errors of the model outputs for each experiment.

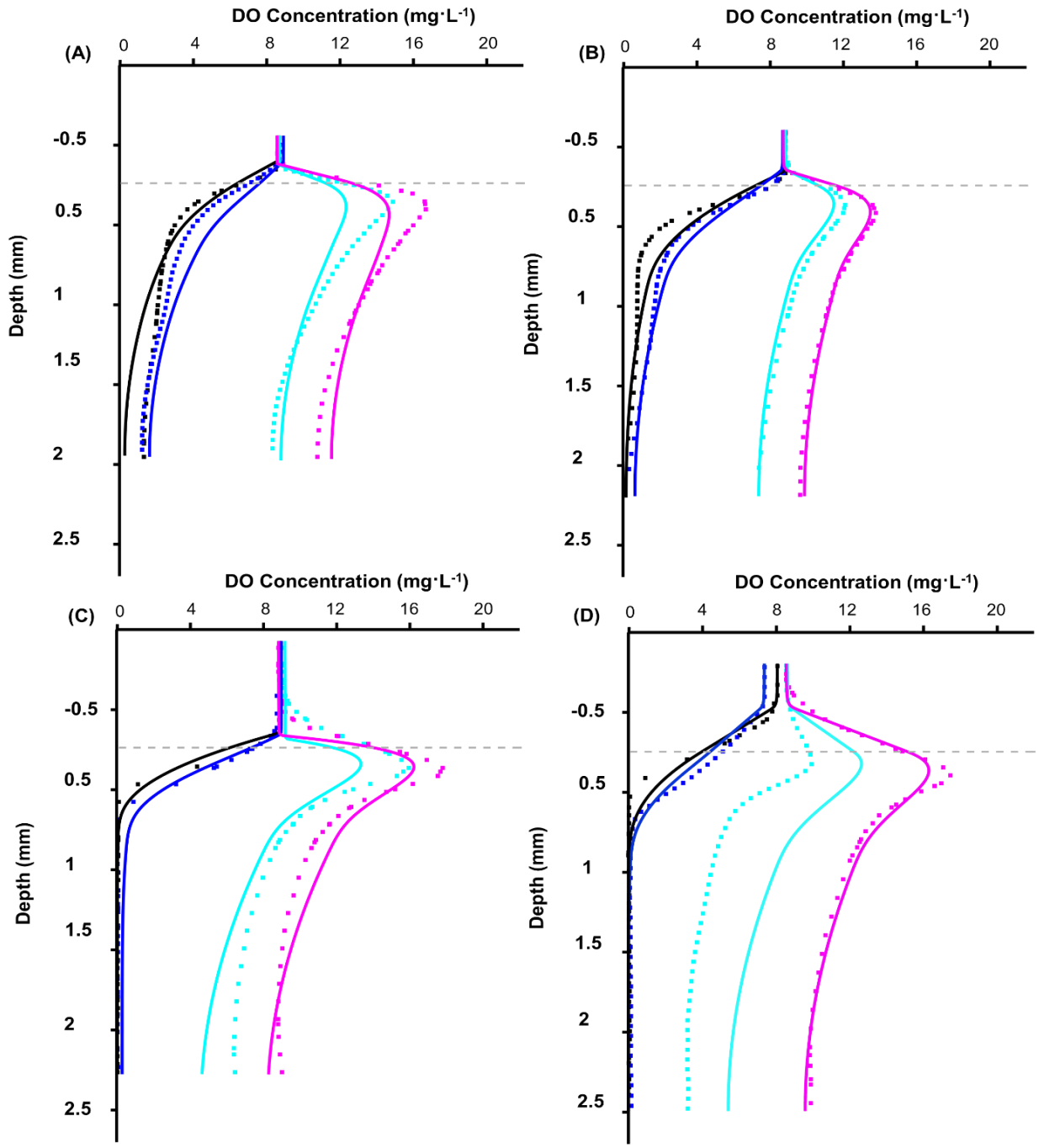

Figure III.4 *Concentration of dissolved oxygen profiles in OPGs with different diameters exposed to different light intensities (black: 0, blue: 10, cyan: 60, magenta: 80 µmoles$_{PAR}$·m^{-2}·s^{-1}), and environment amended with 30 mg$_{COD}$·L-1 acetate of acetate. (A) OPG with diameter of 3.2 mm (B) OPG with diameter of 3.7 mm. (C) OPG with diameter of 4.5 mm (D) OPG with diameter of 5 mm. Points indicates the experimental measurement and solid lines indicates the model results. Grey dashed line represents the interface photogranule-bulk.*

3.2. Anoxic microenvironments in the OPGs

Using measured and modeled oxygen profiles, our goal was to study how anoxic zones favoring potential simultaneous nitrification and denitrification (SND) change in OPGs with illumination, dCOD and OPG size. The anoxic biovolume of OPGs of different diameters (3.2 to 5 mm) but same illumination and dCOD were extracted from oxygen microprofiling (**Figures III.3** and **III.4**), considering an ideal spherical shape of OPGs. An oxygen concentration below 0.5 $mg \cdot L^{-1}$ was set as threshold for anoxia. Dots in **Figure III.5** shows the percentage of anoxic biovolume in OPGs as a function of light intensity. As expected, the anoxic biovolume decreased when the light intensity increased. An increase in dCOD correlated with an increase in the anoxic biovolume of the CSTR OPG (**Figure III.5 A**). An increase in diameter of SBR OPGs correlated with an increase in the anoxic biovolume (**Figure III.5 B**).

Modeled anoxic biovolumes were then calculated using modeled oxygen concentration profiles (**Figures III.3** and **III.4**) with the same approach. Modeled anoxic biovolumes for the different test conditions fitted well with the experimental measurements, except for the anoxic biovolume in CSTR OPG with high concentration of acetate under dark conditions. The model also allowed interpolating anoxic biovolume values for a wide range of light intensities, even though no experimental data is available. For the CSTR OPG, no anoxic zone was predicted even at low light intensities when the medium is poor in acetate (orange plain line in **Figure III.5 A**). With high acetate (500 $mg \cdot L^{-1}$) the model predicted a decrease in the anoxic zone for light intensities between 0 and 35 $\mu moles_{PAR} \cdot m^{-2} \cdot s^{-1}$, with a maximum of 11% of total biovolume under dark (blue plain line in **Figure III.5 A**). As mentioned above, the anoxic biovolume predicted for this OPG with high acetate was not accurate in dark conditions (70% of anoxic biovolume measured), however biovolumes predicted for light intensities above 20 $\mu moles_{PAR} \cdot m^{-2} \cdot s^{-1}$ are accurate as shown by oxygen concentration profiles (**Figure III.3**). Regarding the OPGs from SBR, the predicted anoxic biovolume decreases as a function of light for all diameters (plain lines in **Figure III.5 B**). Maximal anoxic biovolumes are found in dark condition ranging from 4 to 63% of total biovolume. The anoxic zones disappear completely at a light intensity between (10-50) $\mu moles_{PAR} \cdot m^{-2} \cdot s^{-1}$. Consistently with measured anoxic biovolumes, the predicted anoxic biovolumes are larger for larger OPGs.

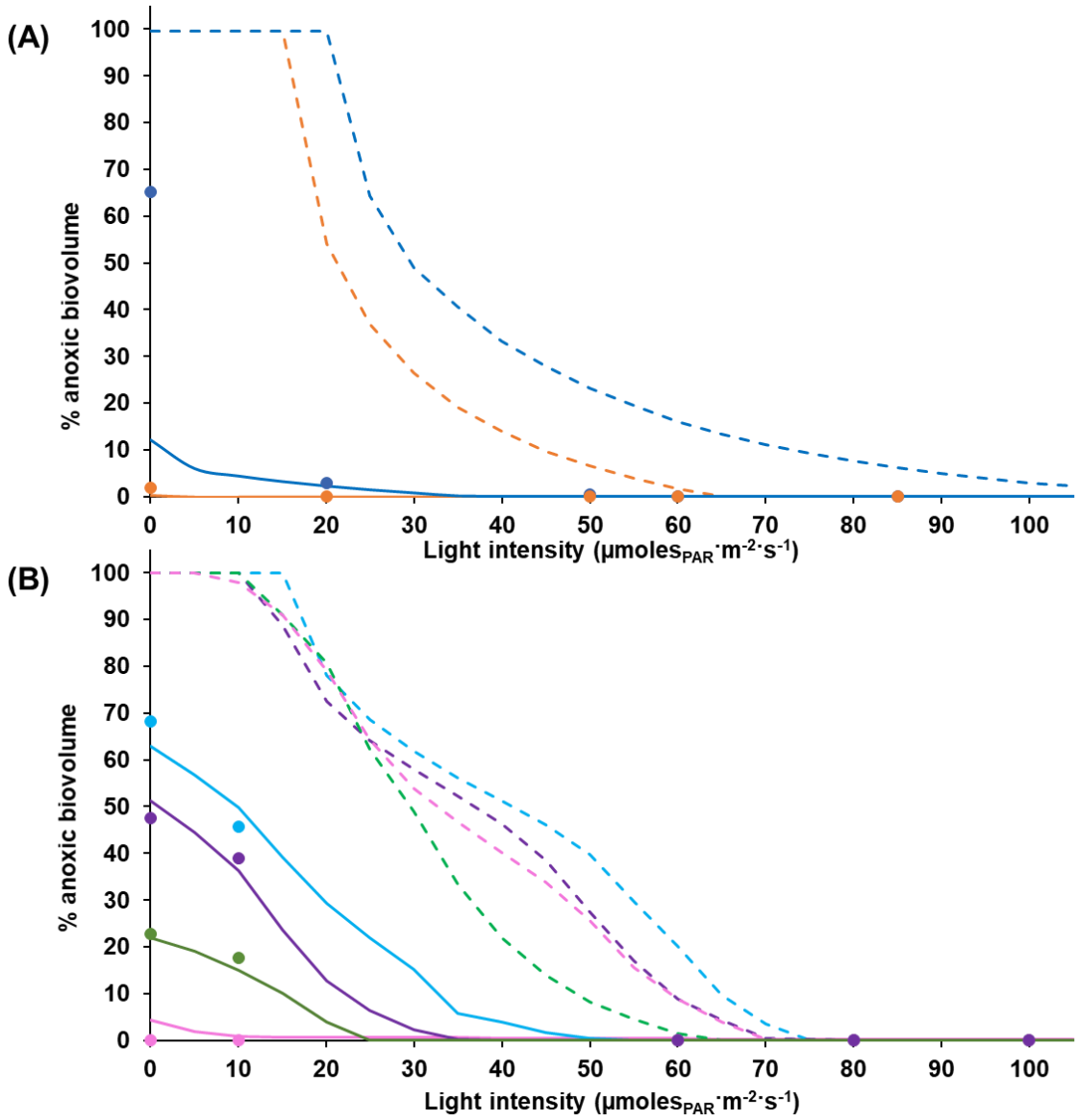

Figure III.5 *Percentage of anoxic biovolume of the OPG at different tested conditions of light intensities and carbon availability in the environment saturated with air. (A) Anoxic biovolume in CSTR OPG with a diameter of 4.5 mm, dots indicate experimental measures and the solid lines indicate the model prediction under different acetate conditions: orange acetate=0 $mg_{COD}·L^{-1}$, blue acetate=500 $mg_{COD}·L^{-1}$. Dashed lines indicate the model prediction of the anoxic biovolume when the DO_{bulk} =0.05 $mg·L^{-1}$. (B) Anoxic biovolume in SBR OPGs, dots indicate experimental measurements and the solid lines indicate the model prediction under acetate =30 $mg_{COD}·L^{-1}$ for different OPG diameter: pink :3.2-3.4 mm, green 3.7 mm, violet 4.5 mm, and cyan 5 mm. Dashed lines indicate the model prediction of anoxic biovolumes when DO_{bulk} =0.05 $mg·L^{-1}$.*

In the context of wastewater treatment, DO in the bulk is normally kept at very low concentrations. Here due to the experimental design, measurements were performed under air saturation condition. Model predictions for low oxygen concentration in the bulk (DO_{bulk} =0.05 $mg \cdot L^{-1}$) are shown as dotted lines in **Figure III.5**. For all the tested photogranules and all acetate values, the predicted anoxic zones increased in this low oxygen concentration condition. In all cases, the anoxic biovolume was 100% of the total biovolume in the dark, and it decreased with increasing light reaching 0% for light intensities ranging from 60 to 135 $\mu moles_{PAR} \cdot m^{-2} \cdot s^{-1}$. Again, the anoxic biovolume increases with acetate concentration. However, the photogranules size appeared to have only a low impact on anoxic zones in that case (dashed lines in **Figure III.5 B**).

4. Discussion

4.1. Light penetration in OPGs

Light availability is the main abiotic driver involved in the development of phototrophic biofilms (Zippel and Neu, 2005). Knowing the light penetration and its approximation inside phototrophic biofilms allows a better understanding and can simplify modeling by forgoing complex approaches that take into account the fate of each light photon such as Monte Carlo simulations (Zhu and Liu, 2013). The optical properties differ from one phototrophic biofilm to another due to differences in microbial diversity and to the presence of abiotic particles. Here, light attenuation in the OPGs is exponential thus following a Lambert-Beer type law (**Figure III.2 A).** The global scalar irradiance attenuation coefficient found in this study (K_{eobs} = 6.4 mm^{-1}) falls within the range of those found for epilithic cyanobacterial biofilm (~ 5 mm^{-1}) (Kuhl et al., 1996) or phototrophic microbial mats (4.6, 6.6, 13.4 mm^{-1}) (Al-Najjar et al., 2012). This indicates that in terms of light attenuation, OPGs have similar properties as other phototrophic biofilms. The thickness of the euphotic zone was around 700 µm in OPGs (**Figure III.2 A**), whatever the OPG size analyzed within a range of diameter of 2 to 4 mm. This is in line with the thickness of cyanobacterial layers reported by Abouhend et al. (2020) who analyzed cross-sections of OPGs with different diameters.

4.2. Spatial distribution of microbial activities in photogranules

Here, we used a 1D reaction–diffusion model to reproduce experimental oxygen gradients (**Figures III.3** and **III.4**) based on spatial distributions of phototrophic and heterotrophic activities in the OPGs (**Figure III.2 B**). Considering these heterogeneous distributions of activities appeared mandatory. Indeed, a preliminary modeling work taking into account light attenuation and oxygen

and carbon availabilities but using uniform spatial distributions for phototrophic and heterotrophic activities was not able to reproduce the trends observed in the oxygen gradients. Therefore, besides the light penetration, the model demonstrates the importance of biomass activity profiles on the establishment of oxygen gradients within the OPGs. The activity profiles predicted for phototrophs are in agreement with microscopic observation realised by Abouhend et al. (2020). Indeed, as mentioned above, they observed that cyanobacterial fluorescence was mainly found in the surface layers of OPGs.

Furthermore, the modelling results showed the need of different biological activities related to the origin of the OPGs (**Figure III.2 B** & **Supplementary material Table S02**). The OPGs from SBR intended for treating synthetic wastewater presented high photosynthetic and heterotrophic activities compared with the OPG from the CSTR intended for effluent polishing. This difference in activities may be related either to the type and amount of substrate used (mainly acetate vs. methane) or to the type of reactor (SBR vs. CSTR). In aerobic granular sludge, the composition of the wastewater appears to govern the microbial community composition, granulation kinetics, settling properties, and nutrient removal (Adler et al., 2017; Layer et al., 2019). This indicates that the difference in substrates might be the main reason for the differences between SBR and CSTR OPGs studied here. The impact of wastewater composition in terms of biological activity, diversity of the microbial community and the morphology remains however to be studied in details.

4.3. Spatial syntrophy of bacteria in OPGs

Our model indicates that heterotrophic and phototrophic activities are co-localized (**Figure III.2 B**). The co-localization of phototrophs and heterotrophs has previously been identified in other *in situ* and *in silico* phototrophic biofilms (Cole et al., 2014; Muñoz Sierra et al., 2014). This close spatial co-localization is explained by the syntrophy between phototrophs and heterotrophs, but also by the competition for the nutrients between heterotrophs. Oxygen, CO_2 and EPS have been determined to be the key compounds that drive the microbial interactions in OPGs (Milferstedt et al., 2017b).

The co-localization of activities in the outer layer of the granule doesn't necessarily mean that heterotrophs and phototrophs are absent in the center of the OPG. If one OPG grow starting from a small OPG, the top layers of phototrophs and heterotrophs found in mature OPG have then probably grown over older layers of phototrophs and heterotrophs. These old layers are then buried

at the center of the granule and became inactive due to the unavailability of light and nutrients. A one-dimensional model is here not enough for elucidating the formation of the tree dimensional spatial structure of the OPGs. A multidimensional model such as those developed by Nadell et al. (2016) or Picioreanu et al. (2005) could provide more insights on the role and contribution of microbial communities on the formation and spatial organization of OPGs.

4.4. Controlling anoxic zones in photogranules

The formation of the oxygen gradients is one of the advantages and motivations for the use of compact biological systems such as phototrophic biofilms and aerobic granular sludge in wastewater treatment (Guzzon et al., 2019; Strieth et al., 2018; Winkler et al., 2018). Indeed, the presence of oxygen gradients allows the formation of both, oxic and anoxic zones and the occurrence of simultaneous nitrification and denitrification (SND) (Puznava et al., 2001). Therefore, it is important to find operating conditions that generate oxic/anoxic zones and favor SND. In this study, four parameters (OPG diameter, incident light intensity, dCOD and DO in the bulk) were determined to be the most influential in the formation of oxic/anoxic zones (**Figure III.5 A & B**). When dCOD increases, oxygen consumption increases in the outer layer of the OPG and the anoxic biovolume deep in the OPG increases (**Figure III.5 A)**. Conversely when oxygen in the bulk increases, oxygen diffusion in the OPG increases and the anoxic biovolume decreases (**Figure III.5 A & B)**. The diameter of the OPG plays an important role when oxygen in the bulk is high. Big OPGs contain more biomass and thus consume more oxygen in their outer layer and limit oxygen penetration (plain lines in **Figure III.5 B**). On the contrary when oxygen in the bulk is low, both oxygen production and consumption increase when the diameter increase and oxygen penetration does not change significantly (dotted lines in **Figure III.5 B**). Finally, in all cases, oxygen production increases when light intensity increases (**Figure III.5 A & B**) and the anoxic biovolume decreases. Using graphs such as those shown in **Figure III.5**, , it would thus be possible to adjust light intensity depending on dCOD and DO values to keep the deeper zones anoxic and thus provide the right conditions for denitrification as reported for aerobic granular sludge (Layer et al., 2020; Li et al., 2020, 2008; Volcke et al., 2012). Selecting large OPGs would also ensure an easier preservation of anoxic zones in cases when the dissolved oxygen in the bulk reaches high concentrations. This control on anoxic zones depends on rates and activities distribution in the various types of photogranules as pointed out by the modeling approach. However, even with very different OPGs such as those analyzed here, the model predicts that a common range of light

intensity comprised between 30 and 50 PAR would allow keeping anoxic zones for all types of OPGs when there is no oxygen in the bulk. These predictions however need to be confirmed by dedicated experiments.

During reactor operation, famine phases might induce an increase in DO in the micro and macroenvironment of the OPGs. This would lead to the disappearance of anoxic zones, to the inhibition of nitrate reduction and probably to the decay of anaerobic denitrifiers. This further emphasize the importance on dynamically controlling light intensity depending on dCOD and DO parameters. The light energy demand in the famine period could be much lower than that in the feast period, i.e., the light intensity could be reduced substantially in the famine period. Obviously, a considerable amount of energy might be saved using this strategy, however more studies are needed to measure its possible influence on nutrient removal performances and on granulation (Liu and Liu, 2006; Mosquera Corral et al., 2005).

Finally, the results established in this study assumed that the OPGs receive a continuous and constant light intensity, which is different from in-situ conditions. In practice, along its trajectory in the photobioreactor, an OPG receives light with varying intensity depending on the mixing rate and on biomass concentration (Gernigon et al., 2019; Loomba et al., 2018). These intermittent light conditions need to be considered for the control of anoxic zones and the optimization of the bioprocess.

5. Conclusion

This study provided insights into the photosynthetic activity of OPGs.

Light attenuation appeared to be a key factor which determines the phototrophic layer thickness. Independently of OPG diameter, light penetration depth was limited to around 700 µm.

Oxygen profiles measured in the photogranules using oxygen microelectrodes appeared to depend on light intensity and dCOD. These profiles were modeled considering phototrophic and heterotrophic activities in the photogranules. The spatial distribution of these activities was a key factor for the adequate modeling of oxygen profiles. The distributions appeared to depend on the origin of the photogranule, *i.e.*, different distributions were used for the modeling of the photogranule from CSTR and for the photogranules from SBR. However, a unique distribution was used for the 5 SBR photogranules indicating a homogenous composition of photogranules with a

same origin. In all cases, phototrophic and heterotrophic activities appeared colocalized in the phototrophic layer (first 700 µm).

Using the model, it was finally possible to devise strategies for the control of oxygen gradients in photogranules:

- Selective biomass harvesting, i.e., of OPGs above or below a certain diameter, may be a lever to engineer an OPG population with a desirable oxygen distribution.
- Illumination and addition of organic carbon can both be used as levers to control oxygen gradients within OPGs and maintain anoxic zones favoring SND.

6. Funding and acknowledgements

This work was financed through the French "Agence Nationale de la Recherche" grant ANR-16-CE04-0001-01 ("PSST: Photogranules shake sewage treatment up") and the INRAE department MICA. A support for international scientific and technological exchange for authors from France, the Netherlands and Norway, was financed through the Campus France Partenariats Hubert Curien (PHC) programs Van Gogh (42571TG) and Aurora (43048XE). We express our gratefulness to Philipe Sousbie for assisting in reactor operation during this research.

Chapter IV

Optimization of the use of light for photogranules under SBR operating conditions

In the previous chapter, I developed a model for the prediction of oxygen gradients in photogranules from different types of reactors. The predicted gradients depend on photogranule diameter, dissolved organic carbon, incident light and dissolved oxygen. The experimental conditions tested were however limited. In this chapter, I will extend this study and make a thorough analysis of the combined effects of the parameters on oxygen profiles for 6 SBR photogranules. I will then evaluate the predictions of the model developed in chapter III, expand it, and apply it for the modeling of the new results. Possible strategies for the control of an OPG-based photobioreactor will then be evaluated and expanded according to the new results.

1. Introduction

The sequencing batch reactor (SBR) with oxygenic photogranules (OPGs) represents a promising alternative to conventional activated sludge plants (Abouhend et al., 2020, 2018; Milferstedt et al., 2017b). OPGs can be described as dense phototrophic aggregates containing millions of organisms embedded in gel-like matrix of extracellular polymeric substances (EPS), including within them different bacterial species that play different roles in wastewater treatment such as organic carbon removal, nitrification and denitrification (Milferstedt et al., 2017b; Trebuch et al., 2020). The morphological structure of OPGs provides many advantages in comparison to the activated sludge process: (i) fast settling, which facilitates the harvesting (i.e., no need for external settlers) or the retention of the biomass (Milferstedt et al., 2017a) and (ii) the existence of oxygen and organic carbon gradients along the radius of each photogranule, which may allow simultaneous aerobic, anoxic and anaerobic processes into the same photogranule ((Ouazaite et al., 2020) and **chapter III**). To date, research on OPGs has focused on both their formation mechanisms and their potential for wastewater treatment (Abouhend et al., 2018; Ansari et al., 2019; Milferstedt et al., 2017b; Trebuch et al., 2020), as well as on the micro-scale activities of these granules (Ouazaite et al., 2020). The latter allow to understand, at the first level, the spatial interactions and mass transfer that may be key factors leading to the spatial arrangement of microorganisms within photogranules. In addition, the study of micro-scale activities provided valuable information for OPG-based bioprocess monitoring such as anoxic biovolume (**chapter III**) and external oxygen diffusion condition (**chapter II**).

In a SBR, the substrate (e.g., acetate) is fed in a short period of time at the beginning of each cycle. The microorganisms then encounter an environment with lots of available carbon, which triggers the heterotrophic activity if oxygen is available. Over the cycle, the available carbon decrease in the bulk due to the heterotrophic activity until all available carbon is consumed. The heterotrophic activity then stops and oxygen concentration increases in the bulk reaching in some cases air saturation oxygen concentration. Regarding the oxygenic photogranules, we showed in **chapter III** that respiration rates and anoxic microzones were impacted by available carbon and dissolved oxygen. The model developed allowed predicting optimal light intensity ranges depending on those parameters. This could be used to devise optimal strategies for the control of light intensity over SBR cycles in an OPG-based photobioreactor. However, model predictions need to be validated over wide parameter ranges.

Here we extend the study from **chapter III** with the measurement and analysis of oxygen microprofiles of 6 SBR photogranules with wide ranges of light intensities and dissolved organic carbon. A new experimental design was developed that allowed regulating dissolved oxygen concentration in the bulk to either air saturation or low concentration. 54 oxygen profiles were thus obtained and used for mapping the areal net photosynthesis and percentages of anoxic biovolume as function of the parameters. The model developed in **chapter III** was then used to model the profiles and refine the maps. The engineering implications of the findings are discussed. It is expected that this work can offer useful information about the optimization of OPG-based SBR operation.

2. Materials and methods

2.1. Photogranule cultivation

Oxygenic photogranules were cultivated in a lab-scale sequencing batch reactor (SBR) of 4-liter working volume with 6-hour cycles under continuous illumination of 100 $\mu moles_{PAR} \cdot m^{-2} \cdot s^{-1}$ of photosynthetic active radiation (PAR) at the reactor surface. Mixing was set to 100 rpm. Synthetic wastewater used for photogranule cultivation consisted of sodium acetate 138 $mg \cdot L^{-1}$, KH2PO4 11.7 $mg \cdot L^{-1}$, MgHPO4·3 H2O 14.5 $mg \cdot L^{-1}$, NH4Cl 34.2 $mg \cdot L^{-1}$, FeSO4·7 H2O 2.9 $mg \cdot L^{-1}$. This composition gave a chemical oxygen demand (COD) of 100 $mg \cdot L^{-1}$. Six granules were chosen randomly at the end of SBR cycles. The granules hereafter numbered OPG1-6 had diameters of 3.5, 4, 3.8, 4.1, 3.9 and 3.4 mm respectively.

2.2. Oxygen gradients measurement

Measurements of spatially resolved oxygen profiles were performed in a flow cell (**Figure IV.1)** outside the photobioreactor. Flow was ensured by a recirculation peristaltic pump with a flow rate of 1.5 $L \cdot min^{-1}$. The photogranule was fixed in a loop of a nylon thread, connected to a pipet loader tip and placed in the middle of the cross-sectional area of the plastic box. The microelectrode was mounted on the micromanipulator and driven into the granules in steps of 50 or 100 mm. Profiles were measured at the equator of the granules, perpendicularly to the flow. Oxygen microelectrodes were of the Clark type, from Unisense A/S Denmark (www.unisense.com). Tip diameter was about 50 mm. The medium used for measurement was tap water with acetate (**Table IV.1**). The medium was either saturated with atmospheric oxygen (oxygen concentration about 8.5 $mg \cdot L^{-1}$) or deoxygenated with nitrogen bubbling (oxygen concentration less than 1 $mg \cdot L^{-1}$) in a mixing vessel.

The conditions for oxygen gradients measurement are summed up in **Table IV.1**. For example, "*Granule 2/3*" represents the 3rd measurement of oxygen gradients in photogranule 2 which was performed for 10 PAR, 100% O_2 in the bulk and 20 $mg_{COD} \cdot L^{-1}$. In all cases, the photogranule was placed in the flow cell half an hour before the first measurement in order to record only pseudo steady state profiles (balance of oxygen transport and consumption).

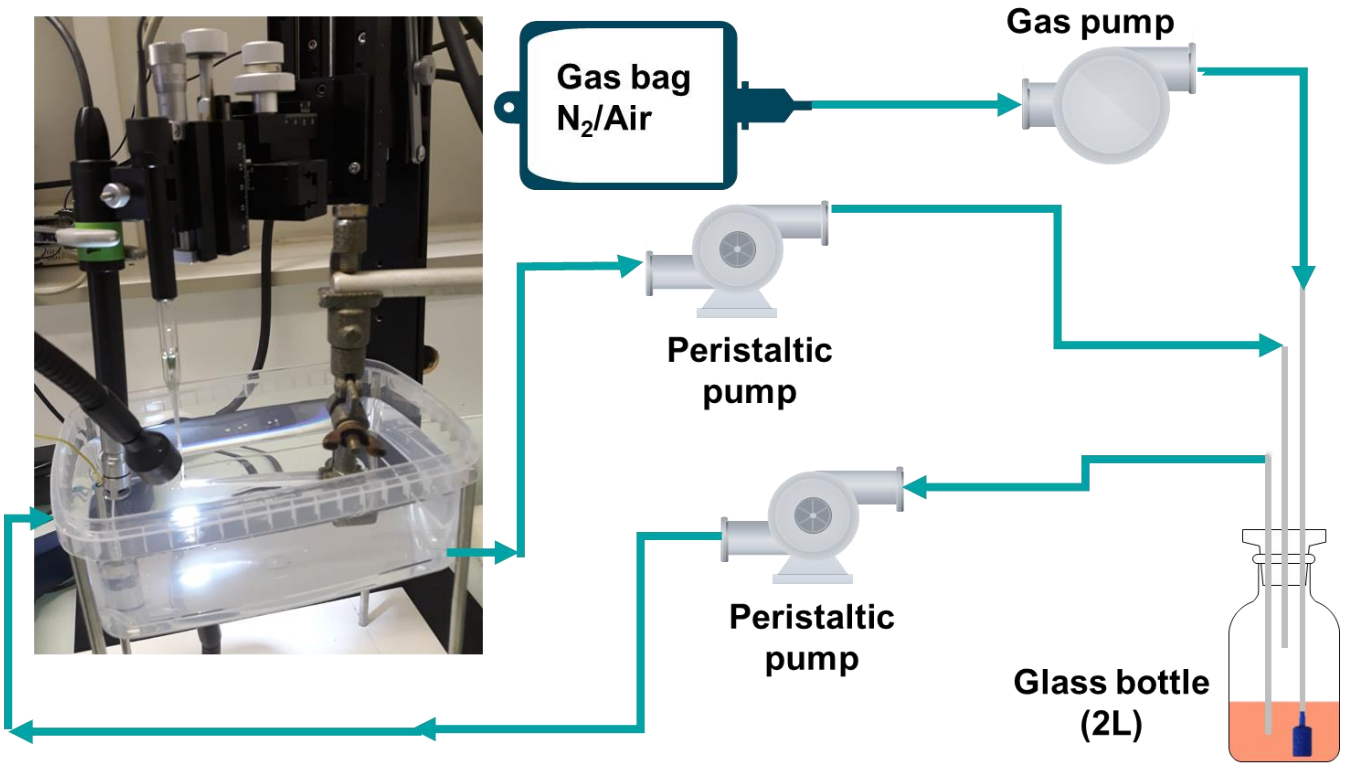

Figure IV.1 *Flow cell dispositive for oxygen microelectrode measurement under different conditions presented in Table 1. Arrows indicate flow direction.*

Table IV.1 *Experimental plan illustrating the applied conditions for each oxygen profile measurement. Each color corresponds to a photogranule with a diameter ranging from 3.4 to 4.1 mm, and the expression "*X/Y*" represents the* Y^{th} *measurement of oxygen gradients in the* X^{th} *photogranule.*

Acetate ($mg_{COD}·L^{-1}$)	O_2 Bulk (% air sat)	Light Intensity ($\mu moles_{PAR}·m^{-2}· s^{-1}$)				
		0	10	20	40	80
0	≈0%		1/1	3/1	5/1	1/2
	100%	2/2	4/1	6/2	2/1	6/1
5	≈0%		6/3	5/2	1/3	3/2
	100%	5/3	2/3	4/2	4/3	2/4
20	≈0%		4/4	1/5	1/4	3/3
	100%	6/5	6/4	5/4	6/6	5/5
50	≈0%		3/4	2/6	4/5	2/5
	100%	3/5	5/7	6/8	6/7	5/6
100	≈0%		2/7	4/7	2/8	4/6
	100%	4/8	3/6	1/6	5/8	1/7
500	≈0%		3/7	3/8	5/9	6/9
	100%	1/9	1/8	2/9	3/9	4/9

OPG	Diameter (mm)
1	3.5
2	3.8
3	3.7
4	3.9
5	4.1
6	3.4

2.3. Oxygen gradients modeling

Oxygen production, consumption and, diffusion processes in the photogranules were modeled with the one-dimensional reaction diffusion model programmed in COMSOL Multiphysics 5.4 (COMSOL Inc., Burlington, MA, USA) (see details in **chapter III**)The model distinguishes between the different metabolism of photoautotrophs (i.e., oxygen production when light is presents and oxygen consumption when light is absent). The model considers also two different mechanisms for the heterotrophic metabolism: consumption of EPS or of organic carbon (i.e., acetate) when available. Parameters of the model were optimized based on fitting the models results to the measured oxygen gradients in the photogranules. The fitting approach used in study is however different from the one used in the previous work. Some profiles were difficult to fit and were associated with very high associated errors. They were thus preventing the global optimization of the model based on minimization of the sum of squared errors (SSE). This problem might be due to experimental incidents such as electronic noises which are reported for such systems (Chaturvedi et al., 2013). The parameters estimation was then done in five steps:

- Kinetics parameters from the previous work were used as a starting point and the experimental data were fitted by optimizing the biomass population distribution in the photogranules until a minimum was find.
- The kinetics parameters were then optimized until a minimum was find again.
- The profiles with an SSE higher than two-fold of the average SSE were discarded.
- The data were fitted again by optimizing the biomass population distribution in the photogranules until a minimum was find.

- Finally, the kinetics parameters were optimized until a minimum was found again.

2.4. Net photosynthesis calculation

Oxygen microprofiles within the photogranules result from the balance between production, consumption, and diffusion of oxygen. This equilibrium is governed by the reaction-diffusion equation:

$$-\mathrm{D}_{\mathrm{O}_2} \cdot \nabla^2 \mathrm{C}_{\mathrm{O}_2} = \mathrm{P}(\mathrm{z}) - \mathrm{C}(\mathrm{z}) \qquad \textbf{\textit{(Equation IV.1)}}$$

Where D_{O_2} is the molecular diffusion coefficient of the oxygen. z, represents the depth coordinate, scaled 0 at the photogranule–bulk interface, scaled positively downward. P(z) and C(z) represent respectively the oxygen production and consumption rate at depth z.

The steady state profile of oxygen concentration will change because of ongoing diffusion, oxygen consumption and production (**Equation IV.1**). Thus, the areal net photosynthesis Pg ($mg_{O2} \cdot m^{-2} \cdot s^{-1}$) is expressed as follow

$$\mathrm{P_n} = \int_0^{D/2} (\mathrm{P}(\mathrm{z}) - \mathrm{C}(\mathrm{z})) \cdot \delta \mathrm{z} = \int_0^{D/2} -D_{O_2} \cdot \nabla^2 \mathrm{C}_{\mathrm{O}_2} \cdot \delta \mathrm{z} \approx \sum_{\mathrm{z_i}=0}^{\mathrm{z_i}=\mathrm{D}/2} -\mathrm{D}_{\mathrm{O}_2} \cdot \nabla^2 \mathrm{C}_{\mathrm{O}_2} \cdot \Delta \mathrm{z}$$

(***Equation IV.2***)

The average volumetric net photosynthesis Pn, Volumetric ($mg \cdot m^{-3} \cdot s^{-1}$)

$$\mathrm{P}_{n,\mathrm{volumetric}} = \frac{\mathrm{P_n}}{\frac{\mathrm{D}}{2}} \qquad \textbf{\textit{(Equation IV.3)}}$$

The net photosynthesis calculations were realized based on the experimental measurements or/and on the mathematical model simulated results for each half-hemisphere. The averaged values were the generated as surface response. "*ScatteredInterpolant"* MATLAB R2018b (version R2018b, MathWorks, USA) function was used to perform interpolation at a very fine mesh grid used in the experimental data or for the model outputs.

3. Results

3.1. Steady state oxygen profiles

Using microelectrodes, the oxygen concentration profiles of the six photogranules incubated under different environment conditions as shown in **Table IV.1** were measured. The shape of oxygen profiles depended on light conditions, on the presence of the organic carbon and on the

photogranule size (dots in **Figure IV.2** and **Figures S01-S06 supplementary material**). At low intensities and high organic carbon (i.e., below 20 $\mu moles_{PAR} \cdot m^{-2} \cdot s^{-1}$ and above 50 $mg \cdot L^{-1}$ of dCOD), the oxygen penetrates only the first hundred micrometer and no peak of oxygen was observed. For higher light intensities (above 40 $\mu moles_{PAR} \cdot m^{-2} \cdot s^{-1}$), the oxygen concentration under the surface reached oversaturation with a maximum of 20 $mg \cdot L^{-1}$. Deeper in the photogranule, the oxygen concentration decreases rapidly toward the inner core of the photogranule. Globally, the presence of oxygen ranged from 0.1 mm to 2.5 mm. Furthermore, with increasing oxygen concentration in the bulk, a shift of the oxygen gradient to higher concentrations occurred

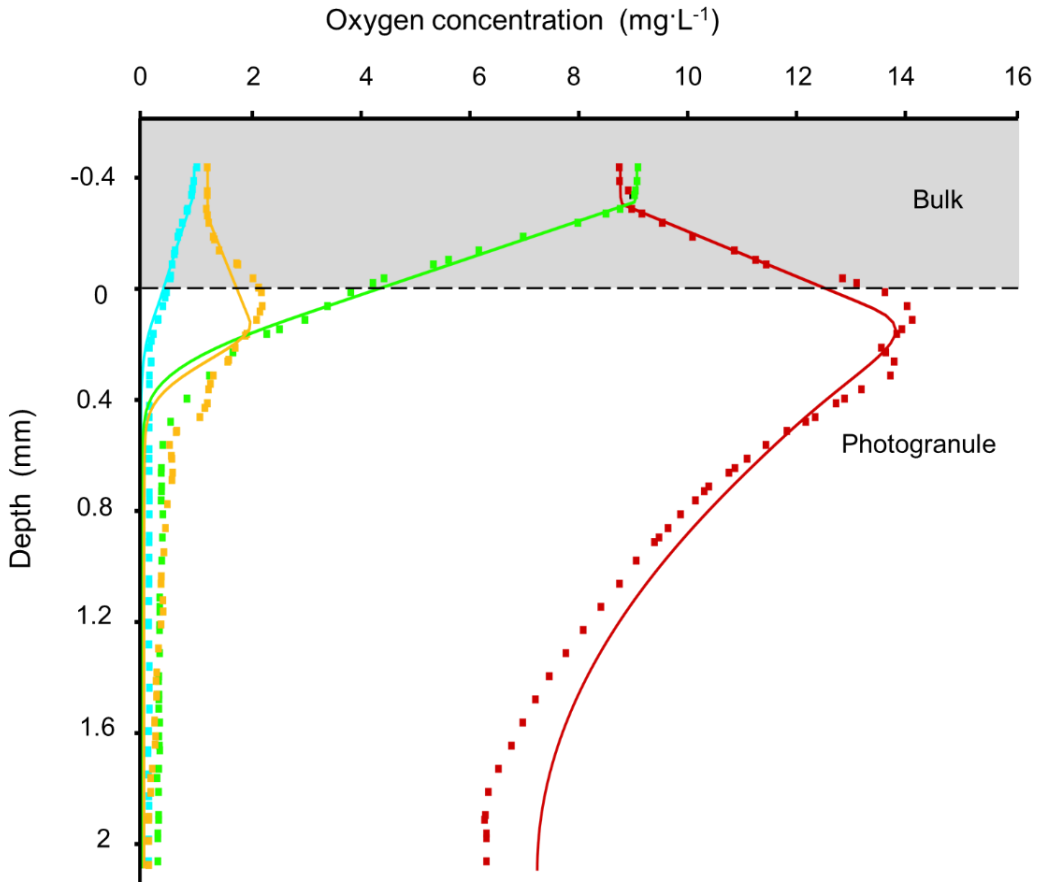

Figure IV.2 *Concentration of dissolved oxygen profiles within the first hemisphere of oxygenic photogranule N° 6 under conditions measurement (Marron: measure 1 (I=80 $\mu moles_{PAR} \cdot m^2 \cdot s^{-1}$, dCOD=0 $mg \cdot L^{-1}$, O_{2b}= 8.8 $mg \cdot L^{-1}$), cyan: measure 3 (I=10 $\mu moles_{PAR} \cdot m^2 \cdot s^{-1}$, dCOD=5 $mg \cdot L^{-1}$, O_{2b}= 0.98 $mg \cdot L^{-1}$), green: measure 8 (I=20 $\mu moles_{PAR} \cdot m^2 \cdot s^{-1}$, dCOD=50 $mg \cdot L^{-1}$, O_{2b}= 9 $mg \cdot L^{-1}$) , gold: measure 9 (I=80 $\mu moles_{PAR} \cdot m^2 \cdot s^{-1}$, dCOD=500 $mg \cdot L^{-1}$, O_{2b}= 0 $mg \cdot L^{-1}$). Grey dashed line represents the interface photogranule-bulk.*

3.2. Net photosynthesis and light compensation point

The areal net photosynthesis was calculated by integrating dissolved oxygen microprofile data over the half hemisphere of every photogranule as explained in section **3.2**. Results are shown as contour plots in **Figure IV.4 A & B.** Relating the net photosynthesis with the incident light intensity and dissolved organic carbon availability (dCOD), allows determining the light compensation point *Ic*, *i.e.*, light intensity needed for photosynthesis to compensate respiration and diffusion. A negative value indicates that oxygen diffuses from the water to the granule, and a positive one indicates the opposite. Globally, the areal net photosynthesis appeared to increase with the light intensity and decrease with the availability of organic carbon in the surrounding environment of the photogranules. Negative and low rates of net photosynthesis were found in most experiments when oxygen concentration in the bulk was high (**Figure IV.3 B**) and the *Ic* is ranged from less than 25 to 80 $\mu moles_{PAR} \cdot m^{-2} \cdot s^{-1}$. On the contrary, when the oxygen was low in the bulk (**Figure IV.3 A**), positive areal net photosynthesis rates were found for most experiments and the *Ic* ranged from 12 to 60 $\mu moles_{PAR} \cdot m^{-2} \cdot s^{-1}$. Overall, the areal net photosynthesis rate didn't show a saturation or a photoinhibition with the increase of the light intensity. However, the plots appear to be irregular with several local minima and maxima and are difficult to interpret. This identification is due to the integration of measurements on photogranules with various diameters and to variations in oxygen concentration in the bulk due to technical limitations. Therefore, to overcome these challenges, we used one dimensional reaction diffusion model to reproduce the steady state oxygen profiles and then extrapolated the areal net photosynthesis for each photogranule and various concentrations of oxygen in the bulk.

The results of the simulations are shown as lines together with the measured profiles in **Figure IV.2** and **Figures S01-S06 supplementary materials.** The estimated parameters are presented in **Table S01** in **supplementary material**. The model was then used to reproduce the oxygen gradients for each photogranule under all conditions presented in **Table IV.1**. The simulated gradients were used to calculate the areal net photosynthesis for each photogranule separately.

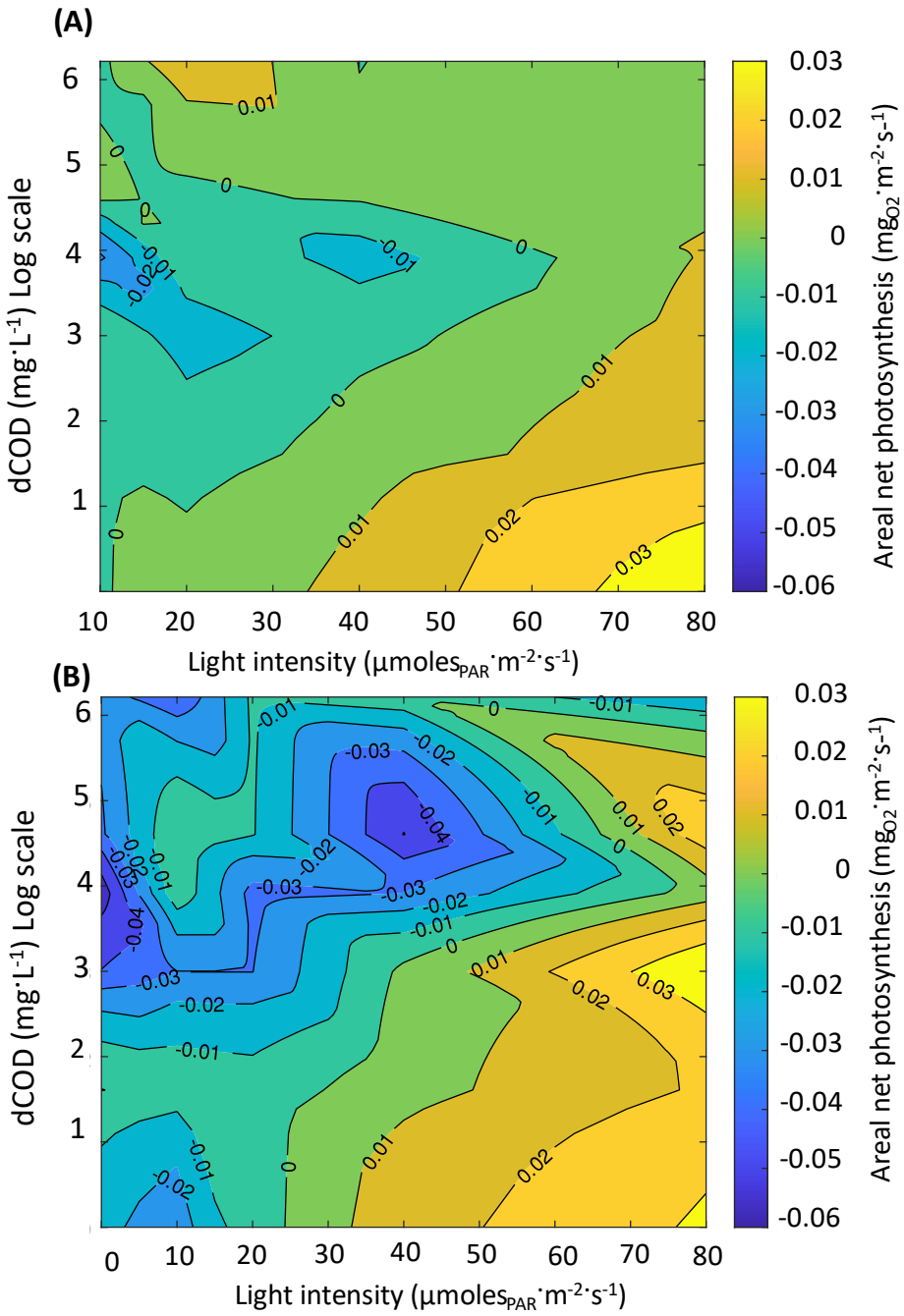

Figure IV.3 *Response surface plots showing the effects of light intensity and organic carbon (acetate) on the areal net photosynthesis based on the experimental measurements (A) contour plot of net photosynthesis when the concentration of dissolved oxygen in the bulk was low < 1.5 mg·L^{-1}, the light intensity in this panel starts at an intensity of 10 µmoles$_{PAR}$·m^2·s^{-1} given that no oxygen profile was measured in the dark (B) contour plot of net photosynthesis when the dissolved oxygen in the bulk was at air saturation*

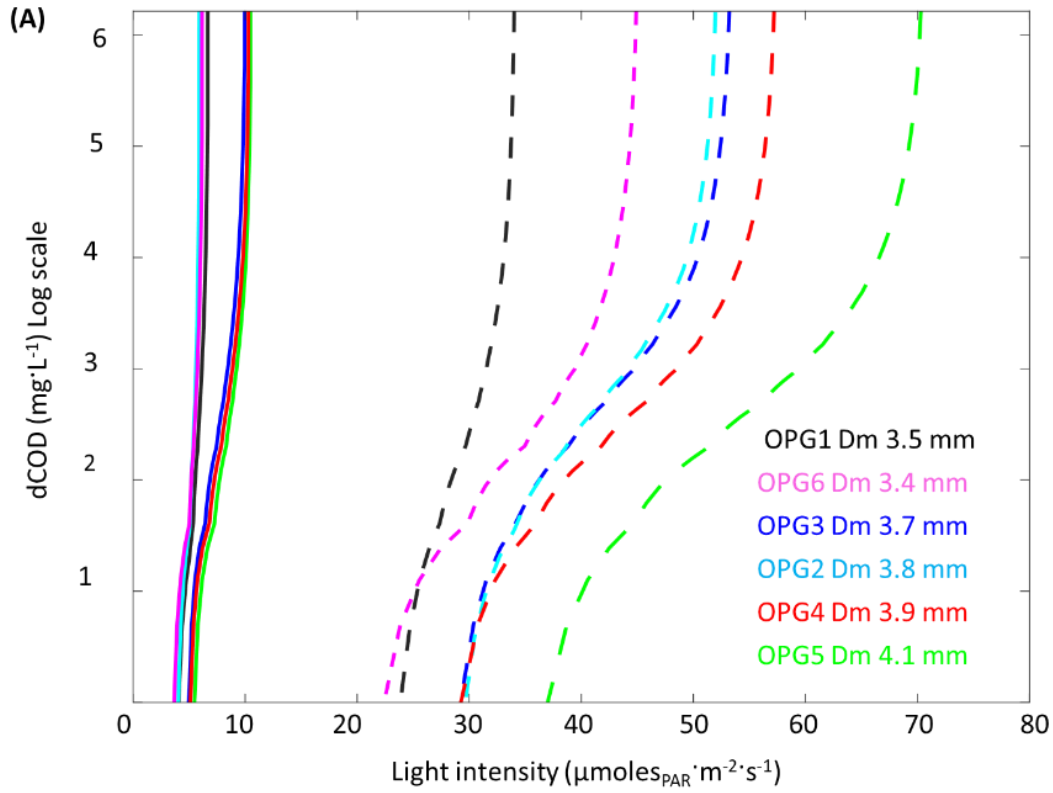
(A)
dCOD (mg·L-1) Log scale
Light intensity (µmolesPAR·m-2·s-1)
OPG1 Dm 3.5 mm
OPG6 Dm 3.4 mm
OPG3 Dm 3.7 mm
OPG2 Dm 3.8 mm
OPG4 Dm 3.9 mm
OPG5 Dm 4.1 mm

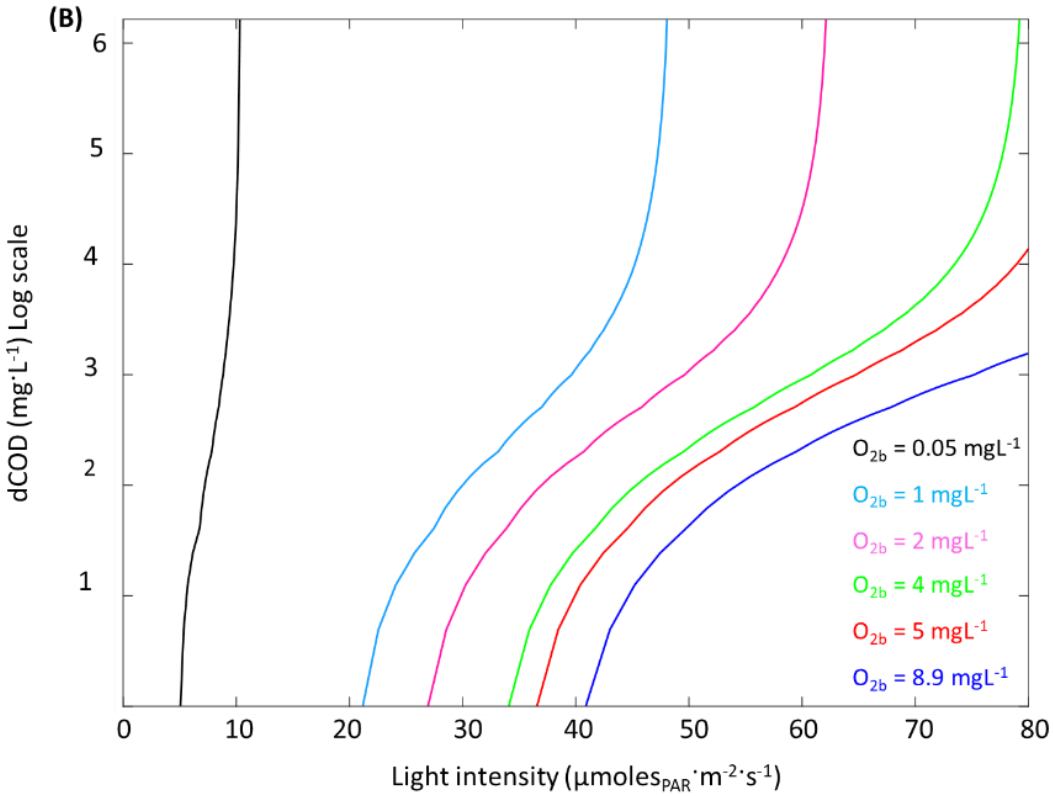
(B)
dCOD (mg·L-1) Log scale
Light intensity (µmolesPAR·m-2·s-1)
O2b = 0.05 mgL-1
O2b = 1 mgL-1
O2b = 2 mgL-1
O2b = 4 mgL-1
O2b = 5 mgL-1
O2b = 8.9 mgL-1

Figure IV.4 *The isolines plot showing the effects of light intensity and organic carbon (acetate) on the net photosynthesis (A) Isoline plot of net photosynthesis for each photogranule when the dissolved oxygen in the bulk is low (i.e., O_{2b}= 0.05 mg·L^{-1}): solid lines correspond to an areal net photosynthesis of a value null, dashed lines correspond to an areal net photosynthesis of value 0.02 mg·m^{-1}·s^{-1}. (B) Isolines plot of areal net photosynthesis of a value null under different level of oxygen concentration in the bulk for a photogranule with diameter of 3.4 mm.*

The areal net photosynthesis was then calculated for each photogranule when the oxygen in the bulk is low (O_{2b} = 0.05 mg·L^{-1}) (**Figure IV.4 A**). The results revealed that in general all the photogranules start exporting oxygen at low light intensities (i.e., the *Ic* is below 10 µmoles$_{PAR}$·m^{-2}·s^{-1}) (solid lines in **Figure IV.4 A**). When comparing a high level of areal net photosynthesis (i.e., 0.02 mg·L^{-1}·s^{-1}) for the different photogranules, the simulations results showed that with the increase of the photogranule diameter (3.4 mm to 4.1 mm), an increase of light is needed to achieve the same level of areal net photosynthesis (dashed lines in **Figure IV.4 A**). For example, for 500 mg·L^{-1} COD (i.e., 6.2 log scale) an increase from 25 µmoles$_{PAR}$·m^{-2}·s^{-1} to 70 µmoles$_{PAR}$·m^{-2}·s^{-1} is needed.

To study the effects of dissolved oxygen in the bulk, we the oxygen concentration was varied in the range of 0.05 mg·L^{-1} to 8.9 mg·L^{-1} in the model. The areal net photosynthesis was then evaluated. The **Figure IV.4 B** illustrates the isolines corresponding to null areal net photosynthesis for the photogranule number 6 with diameter of 3.4 mm under different level of oxygen concentration in the bulk. At low oxygen concentrations (i.e., below 2 mg·L^{-1}), the photogranule diffused oxygen for low light intensities (i.e., *Ic* is below 60 µmoles$_{PAR}$·m^{-2}·s^{-1}). On the other hand, when the oxygen in the bulk is high (i.e., above 4 mg·L^{-1}) the *Ic* ranged from 35 to up 80 µmoles$_{PAR}$·m^{-2}·s^{-1} under high concentration of the dCOD in the surrounding environment.

The model allowed also evaluating the volumetric net photosynthesis (Pn). The net photosynthesis increased linearly the with increasing irradiance with a slope of 0.015 ± 0.9 mmol·L^{-1}·s^{-1}·(µmoles$_{PAR}$·m^{-2}·s^{-1})$^{-1}$. The photogranules showed a maximum endogenous respiration rate of 0.1 ± 0.02 µmmol·L^{-1}·s^{-1} and a maximum heterotrophic respiration on acetate of 0.21 ± 0.03 µmmol·L^{-1}·s^{-1}.

3.3.Anoxic microzones

Here, zones where oxygen concentrations were below 0.5 $mg \cdot L^{-1}$ were considered as anoxic zones in the photogranules. It was also assumed that photogranules were spherical. **Figure IV.5** shows the percentages of anoxic biovolumes in photogranules as a function of light intensity and available organic carbon when the oxygen concentration in the bulk is low (O_{2b}<1.5 $mg \cdot L^{-1}$ **panel A**) and when the oxygen concentration is high in the bulk ($O_{2b} \approx 8.9$ $mg \cdot L^{-1}$ **panel B**). As expected, high anoxic biovolumes (i.e., above 50 %) are more present when the oxygen concentration is low in the bulk (**Figure IV.5 A**). An increase in light intensity was associated in general to a decrease in the anoxic biovolume of the photogranules **(Figure IV.5 A** and **B)**. On the other hand, an increase dCOD availability was associated to an increase in the anoxic biovolume (**Figure IV.5 A** and **B)**. However, interpretation of these plots is difficult for the same reasons mentioned earlier (see section 3.2). Therefore, we used the developed model to map all conditions presented in **Table IV.1** and generate oxygen profiles for each photogranules.

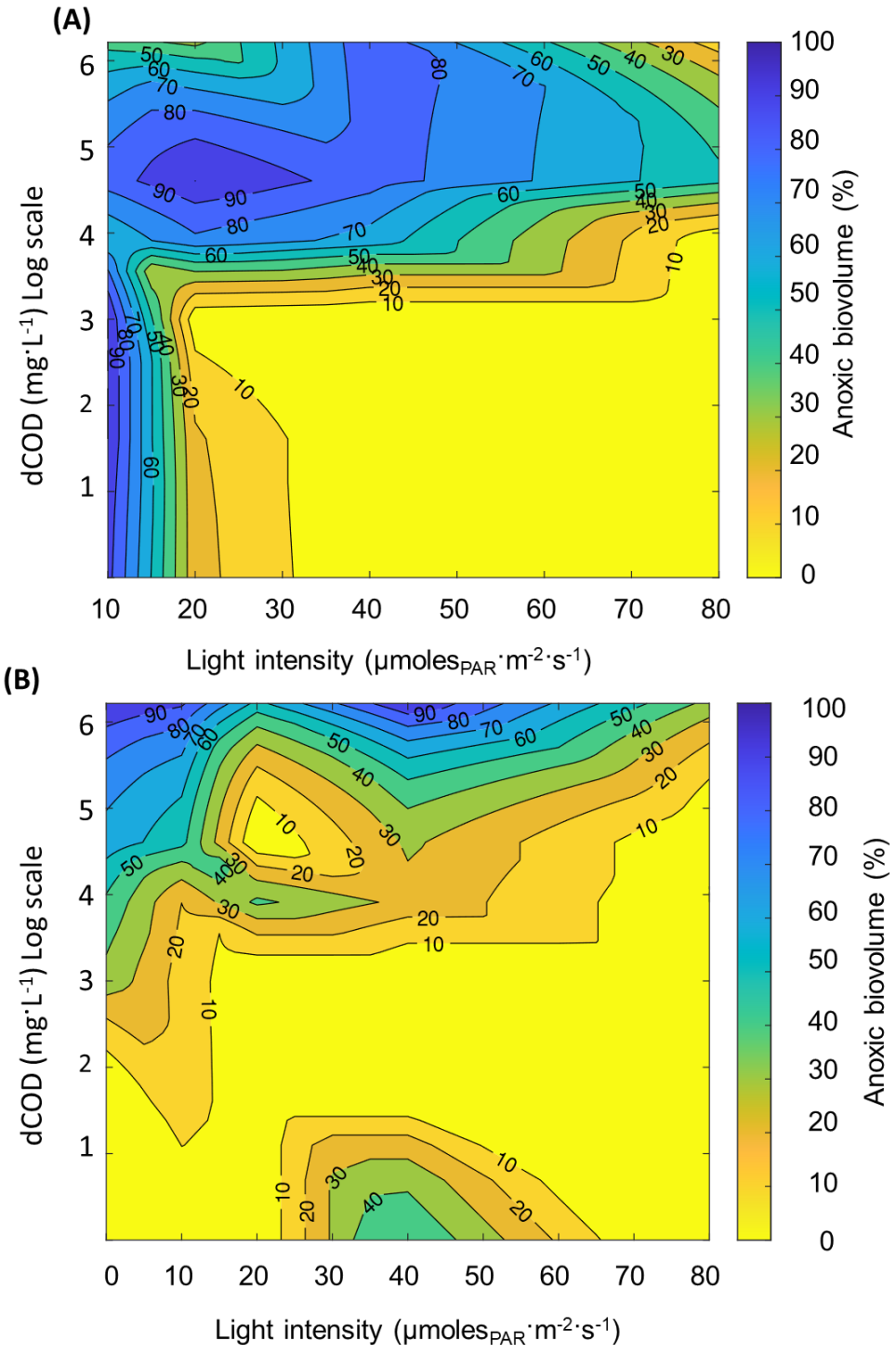

Figure IV.5 *The response surface plot showing the effects of light intensity and organic carbon (acetate) on the anoxic biovolume (oxygen concentration < 1.5 mg·L^{-1}) based on the experimental measurements. (A) Anoxic zone when the oxygen in the bulk is low. (B) Anoxic zone when the oxygen in the bulk is at air saturation concentration.*

Based on simulated oxygen concentration profiles via the developed model, anoxic biovolumes for each photogranules were calculated using the same approach as the one used for the experimental ones. A wide range of macroenvironmental condition were mapped light from 0 to 80 $\mu moles_{PAR} \cdot m^{-2} \cdot s^{-1}$ with a step of 5 $\mu moles_{PAR} \cdot m^{-2} \cdot s^{-1}$, dCOD from 0 to 500 $mg \cdot L^{-1}$ with a step of 2 $mg \cdot L^{-1}$ and finally oxygen in the bulk from 0 to 8.9 $mg \cdot L^{-1}$. As expected, the results showed that larger photogranules showed higher anoxic biovolume (**Figure IV.6 A**). Yet, this is only straightforward when the oxygen in the bulk is high and when comparing a higher percentage of anoxic biovolume (**Figures S07- S09 in supplementary material**). Interestingly, the models indicate that, except for OPG1, when oxygen is low (concentration < 1 mg/l) and dCOD is high (concentration > 20 mg/l *i.e.*, 3 in the log scale) anoxic zones are found in all photogranules even with light intensities up to 80 $\mu moles_{PAR} \cdot m^{-2} \cdot s^{-1}$ (**Figures S01 & S02**). This is also confirmed by the experimental plot (**Figure IV.5 A**). The results also showed that dissolved oxygen in the bulk had a significant impact on the regulation of the anoxic biovolume (**Figure IV.6** and **Figures S07-S09 in supplementary material**). The **Figure IV.6 B** illustrates the isolines corresponding to 30 % of anoxic biovolume for the photogranule number 6 with diameter of 3.4 mm under different levels of oxygen concentrations in the bulk. It confirms that the increase of the oxygen in the bulk induces a decrease of the anoxic biovolumes. For this small photogranule, the anoxic biovolume decreases up to a point where there is no anoxic biovolume when the bulk is saturated with air and dCOD is low even if the light if off (**Figure S03**). However, for larger photogranules with diameters of 3.7, 3.8- and 4.1-mm diameter, it is possible to keep a small anoxic biovolume in those conditions with high oxygen and low dCOD by shutting off the light (**Figure S03**).

(A)

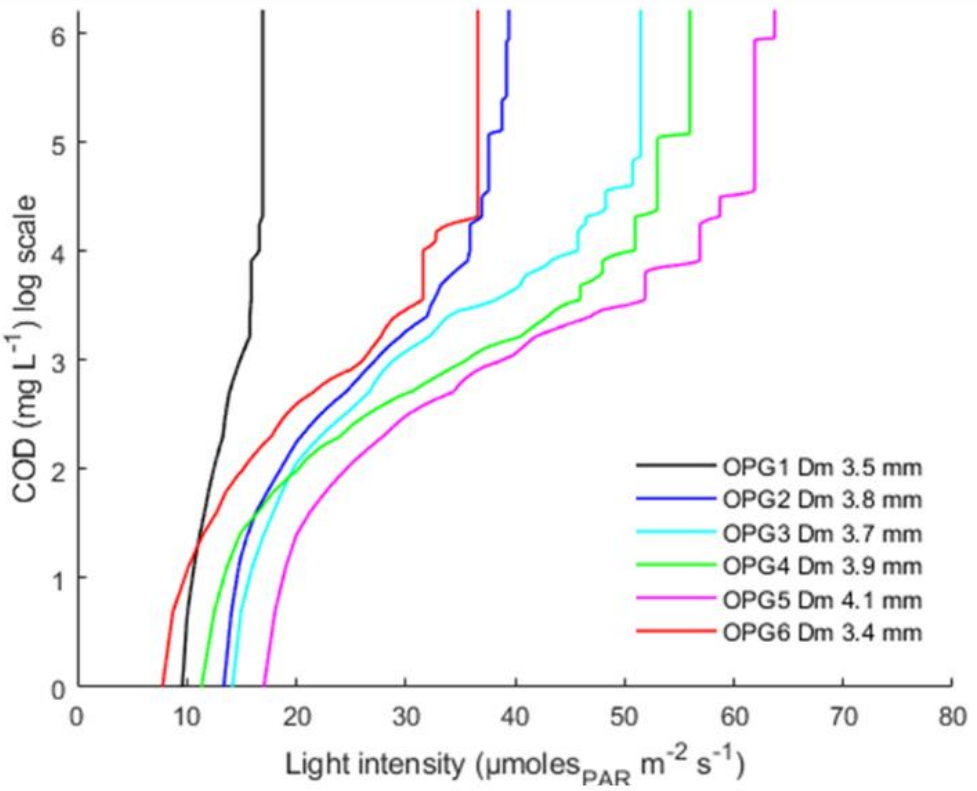
COD (mg L-1) log scale
Light intensity (µmolesPAR m-2 s-1)
OPG1 Dm 3.5 mm
OPG2 Dm 3.8 mm
OPG3 Dm 3.7 mm
OPG4 Dm 3.9 mm
OPG5 Dm 4.1 mm
OPG6 Dm 3.4 mm

(B)

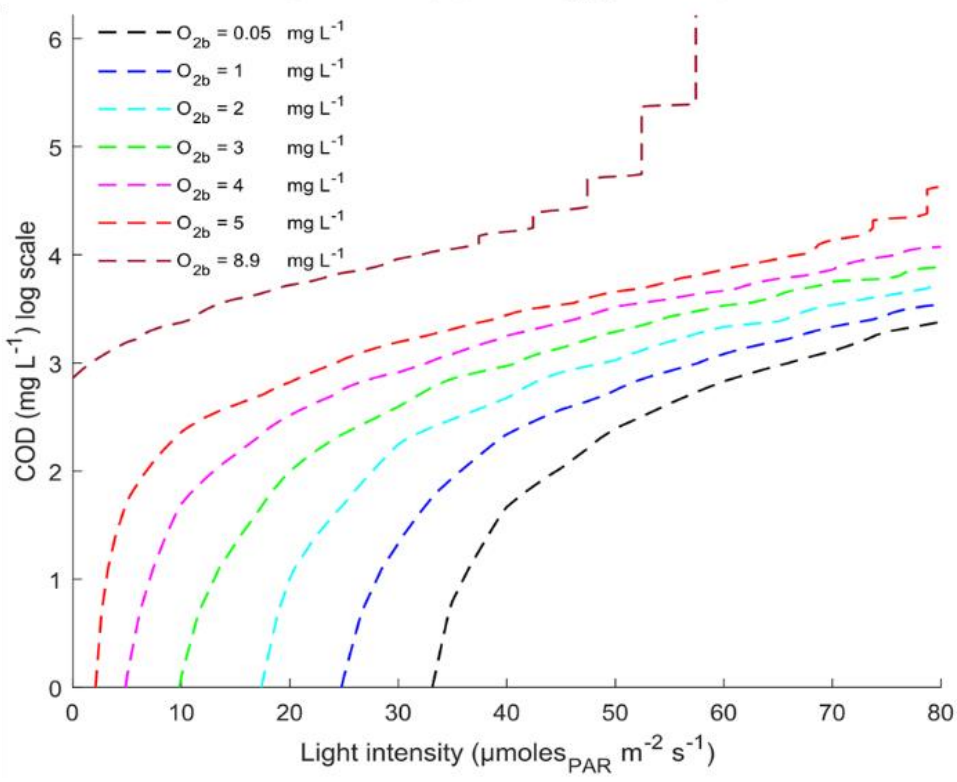
O2b = 0.05 mg L-1
O2b = 1 mg L-1
O2b = 2 mg L-1
O2b = 3 mg L-1
O2b = 4 mg L-1
O2b = 5 mg L-1
O2b = 8.9 mg L-1
COD (mg L-1) log scale
Light intensity (µmolesPAR m-2 s-1)

Figure IV.6 *The isolines plot showing the effects of light intensity and organic carbon (acetate) on the percentage of anoxic biovolume (A) Isoline plot of 70 % of anoxic biovolume for each photogranule when the dissolved oxygen in the bulk is low (i.e., O_{2b} =0.05 $mg \cdot L^{-1}$) for different diameters: black 3.4 mm, blue 3.5 mm, cyan 3.7 mm, green 3.8 mm, magenta 3.9 mm, red 3.4 mm. (B) Isoline plot of 30 % of anoxic biovolume for photogranule with diameter 3.4 mm (OPG6) under different dissolved oxygen concentration in the bulk (black 0.05 $mg \cdot L^{-1}$, blue 1 $mg \cdot L^{-1}$, cyan 2 $mg \cdot L^{-1}$, green 3 $mg \cdot L^{-1}$, magenta 5 $mg \cdot L^{-1}$, red 8.9 $mg \cdot L^{-1}$).*

4. Discussion

Earlier modeling research have shown in photogranules that phototrophs and heterotrophs dominate in the outermost layers, since they position themselves near to the source of light dissolved oxygen and organic carbon. Here, the present study predicts phototrophic and heterotrophic microorganisms' radial coexistence, more particularly in the phototrophic layer. This result is consistent with the previous studies that is reported in the **chapter III**. However, the stratification of activities in the photogranules tested was not uniform. The **Figures S01-S06 supplementary materials** illustrate the different stratification of activities in the photogranules. The granule N° 1 with diameter of 3.5 mm showed a low heterotrophic activity in comparison with other photogranules which may explain the low effect of the dCOD on the anoxic microzones (black line in **Figure IV.6 A).** This suggests that within a photobioreactor, the operation conditions may cause substantially varied profiles of biological activities with distinct functions in the photogranules. An understanding of the factors controlling the stratification of the bacterial physiological and community structure in the photogranules is important to engineer bacteria ecosystems with different or specific functionalities and further to optimize their application for biological wastewater treatments.

Evaluation of the biological activities at the scale of the photogranules is essential to understand the regulation of the photosynthesis activity and to provide valuable information for monitoring an OPG based bioprocess. The modeling results showed that the photosynthesis is linearly dependent to the applied light intensity with a slope of 0.015 $nmol \cdot L^{-1} \cdot s^{-1}$ $(\mu moles_{PAR} \cdot m^{-2} \cdot s^{-1})^{-1}$ in accordance with the slope range (i.e., 0.01 to 0.02) found in the literature for microbial mats and cyanobacteria biofilm (Kühl et al., 1996; Polerecky et al., 2008) and a maximum volumetric rate of heterotrophic respiration of 0.21 $\mu mol \cdot L^{-1} \cdot s^{-1}$ was estimated. The range estimated for the volumetric rate of

respiration is comparable with the values ranging from 0.1 to 1.5 $\mu mol \cdot L^{-1} \cdot s^{-1}$ found in the literature for different types of phototrophic biofilms (Kühl et al., 1996; Ploug, 2008; Rubol et al., 2018) and ranging from 0.1 to 3.32 $\mu mol \cdot L^{-1} \cdot s^{-1}$ for aerobic granular and activated sludge (de Kreuk et al., 2005). This finding indicates that in practice, an OPGs bioprocess could be monitored and controlled in the tested light range without inducing photoinhibition and saturation. However, in prospect of the use of natural light (high light intensities up 1000 $\mu moles_{PAR} \cdot m^{-2} \cdot s^{-1}$) as energy source OPGs, the phenomena of photosaturation and photoinhibition may occur. Many studies of cyanobacterial mats and biofilm and pure cultures showed photosynthesis saturation occurs at wide range of scalar irradiances ranging from 50 to more than 1000 $\mu moles_{PAR} \cdot m^{-2} \cdot s^{-1}$ (Kirst et al., 2014; Tilzer, 1987). More studies are required to investigate the photoinhibitory effects in photogranules.

The evaluation of the net photosynthesis of the photogranule versus scalar irradiance and the organic carbon availability (**Figure IV.3** and **Figure IV.4**), allows determining the irradiance value where oxygen production counterbalanced the oxygen consumption and inward diffusion, i.e., the irradiance needed to make the photogranule self-sufficient in term of oxygen requirement for aerobic respiration, which is called compensation point *Ic*. This later was reported to be in the range of 17.5 to 60 $\mu moles_{PAR} \cdot m^{-2} \cdot s^{-1}$ for natural cyanobacterial mat or biofilm (Garcia-Pichel and Belnap, 1996; Kuhl et al., 1996; Pringault and Garcia-Pichel, 2000; Wieland and Kühl, 2000). Similarly, in this study, the compensation point of 40 $\mu moles_{PAR} \cdot m^{-2} \cdot s^{-1}$ was observed for starve carbon environment. However, higher *Ic* value of 70 $\mu moles_{PAR} \cdot m^{-2} \cdot s^{-1}$ was observed for enriched carbon environment (i.e., up to 100 $mg \cdot L^{-1}$ of dCOD), due to heterotrophs respiration enhancement. Here we determined how this value depends on oxygen concentration in bulk as well as on the photogranule diameter (**Figure IV.4**). This information can be used to manage the functioning and optimization of an OPG photobioreactor intended for wastewater treatment. In fact, the *Ic* could be an indicator even more a control parameter to determine the time point of photogranule harvest, to ensure a desirable functioning of the photobioreactor. At the photobioreactor scale, it would however be necessary to investigate the impact of agitation on the average intensity of the light received by the photogranule as it travels through the reactor using a similar approach as Andersson et al., (2019) or Gernigon et al. (2019) for phototrophic organisms cultivated in photobioreactor. The other aspect to consider is the response of photogranules to intermittent light. Such studies are conducted for suspension culture of microalgae and cyanobacteria and have shown that with

intermittent light the photoinhibition of photosynthesis has less impact than with continuous light. (Nedbal et al., 1996).

As discussed, earlier photogranules have a layered zone comprising oxic and anoxic zones from the surface to the center of the granule. Thus, photogranules present a potential for simultaneous nitrification and denitrification even the oxygen concentration in the bulk solution is high (**Figure IV.5** and **Figure IV.6**). However, it was shown that continuous illumination allows photogranule to continuously produce oxygen, which can inhibit the denitrification process. Indeed, nitrogen removal from wastewater has been successfully achieved in OPGs based bioprocess by adopting the strategy of dark-light and light-dark cycles (Abouhend et al., 2018). The latter revealed a total dissolved nitrogen removal efficiency ranging from 28 to 71 % was achieved by bioassimilation and nitrification/denitrification metabolism. However, the oxygen concentration in the bulk of the reactor was not mentioned. Here we showed that it is possible to use light intensities up to 80 $\mu moles_{PAR} \cdot m^{-2} \cdot s^{-1}$ when dCOD is high (concentration > 20 $mg \cdot L^{-1}$) and oxygen is low (concentration < 1 $mg \cdot L^{-1}$), however it would be necessary to cut off the light when dCOD decreases and oxygen increases. This would enable keeping anoxic zones in large photogranules even in famine conditions (low dCOD and high oxygen). These finding could be extrapolated to the small size of photogranules, e.g., photogranules with small size (i.e., below 2 mm) would have no anoxic zone over the course of an SBR cycle (feast to famine conditions). Therefore, no denitrification would be possible. These imply that for photogranules in SBRs with a typical radius from 0.5 to 2.0 mm usually found in full scale aerobic granular bioprocess (de Graaff et al., 2020; Pronk et al., 2015), SND would not occur.

5. Conclusion

In this chapter, gradients of oxygen find in SBR photogranules were measured for a wide range parameter: light intensity ranging from 0 to 80 PAR, dCOD ranging from 0 to 500 $mg \cdot L^{-1}$ and oxygen concentration either low (around 1 $mg \cdot L^{-1}$) or at air saturation (8.9 $mg \cdot L^{-1}$). This was done for 6 different photogranules with diameters ranging from 3.4 to 4.1 mm. The analysis of the results indicates that biomass distribution in photogranules is more diverse than what was previously expected (**chapter III**). This prevents using a single model for the prediction of photogranules performances. However, despite this diversity, conclusions can be drawn for the control of OPG based photobioreactors. Indeed, it appears possible to use high light intensities (80 PAR) during

feast periods when dCOD is high (> 20 $mg \cdot L^{-1}$) and oxygen is low (< 1 $mg \cdot L^{-1}$). This would enable high dCOD consumption rates and at the same time keeping anoxic zones in most of the photogranules to allow SND. During famine periods when dCOD is low (< 20 $mg \cdot L^{-1}$) and oxygen is high (> 1 mg/l) it would however be necessary to shut off the light to preserve anoxic zones. In that case it appears important to have large photogranules (~4 mm diameter) to preserve anoxic zone during these periods. Indeed, the small granules (diameters 3.4 and 3.5) are fully oxic when oxygen concentration in the bulk reaches air saturation.

The approach developed here coupling measurements of oxygen profiles for a small sample of photogranules with modeling could be generalized for the control of various OPG based photo-bioprocesses with different type of reactors (CSTR, SBR…), substrates and objectives (depollution, biomass production…).

6. Acknowledgments

We express our gratefulness to Philipe Sousbie for assisting in reactor operation during this research and helping in mounting the experimental set-up.

7. Funding

This work was financed through the French “Agence Nationale de la Recherche” grant ANR-16-CE04-0001-01 (“PSST: Photogranules shake sewage treatment up”) and the INRAE department MICA. An exchange between French and Nederland scientists was financed through the PHC Van Gogh program, grant 42571TG.

Chapter V

General conclusions and perspectives

1. General conclusions

A photogranule ecosystem like a laboratory-scale bioreactor harbors a wide diversity of photogranule morphologies. Photogranule morphology and size are key parameters that determine the development of oxygen, redox or pH gradients within a photogranule. They need to be captured in a future unified mathematical description of a photogranular system to obtain a predictive tool of the full-system activity of a photogranule bioreactor.

Data to calibrate such a model are currently difficult to obtain, as we do not possess one common toolset that allows us to analyze the spatially resolved syntrophic activity in photogranules ranging from filamentous, ill-defined, and soft to sharply defined, smooth and rigid photogranules, with all their intermediate morphologies. Here, I introduced the use of optodes **(Chapter II)** and was able to describe the spatio-temporal distribution of oxygen concentration and afterward mapping the biological activities of a filamentous photogranule via a two-dimensional model. Several messages can be highlighted by the results presented throughout this thesis (**Chapter II**):

- The planar optode allowed to visualize in 2D the oxygen gradients at the sub-micrometric scale without intruding into the heterogeneous sample. This technology is commercially available and is practically easy to apply in the laboratory. However, it should be employed with caution, given that it is limited to the characterization of the surface in contact but not deep in the denser regions even. Moreover, large record time and light bleaching limited also its application. Nonetheless, the methods and approach described proved useful for measuring oxygen distribution. Other types of optodes could be used for complementary investigations such as measurements of pH and CO_2 dynamics during static photogranulation.
- The simple modeling approach using two trophic groups and reaction-diffusion equations allowed explaining the experimental results at the micro-scale. This model was able to show that light penetration into the photogranule was the factor controlling photogranule activities and that the spatial distribution of heterotrophs and phototrophs had less impact. Furthermore, the model revealed that the photosynthetic response of filaments to light was detectable within seconds. This indicates that the photogranule's biological activity is in a non-stationary state when it flows between dark and light zones in a bioreactor. It is then essential to emphasize the need to analyze dynamics of light exposure of individual photogranules and its impact on their growth in photobioreactors.

At the same time, using classic microelectrodes, I performed direct measurement and characterization of oxygen and light micro-scale environment within oxygenic photogranules **(Chapter III & Chapter IV).** With optodes, the denser regions of a photogranule were not accessible, but microelectrodes gave access to intra-photogranule oxygen gradients. findings have been outlined from this study **(Chapter III & Chapter IV):**

- It was shown that light penetrates up to 700 µm. The extinction of light below the photogranule surface is a common feature in cyanobacterial biofilms (Al-Najjar et al., 2014). It appears here to be a key factor in the stratification of the photogranules, i.e., it determines the thickness of the phototrophic layer.
- The net photosynthesis rate of the photogranules appears to increase linearly with the light intensity at the range of 0-150 $\mu moles_{PAR} \cdot m^{-2} \cdot s^{-1}$.
- The modeling approach allowed to investigate the spatial distribution of biological activities in photogranules. It predicted the co-localization of phototrophic and heterotrophic activities and clear differences in oxygenic photosynthesis and respiration rates between different runs and different systems (e.g., CSTR and SBR).
- Steep concentration gradients of oxygen were found in the photogranules. Depending on the conditions, anoxic microzones were identified. Their formation was dependent on light intensity, on available organic carbon, on dissolved oxygen in the bulk and on the size of the photogranules. As the anoxic conditions are crucial for the establishment of simultaneous nitrification and denitrification, controlling such redox stratification in the photogranules appears essential. Here I introduced a strategy for the control of anoxic zones based on light intensity regulation using nomograms predicted by the model. Furthermore, anoxic biovolumes were also shown to depend on the diameter of the photogranule. Developing strategies based on the selection of a narrow range of photogranules size may sound feasible (e.g., cyclone reactors or reactor with sieve stage). However, this may disturb the photogranulation cycle and adds operational constraints.
- Regulating the incident light intensity may be a simple and efficient approach to optimize the oxygen microzones (i.e., oxic/anoxic zone) and the oxygen supply to the surrounding environment. However, in order to apply these results in photobioreactors, the real light received by a photogranule over time needs to be evaluated. In that case, the interrelationships between the optical path in the photobioreactor and the biological activities of the photogranules need to

be considered. Furthermore, ensuring the availability of light in deeper region within the photobioreactor is necessary for their application to be economically feasible.

Differences and shared properties have thus been delineated between photogranule morphologies. In both cases the phototrophic and heterotrophic activities appeared co-localized. However, when comparing oxygen diffusion fluxes, filamentous photogranule may behave different than the smooth granules. Due to large contact surface contact with the bulk, filamentous photogranules showed higher mass transfer than the smooth photogranules.

Here, I developed a methodological foundation and established a benchmark for directly measuring photosynthetic parameters in photogranules. This extends our fundamental knowledge of the biology of photogranules and brings new elements for the design and control of efficient, OPG-based bioprocesses. My results also highlight several important perspectives for the development of this biotechnology such as considering the effects of mixing and the movement of photogranules in the photobioreactor, investigating pH and nitrogen microenvironment and deciphering the mechanisms explaining the spatial structuration of photogranules. These perspectives are developed in more details in the following section.

2. Perspectives

Three areas of research seem to me most important to advance:

- Illumination conditions and how they affect photogranule activities
- Physico-chemical characterization of the photogranule environment
- The development of the spatial structure of photogranules

On the next pages, I provide more details on how to pursue these areas of research.

2.1. Relating illumination conditions occurring in a photobioreactor to photogranule activity

A major cost of operating an OPG bioprocess may be illumination, if artificial light is used. Optimizing the illumination may be an important contribution to decrease the operational costs and the environmental impact of an OPG-based bioprocess. Optimized light energy usage by phototrophs may be achieved using tailored emission spectra of artificial light sources. Another strategy could be the use of intermittent lighting instead of continuous illumination (Abu-Ghosh et al., 2015; Schulze et al., 2017).

Photogranules may already be exposed to intermittent illumination as a population of submerged OPGs in a bioreactor does not at all instances receive the same illumination. OPGs are moving between the center of the reactor towards the reactor walls, where in our laboratory setting, they receive most light. We do not know how the fluctuating illumination conditions on the trajectory of a photogranule through the reactor environment influence photogranule activity. I consider it crucial to investigate experimentally and in a mathematical model the effect of these short-term fluctuations of light.

This study may be realized in-situ by measuring the light gradient inside the photobioreactor using a light sensor at different oxygenic photogranule concentrations and different mixing rates (**Figure V.1**). An in-silico study could also be combined to the experimental studies. Modeling the motion of photogranules in light fields measured experimentally will allow determining the amount of light that a single photogranule receives during its trajectory in the fluid system while including variety of forces such as gravity and drag forces. In fact, the in-silico study is important since the light measured by the experimental approach is intensity in the bulk which is not the real intensity received by the photogranules. Modeling the hydrodynamics combined with particle tracking and

light attenuation in the reactor will provide indications on the frequency at which a single photogranule will encounter a certain light intensity depending on mixing conditions.

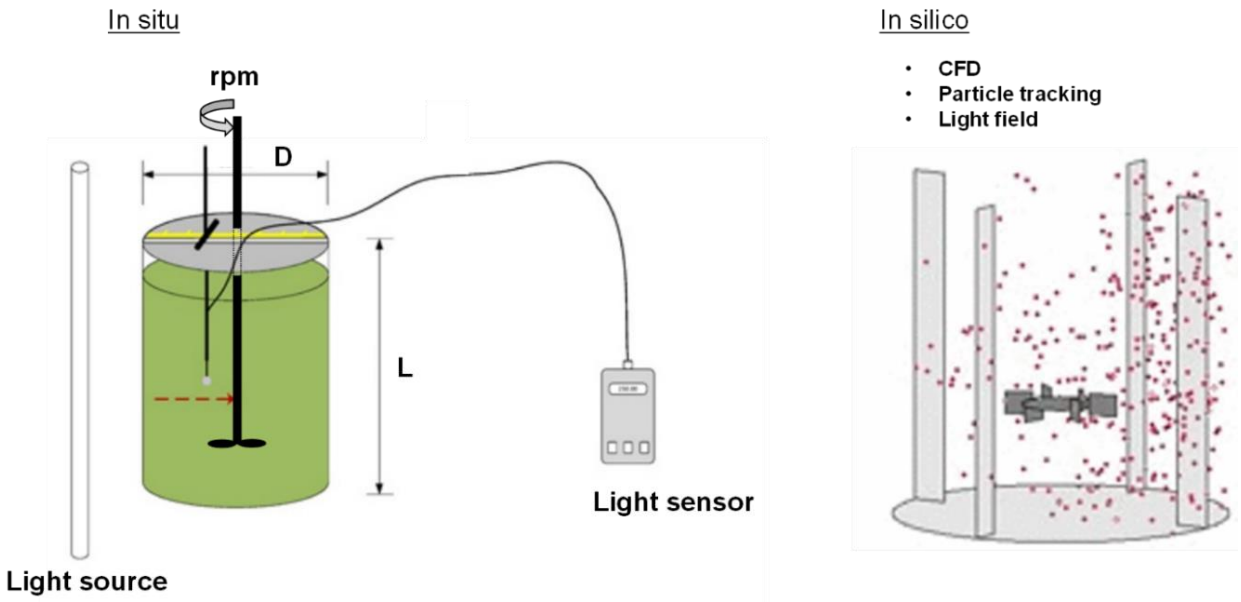

Figure V.1 *Proposed strategy for light investigation inside an OPGs photobioreactor (illustration adapted from Naderi et al, (2017) and www.comsol.com).*

I suggest studying the effect of flashing light on the photosynthetic activity of single photogranules. The suggested range of flashing light /dark frequencies were: 0.1-10 kHz and intensity of 10, 40, 80, 100 and 150 $\mu moles_{PAR} \cdot m^{-2} \cdot s^{-1}$ respectively.

The performances of photogranules could then, be compared to performances of photogranules under continuous illumination (**Figure V.2**). The finding of this study may help determining the response of the photogranules activities over time. It can also facilitate the formulation of hypotheses when modeling the performances of an OPG-based bioreactor. The study could be also extended to the process level and evaluate the effect of intermittent light on the nutrient removal. It may then be possible to derive an optimized illumination protocol for bioreactor operation in terms of mixing and illumination at the reactor surface.

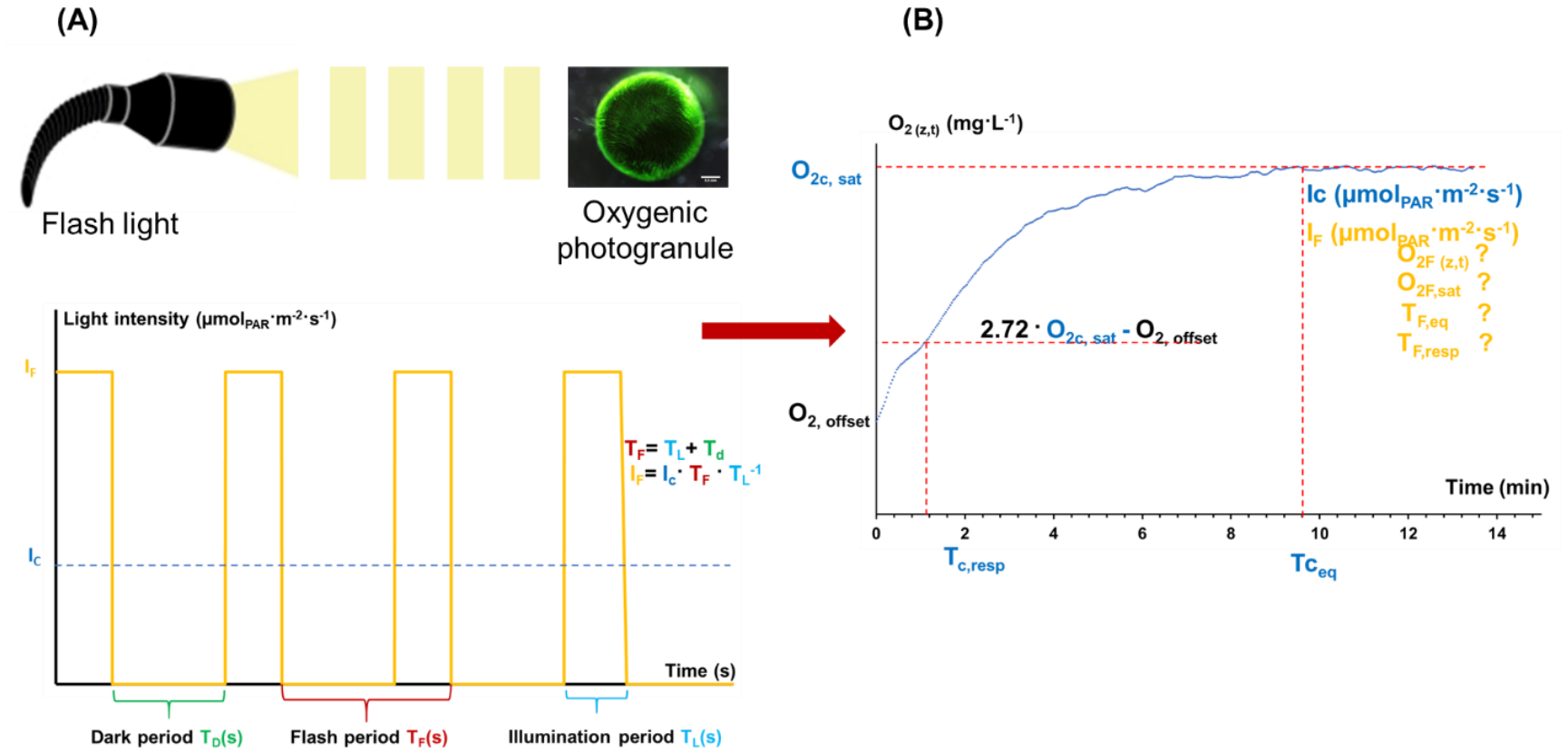

Figure V.2 *Simplified scheme of flash and continuous light experimental investigation on the oxygenic photogranules. (A) A suggested experimental methods and materials for flash light investigation. (B) Oxygen concentration dynamics to continuous light and potential extracted parameters (Data measured during the collaboration and the supervision of student in the frame work of the scientific cooperation France-Mexico ECOS)*

2.2. More detailed physico-chemical characterization inside a photogranules: pH, redox, nitrogen and light

Cyanobacteria can survive in wide range of pH conditions (Stal, 1995). Slight alkaline condition favors the growth of cyanobacteria. The relation between environmental pH levels and cyanobacterial growth has been broadly studied, but little is known regarding the pH microenvironment within photogranules. The pH is linked to the speciation of the dissolved inorganic carbon (CO_2(aq), HCO_3^-, CO_3^{2-}). The dissolved inorganic carbon is the key element for the phototrophic growth. Thus, determining the pH variations inside the photogranules will give insight on pH regulation in photogranules and its relation with the external pH. Furthermore, the information on the pH inside the photogranules will help understanding the precipitation of calcite in the inner core reported by (Milferstedt et al., 2017a) or any other chemical component precipitation such as struvite for phosphorus recovery by algal biofilm (Hillman and Sims, 2020).

Phototrophic biofilms are characterized by steep gradient of redox because of strong gradients of both electrons acceptors and donors (Roeselers et al., 2008) and in this work I showed that steep oxygen gradients are also found in photogranules. In the activated sludge systems, monitoring redox allows to determine whether biological reactions are occurring and whether any processes changes are required to improve the efficiency of those reactions. For instance, the nitrification process is performed by nitrifying bacteria when the redox value is in the region of +100 to +350 mV. In this condition the process is turning ammonia (NH_3) into nitrate (NO^{3-}). The denitrification process reduces nitrate (NO_3^-) to nitrogen (N_2). The denitrifying bacteria require the wastewater to have a redox potential in the range -50 to +50 mV. In fact, during the operation of an OPG-based bioprocess, we only have access to the macro scale information (i.e., the bulk). However, this information does not represent completely the micro-scale environment. It is then recommended to investigate the redox microenvironment and relate it to the macroenvironment information.

Understanding biochemistry of the nitrogen conversions within the photogranules requires microscale measurements of nitrogen-containing compounds. The interactions of these conversions have been successfully studied using microsensors for NO_3^-, NO_2^-, and N_2O in stratified microbial communities, such as biofilms, aggregates, and sediments. Such study on photogranules will enable valuable knowledge on structure and nitrifying activity along with regulation effects of oxygen and ammonium.

2.3. Development of spatial structures

Understanding the formation of spatialized biological aggregates (e.g., microbial biofilms, granules, and flocs) has been a big challenge in the past decades. Numerous combinations of mechanical, physiochemical, and biological forces are involved at different time scales. Deciphering the mechanisms of the spatial arrangements will eventually provide insights how the photogranulation phenomenon occurs. This will require considering the specificities of the photogranule populations, i.e., the filamentous nature of cyanobacteria and the difference in cell size (**Figure V.3)**.

Individual-based models (IbMs) might be used to decipher photogranulation mechanisms. In these models, functional groups are represented as a collection of individuals and mass transfer/reaction are solved in a continuum approach (Alpkvist et al., 2006; Batstone et al., 2006; Storck et al., 2014). They are bottom-up models which allow studying behaviors of an ecosystem via investigating the interactions among autonomous individuals with each other and their abiotic environment (DeAngelis and Grimm, 2014). In addition, they allow also studying how the characteristics of microorganisms (e.g., motility, elasticity, cells shape) may generate spatially complex structures (e.g., filamentous photogranules).

As a long-term perspective, I recommend developing an individual based model to decipher the mechanism of photogranulation. The model needs to combine and study the role of the following (i) the phototropism of cyanobacteria which allows them to position themselves in the optimal condition of light for their survival, (ii) the biogeochemical and physical environment in order to elucidate if colocalization of syntrophic interactions can be justified by nutrients exchange only, or whether other mechanisms, such as quorum sensing or toxin release need to be considered, (iii) the mechanical interactions in order to investigate how the different morphologies of cells (filamentous, sphere, rod), as well the mechanical properties such as (elasticity, collisions, etc.) are involved in specific shapes of the photogranules.

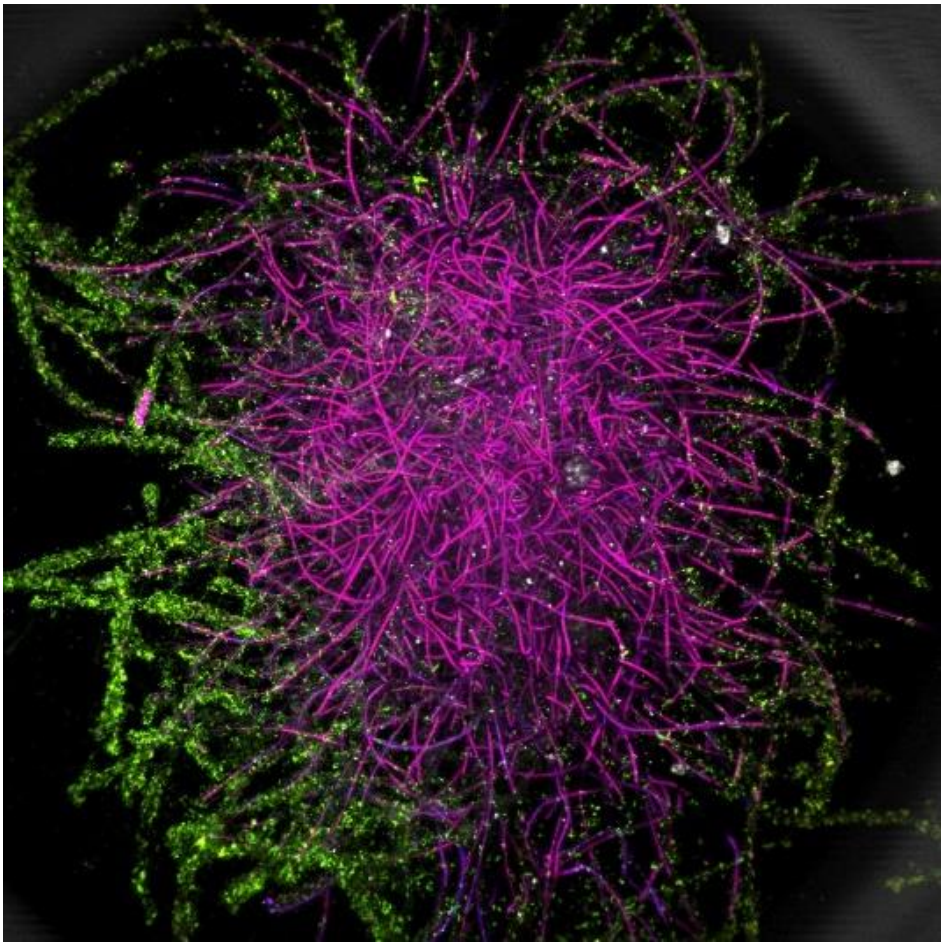

Figure V.3 *A Confocal Laser Scanning Microscopy image with maximum projection of portion extracted from the phototrophic layer of an oxygenic photogranule. Magenta: filamentous cyanobacteria, green: bacteria (Copyright: Thomas Neu, image taken during the 13th advanced biofilm course, 2018, UFZ Magdeburg).*

References

Abed, R.M.M., 2010. Interaction between cyanobacteria and aerobic heterotrophic bacteria in the degradation of hydrocarbons. Int. Biodeterior. Biodegrad. 64, 58–64. https://doi.org/10.1016/j.ibiod.2009.10.008

Abouhend, A.S., McNair, A., Kuo-Dahab, W.C., Watt, C., Butler, C.S., Milferstedt, K., Hamelin, J., Seo, J., Gikonyo, G.J., El-Moselhy, K.M., Park, C., 2018. The oxygenic photogranule process for aeration-free wastewater treatment. Environ. Sci. Technol. 52, 3503–3511. https://doi.org/10.1021/acs.est.8b00403

Abouhend, A.S., Milferstedt, K., Hamelin, J., Ansari, A.A., Butler, C., Carbajal-González, B.I., Park, C., 2020. Growth progression of oxygenic photogranules and its impact on bioactivity for aeration-free wastewater treatment. Environ. Sci. Technol. 54, 486–496. https://doi.org/10.1021/acs.est.9b04745

Adler, A.S., Reynaert, E., Layer, M., Derlon, N., Morgenroth, E., Holliger, C., 2017. Influence of wastewater composition on microbial communities of Aerobic granules and their nutrient removal performances, in: Biofilms 2017 Conference Office,. Epfl scientific publications, Dublin, Ireland. https://doi.org/https://infoscience.epfl.ch/record/229315?ln=en

Ahmad, J.S.M., Cai, W., Zhao, Z., Zhang, Z., Shimizu, K., Lei, Z., Lee, D.-J.J., 2017. Stability of algal-bacterial granules in continuous-flow reactors to treat varying strength domestic wastewater. Bioresour. Technol. 244, 225–233. https://doi.org/https://doi.org/10.1016/j.biortech.2017.07.134

Al-Najjar, M.A.A., de Beer, D., Kühl, M., Polerecky, L., 2012. Light utilization efficiency in photosynthetic microbial mats. Environ. Microbiol. 14, 982–992. https://doi.org/10.1111/j.1462-2920.2011.02676.x

Al-Najjar, M.A.A., Ramette, A., Kühl, M., Hamza, W., Klatt, J.M., Polerecky, L., 2014. Spatial patterns and links between microbial community composition and function in cyanobacterial mats. Front. Microbiol. 5, 406. https://doi.org/10.3389/fmicb.2014.00406

Albertano, P., 2012. Cyanobacterial biofilms in monuments and caves, in: Whitton, B.A. (Ed.), Ecology of Cyanobacteria II. Springer Netherlands, Dordrecht, pp. 317–343.

https://doi.org/10.1007/978-94-007-3855-3_11

Ali, M., Wang, Z., Salam, K.W., Hari, A.R., Pronk, M., Van Loosdrecht, M.C.M., Saikaly, P.E., 2019. Importance of species Sorting and immigration on the bacterial assembly of different-sized aggregates in a full-scale aerobic granular sludge plant. Environ. Sci. Technol. 53, 8291–8301. https://doi.org/10.1021/acs.est.8b07303

Alpkvist, E., Klapper, I., 2007. A multidimensional multispecies continuum model for heterogeneous biofilm development. Bull. Math. Biol. 69, 765–789. https://doi.org/10.1007/s11538-006-9168-7

Alpkvist, E., Picioreanu, C., Van Loosdrecht, M.C.M., Heyden, A., 2006. Three-dimensional biofilm model with individual cells and continuum EPS matrix. Biotechnol. Bioeng. 94, 961–979. https://doi.org/10.1002/bit.20917

Andersson, B., Shen, C., Cantrell, M., Dandy, D.S., Peers, G., 2019. The fluctuating cell-specific light environment and its effects on cyanobacterial physiology. Plant Physiol. 181, 547–564. https://doi.org/10.1104/pp.19.00480

Ansari, A.A., Abouhend, A.S., Park, C., 2019. Effects of seeding density on photogranulation and the start-up of the oxygenic photogranule process for aeration-free wastewater treatment. Algal Res. 40, 101495. https://doi.org/10.1016/j.algal.2019.101495

Anwar, H., Strap, J.L., Costerton, J.W., 1992. Establishment of aging biofilms: possible mechanism of bacterial resistance to antimicrobial therapy. Antimicrob. Agents Chemother. 36, 1347–1351. https://doi.org/10.1128/AAC.36.7.1347

Aqeel, H., Weissbrodt, D.G., Cerruti, M., Wolfaardt, G.M., Wilén, B.-M., Liss, S.N., 2019. Drivers of bioaggregation from flocs to biofilms and granular sludge. Environ. Sci. Water Res. Technol. 5, 2072–2089. https://doi.org/10.1039/C9EW00450E

Arajo, F.O. de Q., de Medeiros, J. L., Maria, R., 2014. CO2 utilization: a process systems engineering vision, in: Medeiros, José Luiz de (Ed.), CO2 Sequestration and Valorization. InTech, Rijeka, p. Ch. 2. https://doi.org/10.5772/57560

Arcila, J.S., Buitrón, G., 2017. Influence of solar irradiance levels on the formation of microalgae-bacteria aggregates for municipal wastewater treatment. Algal Res. 27, 190–197.

https://doi.org/10.1016/j.algal.2017.09.011

Arcila, J.S., Buitrón, G., 2016. Microalgae–bacteria aggregates: effect of the hydraulic retention time on the municipal wastewater treatment, biomass settleability and methane potential. J. Chem. Technol. Biotechnol. 91, 2862–2870. https://doi.org/10.1002/jctb.4901

Babauta, J.T., Atci, E., Ha, P.T., Lindemann, S.R., Ewing, T., Call, D.R., Fredrickson, J.K., Beyenal, H., 2014. Localized electron transfer rates and microelectrode-based enrichment of microbial communities within a phototrophic microbial mat. Front. Microbiol. 5, 1–12. https://doi.org/10.3389/fmicb.2014.00011

Batstone, D.J., Keller, J., 2001. Variation of bulk properties of anaerobic granules with wastewater type. Water Res. 35, 1723–1729. https://doi.org/https://doi.org/10.1016/S0043-1354(00)00446-2

Batstone, D.J., Keller, J., Angelidaki, I., Kalyuzhnyi, S. V, Pavlostathis, S.G., Rozzi, A., Sanders, W.T.M., Siegrist, H., Vavilin, V.A., 2002. The IWA Anaerobic Digestion Model No 1 (ADM1). Water Sci. Technol. 45, 65–73. https://doi.org/0273-1223 (Print)

Batstone, D.J., Picioreanu, C., Van Loosdrecht, M.C.M., 2006. Multidimensional modelling to investigate interspecies hydrogen transfer in anaerobic biofilms. Water Res. 40, 3099–3108. https://doi.org/https://doi.org/10.1016/j.watres.2006.06.014

Béchet, Q., Shilton, A., Guieysse, B., 2013. Modeling the effects of light and temperature on algae growth : State of the art and critical assessment for productivity prediction during outdoor cultivation. Biotechnol. Adv. 31, 1648–1663. https://doi.org/10.1016/j.biotechadv.2013.08.014

Besemer, K., 2015. Biodiversity, community structure and function of biofilms in stream ecosystems. Res. Microbiol. 166, 774–781. https://doi.org/https://doi.org/10.1016/j.resmic.2015.05.006

Bharti, A., Velmourougane, K., Prasanna, R., 2017. Phototrophic biofilms: diversity, ecology and applications. J. Appl. Phycol. 29, 2729–2744. https://doi.org/10.1007/s10811-017-1172-9

Bishop, P.L., Rittmann, B.B., 1995. Modelling heterogeneity in biofilms: Report of the discussion session. Water Sci. Technol. 32, 263–265. https://doi.org/10.1016/0273-

1223(96)00035-2

Blanken, W., Magalhães, A., Sebestyén, P., Rinzema, A., Wijffels, R.H., Janssen, M., 2017a. Microalgal biofilm growth under day-night cycles. Algal Res. 21, 16–26. https://doi.org/10.1016/j.algal.2016.11.006

Blanken, W., Schaap, S., Theobald, S., Rinzema, A., Wijffels, R.H., Janssen, M., 2017b. Optimizing carbon dioxide utilization for microalgae biofilm cultivation. Biotechnol. Bioeng. 114, 769–776. https://doi.org/10.1002/bit.26199

Boedeker, C., Immers, A., 2009. No more lake balls (*Aegagropila linnaei* Kützing, Cladophorophyceae, Chlorophyta) in The Netherlands? Aquat. Ecol. 43, 891–902. https://doi.org/10.1007/s10452-009-9231-1

Boltz, J.P., Morgenroth, E., Brockmann, D., Bott, C., Jamie Gellner, W., Vanrolleghem, P.A., 2010a. Critical components of Biofilm models for engineering practice. Proc. Water Environ. Fed. 2010, 1072–1098. https://doi.org/10.2175/193864710798158698

Boltz, J.P., Morgenroth, E., Sen, D., 2010b. Mathematical modelling of biofilms and biofilm reactors for engineering design. Water Sci. Technol. 62, 1821–1836. https://doi.org/10.2166/wst.2010.076

Brehm, U., Krumbein, W.E., Palińska, K. a, 2003. Microbial spheres: a novel cyanobacterial–diatom symbiosis. Naturwissenschaften 90, 136–140. https://doi.org/10.1007/s00114-003-0403-x

Brockmann, D., Gérand, Y., Park, C., Milferstedt, K., Hélias, A., Hamelin, J., 2021. Wastewater treatment using oxygenic photogranule-based process has lower environmental impact than conventional activated sludge process. Bioresour. Technol. 319, 124204. https://doi.org/https://doi.org/10.1016/j.biortech.2020.124204

Bryers, J.D., Drummond, F., 1998. Local macromolecule diffusion coefficients in structurally non-uniform bacterial biofilms using fluorescence recovery after photobleaching (FRAP). Biotechnol. Bioeng. 60, 462–473. https://doi.org/10.1002/(SICI)1097-0290(19981120)60:4<462::AID-BIT8>3.0.CO;2-K

Caldwell, D.E., Korber, D.R., Lawrence, J.R., 1993. Analysis of biofilm formation using 2D vs

3D digital imaging. J. Appl. Bacteriol. 74, 52S-66S. https://doi.org/10.1111/j.1365-2672.1993.tb04342.x

Canales, A., Pareilleux, A., Rols, J.L., Goma, G., Huyard, A., 1994. Decreased sludge production strategy for domestic wastewater treatment. Water Sci. Technol. 30, 97–106. https://doi.org/10.2166/wst.1994.0390

Capodaglio, A., Olsson, G., 2019. Energy issues in sustainable urban wastewater management: use, demand reduction and recovery in the urban water cycle. Sustainability 12, 266. https://doi.org/10.3390/su12010266

Capone, D.G., 1997. Trichodesmium, a globally significant marine cyanobacterium. Science. 276, 1221–1229. https://doi.org/10.1126/science.276.5316.1221

Castenholz, R.W., 1967. Aggregation in a thermophilic *Oscillatoria* . Nature 215, 1285–1286. https://doi.org/10.1038/2151285a0

Celler, K., Hödl, I., Simone, A., Battin, T.J., Picioreanu, C., 2014. A mass-spring model unveils the morphogenesis of phototrophic Diatoma biofilms. Sci. Rep. 4, 3649. https://doi.org/10.1038/srep03649

Chaturvedi, P., Taguchi, M., Burrs, S.L., Hauser, B.A., Salim, W.W.A.W., Claussen, J.C., McLamore, E.S., 2013. Emerging technologies for non-invasive quantification of physiological oxygen transport in plants. Planta 238, 599–614. https://doi.org/10.1007/s00425-013-1926-9

Checcucci, G., Sgarbossa, A., Lenci, F., 2003. Photomovements of microorganisms: An introduction, in: CRC Handbook of: Organic Photochemistry and Photobiology, Second Edition. pp. 120–121.

Chen, W., Chen, S., Wu, J., 2020. Biomass segregation in the granules and flocs affects the role of heterotrophic bacteria in the ANAMMOX process. Chem. Eng. J. 392, 123727. https://doi.org/10.1016/j.cej.2019.123727

Chiu, Z.C., Chen, M.Y., Lee, D.J., Wang, C.H., Lai, J.Y., 2007. Oxygen diffusion in active layer of aerobic granule with step change in surrounding oxygen levels. Water Res. 41, 884–892. https://doi.org/10.1016/j.watres.2006.11.035

Cieślik, B.M., Namieśnik, J., Konieczka, P., 2015. Review of sewage sludge management: standards, regulations and analytical methods. J. Clean. Prod. 90, 1–15. https://doi.org/https://doi.org/10.1016/j.jclepro.2014.11.031

Clarelli, F., Di Russo, C., Natalini, R., Ribot, M., 2013. A fluid dynamics model of the growth of phototrophic biofilms. J. Math. Biol. 66, 1387–1408. https://doi.org/10.1007/s00285-012-0538-5

Clarelli, F., Russo, C. Di, Natalini, R., Ribot, M., 2016. A fluid dynamics multidimensional model of biofilm growth: Stability, influence of environment and sensitivity. Math. Med. Biol. 33, 371–395. https://doi.org/10.1093/imammb/dqv024

Cole, J.K., Hutchison, J.R., Renslow, R.S., Kim, Y.M., Chrisler, W.B., Engelmann, H.E., Dohnalkova, A.C., Hu, D., Metz, T.O., Fredrickson, J.K., Lindemann, S.R., 2014. Phototrophic biofilm assembly in microbial-mat-derived unicyanobacterial consortia: Model systems for the study of autotroph-heterotroph interactions. Front. Microbiol. 5, 1–18. https://doi.org/10.3389/fmicb.2014.00109

Cook, J., Edwards, A., Takeuchi, N., Irvine-Fynn, T., 2016. Cryoconite: The dark biological secret of the cryosphere. Prog. Phys. Geogr. 40, 66–111. https://doi.org/10.1177/0309133315616574

Cordero, O.X., Datta, M.S., 2016. Microbial interactions and community assembly at microscales. Curr. Opin. Microbiol. 31, 227–234. https://doi.org/https://doi.org/10.1016/j.mib.2016.03.015

Costerton, J.W., Lewandowski, Z., de Beer, D., Caldwell, D., Korber, D., James, G., 1994. Biofilms, the customized microniche. J. Bacteriol. 176, 2137–2142. https://doi.org/10.1128/JB.176.8.2137-2142.1994

Cuevas-Castillo, G.A., Navarro-Pineda, F.S., Baz Rodríguez, S.A., Sacramento Rivero, J.C., 2020. Advances on the processing of microalgal biomass for energy-driven biorefineries. Renew. Sustain. Energy Rev. 125, 109606. https://doi.org/10.1016/j.rser.2019.109606

Cuny, L., Pfaff, D., Luther, J., Ranzinger, F., Ödman, P., Gescher, J., Guthausen, G., Horn, H., Hille-Reichel, A., 2019. Evaluation of productive biofilms for continuous lactic acid

production. Biotechnol. Bioeng. 116, 2687–2697. https://doi.org/10.1002/bit.27080

D'Acunto, B., Frunzo, L., Klapper, I., Mattei, M.R., Stoodley, P., 2019a. Mathematical modeling of dispersal phenomenon in biofilms. Math. Biosci. 307, 70–87. https://doi.org/10.1016/j.mbs.2018.07.009

D'Acunto, B., Frunzo, L., Luongo, V., Mattei, M.R., 2019b. Mathematical modeling of biofilms, in: Introduction to Biofilm Engineering, ACS Symposium Series. American Chemical Society, pp. 245–273. https://doi.org/10.1021/bk-2019-1323.ch012

D'Acunto, B., Frunzo, L., Luongo, V., Mattei, M.R., 2018. Invasion moving boundary problem for a biofilm reactor model. Eur. J. Appl. Math. 29, 1079–1109. https://doi.org/10.1017/S0956792518000165

Damgaard, L.R., Revsbech, N.P., 1997. A microscale biosensor for methane containing methanotrophic bacteria and an internal oxygen reservoir. Anal. Chem. 69, 2262–2267. https://doi.org/10.1021/ac9611576

Datta, M.S., Sliwerska, E., Gore, J., Polz, M.F., Cordero, O.X., 2016. Microbial interactions lead to rapid micro-scale successions on model marine particles. Nat. Commun. 7. https://doi.org/10.1038/ncomms11965

Davit, Y., Byrne, H., Osborne, J., Pitt-Francis, J., Gavaghan, D., Quintard, M., 2013. Hydrodynamic dispersion within porous biofilms. Phys. Rev. E 87, 12718. https://doi.org/10.1103/PhysRevE.87.012718

de Beer, D., 2011. Microsensors for sediments, microbial Mats, and biofilms, in: Reitner, J., Thiel, V. (Eds.), . Springer Netherlands, Dordrecht, pp. 658–662. https://doi.org/10.1007/978-1-4020-9212-1_149

de Beer, D., Kühl, M., 2000. Interfacial microbial mats and biofilms, in: The Benthic Boundary Layer. Oxford university press, New York, pp. 374–394. https://doi.org/http://bioold.science.ku.dk/mkuhl/pages/PDF/DeBeer&Kuhl2000.pdf

de Beer, D., Schramm, A., 1999. Micro-environments and mass transfer phenomena in biofilms studied with microsensors. Water Sci. Technol. 39, 173–178. https://doi.org/10.1016/S0273-1223(99)00165-1

de Beer, D., Stoodley, P., 2006. Microbial Biofilms, in: Dworkin, M., Falkow, S., Rosenberg, E., Schleifer, K.-H., Stackebrandt, E. (Eds.), The Prokaryotes. Springer New York, New York, NY, pp. 904–937. https://doi.org/10.1007/0-387-30741-9_28

de Beer, D., Stoodley, P., 1995. Relation between the structure of an aerobic biofilm and transport phenomena. Water Sci. Technol. 32, 11–18. https://doi.org/10.1016/0273-1223(96)00002-9

de Beer, D., Stoodley, P., Lewandowski, Z., 1994. Liquid flow in heterogeneous biofilms. Biotechnol. Bioeng. 44, 636–641. https://doi.org/10.1002/bit.260440510

de Graaff, D.R., van Dijk, E.J.H., Van Loosdrecht, M.C.M., Pronk, M., 2020. Strength characterization of full-scale aerobic granular sludge. Environ. Technol. 41, 1637–1647. https://doi.org/10.1080/09593330.2018.1543357

de Kreuk, M.K., Heijnen, J.J., Van Loosdrecht, M.C.M., 2005. Simultaneous COD, nitrogen, and phosphate removal by aerobic granular sludge. Biotechnol. Bioeng. 90, 761–769. https://doi.org/10.1002/bit.20470

de Kreuk, M.K., Van Loosdrecht, M.C.M., 2004. Selection of slow growing organisms as a means for improving aerobic granular sludge stability. Water Sci. Technol. 49, 9–17. https://doi.org/10.2166/wst.2004.0792

de Wit, R., Ende, F.P. Van Den, Gemerden, H. Van, 1995. Mathematical simulation of the interactions among cyanobacteria , purple sulfur bacteria and chemotrophic sulfur bacteria in microbial mat communities 17.

DeAngelis, D.L., Grimm, V., 2014. Individual-based models in ecology after four decades. F1000Prime Rep. 6, 39. https://doi.org/10.12703/P6-39

Decho, A.W., Gutierrez, T., 2017. Microbial Extracellular Polymeric Substances (EPSs) in ocean systems. Front. Microbiol. 8, 922. https://doi.org/10.3389/fmicb.2017.00922

Di Iaconi, C., Ramadori, R., Lopez, A., Passino, R., 2005. Hydraulic shear stress calculation in a sequencing batch biofilm reactor with granular biomass. Environ. Sci. Technol. 39, 889–894. https://doi.org/10.1021/es0400483

Di Pippo, F., Ellwood, N.T.W., Gismondi, A., Bruno, L., Rossi, F., Magni, P., de Philippis, R., 2013. Characterization of exopolysaccharides produced by seven biofilm-forming cyanobacterial strains for biotechnological applications. J. Appl. Phycol. 25, 1697–1708. https://doi.org/10.1007/s10811-013-0028-1

Dusenbery, D.B., 2011. Living at micro scale : the unexpected physics of being small. Harvard University Press, Cambridge, Mass.

Dzianach, P.A., Dykes, G.A., Strachan, N.J.C., Forbes, K.J., Pérez-Reche, F.J., 2019. Challenges of biofilm control and utilization: lessons from mathematical modelling. J. R. Soc. Interface 16, 20190042. https://doi.org/10.1098/rsif.2019.0042

Eberl, H.J., Picioreanu, C., Heijnen, J.J., Van Loosdrecht, M.C.M., 2000. A three-dimensional numerical study on the correlation of spatial structure, hydrodynamic conditions, and mass transfer and conversion in biofilms. Chem. Eng. Sci. 55, 6209–6222. https://doi.org/https://doi.org/10.1016/S0009-2509(00)00169-X

Eberl, H.J., Wade, M.J., 2020. Chapter 16 - Challenges and perspectives in reactor scale modeling of biofilm processes, in: Simoes, M., Borges, A., Chaves Simoes, L.B.T.-R.T. in B.S. and T. (Eds.), Academic Press, pp. 359–383. https://doi.org/https://doi.org/10.1016/B978-0-12-819497-3.00016-7

Ebert, A., Brune, A., 1997. Hydrogen concentration profiles at the oxic-anoxic interface: a microsensor study of the hindgut of the wood-feeding lower Termite *Reticulitermes flavipes* (Kollar). Appl. Environ. Microbiol. 63, 4039–4046. https://doi.org/10.1128/AEM.63.10.4039-4046.1997

Elalami, D., Carrère, H., Monlau, F., Abdelouahdi, K., Oukarroum, A., Barakat, A., 2019. Pretreatment and co-digestion of wastewater sludge for biogas production: Recent research advances and trends. Renew. Sustain. Energy Rev. 114, 109287. https://doi.org/https://doi.org/10.1016/j.rser.2019.109287

Faizi, M., Steuer, R., 2019. Optimal proteome allocation strategies for phototrophic growth in a light limited chemostat. Microb. Cell Fact. 1–18. https://doi.org/10.1186/s12934-019-1209-7

Fang, F., Yang, L., Gan, L., Guo, L., Hu, Z., Yuan, S., Chen, Q., Jiang, L., 2014. DO, pH, and Eh

microprofiles in cyanobacterial granules from Lake Taihu under different environmental conditions. J. Appl. Phycol. 26, 1689–1699. https://doi.org/10.1007/s10811-013-0211-4

Fernández, F.G.A., Camacho, F.G., Pérez, J.A.S., Sevilla, J.M.F., Grima, E.M., 1997. A model for light distribution and average solar irradiance inside outdoor tubular photobioreactors for the microalgal mass culture. Biotechnol. Bioeng. 55, 701–714. https://doi.org/10.1002/(SICI)1097-0290(19970905)55:5<701::AID-BIT1>3.0.CO;2-F

Flemming, H.-C., Neu, T.R., Wozniak, D.J., 2007. The EPS Matrix: The "house of biofilm cells." J. Bacteriol. 189, 7945 LP – 7947. https://doi.org/10.1128/JB.00858-07

Flemming, H.-C., Wingender, J., 2010. The biofilm matrix. Nat. Rev. Microbiol. 8, 623–633. https://doi.org/10.1038/nrmicro2415

Flora, J.R. V, Suidan, M.T., Biswas, P., Sayles, G.D., 1995. Modeling algal biofilms: role of carbon, light, cell surface charge, and ionic species. Water Environ. Res. 67, 87–94. https://doi.org/https://www.jstor.org/stable/25044521?seq=1

Frank, H.A., Cogdell, R.J., 2012. Light capture in photosynthesis, in: Egelman, E.H.B.T.-C.B. (Ed.), Comprehensive Biophysics. Elsevier, Amsterdam, pp. 94–114. https://doi.org/10.1016/B978-0-12-374920-8.00808-0

Garcia-Pichel, F., Belnap, J., 1996. Microenvironments and microscale productivity of cyanobacterial desert crusts. J. Phycol. 32, 774–782. https://doi.org/10.1111/j.0022-3646.1996.00774.x

Garcia-Pichel, F., Castenholz, R.W., 2001. Photomovement of microorganisms in benthic and soil microenvironments, in: Häder, D.-P., Breure, A.M.B.T.-C.S. in P. (Eds.), Photomovement. Elsevier, pp. 403–420. https://doi.org/10.1016/S1568-461X(01)80018-1

Gernigon, V., Chekroun, M.A., Cockx, A., Guiraud, P., Morchain, J., 2019. How mixing and light heterogeneity impact the overall growth rate in photobioreactors. Chem. Eng. Technol. 1–15. https://doi.org/10.1002/ceat.201900102

Gieseke, A., de Beer, D., 2004. Use of microelectrodes to measure in situ microbial activities in biofilms, sediments, and microbial mats, in: Molecular Microbial Ecology Manual, 2nd

Edition, Kluwer Academic Publishers, Dordrecht, pp. 1581–1612. https://doi.org/10.1007/978-1-4020-2177-0_802

Gifuni, I., Pollio, A., Safi, C., Marzocchella, A., Olivieri, G., 2019. Current bottlenecks and challenges of the microalgal biorefinery. Trends Biotechnol. 37, 242–252. https://doi.org/https://doi.org/10.1016/j.tibtech.2018.09.006

Glud, R.N., 2008. Oxygen dynamics of marine sediments. Mar. Biol. Res. 4, 243–289. https://doi.org/10.1080/17451000801888726

Glud, R.N., Tengberg, A., Kühl, M., Hall, P.O.J., Klimant, I., 2001. An in situ instrument for planar O_2 optode measurements at benthic interfaces. Limnol. Oceanogr. 46, 2073–2080. https://doi.org/10.4319/lo.2001.46.8.2073

Gonzalez-Gil, G., Seghezzo, L., Lettinga, G., Kleerebezem, R., 2001. Kinetics and mass-transfer phenomena in anaerobic granular sludge. Biotechnol. Bioeng. 73, 125–134. https://doi.org/10.1002/bit.1044

Großkopf, T., Soyer, O.S., 2016. Microbial diversity arising from thermodynamic constraints. ISME J. 10, 2725–2733. https://doi.org/10.1038/ismej.2016.49

Gupta, S., Ross, T.D., Gomez, M.M., Grant, J.L., Romero, P.A., Venturelli, O.S., 2020a. Investigating the dynamics of microbial consortia in spatially structured environments. Nat. Commun. 11, 2418. https://doi.org/10.1038/s41467-020-16200-0

Gupta, S., Ross, T.D., Gomez, M.M., Grant, J.L., Romero, P.A., Venturelli, O.S., 2020b. Investigating the dynamics of microbial consortia in spatially structured environments. Nat. Commun. 11, 2418. https://doi.org/10.1038/s41467-020-16200-0

Guzzon, A., Di Pippo, F., Congestri, R., 2019. Wastewater Biofilm Photosynthesis in Photobioreactors. Microorganisms 7, 252. https://doi.org/10.3390/microorganisms7080252

Henze, M., Grady, C., Gujer, W., Marais, G., Matsuo, T., 1987. Activated sludge model No. 1. IAWPRC Sci. Tech. Reports 1.

Henze, M., Gujer, W., Mino, T., Van Loosedrecht, M.C.M., 2015. Activated Sludge Models ASM1, ASM2, ASM2d and ASM3. Water Intell. Online 5, 9781780402369–

9781780402369. https://doi.org/10.2166/9781780402369

Hillman, K.M., Sims, R.C., 2020. Struvite formation associated with the microalgae biofilm matrix of a rotating algal biofilm reactor (RABR) during nutrient removal from municipal wastewater. Water Sci. Technol. 81, 644–655. https://doi.org/10.2166/wst.2020.133

Hodson, A., Anesio, A.M., Tranter, M., Fountain, A., Osborn, M., Priscu, J., Laybourn-Parry, J., Sattler, B., 2008. Glacial ecosystems. Ecol. Monogr. https://doi.org/10.1890/07-0187.1

Hol, F.J.H., Galajda, P., Woolthuis, R.G., Dekker, C., Keymer, J.E., 2015. The idiosyncrasy of spatial structure in bacterial competition. BMC Res. Notes 8, 245. https://doi.org/10.1186/s13104-015-1169-x

Holst, G., Klimant, I., Kühl, M., Kohls, O., 1999. Optical microsensors and microprobes, in: Mark Varney (Ed.), Chemical Sensors In Oceanography. Gordon & Breach, pp. 143–188.

Horn, H., Hempel, D.C., 1997. Growth and decay in an auto-/heterotrophic biofilm. Water Res. 31, 2243–2252. https://doi.org/10.1016/S0043-1354(97)00081-X

Horn, H., Lackner, S., 2014. Modeling of biofilm systems: a review, in: Muffler, K., Ulber, R. (Eds.), . Springer International Publishing, Cham, pp. 53–76. https://doi.org/10.1007/10_2014_275

Horn, H., Morgenroth, E., 2006. Transport of oxygen, sodium chloride, and sodium nitrate in biofilms. Chem. Eng. Sci. 61, 1347–1356. https://doi.org/https://doi.org/10.1016/j.ces.2005.08.027

Hosomi, M., 2016. New challenges on wastewater treatment. Clean Technol. Environ. Policy 18, 627–628. https://doi.org/10.1007/s10098-016-1131-1

Houf, W.G., Incropera, F.P., 1980. An assessment of techniques for predicting radiation transfer in aqueous media. J. Quant. Spectrosc. Radiat. Transf. 23, 101–115. https://doi.org/https://doi.org/10.1016/S0022-4073(80)80009-4

Hudcová, H., Vymazal, J., Rozkošný, M., 2019. Present restrictions of sewage sludge application in agriculture within the European Union. Soil Water Res. 14, 104–120. https://doi.org/10.17221/36/2018-SWR

Hulshoff Pol, L.W., de Zeeuw, W.J., Velzeboer, C.T.M., Lettinga, G., 1983. Granulation in UASB-Reactors. Water Sci. Technol. 15, 291–304. https://doi.org/10.2166/wst.1983.0172

Hunt, S.M., Werner, E.M., Huang, B., Hamilton, M.A., Stewart, P.S., 2004. Hypothesis for the role of nutrient starvation in biofilm detachment. Appl. Environ. Microbiol. 70, 7418–7425. https://doi.org/10.1128/AEM.70.12.7418-7425.2004

Imbimbo, P., D'Elia, L., Liberti, D., Olivieri, G., Monti, D.M., 2020. Towards green extraction methods from microalgae learning from the classics. Appl. Microbiol. Biotechnol. 104, 9067–9077. https://doi.org/10.1007/s00253-020-10839-x

Inglezakis, V., Zorpas, A., Karagiannidis, A., Samaras, P., Voukkali, I., Sklari, S., 2014. European Union legislation on sewage sludge management. Fresenius Environ. Bull. 23, 635–639.

Jassby, A.D., Platt, T., 1976. Mathematical formulation of the relationship between photosynthesis and light for phytoplankton. Limnol. Oceanogr. 21, 540–547. https://doi.org/10.4319/lo.1976.21.4.0540

Jeroschewski, P., Steuckart, C., Kühl, M., 1996. An amperometric microsensor for the determination of H_2S in aquatic environments. Anal. Chem. 68, 4351–4357. https://doi.org/10.1021/ac960091b

Jones, A.K., Cannon, R.C., 1986. The release of micro-algal photosynthate and associated bacterial uptake and heterotrophic growth. Br. Phycol. J. 21, 341–358. https://doi.org/10.1080/00071618600650421

Joosten, E., Hamelin, J., Milferstedt, K., 2020. Simple time-lapse imaging for quantifying the hydrostatic production of oxygenic photogranules. Bio-protocol 10, e3784. https://doi.org/10.21769/BioProtoc.3784

Kagawa, Y., Tahata, J., Kishida, N., Matsumoto, S., Picioreanu, C., Van Loosdrecht, M.C.M., Tsuneda, S., 2015. Modeling the nutrient removal process in aerobic granular sludge system by coupling the reactor- and granule-scale models. Biotechnol. Bioeng. 112, 53–64. https://doi.org/10.1002/bit.25331

Karimifard, S., Elowsky, C., Paloni, J., Li, X., Li, Y., 2019. Effect of evolving biofilm structures

on modeling the flow in bio-clogged porous media, in: AGU Fall Meeting Abstracts. pp. H13R-2014.

Kiørboe, T., Grossart, H.-P., Ploug, H., Tang, K., 2002. Mechanisms and rates of bacterial colonization of sinking aggregates. Appl. Environ. Microbiol. 68, 3996–4006. https://doi.org/10.1128/AEM.68.8.3996-4006.2002

Kirst, H., Formighieri, C., Melis, A., 2014. Maximizing photosynthetic efficiency and culture productivity in cyanobacteria upon minimizing the phycobilisome light-harvesting antenna size. Biochim. Biophys. Acta - Bioenerg. 1837, 1653–1664. https://doi.org/10.1016/j.bbabio.2014.07.009

Klapper, I., Dockery, J., 2010. Mathematical description of microbial biofilms. SIAM Rev. 52, 221–265. https://doi.org/10.1137/080739720

Klawonn, I., Bonaglia, S., Brüchert, V., Ploug, H., 2015. Aerobic and anaerobic nitrogen transformation processes in N_2-fixing cyanobacterial aggregates. ISME J. 9, 1456–1466. https://doi.org/10.1038/ismej.2014.232

Klimant, I., Meyer, V., Kühl, M., 1995. Fiber-optic oxygen microsensors, a new tool in aquatic biology. Limnol. Oceanogr. 40, 1159–1165. https://doi.org/10.4319/lo.1995.40.6.1159

Koop-Jakobsen, K., Mueller, P., Meier, R.J., Liebsch, G., Jensen, K., 2018. Plant-sediment interactions in salt marshes – An optode imaging study of O_2, pH, and CO<usb>2</sub> gradients in the rhizosphere. Front. Plant Sci. 9, 1–11. https://doi.org/10.3389/fpls.2018.00541

Kothari, R., Pandey, A., Ahmad, S., Kumar, A., Pathak, V. V, Tyagi, V. V, 2017. Microalgal cultivation for value-added products: a critical enviro-economical assessment. 3 Biotech 7, 243. https://doi.org/10.1007/s13205-017-0812-8

Kreft, J.U., Picioreanu, C., Wimpenny, J.W.T., Van Loosdrecht, M.C.M., 2001. Individual-based modelling of biofilms. Microbiology 147, 2897–2912. https://doi.org/10.1099/00221287-147-11-2897

Kuhl, M., Glud, R.N., Ploug, H., Ramsing, N.B., 1996. Microenvironmental control of photosynthesis and photosynthesis-coupled respiration in an epilithic cyanobacterial biofilm.

J. Phycol. 32, 799–812. https://doi.org/10.1111/j.0022-3646.1996.00799.x

Kühl, M., Glud, R.N., Ploug, H., Ramsing, N.B., 1996. Microenvironmental control of photosynthesis and photosynthesis-coupled respiration in an epilithic cyanobacterial biofilm. J. Phycol. 32, 799–812. https://doi.org/10.1111/j.0022-3646.1996.00799.x

Kühl, M., Jørgensen, B.B., 1992. Microsensor measurements of sulfate reduction and sulfide oxidation in compact microbial communities of aerobic Biofilms. Appl. Environ. Microbiol. 58, 1164–1174. https://doi.org/10.1128/AEM.58.4.1164-1174.1992

Kühl, M., Lassen, C., Jørgensen, B.B., 1994. Optical properties of microbial mats: light measurements with fiber-optic microprobes, in: Stal, L.J., Caumette, P. (Eds.), Microbial Mats. Springer Berlin Heidelberg, Berlin, Heidelberg, pp. 149–166. https://doi.org/10.1007/978-3-642-78991-5_16

Kühl, M., Polerecky, L., 2008. Functional and structural imaging of phototrophic microbial communities and symbioses. Aquat. Microb. Ecol. 53, 99–118.

Kumar, R., Venugopalan, V.P., Kumar, R., 2015. Development of self-sustaining phototrophic granular biomass for bioremediation applications. Curr. Sci. 108, 1653–1661.

Kuroda, K., Nobu, M.K., Mei, R., Narihiro, T., Bocher, B.T.W., Yamaguchi, T., Liu, W.-T., 2016. A single-granule-level approach reveals ecological heterogeneity in an upflow anaerobic sludge blanket reactor. PLoS One 11, e0167788. https://doi.org/10.1371/journal.pone.0167788

Kwok, W.K., Picioreanu, C., Ong, S.L., Van Loosdrecht, M.C.M., Ng, W.J., Heijnen, J.J., 1998. Influence of biomass production and detachment forces on biofilm structures in a biofilm airlift suspension reactor. Biotechnol. Bioeng. 58, 400–407. https://doi.org/10.1002/(SICI)1097-0290(19980520)58:4<400::AID-BIT7>3.0.CO;2-N

Larsen, M., Borisov, S.M., Grunwald, B., Klimant, I., Glud, R.N., 2011. A simple and inexpensive high resolution color ratiometric planar optode imaging approach: Application to oxygen and pH sensing. Limnol. Oceanogr. Methods 9, 348–360. https://doi.org/10.4319/lom.2011.9.348

Lassen, C., Ploug, H., Jørgensen, B.B., 1992. A fibre-optic scalar irradiance microsensor:

application for spectral light measurements in sediments. FEMS Microbiol. Lett. 86, 247–254. https://doi.org/https://doi.org/10.1016/0378-1097(92)90788-P

Lawrence, J.R., Korber, D.R., Hoyle, B.D., Costerton, J.W., Caldwell, D.E., 1991. Optical sectioning of microbial biofilms. J. Bacteriol. 173, 6558–6567. https://doi.org/10.1128/jb.173.20.6558-6567.1991

Layer, M., Adler, A., Reynaert, E., Hernandez, A., Pagni, M., Morgenroth, E., Holliger, C., Derlon, N., 2019. Organic substrate diffusibility governs microbial community composition, nutrient removal performance and kinetics of granulation of aerobic granular sludge. Water Res. X 4, 100033. https://doi.org/10.1016/j.wroa.2019.100033

Layer, M., Villodres, M.G., Hernandez, A., Reynaert, E., Morgenroth, E., Derlon, N., 2020. Limited simultaneous nitrification-denitrification (SND) in aerobic granular sludge systems treating municipal wastewater: Mechanisms and practical implications. Water Res. X 7, 100048. https://doi.org/10.1016/j.wroa.2020.100048

Lee, W., de Beer, D., 1995. Oxygen and pH microprofiles above corroding mild steel covered with a biofilm. Biofouling 8, 273–280. https://doi.org/10.1080/08927019509378280

Lettinga, G., Zehnder, A.J.., Grotenhuis, J.T.., (Eds.), L.. H.P., 1987. The ‘spaghetti theory’ on anaerobic sludge formation, or the inevitability of granulation. Granul. Anaerob. sludge Microbiol. Technol. Pudoc. Wageningen, Netherlands 146–152.

Levasseur, W., Perré, P., Pozzobon, V., 2020. A review of high value-added molecules production by microalgae in light of the classification. Biotechnol. Adv. 41, 107545. https://doi.org/https://doi.org/10.1016/j.biotechadv.2020.107545

Lewin, R.A., 1956. Extracellular polysaccharides of green algae. Can. J. Microbiol. 2, 665–672. https://doi.org/10.1139/m56-079

Li, C., Wagner, M., Lackner, S., Horn, H., 2016. Assessing the influence of biofilm surface roughness on mass transfer by combining optical coherence tomography and two-dimensional modeling. Biotechnol. Bioeng. 113, 989–1000. https://doi.org/10.1002/bit.25868

Li, H., Wang, S., Zhao, F., Fang, F., Chen, Y., Yan, P., Yang, J., Gu, S., Guo, J., 2020.

Evaluating the effects of micro-zones of granular sludge on one-stage partial nitritation–anammox nitrogen removal. Bioprocess Biosyst. Eng. 43, 1037–1049. https://doi.org/10.1007/s00449-020-02302-y

Li, J., Cai, A., Wang, D., Chen, C., Ni, Y., 2014. Structure analysis of aerobic granule from a sequencing batch reactor for organic matter and ammonia nitrogen removal. Int. J. Environ. Res. Public Health 11, 2427–2436. https://doi.org/10.3390/ijerph110302427

Li, T., Piltz, B., Podola, B., Dron, A., de Beer, D., Melkonian, M., 2016a. Microscale profiling of photosynthesis-related variables in a highly productive biofilm photobioreactor. Biotechnol. Bioeng. 113, 1046–1055. https://doi.org/10.1002/bit.25867

Li, T., Podola, B., Melkonian, M., 2016b. Investigating dynamic processes in a porous substrate biofilm photobioreactor - A modeling approach. Algal Res. 13, 30–40. https://doi.org/10.1016/j.algal.2015.11.006

Li, Y., Liu, Y., Shen, L., Chen, F., 2008. DO diffusion profile in aerobic granule and its microbiological implications. Enzyme Microb. Technol. 43, 349–354. https://doi.org/10.1016/j.enzmictec.2008.04.005

Liehr, S.K., Suidan, M.T., Eheart, J.W., 1990. A modeling study of carbon and light limitation in algal biofilms. Biotechnol. Bioeng. 35, 233–243. https://doi.org/10.1002/bit.260350304

Liehr, S.K., Wayland Eheart, J., Suidan, M.T., 1988. A modeling study of the effect of pH on carbon limited algal biofilms. Water Res. 22, 1033–1041. https://doi.org/10.1016/0043-1354(88)90151-0

Liu, L., Fan, H., Liu, Y., Liu, C., Huang, X., 2017. Development of algae-bacteria granular consortia in photo-sequencing batch reactor. Bioresour. Technol. 232, 64–71. https://doi.org/https://doi.org/10.1016/j.biortech.2017.02.025

Liu, Y., 2006a. Mechanisms of aerobic granulation, in: Tay, J.-H., Tay, S.T.-L., Liu, Y., Show, K.-Y., Ivanov, V.B.T.-W.M.S. (Eds.), Biogranulation Technologies for Wastewater Treatment. Elsevier, pp. 85–I. https://doi.org/https://doi.org/10.1016/S0713-2743(06)80106-6

Liu, Y., 2006b. Factors affecting aerobic granulation, in: Tay, J.-H., Tay, S.T.-L., Liu, Y., Show,

K.-Y., Ivanov, V.B.T.-W.M.S. (Eds.), Biogranulation Technologies for Wastewater Treatment. Elsevier, pp. 99–114. https://doi.org/https://doi.org/10.1016/S0713-2743(06)80107-8

Liu, Y., Liu, Q.S., 2006. Causes and control of filamentous growth in aerobic granular sludge sequencing batch reactors. Biotechnol. Adv. 24, 115–127. https://doi.org/10.1016/j.biotechadv.2005.08.001

Liu, Y., Ngo, H.H., Guo, W., Wang, D., Peng, L., Wei, W., Ni, B.-J., 2020. Impact of coexistence of sludge flocs on nitrous oxide production in a granule-based nitrification system: A model-based evaluation. Water Res. 170, 115312. https://doi.org/https://doi.org/10.1016/j.watres.2019.115312

Liu, Y., Tay, J.H., 2002. The essential role of hydrodynamic shear force in the formation of biofilm and granular sludge. Water Res. 36, 1653–1665. https://doi.org/10.1016/S0043-1354(01)00379-7

Liu, Y.Q., Liu, Y., Tay, J.H., 2005. Relationship between size and mass transfer resistance in aerobic granules. Lett. Appl. Microbiol. 40, 312–315. https://doi.org/10.1111/j.1472-765X.2005.01695.x

Liu, Y.Q., Liu, Y., Tay, J.H., 2004. The effects of extracellular polymeric substances on the formation and stability of biogranules. Appl. Microbiol. Biotechnol. 65, 143–148. https://doi.org/10.1007/s00253-004-1657-8

Longo, S., D'Antoni, B.M., Bongards, M., Chaparro, A., Cronrath, A., Fatone, F., Lema, J.M., Mauricio-Iglesias, M., Soares, A., Hospido, A., 2016. Monitoring and diagnosis of energy consumption in wastewater treatment plants. A state of the art and proposals for improvement. Appl. Energy 179, 1251–1268. https://doi.org/10.1016/j.apenergy.2016.07.043

Loomba, V., Huber, G., von Lieres, E., 2018. Single-cell computational analysis of light harvesting in a flat-panel photo-bioreactor. Biotechnol. Biofuels 11, 149. https://doi.org/10.1186/s13068-018-1147-3

Lu, L., Guest, J.S., Peters, C.A., Zhu, X., Rau, G.H., Ren, Z.J., 2018. Wastewater treatment for

carbon capture and utilization. Nat. Sustain. 1, 750–758. https://doi.org/10.1038/s41893-018-0187-9

Mancuso, S., Papeschi, G., Marras, A.M., 2000. A polarographic, oxygen-selective, vibrating-microelectrode system for the spatial and temporal characterisation of transmembrane oxygen fluxes in plants. Planta 211, 384–389. https://doi.org/10.1007/s004250000296

Mannina, G., Trapani, D. Di, Viviani, G., Ødegaard, H., 2011. Modelling and dynamic simulation of hybrid moving bed biofilm reactors: Model concepts and application to a pilot plant. Biochem. Eng. J. 56, 23–36. https://doi.org/10.1016/j.bej.2011.04.013

Mattei, M.R., Frunzo, L., D'Acunto, B., Pechaud, Y., Pirozzi, F., Esposito, G., 2017. Continuum and discrete approach in modeling biofilm development and structure: a review. J. Math. Biol. 1–59. https://doi.org/10.1007/s00285-017-1165-y

Milferstedt, K., Hamelin, J., Park, C., Jung, J., Hwang, Y., Cho, S.K., Jung, K.W., Kim, D.H., 2017a. Biogranules applied in environmental engineering. Int. J. Hydrogen Energy 42, 27801–27811. https://doi.org/10.1016/j.ijhydene.2017.07.176

Milferstedt, K., Kuo-Dahab, W.C., Butler, C.S., Hamelin, J., Abouhend, A.S., Stauch-White, K., McNair, A., Watt, C., Carbajal-González, B.I., Dolan, S., Park, C., 2017b. The importance of filamentous cyanobacteria in the development of oxygenic photogranules. Sci. Rep. 7, 1–15. https://doi.org/10.1038/s41598-017-16614-9

Mobberley, J.M., Lindemann, S.R., Bernstein, H.C., Moran, J.J., Renslow, R.S., Babauta, J., Hu, D., Beyenal, H., Nelson, W.C., 2017. Organismal and spatial partitioning of energy and macronutrient transformations within a hypersaline mat. FEMS Microbiol. Ecol. 93, 1–13. https://doi.org/10.1093/femsec/fix028

Monod, J., 1949. The growth of bacterial cultures. Annu. Rev. Microbiol. 3, 371–394. https://doi.org/10.1146/annurev.mi.03.100149.002103

Morgenroth, E., Milferstedt, K., 2009. Biofilm engineering: Linking biofilm development at different length and time scales. Rev. Environ. Sci. Biotechnol. 8, 203–208. https://doi.org/10.1007/s11157-009-9163-1

Mosquera Corral, A., de Kreuk, M.K., Heijnen, J., Van Loosdrecht, M.C.M., 2005. Effects of

oxygen concentration on N-removal in an aerobic granular sludge reactor. Water Res. 39, 2676–2686. https://doi.org/10.1016/j.watres.2005.04.065

Muñoz Sierra, J.D., Picioreanu, C., Van Loosdrecht, M.C.M., 2014. Modeling phototrophic biofilms in a plug-flow reactor. Water Sci. Technol. 70, 1261–1270. https://doi.org/10.2166/wst.2014.368

Nedbal, L., Tichý, V., Xiong, F., Grobbelaar, J.U., 1996. Microscopic green algae and cyanobacteria in high-frequency intermittent light. J. Appl. Phycol. 8, 325–333. https://doi.org/10.1007/BF02178575

Nopens, I., Capalozza, C., Vanrolleghem, P.A., 2001. Stability analysis of a synthetic municipal wastewater. Tech. Rep. Dept. Appl. Math. Biometrics Process Control. Univ, Gent. https://doi.org/https://modeleau.fsg.ulaval.ca/fileadmin/modeleau/documents/Publications/pvr334.pdf

Nultsch, W., Häder, D.-P., 1979. Photomovement of motile microorganisms. Photochem. Photobiol. 29, 423–437. https://doi.org/10.1111/j.1751-1097.1979.tb07072.x

Okabe, S., Oshiki, M., Takahashi, Y., Satoh, H., 2011. N_2O emission from a partial nitrification–anammox process and identification of a key biological process of N_2O emission from anammox granules. Water Res. 45, 6461–6470. https://doi.org/10.1016/j.watres.2011.09.040

Orf, I., Timm, S., Bauwe, H., Fernie, A.R., Hagemann, M., Kopka, J., Nikoloski, Z., 2016. Can cyanobacteria serve as a model of plant photorespiration? – a comparative meta-analysis of metabolite profiles. J. Exp. Bot. 67, 2941–2952. https://doi.org/10.1093/jxb/erw068

Oswald, W.J., Gotaas, H.B., Ludwig, H.F., Lynch, V., 1953. Algae symbiosis in oxidation ponds: III. photosynthetic oxygenation. Sewage Ind. Waste. 25, 692–705.

Ouazaite, H., Milferstedt, K., Hamelin, J., Desmond-Le Quéméner, E., 2020. Mapping the biological activities of filamentous oxygenic photogranules. Biotechnol. Bioeng. bit.27585. https://doi.org/10.1002/bit.27585

Paerl, H.W., 1977. Role of heterotrophic bacteria in promoting N_2 fixation by *Anabaena* in aquatic habitats. Microb. Ecol. 4, 215–231. https://doi.org/10.1007/BF02015078

Parikh, A., Madamwar, D., 2006. Partial characterization of extracellular polysaccharides from cyanobacteria. Bioresour. Technol. 97, 1822–1827. https://doi.org/10.1016/j.biortech.2005.09.008

Park, C. & Dolan, S., 2015. Algal-sludge granule for wastewater treatment and bioenergy feedstock generation. Pat. Appl. WO 2015112654 A2.

Park, C., Seynhaeve, L., Sialve, B., Carrère, H., 2015. The anaerobic digestibility of algal-sludge granules, in: Water Environment Federation Residual and Biosolids. Washington D.C., USA.

Perera, I.A., Abinandan, S., Subashchandrabose, S.R., Venkateswarlu, K., Naidu, R., Megharaj, M., 2019. Advances in the technologies for studying consortia of bacteria and cyanobacteria/microalgae in wastewaters. Crit. Rev. Biotechnol. 39, 709–731. https://doi.org/10.1080/07388551.2019.1597828

Picioreanu, C., Batstone, D.J., Van Loosdrecht, M.C.M., 2005. Multidimensional modelling of anaerobic granules. Water Sci. Technol. 52, 501–507. https://doi.org/10.2166/wst.2005.0559

Picioreanu, C., Blauert, F., Horn, H., Wagner, M., 2018. Determination of mechanical properties of biofilms by modelling the deformation measured using optical coherence tomography. Water Res. 145, 588–598. https://doi.org/10.1016/j.watres.2018.08.070

Picioreanu, C., Van Loosdrecht, M.C.M., Curtis, T.P., Scott, K., 2010. Model based evaluation of the effect of pH and electrode geometry on microbial fuel cell performance. Bioelectrochemistry 78, 8–24. https://doi.org/10.1016/j.bioelechem.2009.04.009

Picioreanu, C., Van Loosdrecht, M.C.M., Heijnen, J.J., 2000a. Modelling and predicting biofilm structure, in: Allison, D.G., Lappin-Scott, H.M., Wilson, M., Gilbert, P. (Eds.), Community Structure and Co-Operation in Biofilms, Society for General Microbiology Symposia. Cambridge University Press, Cambridge, pp. 129–166. https://doi.org/DOI: 10.1017/CBO9780511754814.009

Picioreanu, C., Van Loosdrecht, M.C.M., Heijnen, J.J., 2000b. A theoretical study on the effect of surface roughness on mass transport and transformation in biofilms. Biotechnol. Bioeng. 68, 355–369. https://doi.org/10.1002/(SICI)1097-0290(20000520)68:4<355::AID-

BIT1>3.0.CO;2-A

Picioreanu, C., Van Loosdrecht, M.C.M., Heijnen, J.J., 2000c. Effect of diffusive and convective substrate transport on biofilm structure formation: A two-dimensional modeling study. Biotechnol. Bioeng. 69, 504–515. https://doi.org/10.1002/1097-0290(20000905)69:5<504::AID-BIT5>3.0.CO;2-S

Picioreanu, C., Van Loosdrecht, M.C.M., Heijnen, J.J., 1998. A new combined differential-discrete cellular automaton approach for biofilm modeling: Application for growth in gel beads. Biotechnol. Bioeng. 57, 718–731. https://doi.org/10.1002/(SICI)1097-0290(19980320)57:6<718::AID-BIT9>3.0.CO;2-O

Picioreanu, C., Xavier, J.B., Van Loosdrecht, M.C.M., 2004. Advances in mathematical modeling of biofilm structure. Biofilms 1, 337–349. https://doi.org/10.1017/S1479050505001572

Pijuan, M., Ribera-Guardia, A., Balcázar, J.L., Micó, M.M., de la Torre, T., 2020. Effect of COD on mainstream anammox: Evaluation of process performance, granule morphology and nitrous oxide production. Sci. Total Environ. 712, 136372. https://doi.org/https://doi.org/10.1016/j.scitotenv.2019.136372

Pischedda, L., Poggiale, J.C., Cuny, P., Gilbert, F., 2008. Imaging oxygen distribution in marine sediments. The importance of bioturbation and sediment heterogeneity. Acta Biotheor. 56, 123–135. https://doi.org/10.1007/s10441-008-9033-1

Ploug, H., 2008. Cyanobacterial surface blooms formed by *Aphanizomenon* sp. and *Nodularia spumigena* in the Baltic Sea: Small-scale fluxes, pH, and oxygen microenvironments. Limnol. Oceanogr. 53, 914–921. https://doi.org/10.4319/lo.2008.53.3.0914

Polerecky, L., Lott, C., Weber, M., 2008. In situ measurement of gross photosynthesis using a microsensor-based light-shade shift method. Limnol. Oceanogr. Methods 6, 373–383. https://doi.org/10.4319/lom.2008.6.373

Polizzi, B., Bernard, O., Ribot, M., 2017. A time-space model for the growth of microalgae biofilms for biofuel production. J. Theor. Biol. 432, 55–79. https://doi.org/10.1016/j.jtbi.2017.08.017

Pringault, O., Garcia-Pichel, F., 2000. Monitoring of oxygenic and anoxygenic photosynthesis in a unicyanobacterial biofilm, grown in benthic gradient chamber. FEMS Microbiol. Ecol. 33, 251–258. https://doi.org/10.1016/S0168-6496(00)00068-4

Pronk, M., Abbas, B., Al-zuhairy, S.H.K., Kraan, R., Kleerebezem, R., Van Loosdrecht, M.C.M., 2015. Effect and behaviour of different substrates in relation to the formation of aerobic granular sludge. Appl. Microbiol. Biotechnol. 99, 5257–5268. https://doi.org/10.1007/s00253-014-6358-3

Pronk, M, de Kreuk, M.K., de Bruin, B., Kamminga, P., Kleerebezem, R., Van Loosdrecht, M.C.M., 2015. Full scale performance of the aerobic granular sludge process for sewage treatment. Water Res. 84, 207–217. https://doi.org/10.1016/j.watres.2015.07.011

Purevdorj-Gage, B., Costerton, W.J., Stoodley, P., 2005. Phenotypic differentiation and seeding dispersal in non-mucoid and mucoid *Pseudomonas aeruginosa* biofilms. Microbiology 151, 1569–1576. https://doi.org/10.1099/mic.0.27536-0

Puznava, N., Payraudeau, M., Thornberg, D., 2001. Simultaneous nitrification and denitrification in biofilters with real time aeration control. Water Sci. Technol. 43, 269–276. https://doi.org/10.2166/wst.2001.0057

Quaranta, M., Borisov, S.M., Klimant, I., 2012. Indicators for optical oxygen sensors. Bioanal. Rev. 4, 115–157. https://doi.org/10.1007/s12566-012-0032-y

Quijano, G., Arcila, J.S., Buitrón, G., 2017. Microalgal-bacterial aggregates: Applications and perspectives for wastewater treatment. Biotechnol. Adv. 35, 772–781. https://doi.org/10.1016/j.biotechadv.2017.07.003

Rahman, K.A., Sudarsan, R., Eberl, H.J., 2015. A mixed-culture biofilm model with cross-diffusion. Bull. Math. Biol. 77, 2086–2124. https://doi.org/10.1007/s11538-015-0117-1

Randall, C.W., Sen, D., 1996. Full-scale evaluation of an integrated fixed-film activated sludge (IFAS) process for enhanced nitrogen removal. Water Sci. Technol. 33, 155–162. https://doi.org/https://doi.org/10.1016/0273-1223(96)00469-6

Renuka, N., Sood, A., Ratha, S.K., Prasanna, R., Ahluwalia, A.S., 2013. Nutrient sequestration, biomass production by microalgae and phytoremediation of sewage water. Int. J.

Phytoremediation 15, 789–800. https://doi.org/10.1080/15226514.2012.736436

Revsbech, N.P., 1989. An oxygen microsensor with a guard cathode. Limnol. Oceanogr. 34, 474–478. https://doi.org/10.4319/lo.1989.34.2.0474

Revsbech, N.P., Jørgensen, B.B., 1986. Microelectrodes: their use in microbial ecology, in: Advances in Microbial Ecology. pp. 293–352. https://doi.org/10.1007/978-1-4757-0611-6_7

Riegman, R., Rutgers, M., Mur, R.R., 1985. Effects of photoperiodicity and light irradiance on phosphate-limited *Oscillatoria agardhii* in chemostat cultures. Arch. Microbiol. 142, 66–71. https://doi.org/10.1007/BF00409239

Rippka, R.B.T.-M. in E., 1988. Isolation and purification of cyanobacteria, in: Cyanobacteria. Academic Press, pp. 3–27. https://doi.org/https://doi.org/10.1016/0076-6879(88)67004-2

Røder, H.L., Olsen, N.M.C., Whiteley, M., Burmølle, M., 2020. Unravelling interspecies interactions across heterogeneities in complex biofilm communities. Environ. Microbiol. 22, 5–16. https://doi.org/https://doi.org/10.1111/1462-2920.14834

Roeselers, G., Van Loosdrecht, M.C.M., Muyzer, G., 2008. Phototrophic biofilms and their potential applications. J. Appl. Phycol. 20, 227–235. https://doi.org/10.1007/s10811-007-9223-2

Roeselers, G., Van Loosdrecht, M.C.M., Muyzer, G., 2007. Heterotrophic pioneers facilitate phototrophic biofilm development. Microb. Ecol. 54, 578–585. https://doi.org/10.1007/s00248-007-9238-x

Rossi, F., De Philippis, R., 2015. Role of cyanobacterial exopolysaccharides in phototrophic biofilms and in complex microbial mats. Life 5, 1218–1238. https://doi.org/10.3390/life5021218

Rubol, S., Freixa, A., Sanchez-Vila, X., Romaní, A.M., 2018. Linking biofilm spatial structure to real-time microscopic oxygen decay imaging. Biofouling 34, 200–211. https://doi.org/10.1080/08927014.2017.1423474

Rusconi, R., Stocker, R., 2015. Microbes in flow. Curr. Opin. Microbiol. 25, 1–8. https://doi.org/10.1016/j.mib.2015.03.003

Salgar-Chaparro, S.J., Lepkova, K., Pojtanabuntoeng, T., Darwin, A., Machuca, L.L., 2020. Nutrient level determines biofilm characteristics and subsequent impact on microbial corrosion and biocide effectiveness. Appl. Environ. Microbiol. 86, e02885-19. https://doi.org/10.1128/AEM.02885-19

Salomon, P.S., Janson, S., Granéli, E., 2003. Molecular identification of bacteria associated with filaments of Nodularia spumigena and their effect on the cyanobacterial growth. Harmful Algae 2, 261–272. https://doi.org/https://doi.org/10.1016/S1568-9883(03)00045-3

Santegoeds, C.M., Ferdelman, T.G., Muyzer, G., de Beer, D., 1998. Structural and functional dynamics of sulfate-reducing populations in bacterial biofilms. Appl. Environ. Microbiol. 64, 3731 LP – 3739. https://doi.org/10.1128/AEM.64.10.3731-3739.1998

Schambeck, C.M., Magnus, B.S., de Souza, L.C.R., Leite, W.R.M., Derlon, N., Guimarães, L.B., da Costa, R.H.R., 2020. Biopolymers recovery: dynamics and characterization of alginate-like exopolymers in an aerobic granular sludge system treating municipal wastewater without sludge inoculum. J. Environ. Manage. 263, 110394. https://doi.org/https://doi.org/10.1016/j.jenvman.2020.110394

Schiano di Visconte, G., Spicer, A., Chuck, C.J., Allen, M.J., 2019. The microalgae biorefinery: a perspective on the current status and future opportunities using genetic modification. Appl. Sci. 9, 4793. https://doi.org/10.3390/app9224793

Schneider, C.A., Rasband, W.S., Eliceiri, K.W., 2012. NIH Image to ImageJ: 25 years of image analysis. Nat. Methods 9, 671–675. https://doi.org/10.1038/nmeth.2089

Schramm, A., Larsen, L.H., Revsbech, N.P., Amann, R.I., 1997. Structure and function of a nitrifying biofilm as determined by microelectrodes and fluorescent oligonucleotide probes. Water Sci. Technol. 36, 263–270. https://doi.org/10.1016/S0273-1223(97)00333-8

Segawa, T., Takeuchi, N., Mori, H., Rathnayake, R.M.L.D., Li, Z., Akiyoshi, A., Satoh, H., Ishii, S., 2020. Redox stratification within cryoconite granules influences the nitrogen cycle on glaciers. FEMS Microbiol. Ecol. 96. https://doi.org/10.1093/femsec/fiaa199

Sengar, A., Basheer, F., Aziz, A., Farooqi, I.H., 2018. Aerobic granulation technology: Laboratory studies to full scale practices. J. Clean. Prod. 197, 616–632.

https://doi.org/https://doi.org/10.1016/j.jclepro.2018.06.167

Shoener, B.D., Bradley, I.M., Cusick, R.D., Guest, J.S., 2014. Energy positive domestic wastewater treatment: the roles of anaerobic and phototrophic technologies. Environ. Sci. Process. Impacts 16, 1204–1222. https://doi.org/10.1039/C3EM00711A

Solano, C., Echeverz, M., Lasa, I., 2014. Biofilm dispersion and quorum sensing. Curr. Opin. Microbiol. 18, 96–104. https://doi.org/10.1016/j.mib.2014.02.008

Sood, A., Renuka, N., Prasanna, R., Ahluwalia, A.S., 2015. Cyanobacteria as potential options for wastewater treatment, in: Ansari, A.A., Gill, S.S., Gill, R., Lanza, G.R., Newman, L. (Eds.), Phytoremediation. Springer International Publishing, Cham, pp. 83–93. https://doi.org/10.1007/978-3-319-10969-5_8

Staal, M., te Lintel Hekkert, S., Herman, P., Stal, L.J., 2002. Comparison of models describing light dependence of N_2 fixation in heterocystous Cyanobacteria. Appl. Environ. Microbiol. 68, 4679–4683. https://doi.org/10.1128/AEM.68.9.4679-4683.2002

Staal, M., Thar, R., Kühl, M., Van Loosdrecht, M.C.M., Wolf, G., de Brouwer, J.F.C., Rijstenbil, J.W., 2007. Different carbon isotope fractionation patterns during the development of phototrophic freshwater and marine biofilms. Biogeosciences 4, 613–626. https://doi.org/10.5194/bg-4-613-2007

Stal, L.J., 2002. Cyanobacterial mats and stromatolites, in: Whitton, B.A., Potts, M. (Eds.), The Ecology of Cyanobacteria. Kluwer Academic Publishers, Dordrecht, pp. 61–120. https://doi.org/10.1007/0-306-46855-7_4

Stal, L.J., 1995. Physiological ecology of cyanobacteria in microbial mats and other communities. New Phytol. 131, 1–32. https://doi.org/10.1111/j.1469-8137.1995.tb03051.x

Stal, L.J., van Gemerden, H., Krumbein, W.E., 1985. Structure and development of a benthic marine microbial mat. FEMS Microbiol. Ecol. 1, 111–125. https://doi.org/10.1111/j.1574-6968.1985.tb01138.x

Stauch-White, K., Srinivasan, V.N., Camilla Kuo-Dahab, W., Park, C., Butler, C.S., 2017. The role of inorganic nitrogen in successful formation of granular biofilms for wastewater treatment that support cyanobacteria and bacteria. AMB Express 7, 146.

https://doi.org/10.1186/s13568-017-0444-8

Stewart, P.S., Franklin, M.J., 2008. Physiological heterogeneity in biofilms. Nat. Rev. Microbiol. 6, 199–210. https://doi.org/10.1038/nrmicro1838

Stibal, M., Šabacká, M., Žárský, J., 2012. Biological processes on glacier and ice sheet surfaces. Nat. Geosci. 5, 771–774. https://doi.org/10.1038/ngeo1611

Stillwell, A.S., Hoppock, D.C., Webber, M.E., 2010. Energy recovery from wastewater treatment plants in the United States: A case study of the energy-water nexus. Sustainability 2, 945–962. https://doi.org/10.3390/su2040945

Stolz, J.F., 2000. Structure of microbial mats and biofilms, in: Riding, R.E., Awramik, S.M. (Eds.), Microbial Sediments. Springer Berlin Heidelberg, Berlin, Heidelberg, pp. 1–8. https://doi.org/10.1007/978-3-662-04036-2_1

Stolz, J.F., 1990. Distribution of phototrophic microbes in the flat laminated microbial mat at Laguna Figueroa, Baja California, Mexico. Biosystems 23, 345–357. https://doi.org/https://doi.org/10.1016/0303-2647(90)90016-T

Storck, T., Picioreanu, C., Virdis, B., Batstone, D.J., 2014. Variable cell morphology approach for individual-based modeling of microbial communities. Biophys. J. 106, 2037–2048. https://doi.org/10.1016/j.bpj.2014.03.015

Strieth, D., Ulber, R., Muffler, K., 2018. Application of phototrophic biofilms: from fundamentals to processes. Bioprocess Biosyst. Eng. 41, 295–312. https://doi.org/10.1007/s00449-017-1870-3

Stuart, R.K., Mayali, X., Boaro, A.A., Zemla, A., Everroad, R.C., Nilson, D., Weber, P.K., Lipton, M., Bebout, B.M., Pett-Ridge, J., Thelen, M.P., 2016a. Light regimes shape utilization of extracellular organic C and N in a cyanobacterial biofilm. MBio 7. https://doi.org/10.1128/mBio.00650-16

Stuart, R.K., Mayali, X., Lee, J.Z., Craig Everroad, R., Hwang, M., Bebout, B.M., Weber, P.K., Pett-Ridge, J., Thelen, M.P., 2016b. Cyanobacterial reuse of extracellular organic carbon in microbial mats. ISME J. 10, 1240–1251. https://doi.org/10.1038/ismej.2015.180

Subashchandrabose, S.R., Ramakrishnan, B., Megharaj, M., Venkateswarlu, K., Naidu, R., 2011. Consortia of cyanobacteria/microalgae and bacteria: Biotechnological potential. Biotechnol. Adv. 29, 896–907. https://doi.org/https://doi.org/10.1016/j.biotechadv.2011.07.009

Sudarsan, R., Ghosh, S., Stockie, J.M., Eberl, H.J., 2016. Simulating biofilm deformation and detachment with the immersed boundary method. Commun. Comput. Phys. 19, 682–732. https://doi.org/10.4208/cicp.161214.021015a

Takeuchi, N., Kohshima, S., Seko, K., 2001. Structure, formation, and darkening process of Albedo-reducing material (Cryoconite) on a Himalayan Glacier: A Granular algal mat growing on the glacier. Arctic, Antarct. Alp. Res. 33, 115–122. https://doi.org/10.1080/15230430.2001.12003413

Takeuchi, N., Nishiyama, H., Li, Z., 2010. Structure and formation process of cryoconite granules on Ürümqi glacier No. 1, Tien Shan, China. Ann. Glaciol. 51, 9–14. https://doi.org/10.3189/172756411795932010

Tandeau de Marsac, N., Houmard, J., 1993. Adaptation of cyanobacteria to environmental stimuli: new steps towards molecular mechanisms. FEMS Microbiol. Lett. 104, 119–189. https://doi.org/https://doi.org/10.1016/0378-1097(93)90506-W

Thaveesri, J., Daffonchio, D., Liessens, B., Vandermeren, P., Verstraete, W., 1995. Granulation and sludge bed stability in upflow anaerobic sludge bed reactors in relation to surface thermodynamics. Appl. Environ. Microbiol. 61, 3681–3686. https://doi.org/10.1128/AEM.61.10.3681-3686.1995

Tilzer, M.M., 1987. Light-dependence of photosynthesis and growth in cyanobacteria: Implications for their dominance in eutrophic lakes. New Zeal. J. Mar. Freshw. Res. 21, 401–412. https://doi.org/10.1080/00288330.1987.9516236

Tiron, O., Bumbac, C., Manea, E., Stefanescu, M., Nita Lazar, M., 2017. Overcoming microalgae harvesting barrier by activated algae granules. Sci. Rep. 7, 4646. https://doi.org/10.1038/s41598-017-05027-3

Tiron, O., Bumbac, C., Patroescu, I. V., Badescu, V.R., Postolache, C., 2015. Granular activated algae for wastewater treatment. Water Sci. Technol. 71, 832–839.

https://doi.org/10.2166/wst.2015.010

Trebuch, L.M., Oyserman, B.O., Janssen, M., Wijffels, R.H., Vet, L.E.M.M., Fernandes, T. V., 2020. Impact of hydraulic retention time on community assembly and function of photogranules for wastewater treatment. Water Res. 173, 115506. https://doi.org/10.1016/j.watres.2020.115506

Trego, A.C., Mills, S., Collins, G., 2019. Granular biofilms : formation, function, application, and new trends as model microbial communities. Preprints 1–58. https://doi.org/10.20944/preprints201906.0053.v1

Tschiersch, H., Liebsch, G., Borisjuk, L., Stangelmayer, A., Rolletschek, H., 2012. An imaging method for oxygen distribution, respiration and photosynthesis at a microscopic level of resolution. New Phytol. 196, 926–36. https://doi.org/10.1111/j.1469-8137.2012.04295.x

Tuomainen, J., Hietanen, S., Kuparinen, J., Martikainen, P.J., Servomaa, K., 2006. Community structure of the bacteria associated with *Nodularia* sp. (Cyanobacteria) aggregates in the Baltic Sea. Microb. Ecol. 52, 513–522. https://doi.org/10.1007/s00248-006-9130-0

Tuomainen, J.M., Hietanen, S., Kuparinen, J., Martikainen, P.J., Servomaa, K., 2003. Baltic Sea cyanobacterial bloom contains denitrification and nitrification genes, but has negligible denitrification activity. FEMS Microbiol. Ecol. 45, 83–96. https://doi.org/10.1016/S0168-6496(03)00131-4

Uetake, J., Nagatsuka, N., Onuma, Y., Takeuchi, N., Motoyama, H., Aoki, T., 2019. Bacterial community changes with granule size in cryoconite and their susceptibility to exogenous nutrients on NW Greenland glaciers. FEMS Microbiol. Ecol. 95. https://doi.org/10.1093/femsec/fiz075

Van Benthum, W.A.J., Garrido-Fernández, J.M., Tijhuis, L., Van Loosdrecht, M.C.M., Heijnen, J.J., 1996. Formation and detachment of biofilms and granules in a nitrifying biofilm airlift suspension reactor. Biotechnol. Prog. 12, 764–772. https://doi.org/10.1021/bp960063e

Van Den Hende, S., Beelen, V., Bore, G., Boon, N., Vervaeren, H., 2014. Up-scaling aquaculture wastewater treatment by microalgal bacterial flocs: From lab reactors to an outdoor raceway pond. Bioresour. Technol. 159, 342–354. https://doi.org/10.1016/j.biortech.2014.02.113

Vannecke, T.P.W., Wells, G., Hubaux, N., Morgenroth, E., Volcke, E.I.P., 2015. Considering microbial and aggregate heterogeneity in biofilm reactor models: How far do we need to go? 1692–1699. https://doi.org/10.2166/wst.2015.389

Vassilev, S. V, Vassileva, C.G., 2016. Composition, properties and challenges of algae biomass for biofuel application: An overview. Fuel 181, 1–33. https://doi.org/10.1016/j.fuel.2016.04.106

Vézina, S., Vincent, W.F., 1997. Arctic cyanobacteria and limnological properties of their environment: Bylot Island, Northwest Territories, Canada (73°N, 80°W). Polar Biol. 17, 523–534. https://doi.org/10.1007/s003000050151

Volcke, E.I.P., Picioreanu, C., De Baets, B., Van Loosdrecht, M.C.M., 2012. The granule size distribution in an anammox-based granular sludge reactor affects the conversion: Implications for modeling. Biotechnol. Bioeng. 109, 1629–1636. https://doi.org/10.1002/bit.24443

Walter, M.R., Bauld, J., Brock, T.D., 1976. Microbiology and morphogenesis of columnar Stromatolites (Conophyton, Vacerrilla) from Hot Springs in Yellowstone National Park, in: Walter, M.R.B.T.-D. in S. (Ed.), Stromatolites. Elsevier, pp. 273–310. https://doi.org/10.1016/S0070-4571(08)71140-3

Wang, Q., Zhang, T., 2010. Review of mathematical models for biofilms. Solid State Commun. 150, 1009–1022. https://doi.org/10.1016/j.ssc.2010.01.021

Wanner, O., 2015. Mathematical modeling of biofilms. Water Intell. Online 5, 9781780402482–9781780402482. https://doi.org/10.2166/9781780402482

Wanner, O., Gujer, W., 1986. A multispecies biofilm model. Biotechnol. Bioeng. 28, 314–328. https://doi.org/10.1002/bit.260280304

Wanner, O., Morgenroth, E., 2004. Biofilm modeling with AQUASIM. Water Sci. Technol. a J. Int. Assoc. Water Pollut. Res. 49, 137–144.

Wanner, O., Reichert, P., 1996. Mathematical modeling of mixed-culture biofilms. Biotechnol. Bioeng. 49, 172–184. https://doi.org/10.1002/(SICI)1097-0290(19960120)49:2<172::AID-BIT6>3.0.CO;2-N

Wenzhöfer, F., Glud, R.N., 2004. Small-scale spatial and temporal variability in coastal benthic O2dynamics: Effects of fauna activity. Limnol. Oceanogr. 49, 1471–1481. https://doi.org/10.4319/lo.2004.49.5.1471

Wessel, A.K., Hmelo, L., Parsek, M.R., Whiteley, M., 2013. Going local: technologies for exploring bacterial microenvironments. Nat. Rev. Microbiol. 11, 337–348. https://doi.org/10.1038/nrmicro3010

Wichelns, D., Drechsel, P., Qadir, M., 2015. Wastewater: economic asset in an urbanizing world, in: Drechsel, P., Qadir, M., Wichelns, D. (Eds.), Wastewater. Springer Netherlands, Dordrecht, pp. 3–14. https://doi.org/10.1007/978-94-017-9545-6_1

Wieland, A., Kühl, M., 2000. Short-term temperature effects on oxygen and sulfide cycling in a hypersaline cyanobacterial mat (Solar Lake, Egypt). Mar. Ecol. Prog. Ser. 196, 87–102.

Williamson, K., McCarty, P.L., 1976. A model of substrate utilization by bacterial films. J. (Water Pollut. Control Fed. 48, 9–24.

Wimpenny, J., Manz, W., Szewzyk, U., 2000. Heterogeneity in biofilms. FEMS Microbiol. Rev. 24, 661–671. https://doi.org/10.1111/j.1574-6976.2000.tb00565.x

Winkler, M.-K.H., Meunier, C., Henriet, O., Mahillon, J., Suárez-Ojeda, M.E., Del Moro, G., De Sanctis, M., Di Iaconi, C., Weissbrodt, D.G., 2018. An integrative review of granular sludge for the biological removal of nutrients and recalcitrant organic matter from wastewater. Chem. Eng. J. 336, 489–502. https://doi.org/https://doi.org/10.1016/j.cej.2017.12.026

Wolf, G., Picioreanu, C., Van Loosdrecht, M.C.M., 2007. Kinetic modeling of phototrophic biofilms: The PHOBIA model. Biotechnol. Bioeng. 97, 1064–1079. https://doi.org/10.1002/bit.21306

Wolfbeis, O.S., 2006. Fiber-optic chemical sensors and biosensors. Anal. Chem. 78, 3859–3874. https://doi.org/10.1021/ac060490z

Wood, B.D., Whitaker, S., 1999. Cellular growth in biofilms. Biotechnol. Bioeng. 64, 656–670. https://doi.org/10.1002/(SICI)1097-0290(19990920)64:6<656::AID-BIT4>3.0.CO;2-N

Wu, J., de los Reyes, F.L., Ducoste, J.J., 2020. Modeling cell aggregate morphology during

aerobic granulation in activated sludge processes reveals the combined effect of substrate and shear. Water Res. 170, 115384. https://doi.org/10.1016/j.watres.2019.115384

Xavier, J.B., de Kreuk, M.K., Picioreanu, C., Van Loosdrecht, M.C.M., 2007. Multi-scale individual-based model of microbial and bioconversion dynamics in aerobic granular sludge. Environ. Sci. Technol. 41, 6410–6417. https://doi.org/10.1021/es070264m

Yang, J., Xu, M., Zhang, X., Hu, Q., Sommerfeld, M., Chen, Y., 2011. Life-cycle analysis on biodiesel production from microalgae: Water footprint and nutrients balance. Bioresour. Technol. 102, 159–165. https://doi.org/10.1016/j.biortech.2010.07.017

Yin, Z., Zhu, L., Li, S., Hu, T., Chu, R., Mo, F., Hu, D., Liu, C., Li, B., 2020. A comprehensive review on cultivation and harvesting of microalgae for biodiesel production: Environmental pollution control and future directions. Bioresour. Technol. 301, 122804. https://doi.org/https://doi.org/10.1016/j.biortech.2020.122804

Yuan, S., Gao, M., Zhu, F., Afzal, M.Z., Wang, Y.-K., Xu, H., Wang, M., Wang, S.-G., Wang, X.-H., 2017. Disintegration of aerobic granules during prolonged operation. Environ. Sci. Water Res. Technol. 3, 757–766. https://doi.org/10.1039/C7EW00072C

Zabed, H.M., Akter, S., Yun, J., Zhang, G., Zhang, Y., Qi, X., 2020. Biogas from microalgae: Technologies, challenges and opportunities. Renew. Sustain. Energy Rev. 117, 109503. https://doi.org/10.1016/j.rser.2019.109503

Zhang, B., Guo, Y., Lens, P.N.L., Zhang, Z., Shi, W., Cui, F., Tay, J.H., 2019. Effect of light intensity on the characteristics of algal-bacterial granular sludge and the role of N-acyl-homoserine lactone in the granulation. Sci. Total Environ. 659, 372–383. https://doi.org/10.1016/j.scitotenv.2018.12.250

Zhang, M., Ma, Y., 2019. Energy use and challenges in current wastewater treatment plants. https://doi.org/10.2166/9781789060089_0001

Zhang, Q., Hu, J., Lee, D.-J., 2016. Aerobic granular processes: Current research trends. Bioresour. Technol. 210, 74–80. https://doi.org/10.1016/j.biortech.2016.01.098

Zheng, Y.-M., Yu, H.-Q., Liu, S.-J., Liu, X.-Z., 2006. Formation and instability of aerobic granules under high organic loading conditions. Chemosphere 63, 1791–1800.

https://doi.org/https://doi.org/10.1016/j.chemosphere.2005.08.055

Zhu, C., Liu, Q., 2013. Review of Monte Carlo modeling of light transport in tissues. J. Biomed. Opt. 18, 050902. https://doi.org/10.1117/1.jbo.18.5.050902

Zippel, B., Neu, T.R., 2005. Growth and structure of phototrophic biofilms under controlled light conditions. Water Sci. Technol. 52, 203–209. https://doi.org/10.2166/wst.2005.0202

Appendices

Chapter 2 supplementary materials

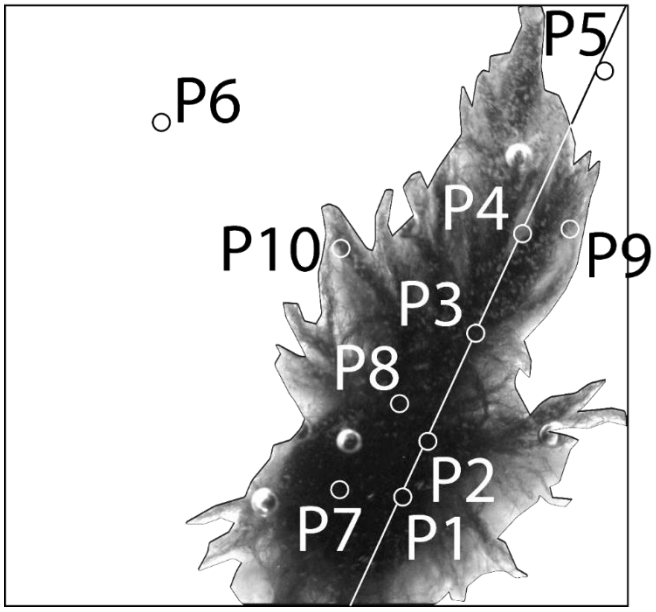

Figure S 1 *OPG stereomicroscopic image and location of points P1 – P10 used for model calibration. P1, P2, P7 and P8 are located near the center of the photogranule. P3, P4, P9 and P10 are within its filaments. P5 and P6 are in the bulk.*

Figures S2 – S11 show the details of the best fits of models for points P1 – P10 associated with scenarios 1 – 8 (see Table 1 in the main text).

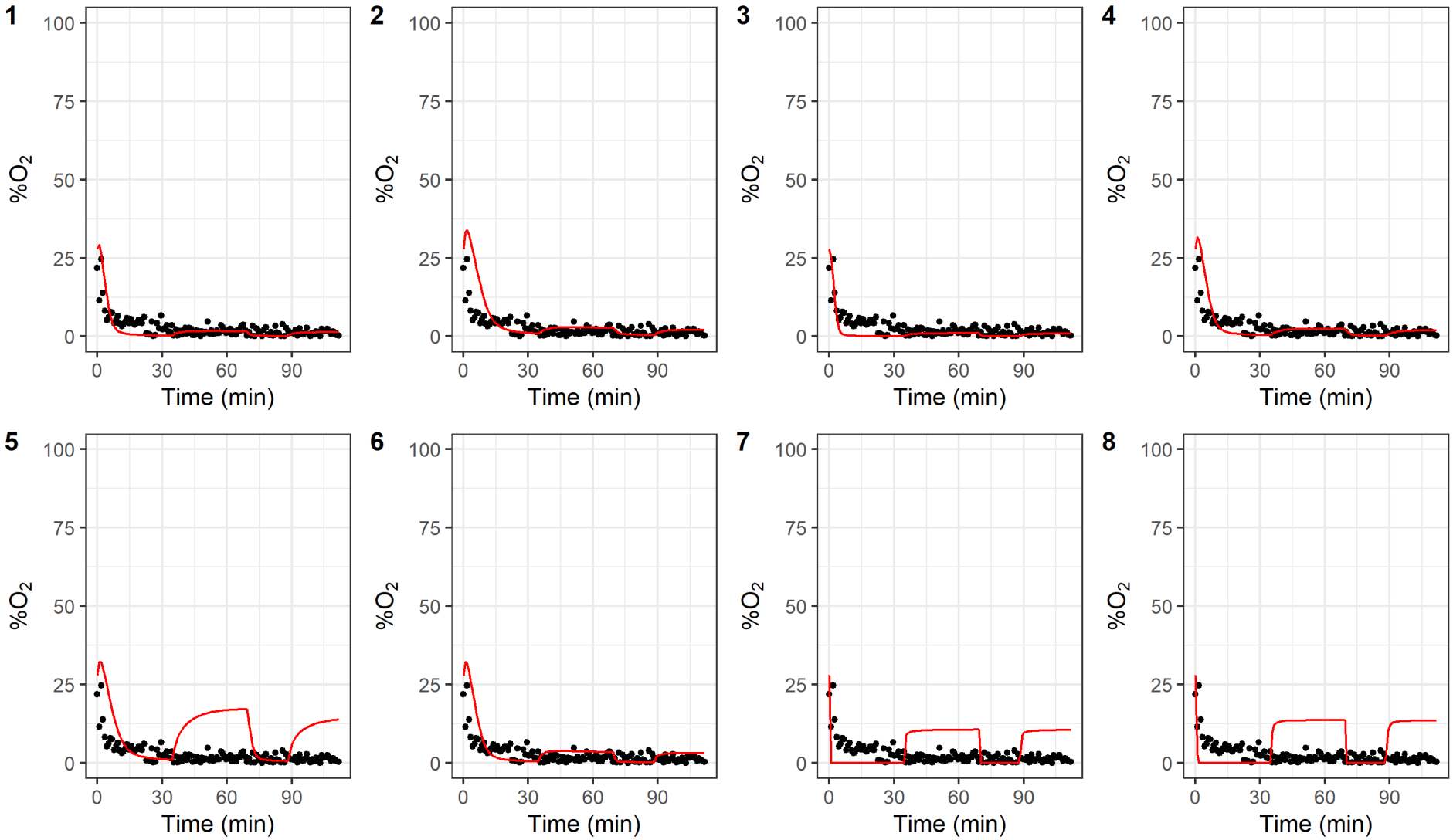

Figure S 2 *Oxygen saturation (with respect to air) at point* ***P1*** *over time. The points are measured data, red solid lines are the model output. Panels 1 - 8 correspond to scenarios 1 - 8 respectively.*

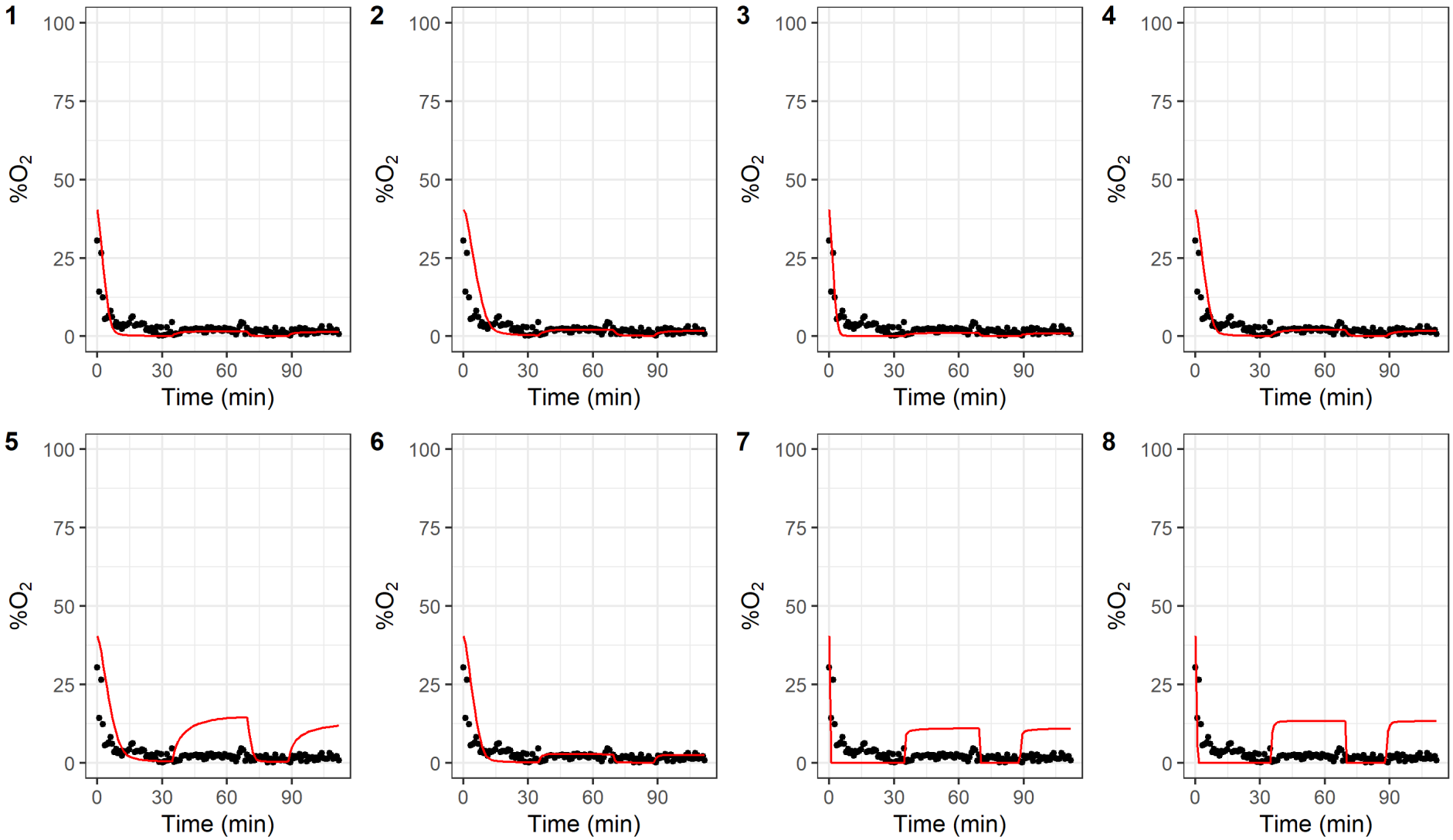

Figure S 3 *Oxygen saturation (with respect to air) at point* ***P2*** *over time. The points are measured data, red solid lines are the model output. Panels 1 - 8 correspond to scenarios 1 - 8 respectively.*

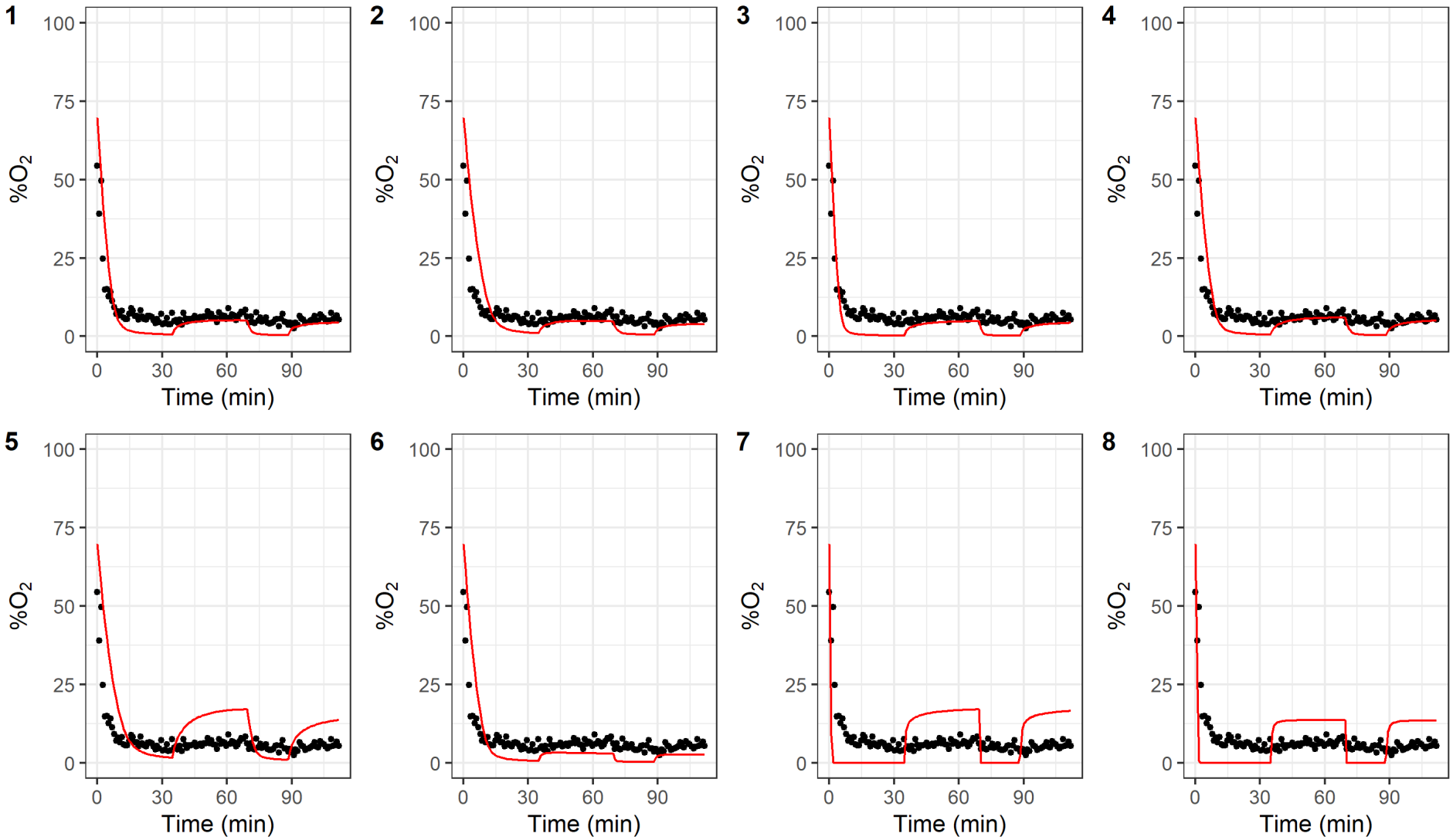

Figure S 4 *Oxygen saturation (with respect to air) at point* ***P3*** *over time. The points are measured data, red solid lines are the model output. Panels 1 - 8 correspond to scenarios 1 - 8 respectively.*

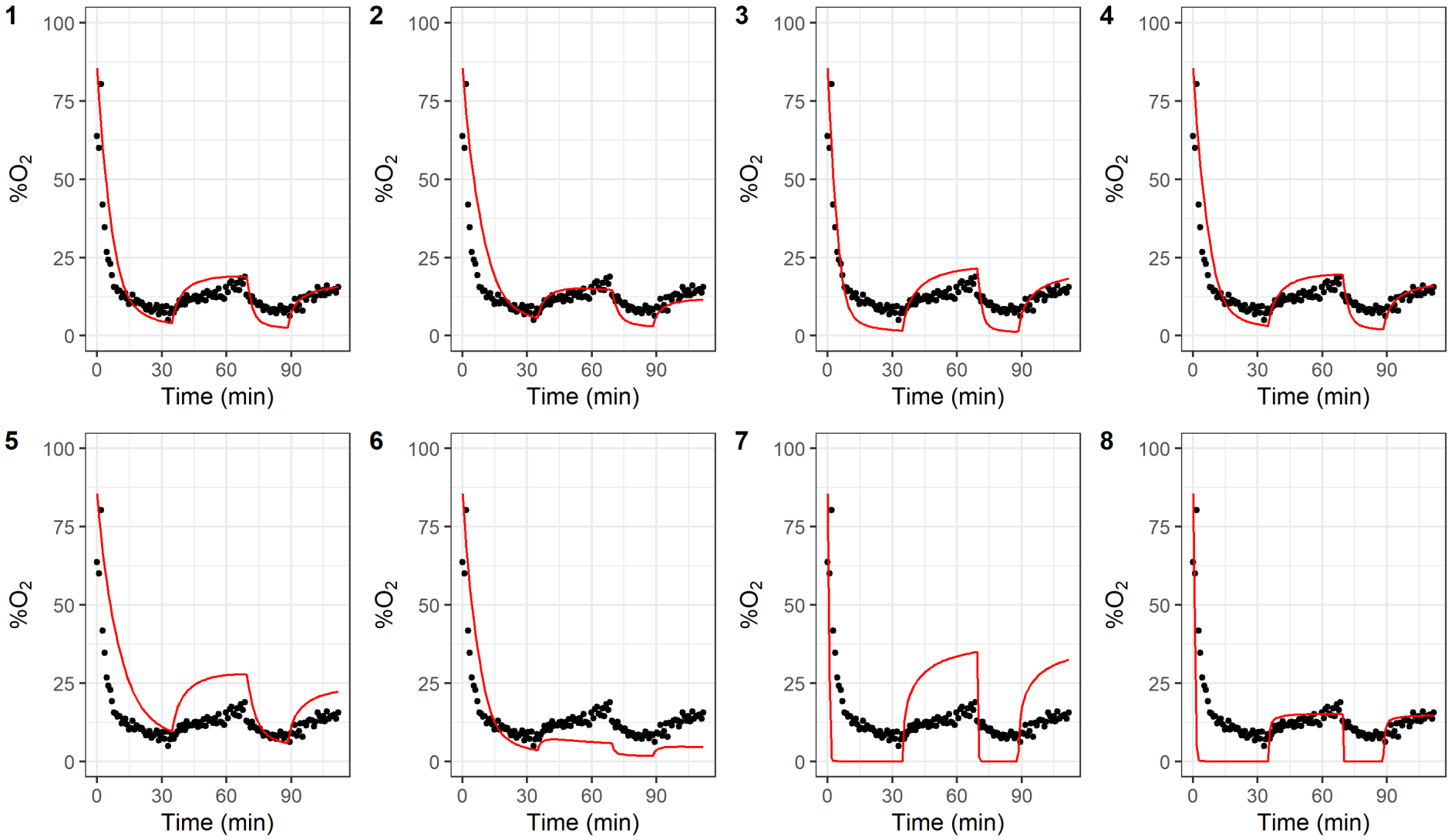

Figure S 5 *Oxygen saturation (with respect to air) at point* ***P4*** *over time. The points are measured data, red solid lines are the model output. Panels 1 - 8 correspond to scenarios 1 - 8 respectively.*

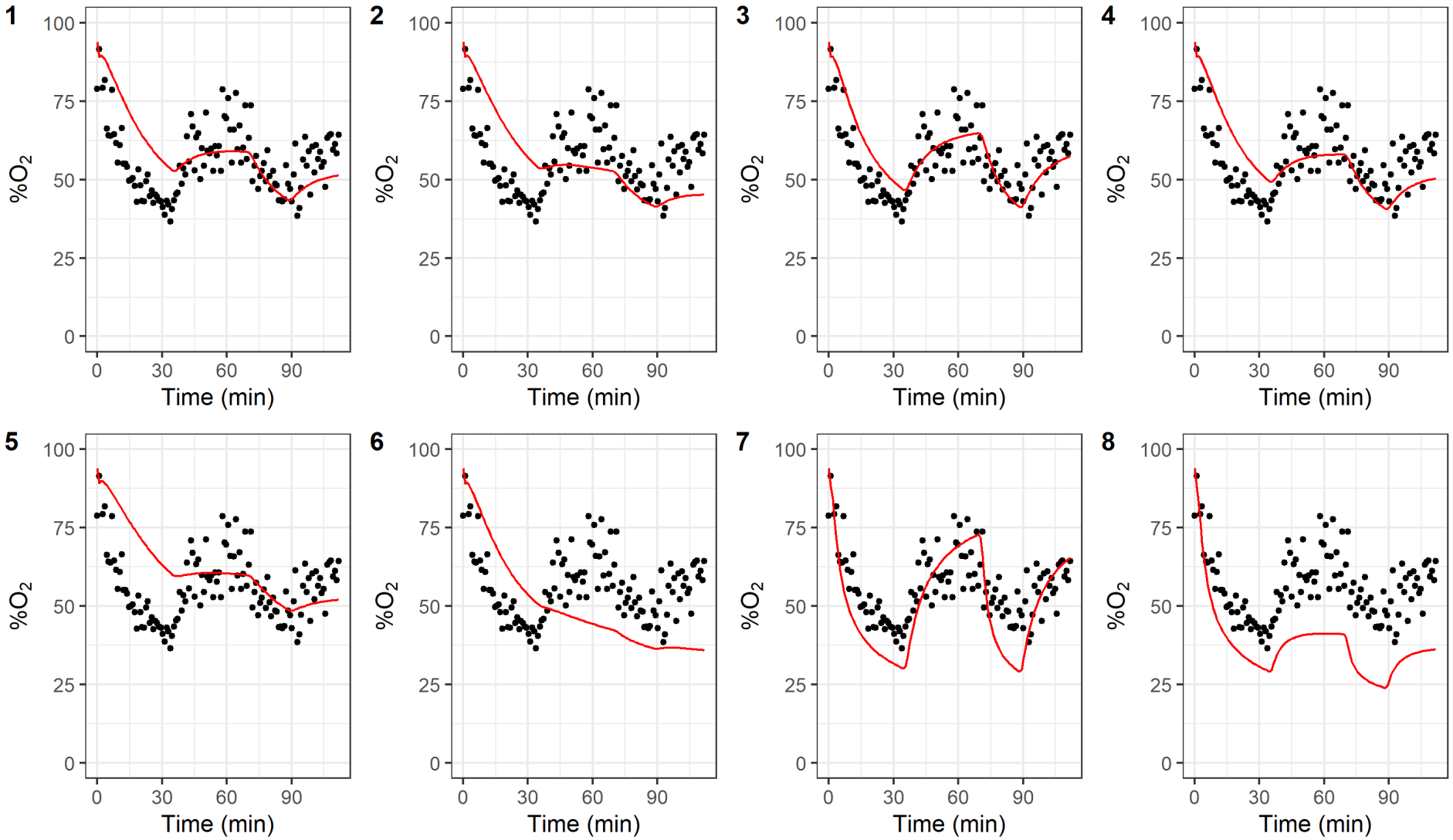

Figure S 6 *Oxygen saturation (with respect to air) at point* ***P5*** *over time. The points are measured data, red solid lines are the model output. Panels 1 - 8 correspond to scenarios 1 - 8 respectively.*

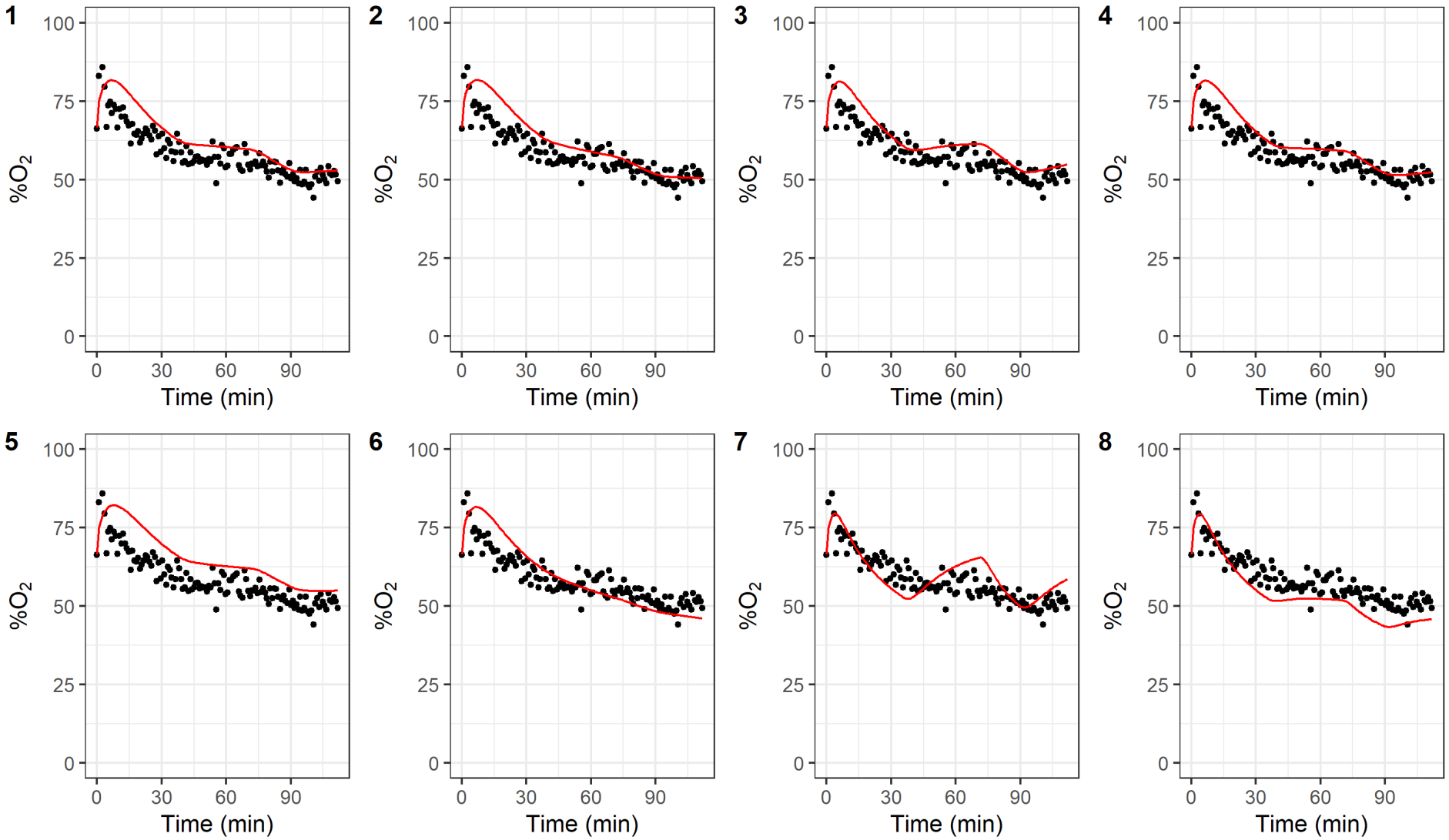

Figure S 7 *Oxygen saturation (with respect to air) at point* ***P6*** *over time. The points are measured data, red solid lines are the model output. Panels 1 - 8 correspond to scenarios 1 - 8 respectively.*

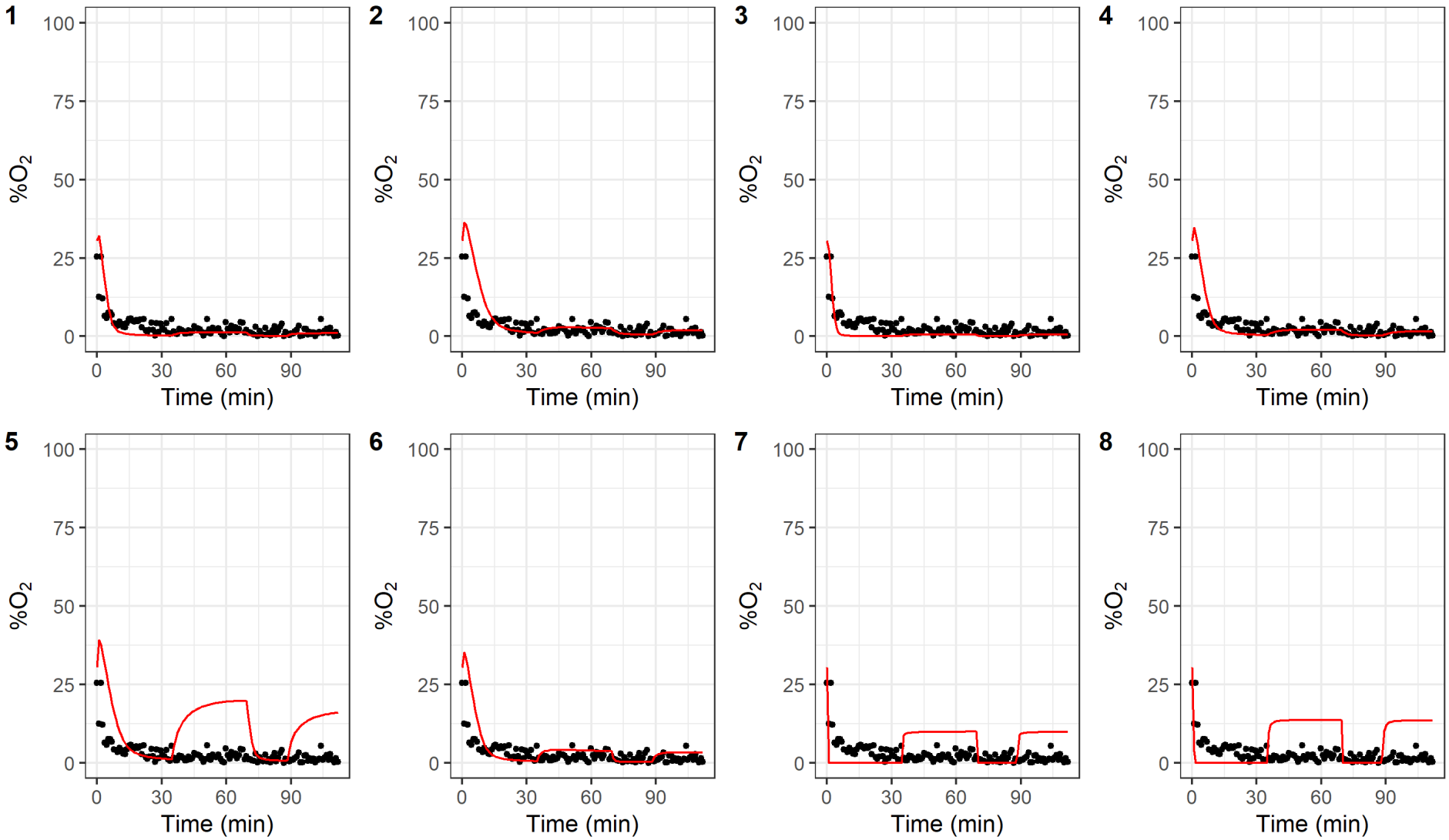

Figure S 8 *Oxygen saturation (with respect to air) at point* ***P7*** *over time. The points are measured data, red solid lines are the model output. Panels 1 - 8 correspond to scenarios 1 - 8 respectively.*

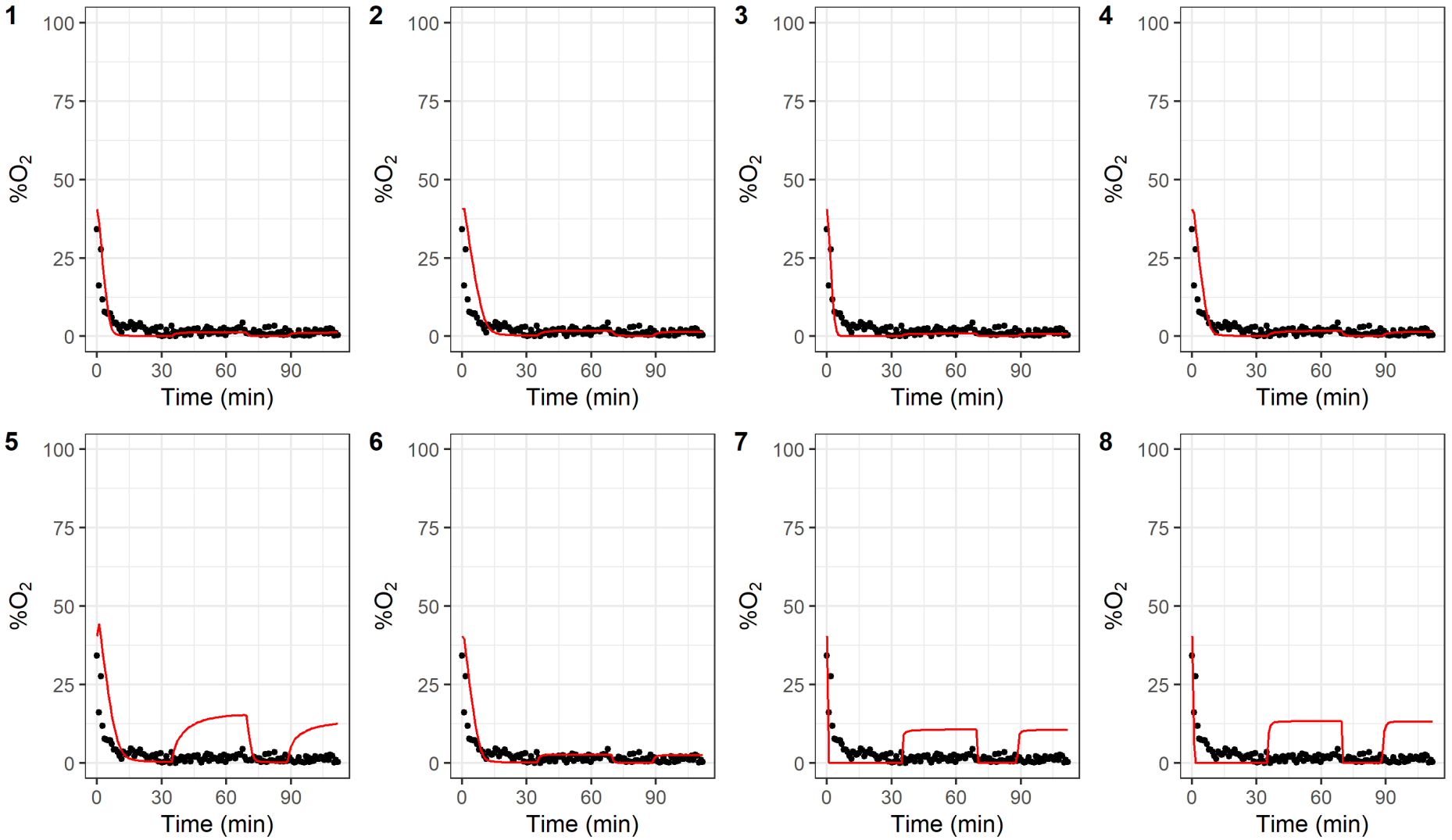

Figure S 9 *Oxygen saturation (with respect to air) at point* ***P8*** *over time. The points are measured data, red solid lines are the model output. Panels 1 - 8 correspond to scenarios 1 - 8 respectively.*

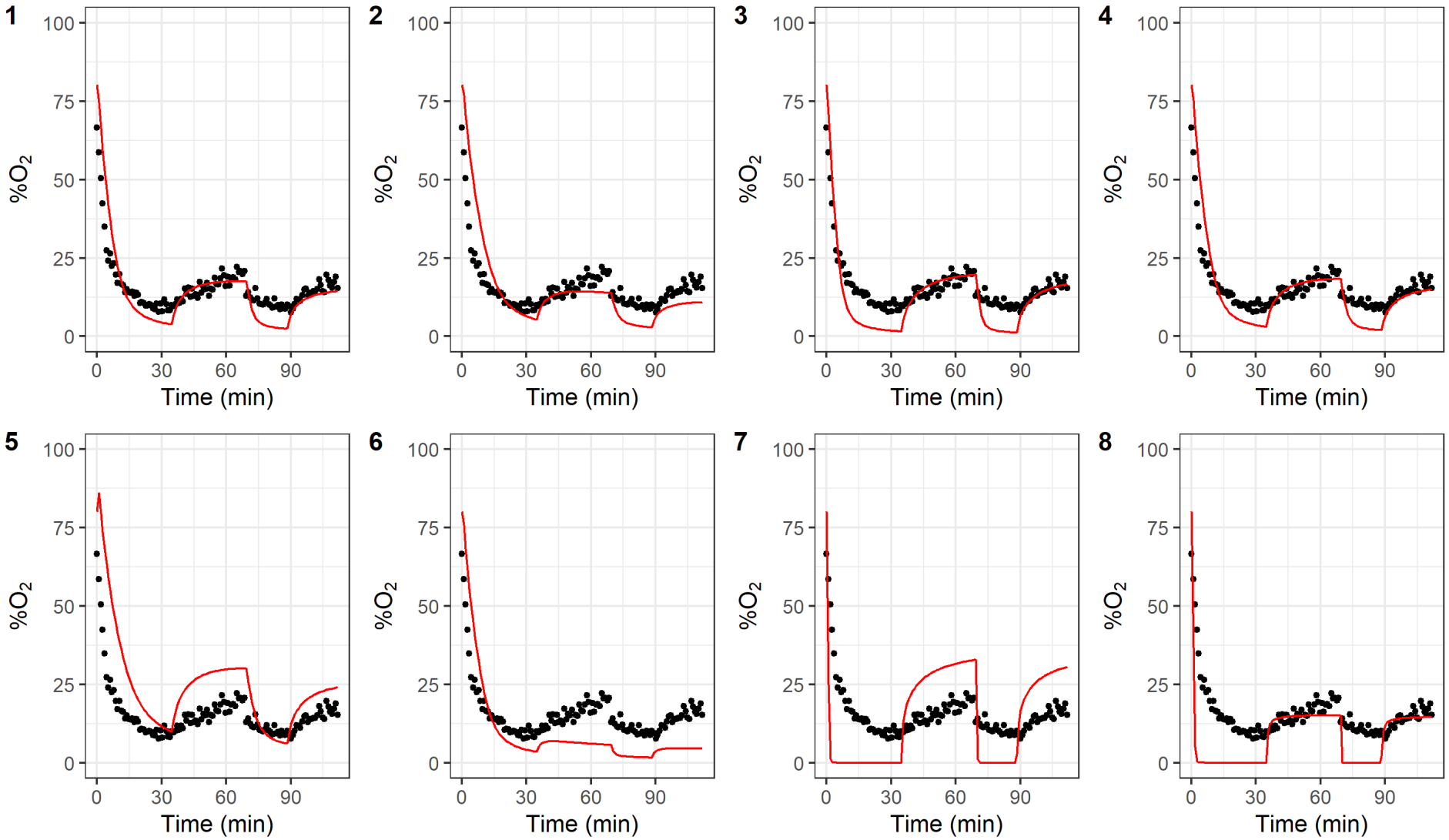

Figure S 10 *Oxygen saturation (with respect to air) at point* ***P9*** *over time. The points are measured data, red solid lines are the model output. Panels 1 - 8 correspond to scenarios 1 - 8 respectively.*

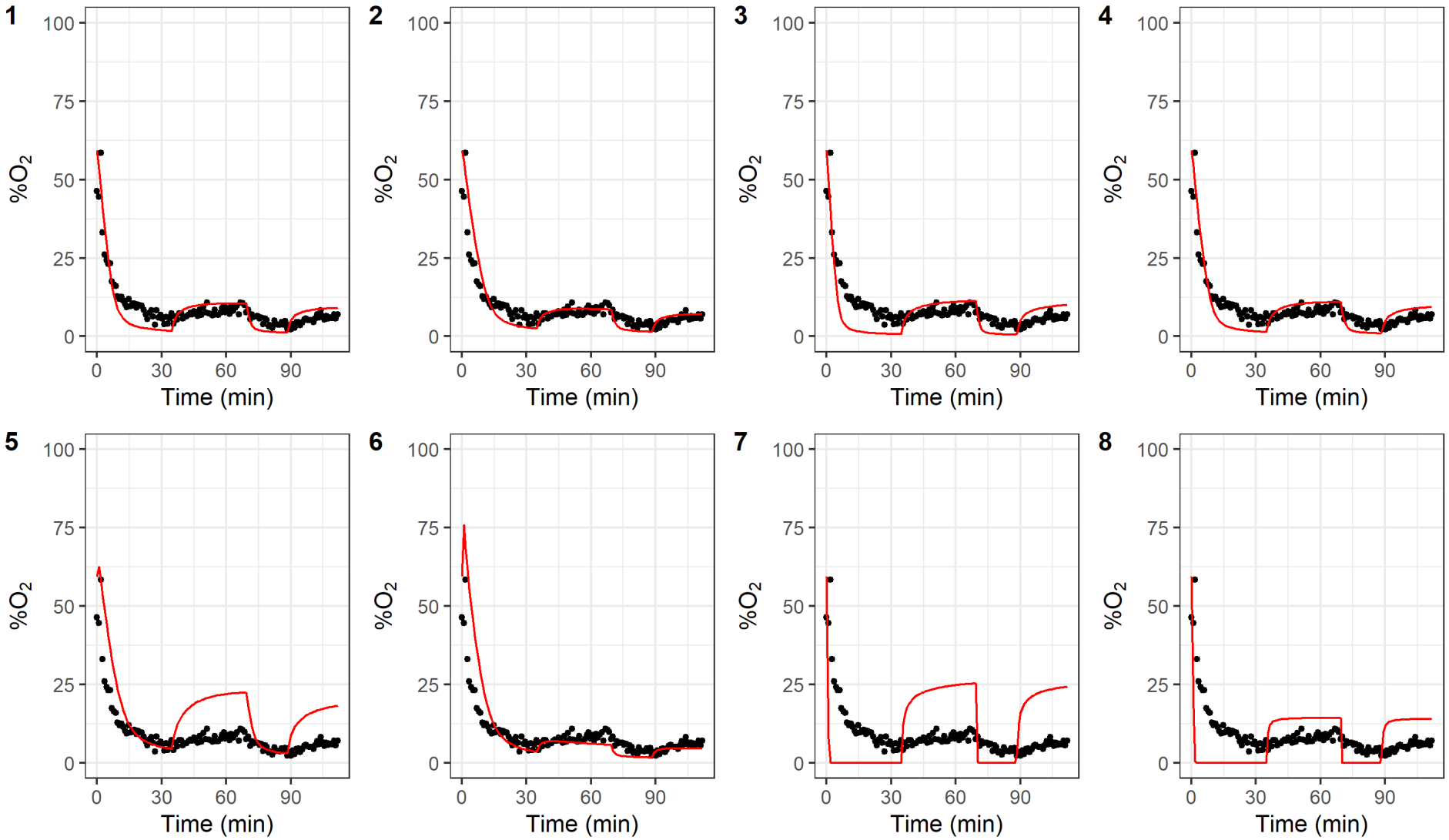

Figure S 11*Oxygen saturation (with respect to air) at point* ***P10*** *over time. The points are measured data, red solid lines are the model output. Panels 1 - 8 correspond to scenarios 1 - 8 respectively.*

Chapter 3 supplementary materials

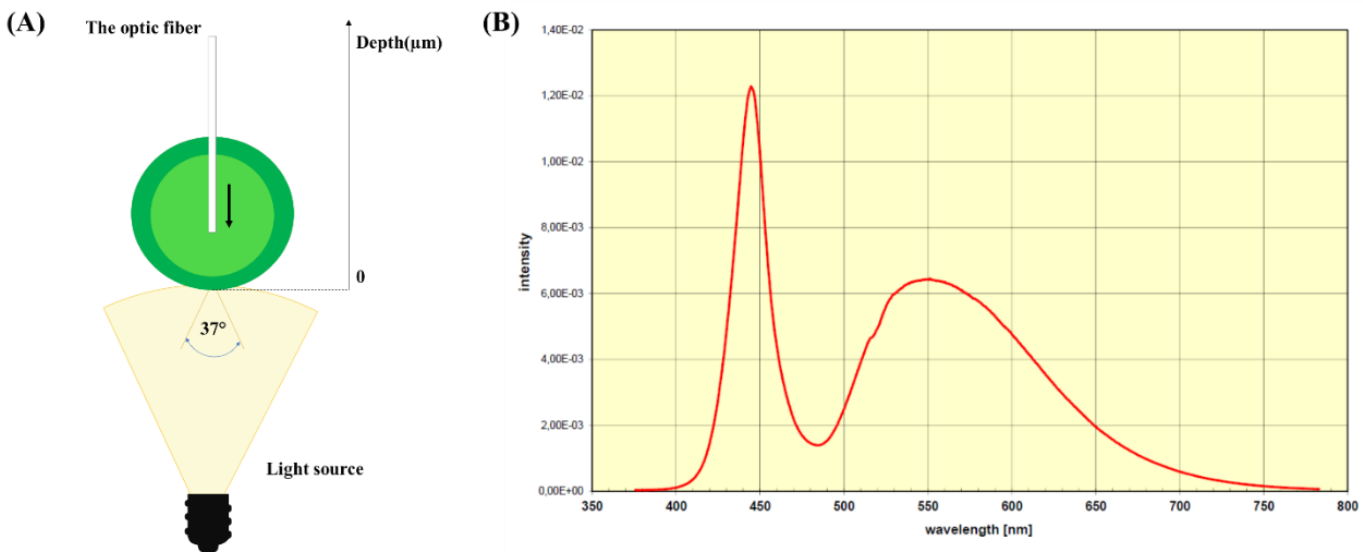

Figure S01: (A) Scheme of experimental steps for light gradients measurement in the oxygenic photogranule. (B) Light spectral of the light source (KL2500LED) (from www.schott.com*)*

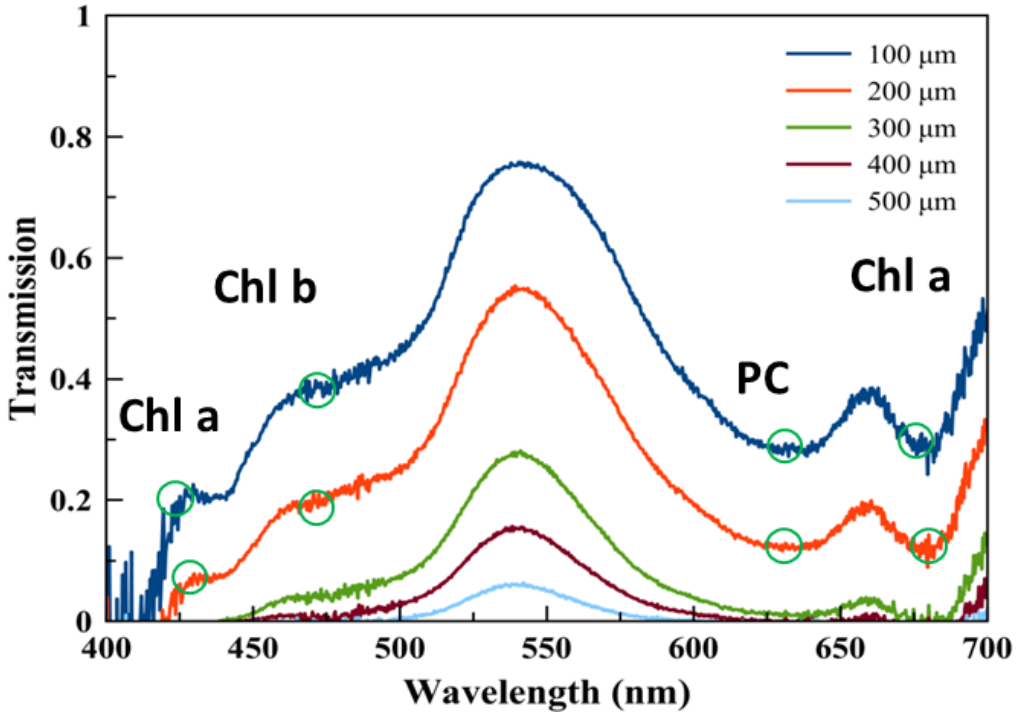

Figure S02 : Scalar irradiance attenuation spectrum at different depth of the photogranules. Circles in green indicate transmission wavelengths of Chl a, Phycocyanin (PC), and Chl b.

Table S01: Model parameter overview of the 1D reaction diffusion model

Model parameter	Symbol	unit	value	Reference
Specific maximum photosynthesis rate	$q_{O2,photo}$	$mmol \cdot m^{-3} \cdot s^{-1}$	31.64 [a] /14.38[b]	Estimated
Specific maximum dark respiration rate of phototrophs	$q_{O2,dark}$	$mmol \cdot m^{-3} \cdot s^{-1}$	0.1[a] /0.07 [b]	Estimated
Specific maximum O_2 consumption rate of heterotrophs using EOMs [(*)]	$q_{O2,het1}$	$mmol \cdot m^{-3} \cdot s^{-1}$	0.62 [a] /0.42 [b]	Estimated
Specific maximum O_2 consumption rate of heterotrophs using Acetate	$q_{O2,het2}$	$mmol \cdot m^{-3} \cdot s^{-1}$	0.67[a] /0.36 [b]	Estimated
Light extinction coefficient	K_e	m^{-1}	6764	Experimental
Onset light saturation intensity	I_k[(**)]	$\mu moles_{PAR} \cdot m^{-2} \cdot s^{-1}$	170	Estimated
Diffusion coefficient of O_2 in water	D_{O2}	$m^2 \cdot s^{-1}$	$2.01\ 10^{-9}$	(Picioreanu et al., 2000c)
Diffusion coefficient of Acetate in water	D_{Ac}	$m^2 \cdot s^{-1}$	$1.2\ 10^{-9}$	(Picioreanu et al., 2000c)
Light inhibition coefficient for phototrophs (dark respiration)	K_{inh}	$\mu moles_{PAR} \cdot m^{-2} \cdot s^{-1}$	≈2	(Wolf et al., 2007)
O_2 half saturation coefficient phototrophs	$K_{S,O2,Ph}$	$mg \cdot l^{-1}$	0.1	(Wolf et al., 2007)
O_2 half saturation coefficient heterotrophs	$K_{S,O2,Het}$	$mg \cdot l^{-1}$	0.1	(Wolf et al., 2007)
Acetate half saturation coefficient heterotrophs	$K_{S,Ac,Het}$	$mg \cdot l^{-1}$	4	(Xavier et al., 2007)
Heterotrophs Acetate conversion yield	$Y_{Ac/O2}$	mol/mol	1	(Xavier et al., 2007)

[(a)] *Correspond to the model parameters used to simulate the dissolved oxygen gradients in the photogranules sampled from the Sequencing batch reactor SBR fed with simple synthentic waste water.*

[(b)] *Correspond to the model parameters used to simulate the dissolved oxygen gradients in the photogranules sampled from the continuous strired reactor CSTR fed with dissolved methane.*

[(*)] *EOMs: Extracellular Organic matters*

[(**)] *Light intensity corresponding to the light saturation regime used in the model of (Jassby and Platt, 1976)*

Table S02: Table of the sum of squared errors between the experimental and model dissolved oxygen gradients in the photogranules depending on the tested experimental conditions.

			Sum of Squared Errors (SSE)							
			Light intensity ($\mu moles_{PAR} \cdot m^{-2} \cdot s^{-1}$)							
Sampling origin	***Diameter (mm)***	***dCOD ($mg_{O2} \cdot L^{-1}$)***	***0***	***10***	***20***	***50***	***60***	***80* / 85*****	***110******	***170***
CSTR for methane effluent polishing	*4.5*	*0*	*13.84*		*15.14*	*4.27*	*7.01*	*8.44*	*18.67*	*50.91*
		500	*22.34*		*6.77*	*6.25*	*19.44*		*15.49*	*167.18*
SBR for synthetic wastewater treatment	*3.2*	*30*	*7.80*	*3.55*			*15.75*	*14.41*		
	3.4		*31.36*	*4.586*			*28.65*	*15.44*		
	3.7		*12.39*	*9.92*			*24.31*	*32.76*		
	4.5		*13.19*	*16.81*			*125.93*	*78.84*		
	5		*8.42*	*26.64*			*87.04*	*31.73*		

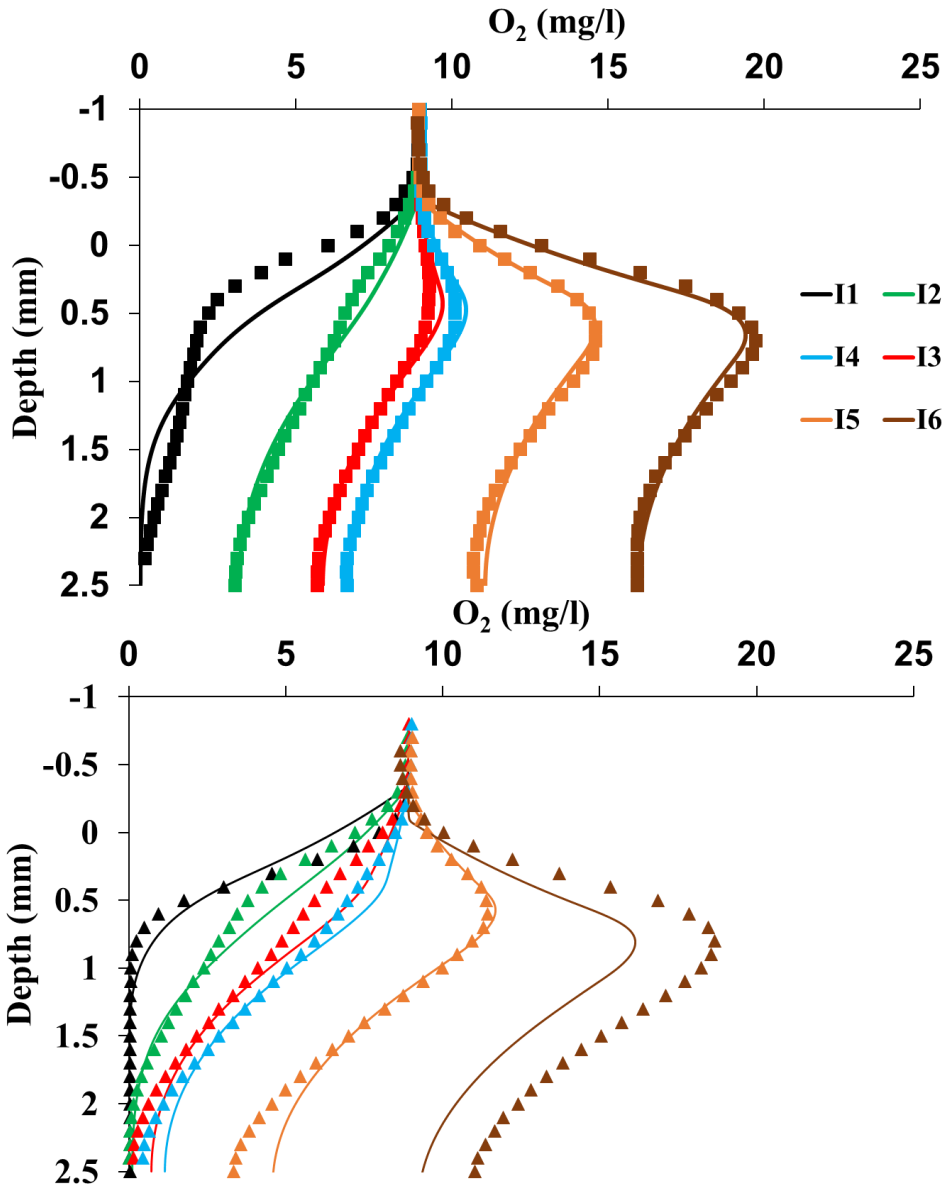

Figure S03: Concentration of dissolved oxygen profiles in the second hemisphere of oxygenic photogranule from CSTR exposed to different light intensities (black: 0, blue: 20, gold: 50, cyan: 60, green: 110, marron: 170 $\mu moles_{PAR} \cdot m^{-2} \cdot s^{-1}$), and within two carbon environment condition. (A) Photogranule exposed a starve carbon environment (only tap water). (B) Photogranule exposed to a rich carbon environment (500 mg·L-1 of Acetate). Circles indicates the experimental measurement and solid lines indicates the model results. Grey dashed line represents the interface photogranule-bulk.

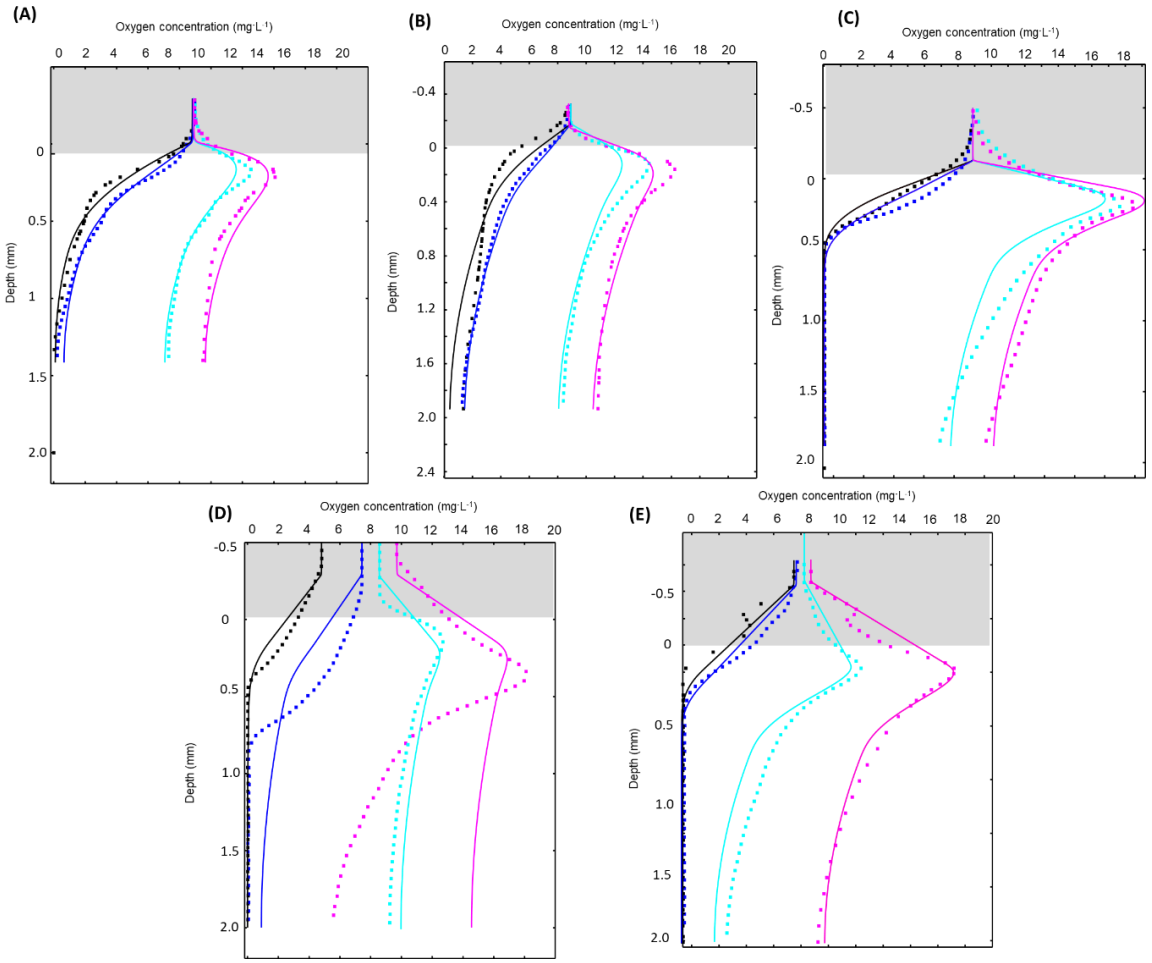

Figure S04: Concentration of dissolved oxygen profiles profiles in the second hemisphere of photogranules from SBR with different diameters exposed to different light intensities (black: 0, blue: 10, cyan: 60, magenta: 80 $\mu moles_{PAR} \cdot m^{-2} \cdot s^{-1}$), and environment amended with 30 $mg_{COD} \cdot L^{-1}$ acetate of acetate. (A) Photogranule with diameter of 3.2 mm (B) Photogranule with diameter of 3.4 mm. (C) Photogranule with diameter of 3.7 mm (D) Photogranule with diameter of 4.5 mm (E) Photogranule with diameter of 5 mm. Points indicates the experimental measurement and solid lines indicates the model results. Grey dashed line represents the interface photogranule-bulk.

Chapter 4 supplementary materials

Table S01: Model parameter overview

Model parameter	Symbol	unit	value	Reference
Specific maximum photosynthesis rate	$q_{O2,photo}$	$mmol \cdot m^{-3} \cdot s^{-1}$	38.24	Estimated
Specific maximum dark respiration rate of phototrophs	$q_{O2,dark}$	$mmol \cdot m^{-3} \cdot s^{-1}$	1.50	Estimated
Specific maximum O_2 consumption rate of heterotrophs using EOMs (*)	$q_{O2,het1}$	$mmol \cdot m^{-3} \cdot s^{-1}$	0.42	Estimated
Specific maximum O_2 consumption rate of heterotrophs using Acetate	$q_{O2,het2}$	$mmol \cdot m^{-3} \cdot s^{-1}$	3.97	Estimated
Light extinction coefficient	K_e	m^{-1}	6764	Experimental
Onset light saturation intensity	I_k(**)	$\mu moles_{PAR} \cdot m^{-2} \cdot s^{-1}$	170	Estimated
Diffusion coefficient of O_2 in water	D_{O2}	$m^2 \cdot s^{-1}$	$2.01\ 10^{-9}$	(Picioreanu et al., 2000c)
Diffusion coefficient of Acetate in water	D_{Ac}	$m^2 \cdot s^{-1}$	$1.2\ 10^{-9}$	(Picioreanu et al., 2000c)
Light inhibition coefficient for phototrophs (dark respiration)	K_{inh}	$\mu moles_{PAR} \cdot m^{-2} \cdot s^{-1}$	≈2	(Wolf et al., 2007)
O_2 half saturation coefficient phototrophs	$K_{S,O2,Ph}$	$mg \cdot l^{-1}$	0.1	(Wolf et al., 2007)
O_2 half saturation coefficient heterotrophs	$K_{S,O2,Het}$	$mg \cdot l^{-1}$	0.1	(Wolf et al., 2007)
Acetate half saturation coefficient heterotrophs	$K_{S,Ac,Het}$	$mg \cdot l^{-1}$	4	(Xavier et al., 2007)
Heterotrophs Acetate conversion yield	$Y_{Ac/O2}$	mol/mol	1	(Xavier et al., 2007)

(*) *EOMs: Extracellular Organic matters*

(**) *Light intensity corresponding to the light saturation regime used in the model of (Jassby and Platt, 1976)*

Table S02: Table of the sum of squared errors between the experimental and model dissolved oxygen gradients in the photogranules depending on the tested experimental conditions.

OPG	Measure	SSE Hemisphere 1	SSE Hemisphere 2	Sum SSE (profile)	Sum SSE (OPG)
1	1	0.37	0.41	0.78	820.30
	2	15.41	22.31	37.71	
	3	1.89	37.29	39.18	
	4	28.88	29.98	58.87	
	5	12.06	7.28	19.35	
	6	34.10	25.41	59.51	
	7	218.62	320.03	538.65	
	8	49.20	8.48	57.68	
	9	1.36	7.22	8.58	
2	1	10.31	27.84	38.15	176.76
	2	2.59	12.99	15.58	
	3	5.75	12.37	18.12	
	4	18.31	32.15	50.46	
	5	1.38	40.38	41.76	
	6	0.07	0.24	0.32	
	7	0.09	0.33	0.42	
	8	0.14	0.31	0.45	
	9	4.59	6.92	11.50	
3	1	15.73	5.95	21.68	982.84
	2	28.17	211.65	239.82	
	3	24.90	574.16	599.06	
	4	16.80	14.97	31.78	
	5	4.52	3.98	8.50	
	6	16.88	2.44	19.32	
	7	0.04	0.04	0.08	
	8	0.02	0.02	0.04	
	9	54.44	8.14	62.57	
4	1	37.55	4.38	41.93	137.93
	2	4.57	4.96	9.53	
	3	3.25	4.18	7.42	
	4	0.09	0.20	0.29	
	5	12.80	0.96	13.77	
	6	15.45	8.12	23.57	
	7	0.08	0.14	0.21	
	8	9.22	9.94	19.16	
	9	20.73	1.32	22.05	
5	1	135.15	199.22	334.37	1114.67
	2	4.42	19.44	23.86	
	3	5.90	1.78	7.67	
	4	42.20	5.60	47.79	

	5	81.43	508.42	589.85	
	6	32.36	30.96	63.32	
	7	7.36	2.36	9.72	
	8	26.61	11.24	37.85	
	9	0.04	0.19	0.23	
6	1	7.10	32.74	39.84	276.13
	2	8.39	0.87	9.26	
	3	0.09	0.82	0.91	
	4	1.52	1.66	3.18	
	5	3.38	1.98	5.36	
	6	35.95	159.74	195.69	
	7	3.09	4.04	7.13	
	8	2.89	1.67	4.56	
	9	4.19	6.02	10.21	

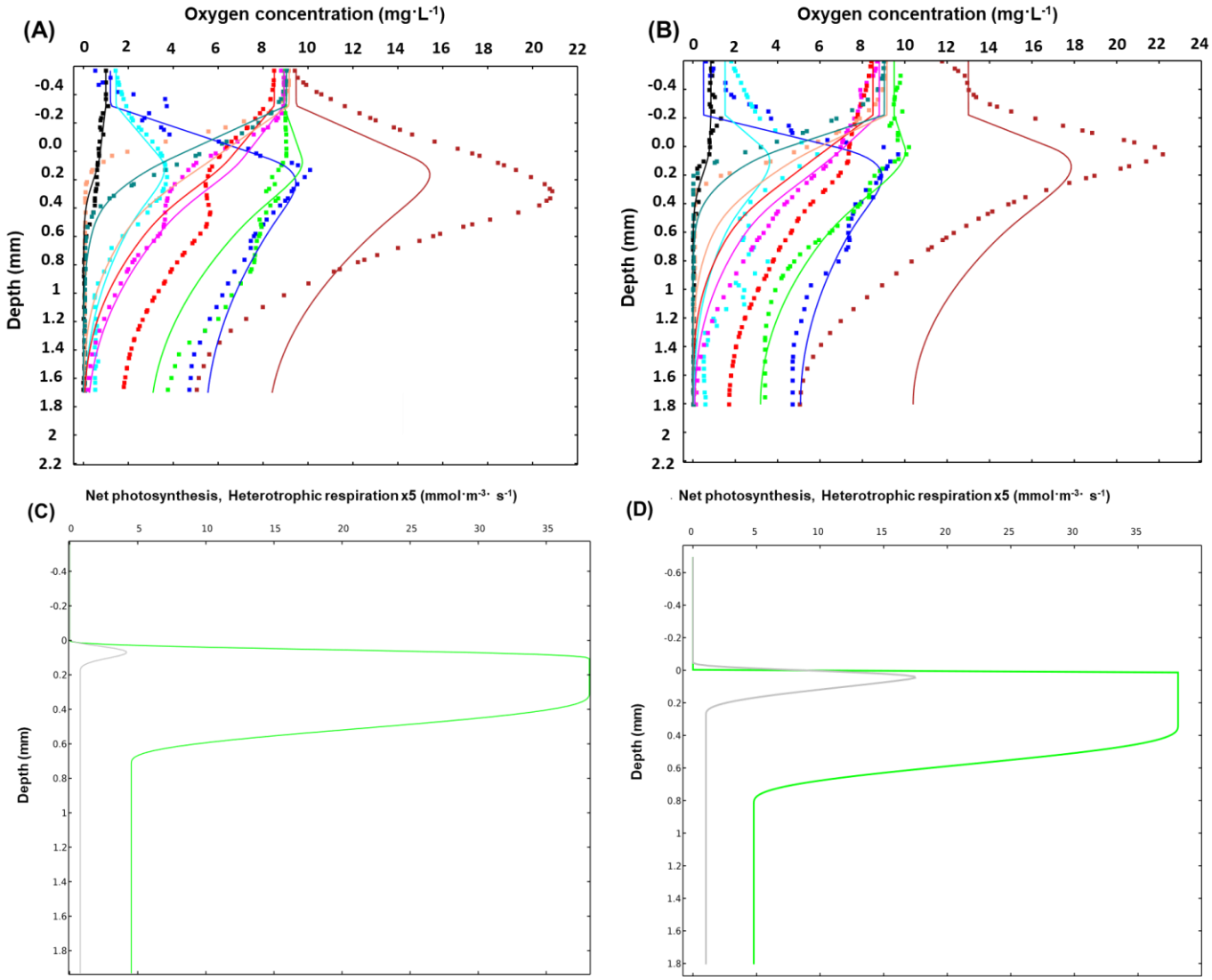

Figure S01: (A) & (B) Concentration of dissolved oxygen profiles in top and bottom hemisphere of oxygenic photogranules N°: 1 under different bulk conditions (Table V.1) (C)& (D) Modelled spatial distribution of metabolic activity in photogranule N°: 1. Green: maximum net photosynthesis. Grey: 5-fold maximum heterotrophic respiration.

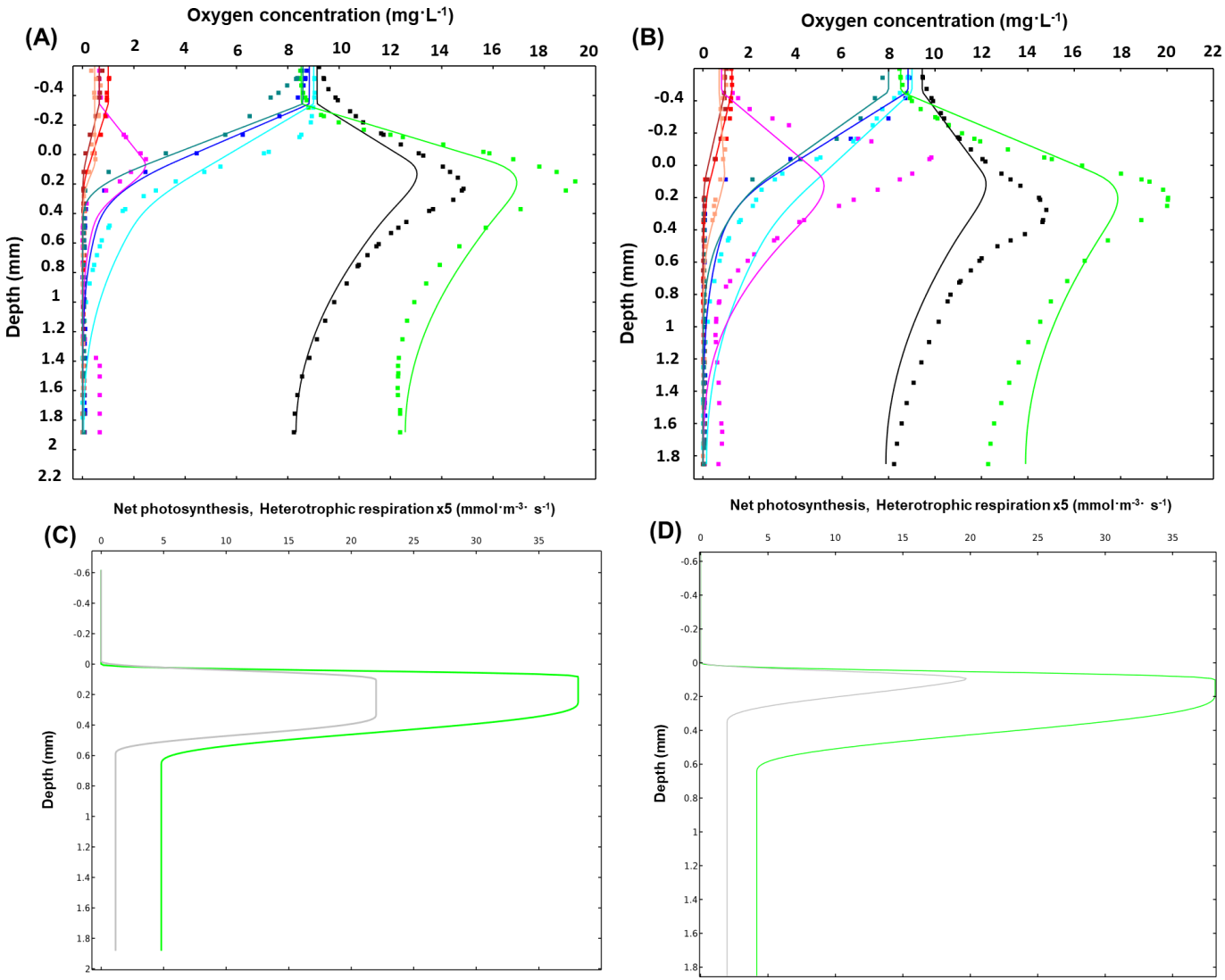

Figure S02: (A) & (B) Concentration of dissolved oxygen profiles in top and bottom hemisphere of oxygenic photogranules N°: 2 under different bulk conditions (Table V.1) (C)& (D) Modelled spatial distribution of metabolic activity in photogranule N°: 2. Green: maximum net photosynthesis. Grey: 5-fold maximum heterotrophic respiration.

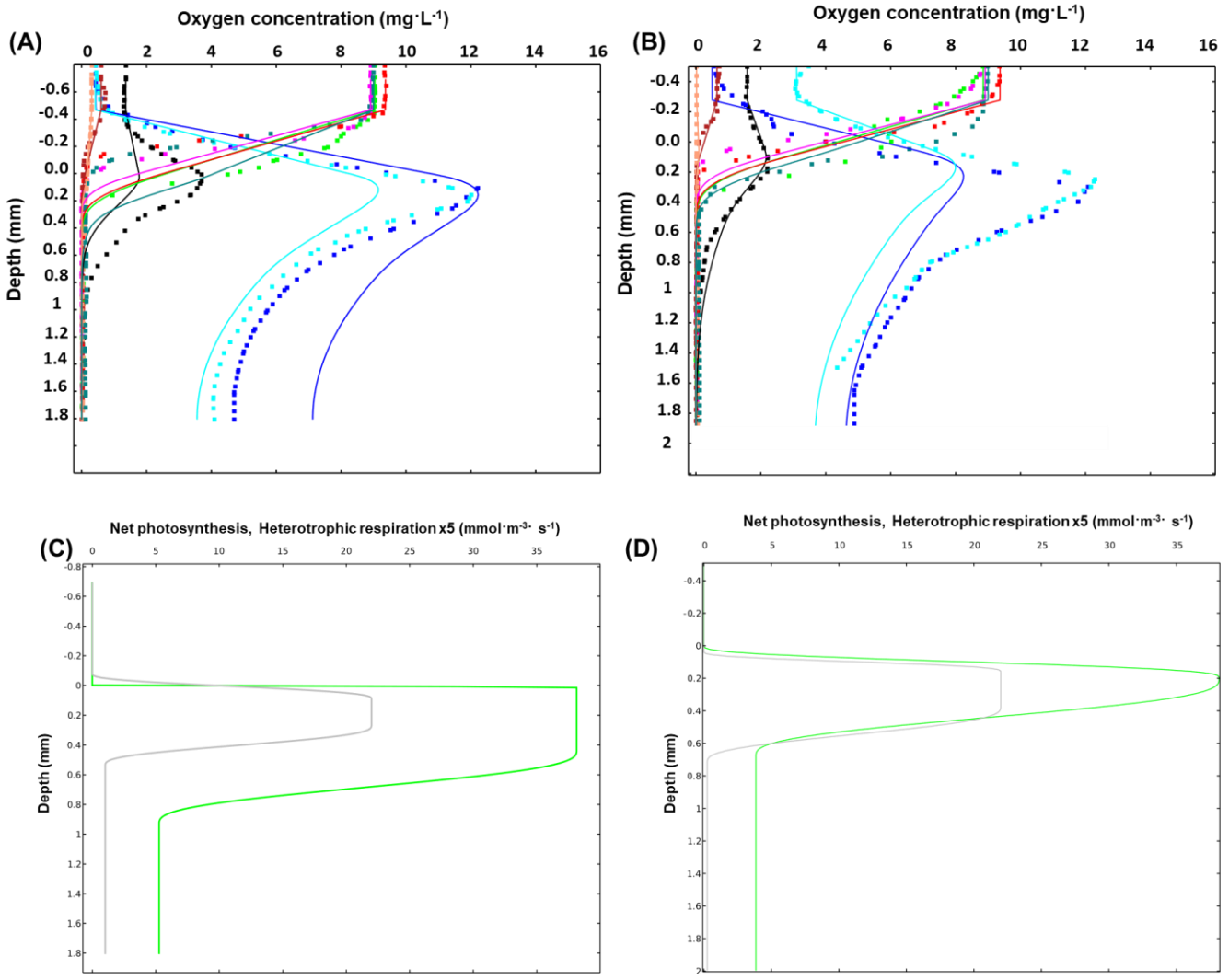

Figure S03:(A) & (B) Concentration of dissolved oxygen profiles in top and bottom hemisphere of oxygenic photogranules N°: 3 under different bulk conditions (Table V.1) (C)& (D) Modelled spatial distribution of metabolic activity in photogranule N°: 3. Green: maximum net photosynthesis. Grey: 5-fold maximum heterotrophic respiration.

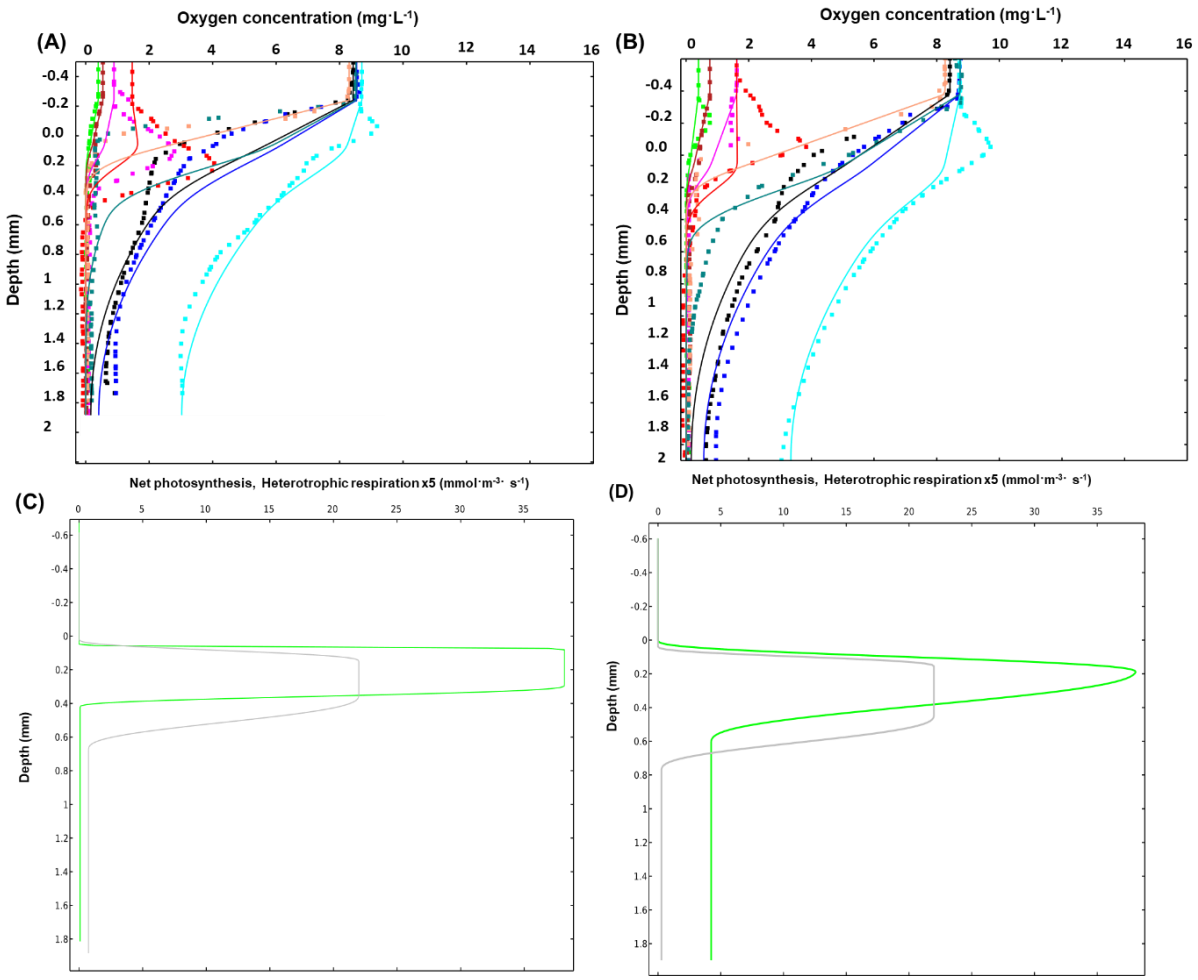

Figure S04: (A) & (B) Concentration of dissolved oxygen profiles in top and bottom hemisphere of oxygenic photogranules N°: 4 under different bulk conditions (Table V.1) (C)& (D) Modelled spatial distribution of metabolic activity in photogranule N°: 4. Green: maximum net photosynthesis. Grey: 5-fold maximum heterotrophic respiration.

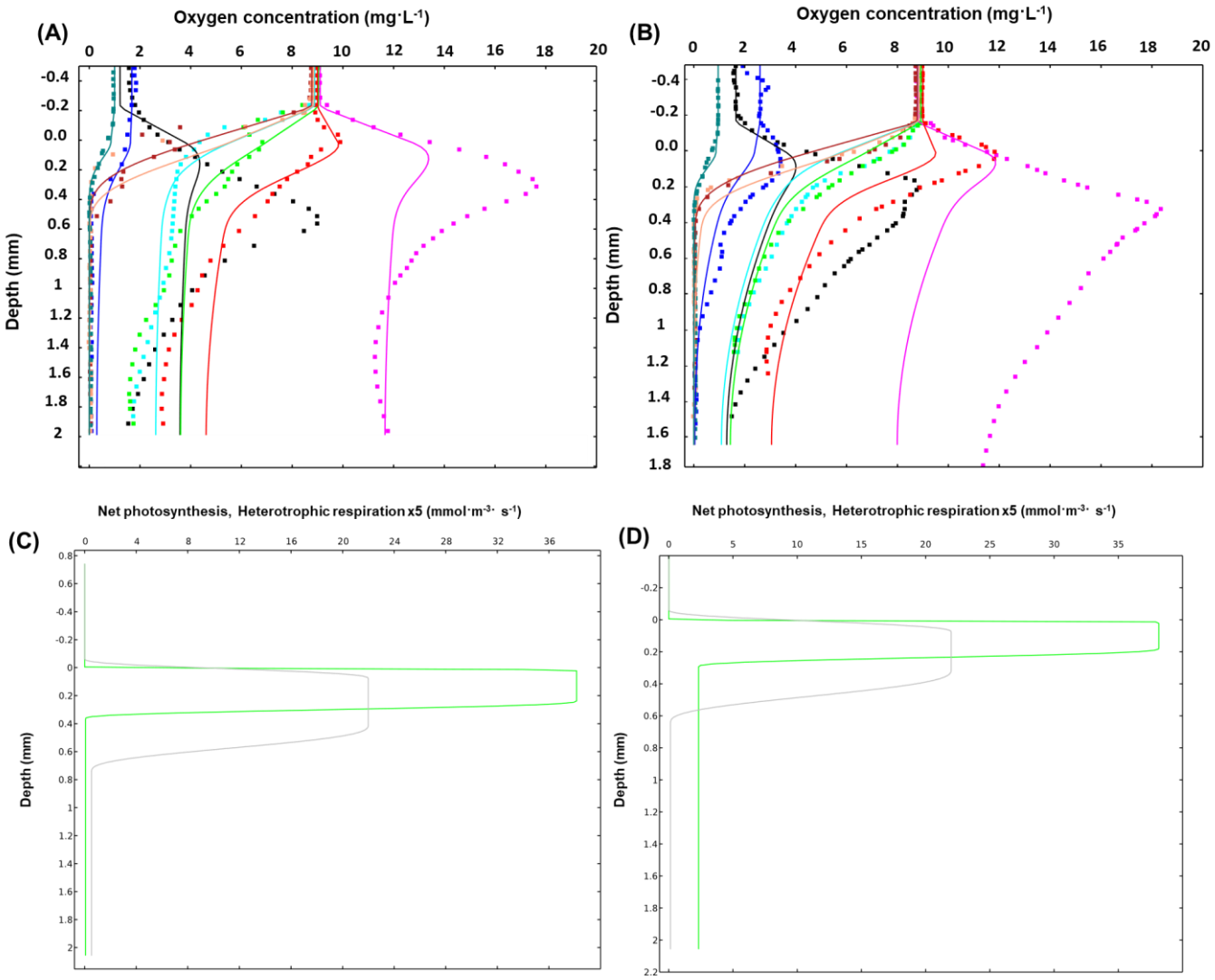

Figure S05: (A) & (B) Concentration of dissolved oxygen profiles in top and bottom hemisphere of oxygenic photogranules N°: 5 under different bulk conditions (Table V.1) (C)& (D) Modelled spatial distribution of metabolic activity in photogranule N°: 5 Green: maximum net photosynthesis. Grey: 5-fold maximum heterotrophic respiration.

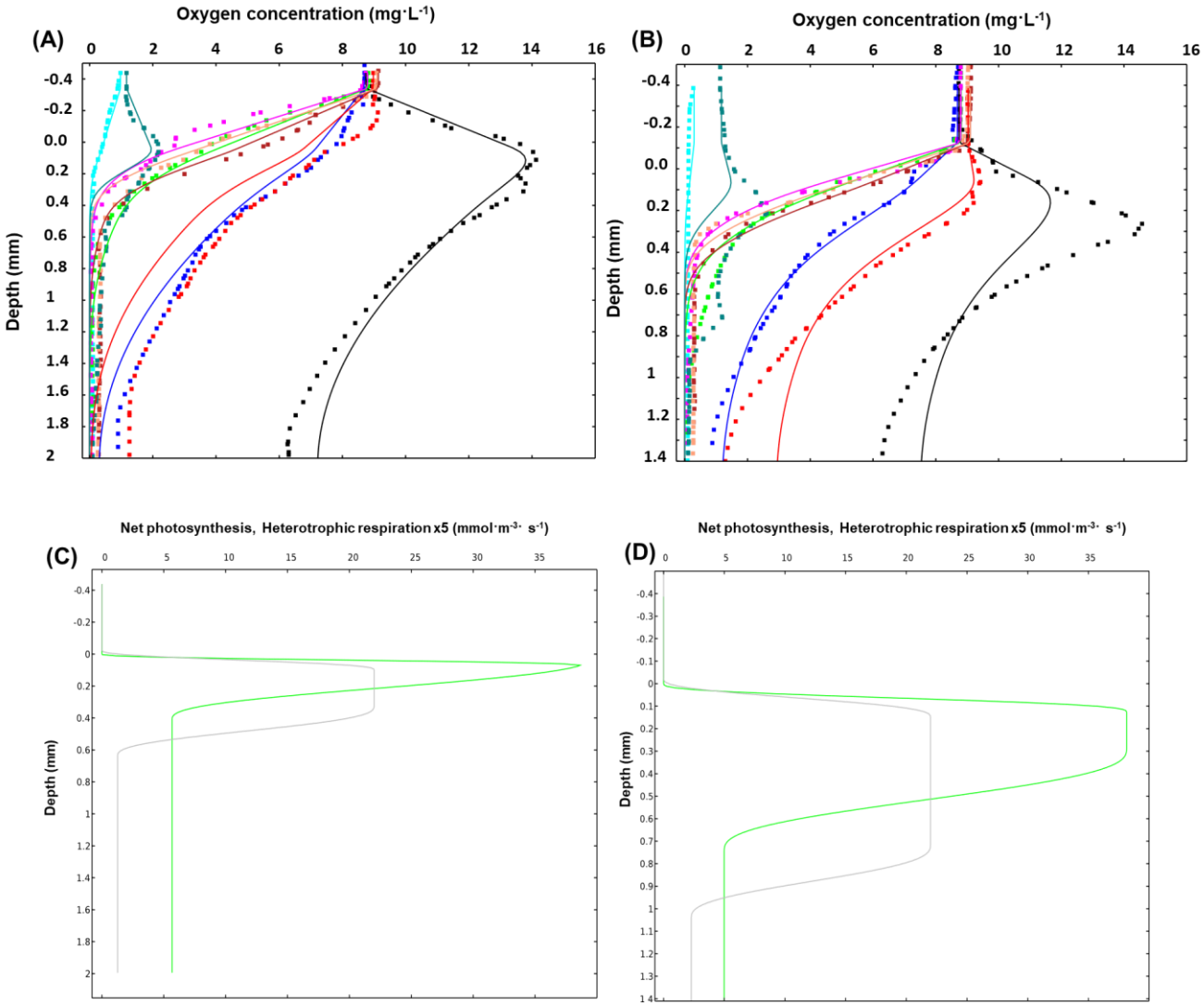

Figure S06: (A) & (B) Concentration of dissolved oxygen profiles in top and bottom hemisphere of oxygenic photogranules N°: 6 under different bulk conditions (Table V.1) (C)& (D) Modelled spatial distribution of metabolic activity in photogranule N°: 6. Green: maximum net photosynthesis. Grey: 5-fold maximum heterotrophic respiration

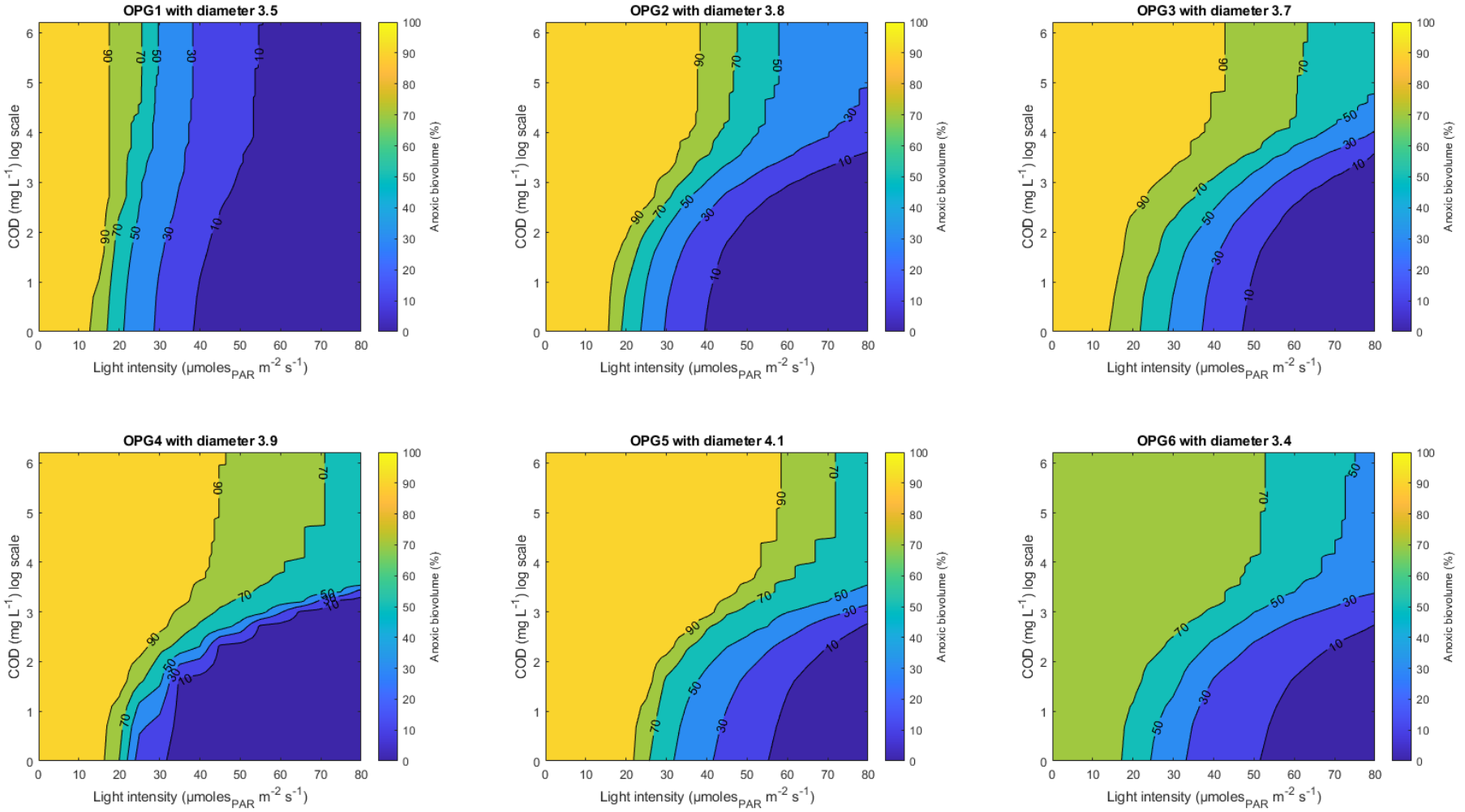

Figure S07: Percentage of anoxic biovolume (%) of the different photogranules size mm under different conditions of dCOD (mg/L log scale), light intensity and 0.05 mg/L oxygen concentration in the bulk.

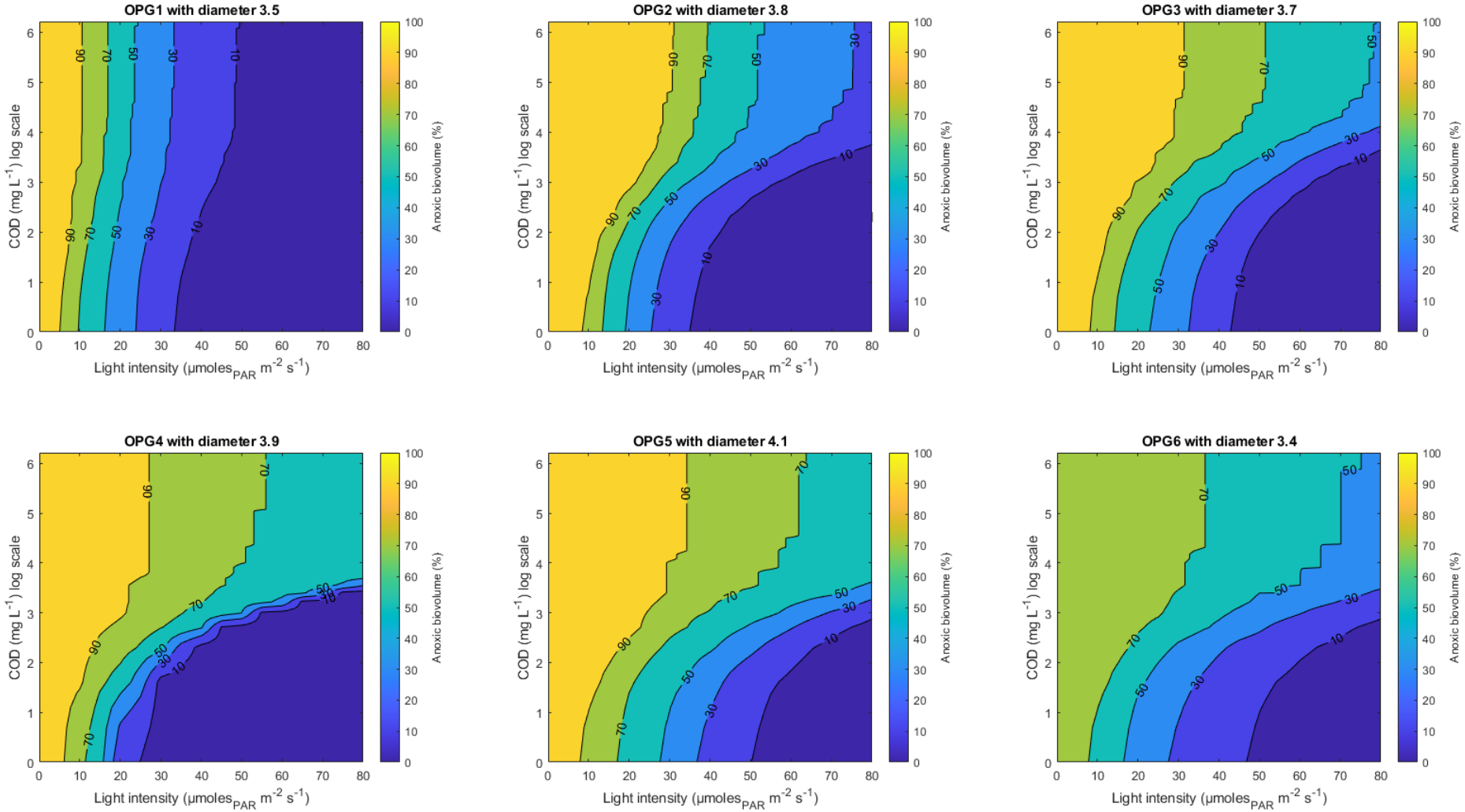

Figure S08 : Percentage of anoxic biovolume (%) of the different photogranules size mm under different conditions of dCOD (mg/L log scale), light intensity and 1 mg/L oxygen concentration in the bulk.

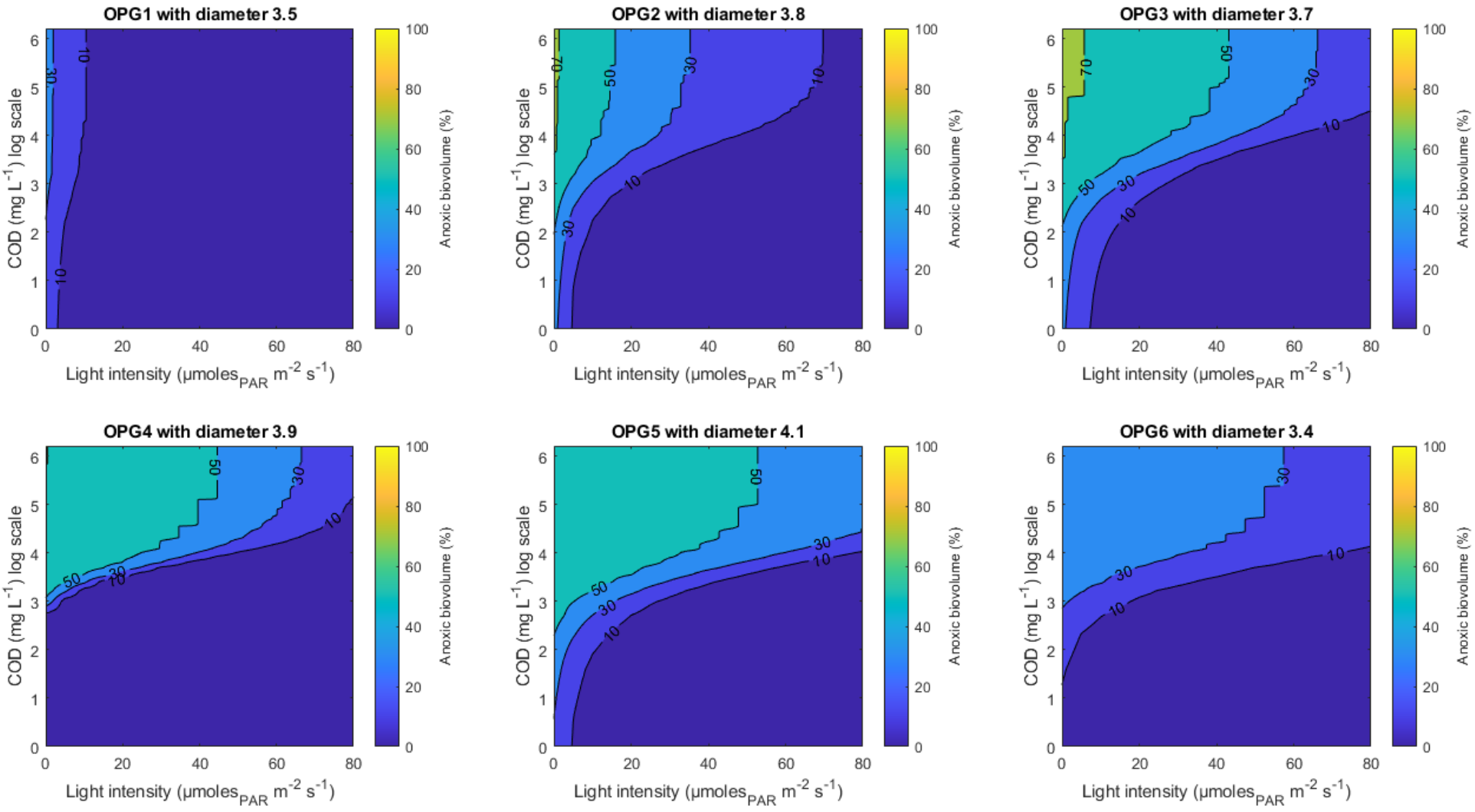

Figure S09: Percentage of anoxic biovolume (%) of the different photogranules size under different conditions of dCOD (mg/L log scale), light intensity and 8.9 mg/L oxygen concentration in the bulk.

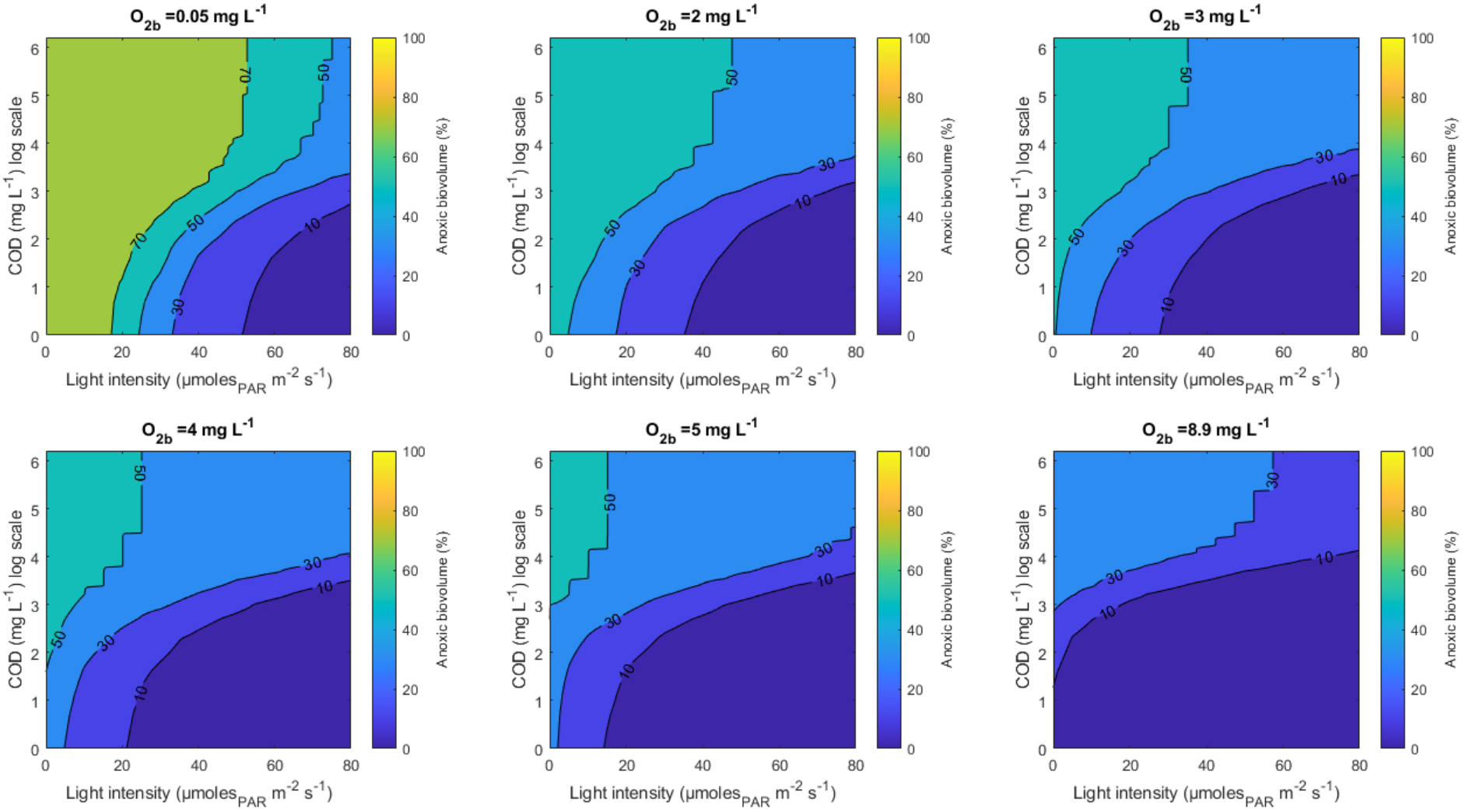

Figure S010 : Percentage of anoxic biovolume (%) of photogranule N°: 6 with diameter 3.4 mm under different conditions of dCOD (mg/L log scale), light intensity and different oxygen concentration in the bulk.

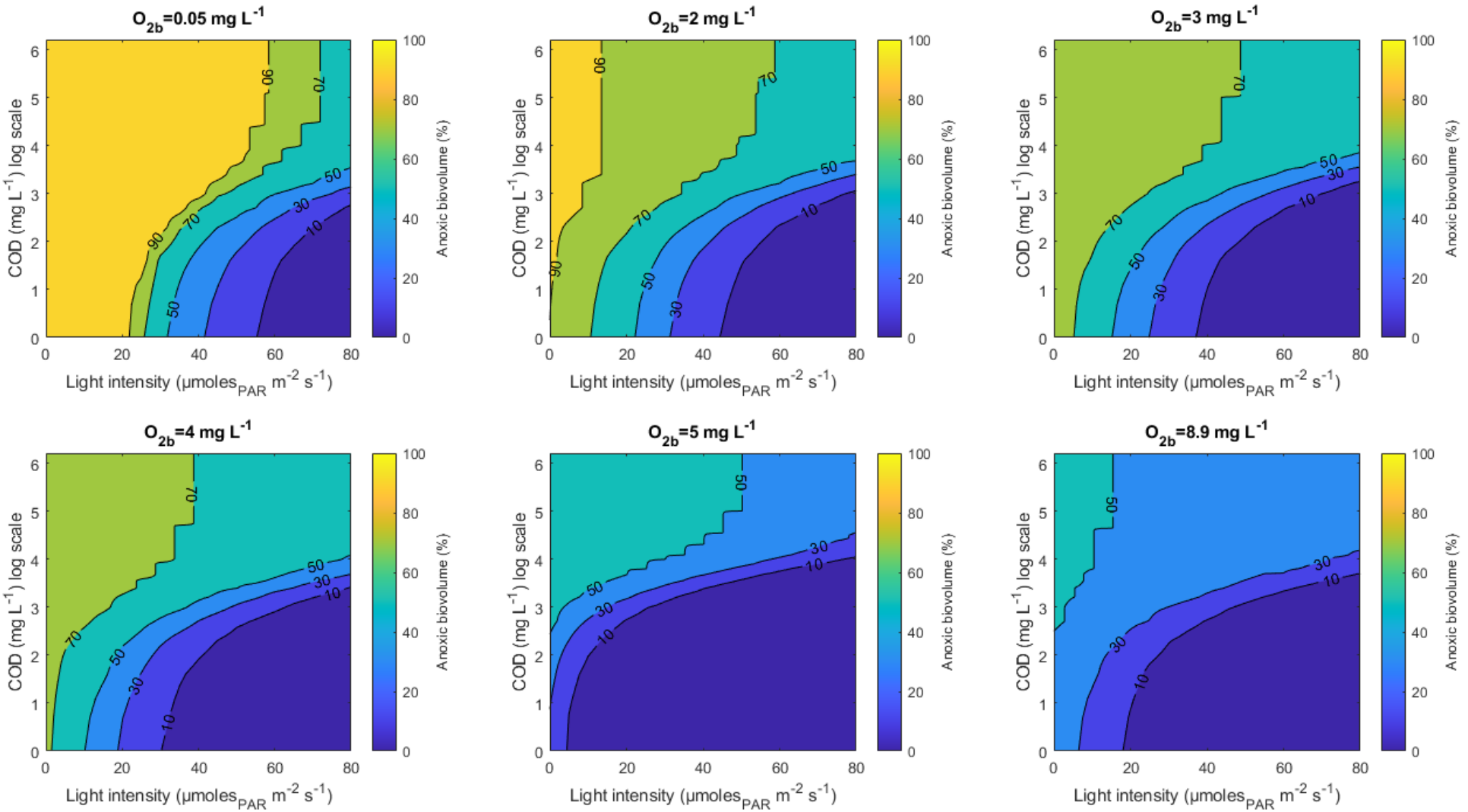

Figure S011: Percentage of anoxic biovolume (%) of photogranule N°: 5 with diameter 3.9 mm under different conditions of dCOD (mg/L log scale), light intensity and different oxygen concentration in the bulk.